Contribution of NMR and Raman imaging for modeling and rationalization of the impregnation process of metallic precursors in porous media

Leonor Duarte Mendes Catita

N°d'ordre NNT : 2017LYSE162

THESE de DOCTORAT DE L'UNIVERSITE DE LYON
opérée au sein de
l'Université Claude Bernard Lyon 1

Ecole Doctorale 206
Ecole Doctorale de Chimie de Lyon

Spécialité de doctorat : Chimie

Soutenue publiquemente le 05/12/2017, par :
Leonor Duarte Mendes Catita

Contribution of NMR and Raman imaging for modeling and rationalization of the impregnation process of metallic precursors in porous media

Devant le jury composé de :

FLORIAN, Pierre	Ingénieur de Recherche (Université d'Orléans)	Rapporteur
LAMONIER, Carole	Professeure (Université de Lille)	Rapporteure
BABONNEAU, Florence	Directrice de Recherche (Université de Paris 6)	Examinatrice
DANIELE, Stephane	Professeur (Université Lyon 1)	Président du jury
FAURE, Paméla	Chargée de Recherche (IFSTTAR)	Examinatrice
LORIDANT, Stephane	Chargé de Recherche (Université Lyon 1)	Examinateur
MAUGE, Francoise	Directrice de Recherche (ENSICAEN)	Examinatrice
PICHON, Christophe	Responsable Industriel (IFPEn)	Directeur de thèse
DELPOUX, Olivier	Responsable de laboratoire (IFPEn)	Invité
GUENNEAU, Flavien	Maître de Conférences (Université Paris 6)	Invité
QUOINEAUD, Anne-Agathe	Ingénieure de Recherche (IFPEn)	Invitée

UNIVERSITE CLAUDE BERNARD - LYON 1

Président de l'Université	M. le Professeur Fréderic FLEURY
Président du Conseil Académique	M. le Professeur Hamda BEN HADID
Vice-président du Conseil d'Administration	M. le Professeur Didier REVEL
Vice-président du Conseil Formation et Vie Universitaire	M. le Professeur Philippe CHEVALIER
Vice-président de la Commission Recherche	M. Fabrice VALLÉE
Directrice Générale des Services	Mme Dominique MARCHAND

COMPOSANTES SANTE

Faculté de Médecine Lyon Est – Claude Bernard	Directeur : M. le Professeur G.RODE
Faculté de Médecine et de Maïeutique Lyon Sud – Charles Mérieux	Directeur : Mme la Professeure C. BURILLON
Faculté d'Odontologie	Directeur : M. le Professeur D. BOURGEOIS
Institut des Sciences Pharmaceutiques et Biologiques	Directeur : Mme la Professeure C. VINCIGUERRA
Institut des Sciences et Techniques de la Réadaptation	Directeur : M. X. PERROT
Département de formation et Centre de Recherche en Biologie Humaine	Directeur : Mme la Professeure A-M. SCHOTT

COMPOSANTES ET DEPARTEMENTS DE SCIENCES ET TECHNOLOGIE

Faculté des Sciences et Technologies	Directeur : M. F. DE MARCHI
Département Biologie	Directeur : M. le Professeur F. THEVENARD
Département Chimie Biochimie	Directeur : Mme C. FELIX
Département GEP	Directeur : M. Hassan HAMMOURI
Département Informatique	Directeur : M. le Professeur S. AKKOUCHE
Département Mathématiques	Directeur : M. le Professeur G. TOMANOV
Département Mécanique	Directeur : M. le Professeur H. BEN HADID
Département Physique	Directeur : M. le Professeur J-C PLENET
UFR Sciences et Techniques des Activités Physiques et Sportives	Directeur : M. Y.VANPOULLE
Observatoire des Sciences de l'Univers de Lyon	Directeur : M. B. GUIDERDONI
Polytech Lyon	Directeur : M. le Professeur E.PERRIN
Ecole Supérieure de Chimie Physique Electronique	Directeur : M. G. PIGNAULT
Institut Universitaire de Technologie de Lyon 1	Directeur : M. le Professeur C. VITON
Ecole Supérieure du Professorat et de l'Education	Directeur : M. le Professeur A. MOUGNIOTTE
Institut de Science Financière et d'Assurances	Directeur : M. N. LEBOISNE

Acknowledgments

Tout d'abord, je tiens à remercier Cécile Barrere-Tricca (directrice de la direction Physique et Analyse à l'IFPEn) et Arnaud Baudot (chef du département Caractérisation des Matériaux) pour leur aimable accueil au sein de la direction.

Je remercie également Didier Espinat (directeur expert de la direction Physique et Analyse) pour avoir partagé avec moi son expertise et son intérêt dans mon travail.

Je voudrais également remercier à Pierre Florian et Carole Lamonier qui ont accepté d'être rapporteurs de ce mémoire et aussi à Florence Babonneau, Stephane Daniele, Paméla Faure, Stephane Loridant et Francoise Maugé d'avoir accepté de participer à ce jury de thèse.

Je tiens aussi à remercier Christophe Pichon, mon directeur de thèse, pour le suivi de mon travail, sa réactivité et ses conseils.

J'adresse un remerciement particulier à mes encadrants: Anne-Agathe Quoineaud et Olivier Delpoux, qui ont fait de ce travail une réussite. Je vous remercie d'avoir partagé votre expertise, j'ai beaucoup appris avec vous. Je vous remercie aussi de m'avoir fait confiance, pour tous vos conseils, pour vos encouragements et pour la bonne ambiance au cours de ces trois années de thèse.

Au sein du département, je remercie d'abord Frédéric Neyret-Martinez pour son aide dans la préparation de mes expériences IRM et pour son accueil au sein du laboratoire. Je remercie Corinne Sagnard pour la formation en Imagerie Raman, sa patience pour m'écouter en période de doute et pour son amitié. Je remercie à tous les techniciens du Pôle 5 et tout particulièrement Frédéric Filali, Laurent Lemaître, Emanuel Soyer et Cedric Plassais pour leur aide et bonne ambiance. Je n'oublie pas Thomas Coquet, David Gonçalves et Alexandre Jouve pour leur aide dans certaines manipulations. Merci aussi à l'équipe de microscopie pour toutes les analyses et leur réactivité à mes demandes.

Je remercie Christophe Boyer (chef du département de Réactions et Modélisation de Réacteurs) et Jean-Marc Schweitzer pour leur intérêt dans ce travail. Un merci particulier à Jean-Marc pour sa collaboration, son expertise et son aide dans la partie de modélisation. Je remercie aussi Elsa Jolimaitre pour son aide et sa rigueur dans la relecture de la dernière partie de ce mémoire. Je tiens aussi à remercier Maxime Moreaud pour sa disponibilité et pour m'avoir aidé en tout ce qui concerne le traitement d'image. En plus, je remercie Alexandra Chaumonnot, Anne-Claire Dubreuil et Denis Uzio pour tous les échanges et discussions.

Je remercie aussi Mickael Rivallan, Loic Sorbier, Antoine Gédéon (UPMC) et Flavien Guenneau (UPMC) pour leur participation aux réunions d'avancement de thèse.

Un grand merci à mes amis de pause cafés, apéros, soirées, pique-nique , co-voiturages et pour tous les très bons moments passés ensemble: Marisa, Sonia, Svetan (je ne pourrais pas oublier de remercier le bus magique!), Fabien, Dina, Matthieu, Clément, Kévin, Coralie, Rick, Caroline, Rosa, Mafalda, Pedro, Alberto et Guillaume.

E agora em português: um especial obrigado aos meus pais por terem feito com que chegasse até aqui. Todos os vossos esforços, a vossa amizade, a vossa confiança...acho que nunca vou ter palavras para vos agradecer. As saudades foram muitas ao longo destes três anos, mas espero que tenha valido a pena.

E por fim a ti, Rúben: obrigada por tudo, obrigada por me apoiares sempre.

Résumé

Cette thèse s'inscrit dans le domaine de la catalyse hétérogène pour des applications en raffinage et en pétrochimie. Nous avons choisi d'étudier le cas des catalyseurs d'hydrotraitement qui sont largement utilisés dans les procédés de conversion du pétrole en carburant. Ces catalyseurs sont constitués d'une phase métallique sulfurée (à base de Mo, Ni, Co) supporté sur un support poreux inorganique (généralement l'alumine).

Dans ce travail, nous nous sommes intéressés à la compréhension et la modélisation de la première étape de préparation d'un catalyseur d'hydrotraitement: l'étape d'imprégnation. Cette étape est déterminante pour l'activité catalytique vu qu'à ce stade sont fixées la dispersion initiale des particules métalliques et la structure chimique des espèces métalliques en interaction avec le support.

Une méthodologie de caractérisation *in-situ* basée sur la technique d'imagerie RMN et sur la technique d'Imagerie Raman a été développée. Elle permet de suivre temporellement et spatialement le transport des espèces au sein de la porosité avec une résolution spatiale de l'ordre de 39×39µm et d'identifier la nature chimique des espèces déposées sur le support avec une résolution spatiale de 16.2×16.2µm respectivement.

L'amélioration des techniques pour atteindre de telles résolutions spatiales et temporelles ont permis de caractériser l'étape d'imprégnation en termes de phénomènes physiques (capillarité et diffusion) et chimiques (adsorption) et permet de proposer des descripteurs clés de cette étape.

En conclusion, ces travaux permettront un meilleur contrôle de l'étape d'imprégnation et donc du profil de distribution des précurseurs actifs et par là même de la phase active.

Mots-clés : Acide citrique, Adsorption, Catalyseur, Cobalt, Diffusion, Hydrotraitement, Imagerie Raman Imprégnation, IRM, Molybdène, Nickel

Abstract

This thesis is in the field of heterogeneous catalysis for applications in refining and petrochemistry. More particularly, a focus on hydrotreatment catalysts is made as they are widely used in the processes of converting petroleum into fuel. These catalysts consist of a transition metal sulfide phase (based on molybdenum, cobalt or nickel) supported on an inorganic porous support (generally alumina).

The aim of this work is to understand and rationalize the first step of the preparation of a hydrotreatment catalysts: the impregnation step. This step is of crucial importance for the catalytic activity, since at this stage most of the initial dispersion and the chemical structure of the metal species are determined.

An *in-situ* characterization methodology based on the Magnetic Resonance Imaging (MRI) and Raman Imaging techniques has been developed. MRI provides temporal and spatial information of the transport of species in impregnation solution within the porosity with a spatial resolution of 39×39 μm. Raman Imaging gives information about chemical nature of the species deposited on the support with a spatial resolution of 16.2×16.2 μm.

The improvement of these techniques to achieve such spatial and temporal resolutions allows one to characterize the impregnation step in terms of physical (capillarity and diffusion) and chemical (adsorption) phenomena and to identify the key descriptors of this step.

In conclusion, this work allows a better control of the impregnation step and therefore of the distribution profiles of the active metal precursors and in the end of the active phase.

Keywords: Adsorption, Catalyst, Cobalt, Citric acid, Diffusion, Hydrotreatment, Impregnation, Molybdenum, MRI, Nickel, Raman Imaging

Résumé Substantiel

«Apport des spectroscopies d'imageries RMN et Raman pour la modélisation et la rationalisation des processus d'imprégnation de précurseurs métalliques dans des matériaux poreux»

Dans l'industrie du raffinage, les procédés d'hydrotraitement (HDT) sont largement utilisés pour éliminer le soufre (hydrodésulfuration - HDS), l'azote (hydrodénitrogénation - HDN) ou encore les métaux, tels que le nickel et le vanadium (hydrométallation - HDM). Ces procédés permettent d'obtenir des carburants propres et il existe aujourd'hui une demande forte liée aux différentes politiques environnementales (par exemple, la norme Euro 7).

Le perfectionnement des performances des procédés d'HDT s'appuie sur le développement de nouveaux catalyseurs plus actifs et plus sélectifs. Parmi les différents axes de recherche, l'optimisation du site actif du catalyseur est un enjeu majeur. La compréhension de l'étape d'imprégnation qui est la première étape de préparation d'un catalyseur hétérogène est donc un challenge important.

Le catalyseur hétérogène d'HDT est constitué d'une phase d'un sulfure de métal du groupe VI (généralement le Mo ou le W) promue on non par un métal du groupe VII (Co ou Ni) et d'un support de type inorganique comme l'alumine, la silice ou encore la silice-alumine. Sa préparation est réalisée en plusieurs étapes : imprégnation, traitements thermiques et sulfuration. Dans ce travail, nous nous sommes particulièrement intéressés à l'étape d'imprégnation. En effet, c'est l'étape d'imprégnation qui permet de déterminer la quantité de précurseurs métalliques introduits et c'est aussi à ce moment clé que sa nature chimique peut être orientée.

Lors de l'imprégnation, le transport du précurseur métallique est influencé à la fois par des phénomènes physiques (capillarité et diffusion) et chimiques (interaction de surface). Ces phénomènes seront impactés par les propriétés de la solution (concentration d'ion métallique, viscosité, pH) et par les propriétés de support (état de la surface, caractère hydrophobe ou hydrophile, porosité et tortuosité).

La plupart des travaux de la littérature concernant l'étape de préparation du catalyseur HDT rapportent seulement la caractérisation des espèces en solution. En revanche, l'étape d'imprégnation a fait l'objet de peu d'études en raison de la difficulté de la caractérisation des interfaces en milieu aqueux.

Des travaux rapportés dans la littérature ont montré tout l'intérêt de la technique d'Imagerie RMN (IRM) pour suivre *in-situ* l'étape d'imprégnation des catalyseurs supportés. En effet, l'IRM peut donner accès à la compréhension du transport de solutions d'imprégnation complexes. D'autre part, ces résultats peuvent être complétés par des caractérisations par spectrométrie Raman pour identifier la

nature chimique des espèces en solution. Ces deux techniques permettre d'obtenir des informations spatiales (IRM et Imagerie Raman) et temporelle (IRM).

Ainsi, ce travail porte sur la caractérisation de l'étape d'imprégnation en termes de phénomènes physiques (capillarité et diffusion) et chimiques (interaction de surface), afin d'identifier les descripteurs clés de cette étape et améliorer la préparation des catalyseurs d'hydrotraitement. Plus particulièrement, il s'agit de suivre spatialement et temporellement le transport des espèces dans la solution d'imprégnation au sein de la porosité à l'aide de l'IRM et de la cartographie Raman. Cette thèse est consacrée à la préparation de catalyseurs Ni(Co)MoP/γ-Al_2O_3.

En présence de métaux et plus encore lorsqu'ils sont paramagnétiques comme le Ni ou le Co, l'observation du signal RMN peut être difficile. Dans ce travail, une approche IRM innovante a été développée pour suivre *in-situ* l'étape d'imprégnation à partir d'une solution composée de plusieurs précurseurs métalliques en présence ou non de phosphore ou d'un additif organique. L'IRM a permis d'accéder à la répartition spatiale de toutes les espèces métalliques ou non au sein de l'extrudé. L'imagerie Raman a permis une identification de la nature chimique des espèces de molybdène déposées sur le support. La méthodologie mise en place a été validée par comparaison avec les distributions métalliques obtenues lors d'une caractérisation par Microsonde de Casting.

Dans une première étude, les phénomènes mis en jeu lors de **l'imprégnation de solutions modèle composés de Ni (Co) avec la présence éventuelle d'un acide carboxylique** ont été étudiés en modifiant les paramètres de la solution, tels que la concentration en métal dans la solution et le pH. Ces expériences modèles ont contribué à l'élaboration d'un modèle mathématique proposé pour rationaliser l'étape d'imprégnation. Ce modèle permet de décrire le transport par diffusion et par capillarité, mais aussi de prendre en compte les phénomènes d'adsorption sur la surface de l'alumine. De plus, ce modèle est sensible à la concentration d'ions métalliques, à la présence d'un additif (en ajoutant un mécanisme d'adsorption compétitive) et à la méthode d'imprégnation (imprégnation à sec ou en régime diffusionel).

Nous avons pu montrer que la capillarité est un processus instantané. Le transport par diffusion semble en compétition avec les interactions avec la surface de l'alumine. Plus particulièrement, nous avons confirmé qu'il s'agit d'une interaction covalente et sélective avec certains groupes hydroxyles de la surface de l'alumine. Lors de l'ajout d'acide citrique à une solution de nitrate de nickel, deux effets différents peuvent être obtenus. En conditions de pH acide (en-dessous de 3), un mécanisme d'adsorption compétitive entre les ions citrate et nickel est mis en évidence. Une affinité plus élevée entre le citrate et l'alumine est suggéré, le nickel ne semble pas complexé par les ions citrate. Au contraire, en augmentant le pH de la solution afin de favoriser la réaction de complexation entre le citrate et le nickel, une affinité plus élevée entre le complexe nickel-citrate et la surface est observée.

Dans une deuxième partie, cette étude a été étendue à la **préparation de catalyseurs d'hydrotraitement, Ni(Co)MoP/γ-Al_2O_3 additivés ou non**. L'IRM est appliquée, pour la première fois, pour suivre *in-situ* l'étape d'imprégnation des catalyseurs d'hydrotraitement avec une solution aqueuse composée simultanément de molybdène, de cobalt et de phosphore en présence d'acide citrique. Plusieurs phénomènes ont été ici évalués, notamment l'impact de la présence de phosphore sur le transport des espèces Mo, la compétition éventuelle d'adsorption entre le P, le Co et le Mo et les effets de la présence d'acide citrique.

Nous avons mis en évidence une affinité préférentielle entre l'additif (phosphore et acide citrique) et la surface de l'γ-alumine.. Nous montrons aussi un impact fort du pH local qui peut être fortement impacté par la présence de phosphore.

Ces travaux permettront un meilleur contrôle de l'étape d'imprégnation et donc du profil de distribution des précurseurs et par là même de la phase active. De plus il pourrait être intéressant d'étendre l'IRM à d'autres noyaux et tout particulièrement le ^{31}P afin d'obtenir une quantification plus précise des espèces phosphates. Dans ce dernier cas, il pourrait être nécessaire d'utiliser les outils innovants d'imagerie à l'angle magique pour améliorer la résolution du signal.

Table of Contents

Nomenclature

Abbreviations

AHM – Ammonium Heptamolybdate

CPMG – Carr-Purcell-Meiboom-Gill

CA – Citric Acid

CCD - Charge Coupled Device

Cit - Citrate

EDTA – Ethlenediaminetetraacetic acid

EPMA – Electron Probe Microanalysis

FID – Free Induction Decay

FOV – Field of View

HDM – Hydrodemetallation

HDN – Hydrodenitrogenation

HDO – Hydrodeoxygnetaion

HDS – Hydrodesulfurization

HDT – Hydrotreatment

HPA – Heteropolyanions

HYD – Hydrogenation

IHP - Inner Helmholtz Plane

M – Metal atom

MRI - Magnetic Resonance Imaging

NMR – Nuclear Magnetic Resonance

OHP – Outer Helmholtz Plane

PZC – Point of Zero Charge

RAREVTR – Rapid Acquisition with Relaxation Time Enhancement

RF – Radiofrequency

SE – Spin-Echo

SNR – Signal to Noise Ratio

SPI – Single Point Imaging

ST – Slice Thickness

TE – Echo Time

TLM –Three Layer Model

TMIS – Transition Metal Ionic Species

TMS - Transition Metal Sulfide

T_1- Relaxation Time related with longitudinal magnetization

T_2 - Relaxation Time related with transverse magnetization

t_p – Encoding time

TR – Repetition Time

UV – Ultraviolet

WUV – Water Uptake Volume

X - Heteroatom

Terminology

Parameter	Description	Units
*	Active site	-
C_i^b	Concentration of element i in impregnation solution	$mol.m^{-3}$
C_i^p	Concentration of element i inside the pore	$mol.m^{-3}$
C_i^*	Concentration of element i in the adsorbed phase	$mol.kg^{-1}$
D	Molecular diffusion coefficient	$m^2.s^{-1}$
D_e	Effective diffusion coefficient	$m^2.s^{-1}$
D_s	Surface diffusion coefficient	$m^2.s^{-1}$
d	Diameter	m
f	Friction coefficient	-
I	Apparent signal intensity profiles	-
I_0	Average radial signal intensity	-
K	Permeability	m^2
	Scaling factor	-
k_i	Kinetic constant of first order for reaction i	$m^3.mol^{-1}.s^{-1}$
L	Catalyst pellet length	m
p1	Pulse length	s
pl1	Transmitter power level	dB
q_t	Total concentration of active sites (OH groups)	$mol.kg^{-1}$
q_*	Concentration of active sites (OH groups)	$mol.kg^{-1}$
R_{pore}	Pore radius	m
S_{BET}	Specific surface area	$m^2.g^{-1}$
$\bar{\mathbf{v}}$	Penetration rate of liquid	$m.s^{-1}$
z	Distance travelled by liquid into the pore	m

Greek letters

Parameter	Description	Units
α	Excitation pulse	°
γ	Interfacial tension	$N.m^{-1}$
ε	Porosity of the solid	-
η	Viscosity	Pa
θ	Wetting angle of the wetting fluid on the surface of the capillary	°
μ	Dynamic viscosity	Pa.s
$\mu_{i,j}$	Stoichiometric coefficient i for a given element j	-
ρ_s	Catalyst solid density	$kg.m^{-3}$

General Introduction

The present thesis is in the field of the preparation of hydrotreament catalysts (HDT). In refining industry, hydrotreatment processes are mainly used to reduce the content of sulfur (hydrodesulfurization - HDS), nitrogen (hydrodenitrogenation - HDN) and metals, such as nickel and vanadium (hydrodemetallation - HDM) from the different petroleum streams [1]. Nowadays, there is a growing need of HDT processes due to two main reasons: emergent need of reduction of sulfur content on gasoline and diesel and increasing use of heavier crudes with high amount of sulfur [2].

To enhance the performance of HDT processes, improvement and development of new catalysts, more active and selective is of crucial importance. Several axes of research can be enumerated, but **optimization of the active site by understanding its genesis, from the impregnation step to the formation of the active phase is a major challenge**.

A heterogeneous HDT catalyst consists of:

- A metal sulfide phase composed of a metal from group VI (generally molybdenum, Mo or tungsten, W) promoted or not by a metal from group VIII (usually nickel, Ni or cobalt, Co). Typically, the concentration by weight of these metals is 1-4% for Co and Ni, 10-25% for Mo and 12-25% for W [1]. These Co(Ni)MoS structures are responsible for the promotion of the catalytic activity.
- An inorganic oxide support, commonly γ-alumina, δ-alumina, silica or even silica-alumina. At industrial scale, the support is a pre-shaped material (pellet, extrudate). Normally, trilobal and quadrulobal extrudates are used to prevent mass transfer limitations [1].

Depending on the objective of the hydrotreatment process, different catalysts formulations can be chosen. For HDS reactions with low pressure (i.e., less than 30 bar), CoMo catalysts are the most active catalysts. Whereas NiMo catalysts are preferred for HDN and hydrogenation reactions [1].

One of the ways to improve the activity and selectivity of hydrotreatment catalysts is to increase the quantity of promoted Co(Ni)Mo(W)S sites. To this end, one can increase the quantity of deposited metal precursors during impregnation step, while maintaining a high dispersion and improving the interactions with the support surface. Therefore, understanding the mechanisms that take place during the impregnation step is a major challenge for the genesis of an optimized active phase. At this stage, the dispersion, the molecular structure of metallic precursors and, to some extent, their interactions with the support are determined.

During impregnation, the transport of the active precursor is influenced by physical and chemical phenomena. The first group concerns the transport by diffusion, while the second one mostly concerns the interactions between the active phase and the support surface, which includes adsorption. Both of

them are influenced by the solution properties (metal ion concentration, viscosity, pH) and the support properties (state of the surface, hydrophobic or hydrophilic character of the support).

Most of the works concerning the preparation step of HDT catalyst only report on the characterization of species in solution [3]. Few studies about the impregnation step have been performed [4–8] due to the difficulty to characterize the support-impregnation solution interfaces in aqueous medium.

Therefore, **the aim of this thesis is to improve the characterization of the impregnation step and to rationalize this preparation step by taking into account the transport by diffusion (physical phenomena) and surface interaction (chemical phenomena). In this study, an innovative characterization methodology based on a spatial and temporal location of the metal precursors inside the catalyst pellet through MRI and Raman Imaging techniques has been developed.**

This manuscript is divided into five chapters. In **Chapter I**, a review of the state of art about the main components involved in the impregnation step from the support to the different metal precursors and additives used in solution are presented. The main physicochemical phenomena occurring during impregnation, namely capillarity, diffusion and surface interaction are described. A review of the characterization techniques mainly used in the literature to monitor the transport of the metals during impregnation and to characterize the main descriptors that influence this step is present. At the end of this chapter, the objectives and the strategy of the thesis are defined.

In **Chapter II**, the experimental procedure concerning the preparation of impregnation solutions and the choice of the catalyst support as well as the impregnation method are explained. The different characterization techniques used in this work, namely Magnetic Resonance Imaging (MRI) and Raman Imaging are described.

In **Chapter III**, the methodology adopted to implement and validate MRI as a technique to characterize the impregnation step with a solution composed of at least two elements is described. Additionally, MRI-Raman Imaging characterizations are applied to study the phenomena that take place during the impregnation of a model solution as well as the impact of the solution properties on this preparation step.

Chapter IV is dedicated to the application of this methodology to the study the impregnation step of a complex case, *i.e.*, a hydrotreatment catalyst composed simultaneously of molybdenum, cobalt and phosphorus. The impact of phosphorus on distribution profiles within a molybdenum based oxide catalyst is investigated. Besides, the impact of the nature of metal promotor (either nickel or cobalt) is also considered. The effect of a carboxylic acid as a way to the modify interactions between metallic precursors and the surface support upon impregnation is also evaluated.

Finally, **Chapter V** concerns the development and validation of a mathematical model to describe the physicochemical phenomena that occur during impregnation step based on MRI experimental results of Chapter III. Moreover, the main descriptors that influence this step are also highlighted.

At the end of Chapter V, the general conclusions of this work and some perspectives for future work are discussed.

Chapter I – Bibliographic Study

A general overview of the hydrotreatment (HDT) process has already been presented in the General Introduction. Since the main objective of this thesis consists in studying the impregnation step, this bibliographic study gives first a brief description of the preparation process of a HDT catalyst. In particular, impregnation step is fully described, concerning the support, metal precursors and additives mainly used. Secondly, the main physicochemical processes involved in impregnation of HDT catalysts are described. In the third part of this chapter, the most suitable characterization techniques to monitor the metal ions during impregnation and to characterize the main parameters that influence this step are presented. The objectives of this work and the strategy adopted are defined at the end of the chapter.

1. Preparation of hydrotreatment catalysts: focus on impregnation step

The preparation of heterogeneous catalysts can generally be divided into four main stages [9,10]:

1. Deposition of the precursors of the active phase onto the support
2. Ageing step, which allows the solute to diffuse throughout the support pore volume
3. Removal of the liquid solvent by drying and potentially a calcination step
4. Transformation of the precursor into the active component

For almost all supported catalysts, one of the major challenges in their preparation is to disperse uniformly the precursors of the active phase. In general, different processes such as impregnation, ion exchange, anchoring, grafting, spreading and wetting and deposition-precipitation can be used to deposit the active precursor onto the support [11]. In the particular case of HDT catalysts, impregnation is the most common method [1,12–14]. Figure 1 gathers the different steps of hydrotreatment catalysts synthesis.

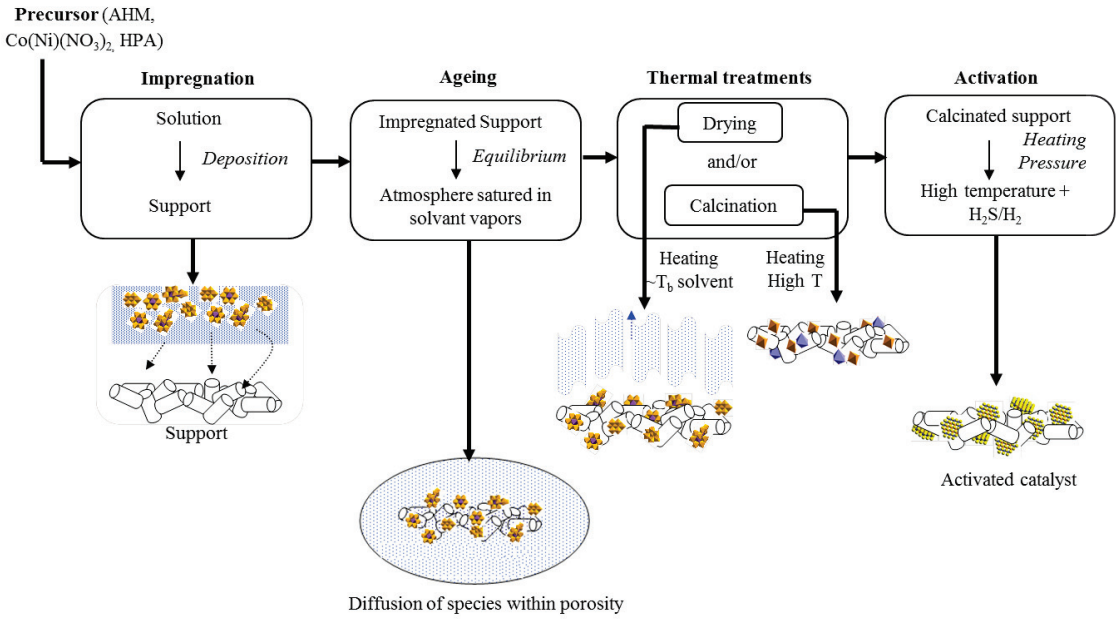

Figure 1 - Stages of hydrotreatment catalysts preparation (adapted from [3])

First, **impregnation solution** is prepared by dissolving the metal salts or oxides in water. At this stage, some additives may be added, such as orthophosphoric acid or organic molecules so as to increase the metal solubility and modify the chemical (speciation of metal species, pH) and physical (viscosity) properties of the solution. The addition of such compounds is discussed in section 1.3.2.

The next step is the **impregnation** itself, during which the solution penetrates within the support porosity. Many phenomena occur during this step involving diffusion/transport properties of the metal solution and interactions between metal/support, which are discussed in section 2.

At laboratory scale, the catalyst is stored at room temperature in a solvent-saturated atmosphere, so that the active phase precursors are distributed in the entire pore volume. This step of **ageing** allows the solution to diffuse throughout the support pore volume. The ageing step is followed by **thermal treatments** (drying and eventually calcination). The last stage consists in the **sulfidation** of metal species to obtain the catalytic active sites. **These two last steps, thermal treatments and sulfidation, are not the subject of this work, therefore they will not be described in this bibliographic study.**

1.1. Impregnation step

The impregnation step is a key step for the genesis of the active phase. Depending on the operating conditions applied, the metal particle size, the aggregation state and the nature of the metal species in interaction with the surface can be modified. The method of introducing the impregnation solution is also critical. Two protocols are conventionally used: dry impregnation and equilibrium adsorption.

Dry impregnation, so-called incipient wetness impregnation, comprises filling the pore volume of the support with the corresponding volume of the precursor solution. It enables to control the exact amount of the deposited species and it does not require a filtration step. Finally, it allows saving a not negligible quantity of solvent [12,15]. This type of impregnation is characterized by a strong exothermicity (due to the replacement of the solid-gas interface by a solid-liquid interface), by an establishment of a capillary pressure in pores and by porosity filling [16].

Equilibrium adsorption (so-called **impregnation in excess**) consists in immersing the support in a large excess volume of the impregnation solution. In order to improve the exchange between the solution and the support, the system is stirred during this step. The quantity of precursors deposited on the support is not known in advance.

Some important parameters must be pointed out [12,15]:

- Viscosity of solution, μ: this parameter indicates the resistance to flow due to shearing. High viscosity solutions tends to limit the diffusion process during impregnation.
- Solubility of the precursor in the impregnation solution and the quantity of the solution linked to the WUV (Water Uptake Volume) determines the maximum content of depositable precursors of the active phase.
- Support properties (porosity and surface) influence the quantity of metal deposited and the dispersion of the active phase. Porosity influences not only the capillary action, but also the permeability of support. For a strong surface interaction and no inhibitor, a low permeability

leads to egg-shell profiles, while homogeneous metal profiles are obtained with a high permeability, Figure 2.

Figure 2 – Metal profile: homogeneous and eggshell distributions (where the shaded area represents the metal) [9]

In dry impregnation, the deposition of the active element takes place in the bulk solution inside the pores, which is known as bulk deposition (see Figure 3). Due to solvent evaporation during drying step, deposition occurs by precipitation in the liquid phase inside the pores [17]. The supported particles formed by bulk deposition are weakly bound to the surface of the support and can be transformed into oxide supported nanoparticles during thermal treatments [14]. This type of deposition leads to a poor dispersion of the supported phase.

In equilibrium adsorption, the deposition takes place during equilibration at the interface developed between the support surface and the aqueous solution (see Figure 3). This interface results from the electrically charged surface of the support. This mode of deposition results in relatively small supported nanoparticles [14] and consequently in a high dispersion of the supported phase.

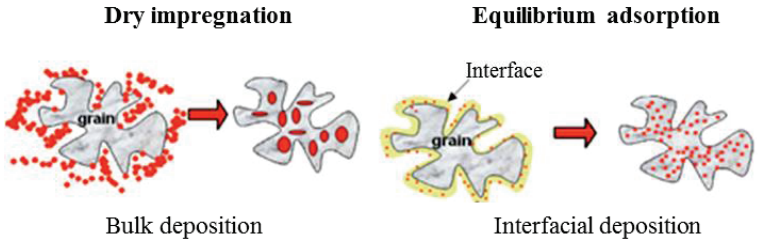

Figure 3 – Deposition of the active component by bulk deposition and interface deposition (adapted from [14])

1.2. Catalyst support: focus on alumina

Alumina, which is an oxide material, is widely used as support for HDT catalysts. Depending on its structure, different types of alumina are considered: the transition alumina (which include here gamma (γ-Al_2O_3), delta (δ-Al_2O_3) and theta (θ-Al_2O_3) alumina) and α-alumina. The main characteristics of interest of this material are low cost, thermal and chemical (hydrothermal) stability, porous network and surface properties.

The **porous network** of alumina comes from the 3D arrangement of the slabs, which defines the meso porous scale of the porous network. Alumina is characterized by its high specific surface area (from 10 to 350 m^2/g), which allows the dispersion of the active phase. Other characteristics such as its porous

volume (from 0.5 to 1 cm^3/g), its pore diameter (from few to hundred nanometers) and its porous distribution (mono and multi modal pore distribution) make this kind of support widely used [18]. Additionally, the porous structure is defined by parameters such as the tortuosity (τ), while the porous volume is related with the porosity (ε), which is defined by the ratio between the porous volume (cm^3/g) and the total network volume ($0 \leq \varepsilon \leq 1$) of the support.

The alumina surface is covered with hydroxyl (OH) groups. The **surface density of OH groups** of the support influences the interaction metal/surface, which may have a strong impact on the dispersion of the supported phase [19] and on the particle size. Moreover, OH groups also play an important role on the local pH and, therefore, on the chemical nature of the metal species in solution. These OH groups are represented as Al-OH and they may behave as acid or basic Brønsted sites [16], depending on the pH of the medium, see Eq. 1 and Eq. 2. Besides the Brønsted acid sites (*i.e.*, an OH group that transfers its proton), Lewis acid sites (*i.e.,* unsaturated Al^{3+} cations that are electron acceptors) also contribute to the acidic character of alumina. Different models have been proposed by Knözinger et al. [20] and Busca et al. [21] to characterize the OH groups of alumina. Digne et al. [22] proposed a model by calculating the OH-stretching frequencies based on Density Functional Theory (DFT). For further details concerning these calculations see [23].

$$Al - OH + H^+ = Al - OH_2^+ \quad \textbf{Eq. 1}$$

$$Al - OH = Al - O^- + H^+ \quad \textbf{Eq. 2}$$

These acid or basic sites of alumina together with the **point of zero charge (PZC)** determine the electrostatic interaction between the support and the metal precursor. PZC corresponds to the value of pH for which the number of positive and negative charges on the surface cancels. If the impregnating solution has a pH below the PZC, protonation of surface OH groups takes place, the net charge of the surface is therefore positive, which leads to anion adsorption. On the contrary, for a pH higher than the PZC, the oxide particles tend to adsorb cations [14,16]. For γ-alumina, PZC is approximately 8 [14,16].

Furthermore, the **support shape** is another important property, since it determines the geometric surface of the material. To avoid diffusion problems extrudates with polylobal shapes have been developed in order to maximize the ratio between the external surface of the extrudate and its volume [12].

1.3. Precursors of the active phase

The historical precursors of HDT catalysts are based on ammonium heptamolybdate (AHM) tetrahydrate ($(NH_4)_6Mo_7O_{24}.4H_2O$) and cobalt or nickel nitrate hexahydrate ($Co(NO_3)_2.6H_2O$ or

$Ni(NO_3)_2.6H_2O$) [12,14]. To remove the nitrogen, which can be harmful for catalyst activity especially for HDT of middle distillates, a calcination step is required.

Additionally, phosphorus is widely used as a third element in industrial HDT catalysts [24]. This component enhances the HDS activity of alumina-supported catalysts due to the following reasons:

- Decreasing of the metal-support interactions, which limits the formation of phases such as $Co(Ni)Al_2O_4$ [25]
- Increasing of the dispersion of Co and Mo species [26], which hinders the precipitation of AHM
- Impact on sintering

Yet, by adding high contents of P, catalyst poisoning may occur [27].

Typically, phosphorus is added in the form of phosphoric acid [12]. The order by which phosphorus is added to the impregnation solution, as well as the Mo/P ratio, influence the nature of the species obtained and their deposition onto the support. For instance, once using a phosphorus-containing Mo solution impregnated in alumina, the formation of Mo heteropolyanions (HPA) is favoured: the majority part of phosphorus is presented as $H_xP_2Mo_5O_{23}^{(6-x)-}$ (the most favorable in thermodynamic terms [28]) and the rest remains in the form of free phosphates. This last component reacts with the hydroxyl groups of alumina, leading to an amorphous $AlPO_4$ layer and an increase in the pH inside the pores [29–31].

1.3.1. *Heteropolyanions (HPA)*

To improve the preparation of HDT catalysts, different approaches have been proposed, such as using new starting compounds for the preparation of impregnation solutions. One of the main examples is the use of heteropolyanions (HPA) as oxide precursors [32–36] due to the following reasons:

- Solubility of HPA in water is higher than conventional precursors, allowing higher metal concentrations to be deposited into the support
- Stability of their structure in high concentration solutions
- Redox and acidic properties, which are related to the presence of the heteroatom
- Enhance the promoting effect of Co (or Ni) ions
- Hinder the dissolution of the support, which is one of the chemical limitations observed during impregnation

HPAs are polyoxometalates with one or more central organizing polyhedrons (the central atom is called the "heteroatom," e.g., Si^{4+}, Ge^{4+}, P^{5+}, or As^{5+}) around which metal-oxygen polyhedrons (e.g., Mo^{6+} or W^{6+}) are arranged. These metal oxide clusters have the following general formula:

$[X_xM_mO_y]^{q-}$, where X is the heteroatom and M is the metal atom. The formation and evolution of HPA species during the impregnation step are somewhat related with the dissolution of the support and precipitation of different species.

Heteropolyanions are classified according to the composition (M/X ratio) and structure and the most common ones are:

- Keggin structure $[XM_{12}O_{40}]$, [37]
- Anderson structure $[XM_6O_{24}]$, [33,38–42]
- Strandberg structure $[X_2M_5O_{23}]$, [43]
- Dawson structure $[X_2M_{18}O_{62}]$, [44]

In following paragraphs, a focus on Anderson and Strandberg structure is done.

Carrier et al [45] reported on the formation of an **Anderson type** alumino heteropolymolybdate, $[Al(OH)_6Mo_6O_{18}]^{3-}$, denoted by $AlMo_6$. This HPA, which is favoured in acidic medium (pH of 4-6) results from the dissolution of alumina due to interactions with Mo species. The adsorbed precursor transfers electron density to the surface aluminum atoms, which enables the detachment of surface Al^{3+} ions from the support lattice by weakening the Al-O bonds [15]. The reaction of the heptamolybdate with the dissolved alumina species is given in Eq. 3.

$$6H^+ + Al^{3+} + 6MoO_4^{2-} \leftrightarrow [Al(OH)_6Mo_6O_{18}]^{3-} \qquad \textbf{Eq. 3}$$

Besides the pH, the ageing time also influences the formation of an Anderson HPA. The formation of this structure is only significant after a significant time of ageing (few hours). Additionally, $AlMo_6$ structure is preserved in the adsorbed phase [45].

Concerning the **Strandberg structure,** the most common anion is based on molybdenum, $P_2Mo_5O_{23}^{6-}$. The formation of this heteropolyanion occurs by simultaneously impregnation of phosphorus and molybdenum (see Eq. 4) [39]. The solubility of the HPA structure is higher than the AHM salt.

$$12MO_4^{2-} + 10H^+ + 2PO_4^{3-} \rightarrow [PMo_5O_{23}]^{6-} + 5H_2O \qquad \textbf{Eq. 4}$$

Besides the use of HPA, organic additives are widely used during the preparation of HDT catalysts, since they improve the chemical and physical properties of the impregnation solution. The most common organic additives are described below.

1.3.2. *Organic additives*

Impregnation solutions used to prepare HDT catalysts are usually acidic solutions and high metal loadings are often used. However, high metal concentration leads to viscosity and solubility issues,

which tend to limit the diffusion process. Moreover, if the solubility limits of the species are exceed, precipitation occurs, leading to uncontrolled and heterogeneous deposition of the precursors. Consequently, a non-uniform dispersion of the active phase is obtained. Therefore, the use of organic additives can help meeting some objectives of this study, due to the following main reasons:

- Increasing metal solubility
- Shifting to higher pH levels the precipitation of oxide precursors, which allows the metal precursor available in solution at a pH value suitable for impregnation [46]
- Modifying the interaction between the metallic precursors and the surface support, which is another chemical limitation observed during the impregnation step

Furthermore, organic molecules can be introduced at different stages:

- In the support synthesis to control the growth of alumina particles and to optimize textural properties [47].
- Before impregnation of metallic precursors on the support (also called pre-impregnation) to reduce the interaction strength between the metallic precursors of the impregnation solution and the hydroxyl groups on the surface [48]. For instance, it can hinder the formation of $AlMo_6$ structure [49].
- With metallic precursors in the impregnation solution (also called co-impregnation) to improve the solubility of species and to favour heteropolyanions formation [50]. In this case, the additive agent may act as a complexing agent, which increases the active phase dispersion.
- After impregnation and drying (also called post-impregnation or post-additivation) to redistribute metallic species on the surface, by hindering metal/support interactions [51].

Organic additives can be divided into two groups:

- **Complexing agents** based on amino-acid (for instance, EDTA (ethylenediaminetetraacetic acid) [52–54]) or carboxylic acid (the most used is citric acid [4,7,28,55–61]).
- **Non-complexing agents** that act mostly on the precursors (by improving dispersion and formation of new species, for instance). They are based on glycol-type additives (for instance, ethylene glycol [62,63], polyethylene glycol [64], and triethylene glycol ([62,65,66]) Two different groups can be distinguished: glycols and ethers of glycols.

Besides that, **sulfiding agents** should also be considered. However, they play an important role during activation, which is not in the scope of this work and therefore they are described.

In the following paragraphs, a focus on the effect of citric acid on the impregnation solution is done.

Citric acid is a tricarboxylic acid, whose speciation in solution highly depends on the pH according to Eq. 5 to Eq. 7, where Cit states for $C_6H_5O_7$ [67].

$$H_3Cit + H_2O \underset{K_{a1}}{\Longleftrightarrow} H_2Cit^- + H_3O^+ \qquad pKa_1 = 3.07 \qquad \textbf{Eq. 5}$$

$$H_2Cit^- + H_2O \underset{K_{a2}}{\Longleftrightarrow} HCit^{2-} + H_3O^+ \qquad pKa_2 = 4.74 \qquad \textbf{Eq. 6}$$

$$HCit^{2-} + H_2O \underset{K_{a3}}{\Longleftrightarrow} Cit^{3-} + H_3O^+ \qquad pKa_3 = 5.40 \qquad \textbf{Eq. 7}$$

Bergwerff et al. [4,7,28,68] studied the complexation of molybdenum by citrate. Catalysts were prepared by pore volume impregnation, using AHM as precursor (15 wt% MoO_3). Citrate was added at the same time of metal precursor. In this study, Raman spectroscopy was performed to monitor the transport of Mo-complexes inside alumina pellets [68]. They reported that the solubility of Mo^{6+} ions is increased in the presence of citrate due to the formation of Mo-citrate complexes. These complexes hinders support dissolution, and therefore the formation of $Al(OH)_6Mo_6O_{18}^{3-}$ species. Additionally, they proposed the following equilibria depending on the pH [68]:

$$4Mo(Hcitrate)O_3^{3-} + 8H^+ \leftrightarrow Mo_4(Hcitrate)_2O_{11}^{4-} + 2H_4citrate + H_2O \qquad \textbf{Eq. 8}$$

$$MoO_4^{2-} + Hcitrate^{3-} + H^+ \leftrightarrow Mo(citrate)O_3^{4-} + H_2O \qquad \textbf{Eq. 9}$$

Figure 4 gathers the different molecular structures of Mo-citrate complexes proposed by Bergwerff [58].

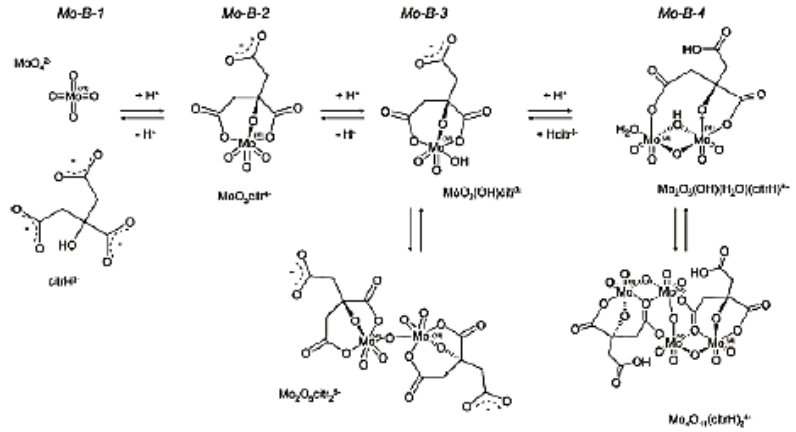

Figure 4 - Different molecular structures of Mo-citrate complexes as a function of pH [58]

Furthermore, the macrodistribution of different types of Co^{2+}-citrate complexes inside alumina-supported catalysts was also studied by Bergwerff [58]. Pore volume impregnation was carried out as impregnation method. The impregnation solution contained cobalt nitrate, sodium hydroxide and citric acid, which was added at the same time as the other precursors. The pH and the concentration of citric acid were varied and the different molecular structures of cobalt-citrate complexes were identified.

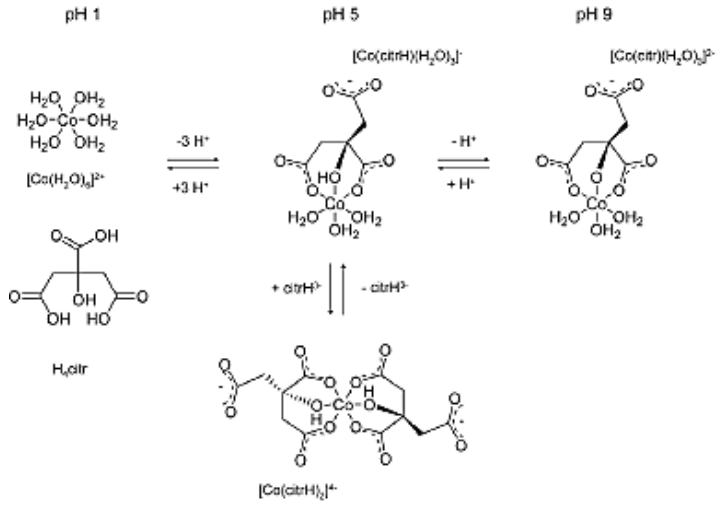

Figure 5 - Different molecular structures of cobalt-citrate complexes as a function of pH [58]

Figure 6 shows the speciation of the different Co-citrate molecular structures as a function of the pH and citrate concentration [7]. Under acidic conditions (pH equal or lower than 1.5), there is no complexation of cobalt ions by citrate, because the carboxylate functions are protonated. Complexation occurs at a pH of approximately 5-6. They proposed that the coordination of cobalt ions takes place through two carboxylate groups and the hydroxyl group of citrate.

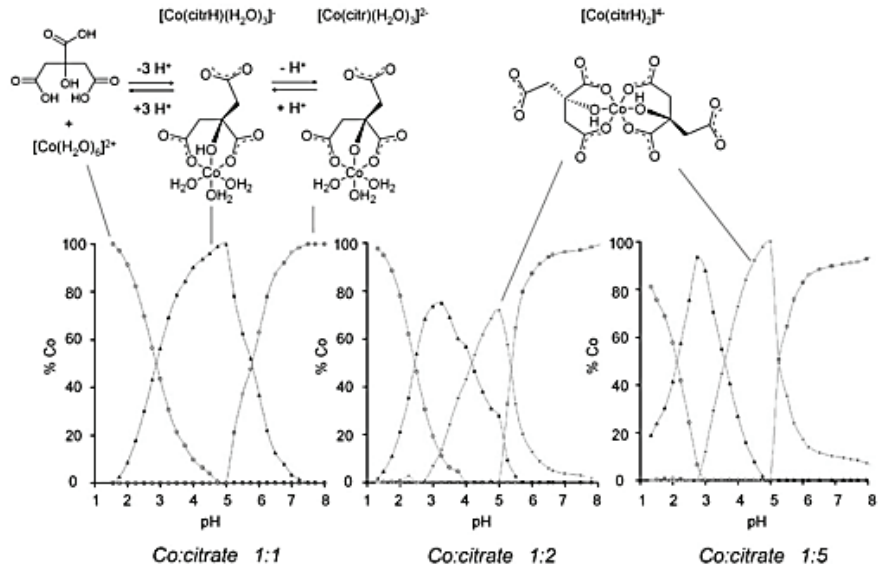

Figure 6 - Speciation of the different molecular structures of cobalt-citrate complexes as a function of pH and citrate concentration [7]

Rinaldi et al. [59] also reported on the effect of citric acid on the impregnated precursor in the case of CoMo/Al catalysts. The effect of citric acid depends on the pH, the CA:Mo ratio and the order by which the additive was added. When citric acid was added by co-impregnation, the formation of a Co–CA complex, such as $[Co(C_6H_5O_7)_2]^{4-}$ was reported for CA:Mo ratios higher than 0.6. These observation are in agreement with the conclusions obtained by Bergwerff et al. [7]. Moreover, these

Co-CA complexes were found to be well dispersed on the surface. They also demonstrated that the addition of citric acid by post-impregnation strongly influences the textural properties of the final catalyst. For instance, in this case, specific surface was increased.

Klimov et al. [60] also proposed a molecular structure of a bimetallic complex between Co, Mo and citrate – $Co_2[Mo_4(C_6H_5O_7)_2O_{11}]$. Citric acid and AHM were used to synthesize the bimetallic compound. NMR data showed the formation of the labile complex $[Mo_4(C_6H_5O_7)_2O_{11}]^{4-}$ with Co^{2+} ions. As Figure 7 shows, cobalt coordinates with the tetrameric anion via the terminal oxygen atom. Oxygen atom is bonded to the outer molybdenum atom *via* the two types of carboxyl groups, one that is not coordinated with Mo and the other monodentate carboxyl group coordinated to the outer Mo via the oxygen atom bonded to the central carbon atom of the citrate ligand.

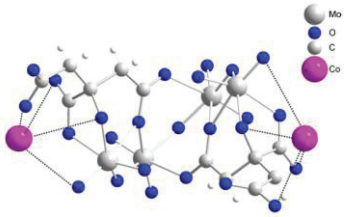

Figure 7 - Molecular structure of a bimetallic complex formed between Co, Mo and citrate – $Co_2[Mo_4(C_6H_5O_7)_2O_{11}]$ [60]

Finally, the effect of citric acid when nickel is present in impregnation solution has also been investigated. According to the literature, complexation of nickel ions by citrate requires the deprotonation of two carboxylic acid groups. Each citrate acts like a tridentate ligand to one nickel atom, coordinated through two carboxylate groups and one hydroxyl group (see Figure 8). The octahedral coordination sphere of nickel remains stable by three bound water [67,69].

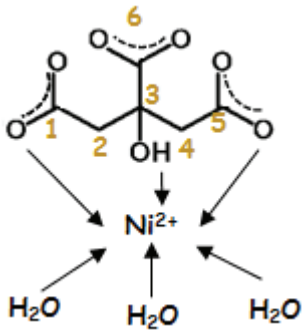

Figure 8 – Nickel citrate species (based on [7,67])

Klimova et al. [70] performed an extensive study of nickel-citrate solutions prepared by co-impregnation. They reported on an increase of solubility of nickel ions in the presence of citric acid. Figure 9 shows the structure and composition of Ni-citric acid complexes depending on solution pH and concentration of citric acid. For very acidic pH, solvated nickel is presented (pH between 0 and

1.8). NiH_2Cit^+, NiHcit and $Ni(HCit)(Cit)^{3-}$ complexes are formed at intermediate pH (between 1.8 and 6.5), and $Nicit_2^{4-}$ is formed at pH ranging from 6.5 to 9.5.

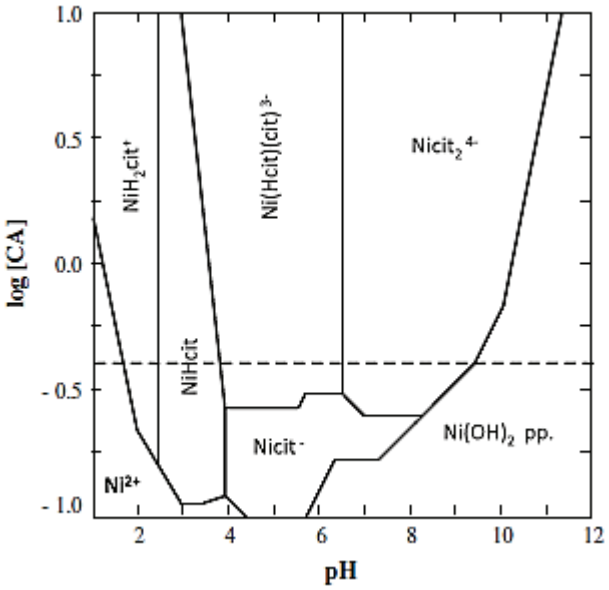

Figure 9 – Diagram for aqueous solution Ni(II)-CA ($[Ni(II)_{aq}]$=0.167M and $[CA]_{aq}$=0.437M) [70]

On the contrary, Bentaleb et al. [71] stated that citric acid does not act as a complexing agent to an important extent when it is only introduced as an additive into the nickel nitrate solutions, and only causes a pH decrease.

Yin et al. [61] also studied the effect of citric acid in NiMoP catalysts supported on alumina. Citric acid led to a decrease of the pH of the impregnation solution. On the other hand, its coordination with Ni^{2+} ions leads to the formation of new species based on Mo. It also prevented the decomposition of Mo-P HPA structures. These studies were done thanks to Raman spectroscopy.

To conclude, the effects of complexing additives are the following:

- Stabilize the surface aluminum atoms and reduce the formation of $AlMo_6$, resulting from dissolution of the support on contact with impregnation solution
- Decrease the interactions between metallic precursors of the impregnation solution and the support during impregnation
- Redistribute the metal species on the surface, allowing the development of new species (such as HPA), which are more easier to sulfide forming a highly dispersed active phase
- Solvate the metal species in solution to promote impregnation and so to enhance the active phase dispersion
- May also be suitable to coordinate cobalt and/or nickel to delay its sulfidation

In the previous paragraphs, a number of components involved in the impregnation step were described: support, solvent, metal precursors and additives. In the following section, a detailed description of the different phenomena that occur during the impregnation step, which are dependent on these components is given.

2. Physicochemical phenomena involved in impregnation

2.1. Chemical behavior of Mo, Co and Ni in solution

Molybdenum lies with the transition metal of the periodic table and its electronic configuration is [Kr] $4d^5$ $5s^1$. Molybdenum (Mo^{6+}) speciation in solution is strongly dependent on pH: at basic pH, only MoO_4^{2-} is present in solution, while acidic pH favours polymerization reactions leading to $Mo_7O_{24}^{6-}$ ions, for instance (see Eq. 10) [14].

$$8H^+ + 7MoO_4^{2-} \leftrightarrow Mo_7O_{24}^{6-} + 4H_2O \qquad \textbf{Eq. 10}$$

Figure 10 represents the evolution of Mo species as a function of pH, at two different Mo concentrations of Mo [3]. For instance, for higher Mo concentration (0.8M [Mo]), either hepta- or octamolybdates are formed.

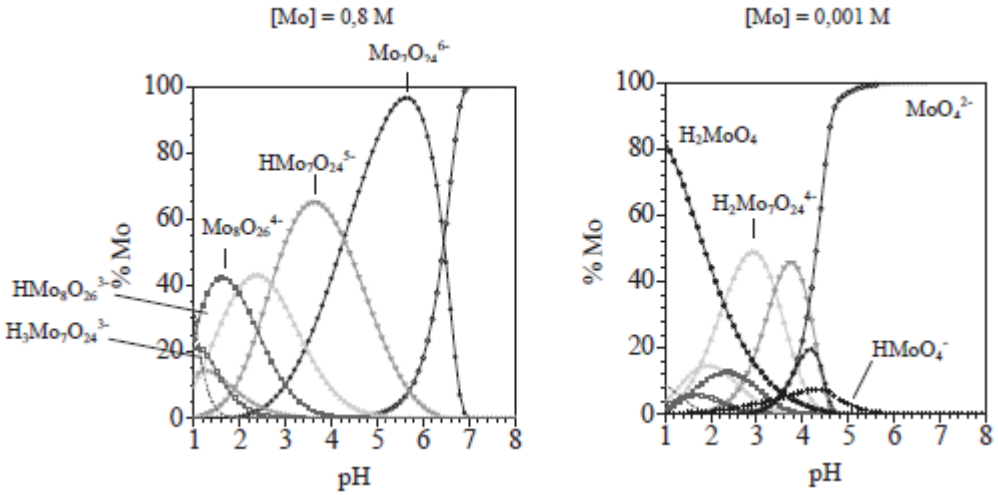

Figure 10 – Diagram of evolution of Mo species as a function of pH, at two different concentrations of Mo in solution [3]

Figure 11 represents the possible stable equilibrium stages of Mo/water system, also known as Pourbaix diagram or potential-pH equilibrium diagram [72]. For instance, Mo^{3+} is stable in reducing acidic medium. Despite, it has a propensity to spontaneously oxidize given either MoO_3 or MoO_2.

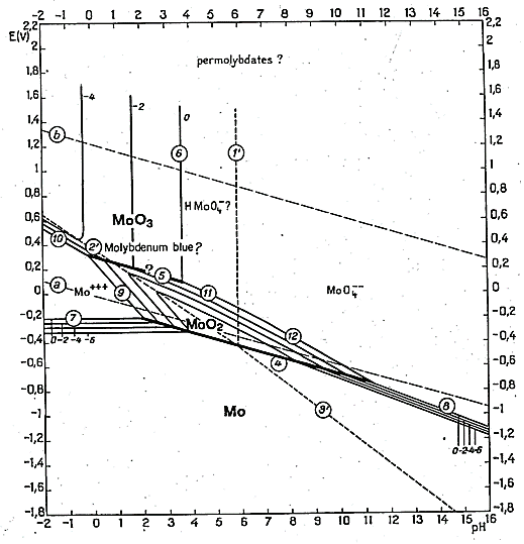

Figure 11 - Pourbaix diagram of Mo/water system at 25°C [72]

When a partial dissolution of the support occurs, Al(III) is present and new Mo species are formed. Analyzing Figure 12, $Al(OH)_6Mo_6O_{18}^{3-}$ known as Anderson-type heteropolyanion is the most predominant species at the natural pH of an AHM solution.

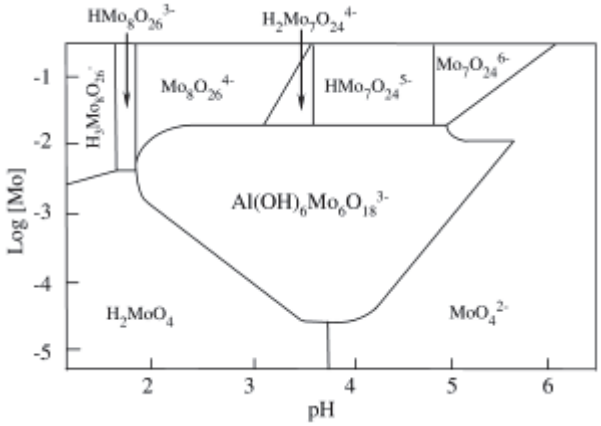

Figure 12 – Diagram of Mo(VI) species in presence of Al(III) [73]

Cobalt is also a transition metal, whose electronic configuration is [Ar] $3d^7$ $4s^2$. The odd number of electrons confers paramagnetic behaviour to cobalt [17]. The only cobalt species used for depositing cobalt on catalytic supports are in the form of $Co(H_2O)_6^{2+}$, which have an octahedral structure (see Figure 13) [17].

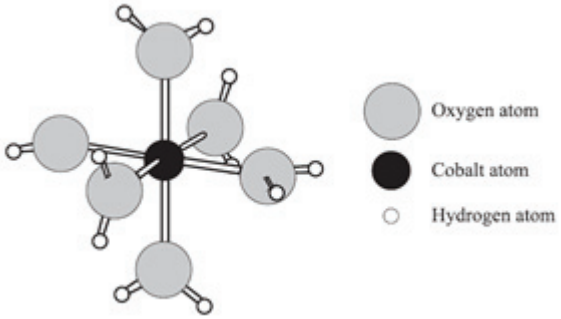

Figure 13 - Octahedral structure of the hydrated cobalt species $Co(H_2O)_6^{2+}$ [17]

$Co(H_2O)_6^{2+}$ is quite stable in a wide range of pH and concentration values, as shown in Figure 14 [17].

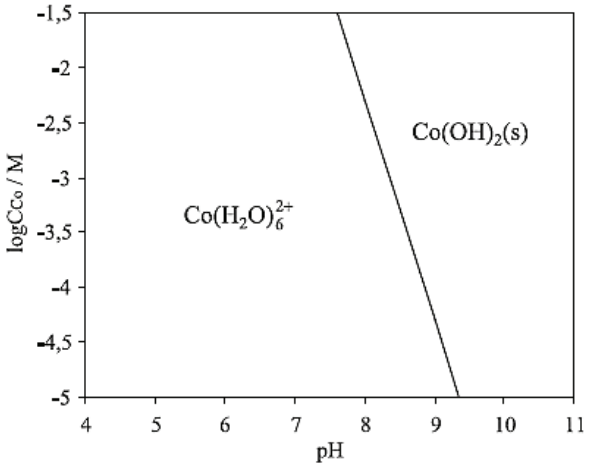

Figure 14 – Predominant cobalt species at 25 °C and I = 0.1 M. The line denote conditions where the two predominant species have equal concentrations. The hydrolysis products $CoOH^+$ are not presented because its concentration is very low compared to that of the other species [17].

The Pourbaix diagram of Co/water system is shown in Figure 15 [72]. The chemistry of cobalt is simpler than molybdenum. In this case, only $Co(H_2O)_6^{2+}$ is stable in solution. In contrast, Co^{3+} ion is a powerful oxidizing agent that decomposes water.

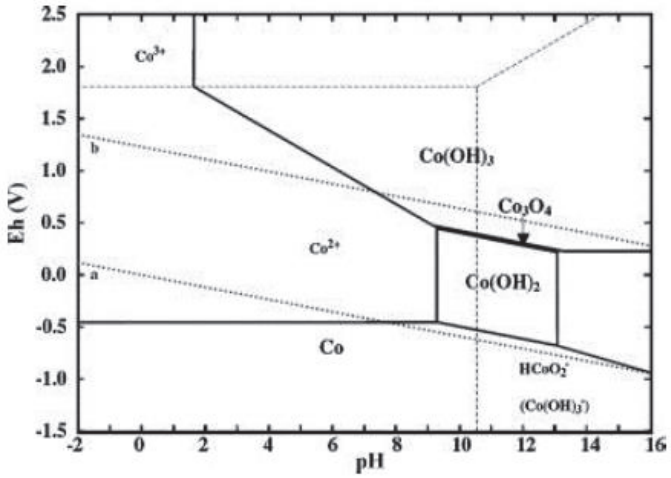

Figure 15 - Pourbaix diagram of Co/water system at 25°C [72]

As the other two metals, **nickel** is also a transition metal, with the following electronic configuration: [Ar] $3d^8\,4s^2$. Nickel compounds exhibit oxidation numbers between 0 and +4, being the most common one +2 due to the relatively low energies in the s and d levels [65]. Therefore, nickel is known for its divalent compounds, such as nickel nitrate.

Complexes of nickel (+3) show low stability and are strong oxidizing agents, which cause fast oxidation of water. Therefore, they are unstable in acidic solutions. The species with oxidation number IV are very strong oxidation agents.

Figure 16 represents the different Ni species in solution as function of the pH. For instance, $Ni(H_2O)_6^{2+}$ predominates for pH lower than 6. Moreover, the neutral complex $[Ni(OH)_2(H_2O)_4]$ is stable for basic pH (10.5-12.5). This complex is also in equilibrium with $[Ni_4OH)_4]^{4+}$, $[Ni(OH)_3(H_2O)_3]^-$ and $[Ni(OH)_4(H_2O)_2]^{2-}$ [74].

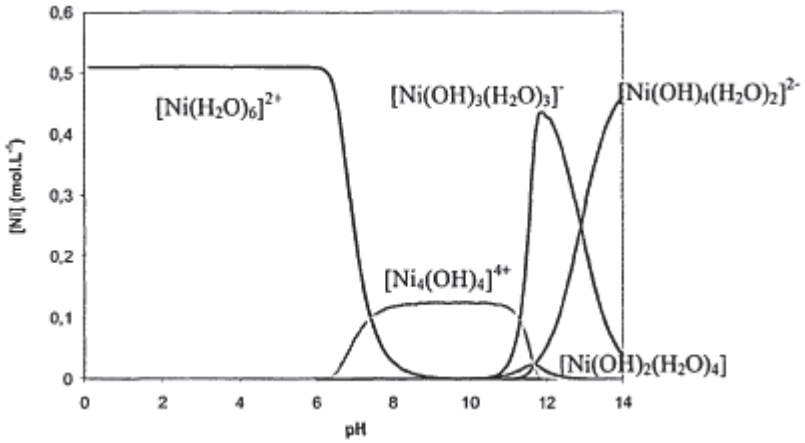

Figure 16 - Predictions of hydrolysis products of Ni(II) species in 0,5M [Ni] aqueous solution and I=1,3M as a function of pH [74]

The neutral complex (also denoted as $[Ni(OH)_2(H_2O)_4](aq)$) is the precursor of the solid phase $Ni(OH)_2$ (s). Furthermore, this solid phase is more stable than the neutral complex. For basic pH, this solid phase can lead to the formation of $Ni(OH)_3^-$, according to Eq. 11 and Eq. 12.

$$Ni(OH)_2(s) \leftrightarrow Ni(OH)_2(aq) \qquad \textbf{Eq. 11}$$

$$Ni(OH)_2(s) + OH^- \leftrightarrow Ni(OH)_3^- \qquad \textbf{Eq. 12}$$

The predominant polymer in Ni^{2+} solutions is $[Ni_4OH)_4]^{4+}$ [75], which is formed for pH less than 10.5. However, this species rapidly disappears as a result of the precipitation of $Ni(OH)_2$, which is stable in basic medium. Nevertheless, in acidic medium, the dissolution of this solid phase might take place, according to Eq. 13.

$$Ni(OH)_{2(s)} + 2H^+ \leftrightarrow [Ni(H_2O)_6]^{2+} + 2H_2O \qquad \textbf{Eq. 13}$$

Pourbaix diagram for Ni/water system is shown in Figure 17 [72]. For instance, Ni^{2+} is stable in an oxidizing acidic medium and formation of $Ni(OH)_2$ is favoured in strongly alkaline solutions, as already explained.

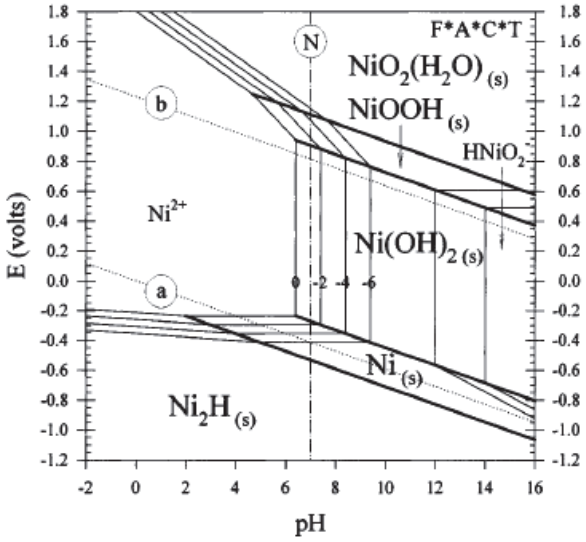

Figure 17 - Pourbaix diagram of Ni/water system at 25°C [72]

2.2. Physical and chemical phenomena

The impregnation step depends on physical and chemical phenomena. Physical phenomena concern capillarity and diffusion, while chemical phenomena are related to adsorption and/or precipitation [14]. All of these phenomena are described in Figure 18. When the support is pre-wetted with the liquid solvent (impregnation in diffusional conditions), no capillary action occurs and the physical phenomena concern only diffusion.

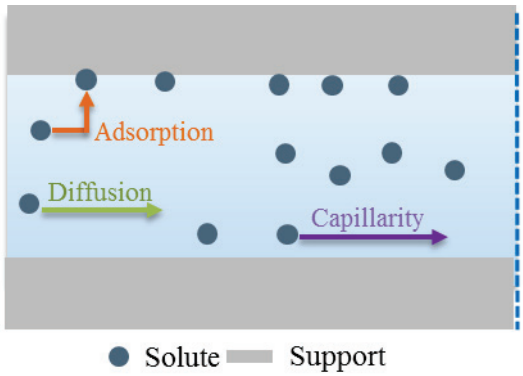

Figure 18 - Physical and chemical phenomena in dry impregnation. The solute migrates into the pore from the left to the right [25]

Capillary transport can be described by Laplace and Poiseuille law [76], while diffusion can be described by Ficks' law. Both of these phenomena are taken into consideration in the mathematical relation that describes the flux density, N_i:

$$N_{iz} = C_A v_z^* + J_{Az} \quad \textbf{Eq. 14}$$

Where, $C_A v_z^*$ corresponds to the convective flux (capillary flow) of the element A along z direction ($mol.m^{-2}.s^{-1}$) and J_{Az} corresponds to the diffusive flux along z direction ($mol.m^{-2}.s^{-1}$).

The mathematical equations that define capillarity and diffusion are described in more detail in section 2.3, respectively.

Adsorption is governed by the capacity of the surface and by the adsorption equilibrium constant, which are determined thanks to the adsorption isotherms. Besides adsorption, other phenomena like acid-base reactions at the surface and in solution, dissolution of the support or precipitation can take place during impregnation [15]. The reversibility of solute-surface interaction strongly influences the homogeneity of the deposition of the species along the pellet diameter at long maturation times.

Therefore, the distribution of the active precursor along the support pores depends on the balance between these phenomena and can be controlled through the maturation time. For instance, in dry impregnation case, if the precursor strongly adsorbs on the support surface, its concentration in solution decreases and so as the diffusion. Moreover, a weak interaction between components in impregnation solution with the support usually leads to a homogeneous distribution over the support pellet, particularly for a long maturation time.

The main phenomena that occur during impregnation are described in the following paragraphs.

2.2.1. *Capillarity phenomenon*

Capillary forces are created by the pore system of the support in the presence of liquid–gas or immiscible liquid interfaces. When the pore space, which contains only ambient air is put in contact with the solution upon impregnation, it will absorb the solution. Part of the air present in the pore space becomes entrapped under the effect of capillary forces. As a result, considerable forces are applied on the pore walls in contact with the imprisoned gas bubbles. The liquid penetration finishes when the capillary pressure is equal to the pressure of the entrapped gas [10]. The determination of the impregnation time must take into consideration the imprisonment air within the pore space and the elimination of this trapped air. Thus, the impregnation is limited by the dissolution of the imprisoned and compressed air and its migration to the outside grain [16]. Normally, this is a very fast phenomenon of the order of the second to a few tens of seconds [77]. Therefore, it is not the limiting step of the transport of the metal ions during impregnation.

Capillarity is related with two different phenomena, wetting and interfacial tension. The capillary flow is mathematically described by equations based on Darcy's law or Poiseuille's law. In its general form, Darcy's law is given by Eq. 15.

$$Q = -KA\left(\frac{\Delta P}{\mu L}\right) \qquad \textbf{Eq. 15}$$

Where, Q is the fluid flow ($m^3.s^{-1}$), K is the permeability (m^2), A is the cross sectional area (m^2), η is the viscosity (Pa) and ΔP is the pressure gradient (Pa).

The Poiseuille's law is given by Eq. 16.

$$Q = \frac{\Delta P \pi r^4}{8\mu L} \qquad \textbf{Eq. 16}$$

Where, Q is the fluid flow ($m^3.s^{-1}$), ΔP is the pressure gradient (Pa), r is the radius (m), μ is the dynamic viscosity (Pa.s) and L is the length (m).

In a mesopore system, the fluid inside the pore space is called capillary. Its pressure is related to the interfacial tension of the liquid that is present at the interface with the surrounding atmosphere [78]. The interface created by the fluid with the solid surface and with the surrounding atmosphere results in a certain angle, which is named as the wetting angle (see Figure 19). This angle reflects the affinity of the fluid for the solid surface and depends on the chemical nature of the fluid and the surface.

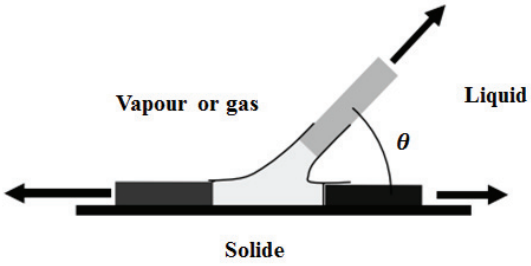

Figure 19 – Wetting angle, θ [78]

When the porous pellets are plunged in the solution, the liquid phase is adsorbed inside the pores by the action of capillary forces. According to the Young-Laplace equation, the driving force of the process is then the capillary pressure, see Eq. 17 [79].

$$P_{cap} = \frac{2\gamma cos\theta}{r} \qquad \textbf{Eq. 17}$$

Where, P_{cap} is the capillary pressure (Pa), γ is the surface tension of the solution ($N.m^{-1}$), θ is the wetting angle (°) and r is the characteristic pore size of the support.

Capillary action is crucial in the case of dry impregnation. In the present work, water is used as solvent, while salts of the metal ion precursor are used as solute. A rapid imbibition of water by the support is expected [5].

2.2.2. *Molecular diffusion*

Diffusion can be described as collisions of molecules, atoms or ions resulting from random thermal agitation [80]. Two different diffusion phenomena must be distinguished: Brownian motion and Fickian diffusion.

2.2.2.1. *Brownian motion*

Brownian motion, which is attributed to Robert Brown, results from molecular collisions and is related to a system at thermal and chemical potential equilibrium [80]. Atoms, molecules or particles suspended in a fluid start to move randomly as a result of thermal agitation. This random motion results from collisions between these particles with those of the fluid. The molecules of the fluid are in constant motion and their velocity is proportional to temperature.

The mathematical treatment of Brownian motion was done by Albert Einstein, who derivated an equation in order to calculate the diffusion coefficient D. This equation, which is known as the Stokes-Einstein relation [80], relates the diffusion coefficient to the viscosity of a solution, the hydodynamic radius and temperature. By assuming the solute as a spherical particle, which diffuses in a continuous solvent medium, the diffusion coefficient is given by Eq. 18.

$$D = \frac{k_B T}{6\pi\mu a} = \frac{k_B T}{f} \qquad \textbf{Eq. 18}$$

Where, D is the diffusion coefficient ($m^2.s^{-1}$), k_B is the Boltzmann constant ($1{,}38 \times 10^{-23}$ $J.K^{-1}$), T is the temperature (K), μ is the solvent dynamic viscosity (Pa.s), a the is hydrodynamic radius (m) and f is friction coefficient.

This equation enables error estimates within 20% in conditions similar to those used for the development of this relation [81]. The diffusion coefficient obtained through Eq. 18 is named as self-diffusion coefficient.

2.2.2.2. *Fickian diffusion*

According to Fick, the driving force for diffusion is the gradient of concentration. There is a net diffusive flux from regions with higher concentrations to the ones with lower concentrations. Fick established a relation between the diffusive flux in a certain direction and the concentration gradient [80]. This relation known as the Fick's First Law is valid for diffusion in steady state and for diluted

and ideal binary solutions of constant density. The proportionality constant between the diffusive flux and the concentration gradient is the diffusion coefficient D, see Eq. 19.

$$J_z = -D\frac{dc}{dz} \qquad \textbf{Eq. 19}$$

Where, J_z is the diffusive flux along z direction ($mol.m^{-2}.s^{-1}$), D corresponds to the diffusion coefficient ($m^2.s^{-1}$) and dc/dz represents the concentration gradient ($mol.m^{-4}$).

Fick also proposed an equation for mass conservation in transient state, which gave rise to the so called Fick's Second Law (see Eq. 20).

$$\frac{\partial C}{\partial t} = D\frac{\partial^2 C}{\partial z^2} \qquad \textbf{Eq. 20}$$

In the above equation, the diffusion coefficient might be also called as the transport diffusion coefficient or as the molecular diffusion coefficient.

Fick's laws have certain limitations, namely for multicomponent systems. Also, they assume that diffusion coefficient is independent of solute concentration. Besides, according to thermodynamics, the true driving force for diffusion is not the gradient of concentration, but the gradient of chemical potential of the solute, μ [80].

For a diluted medium, self-diffusion coefficient and transport diffusion coefficient by Fick's law are the same.

During the diffusion process in a porous material, some resistances to mass transfer are developed (see Figure 20):

- External fluid film resistance, which is determined by hydrodynamic conditions [82]
- Diffusion within micro and mesopores
- Macropores diffusion resistance

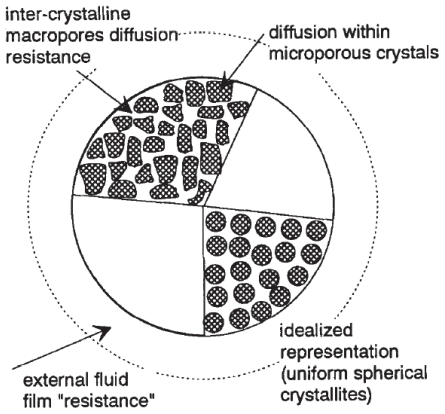

Figure 20 – Three main diffusion resistances [83]

Additionally, three main pore diffusion mechanisms can be differentiate [83]:

- Free molecular diffusion or bulk diffusion
- Knudsen diffusion
- Surface diffusion

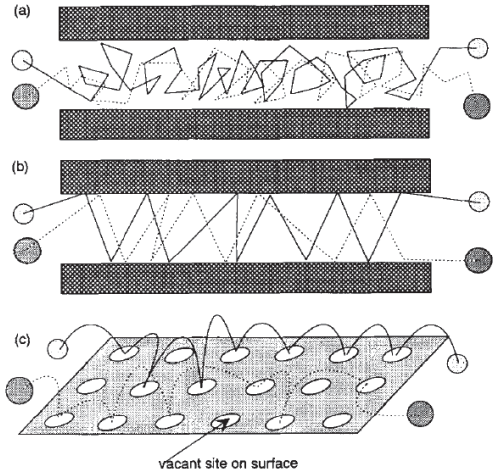

Figure 21 – Three main diffusion mechanisms: (a) Bulk diffusion, (b) Knudsen diffusion, (c) Surface diffusion [83]

In free molecular diffusion, molecule-molecule collisions predominate over molecule-wall collision, as the mean free path of the molecular species is smaller than the pore diameter. This type of mechanism predominates in large pore sizes. Moreover, diffusion is described according to Brownian motion and hence, the diffusion coefficient can be calculated thanks to the Stokes-Einstein relation, Eq. 18. Generally, liquid diffusion coefficients are in the range of 10^{-9} to 10^{-10} $m^2.s^{-1}$ at ambient temperature [82].

In Knudsen diffusion, the opposite behaviour is found. Diffusion is then limited by collisions between molecules and the pore wall and depends on temperature, mean pore radius and molecular weight of

diffusing species [84]. Knudsen diffusion applies only to gases, where the mean free path is higher than in liquids [81].

Surface diffusion is a more complex situation and is significant in micro pore sizes. This type of mechanism is related with the transport of adsorbed molecules. In this case, the transport occurs through the adsorbed layer on the solid surface [84]. Surface diffusion is an activated process and transport of molecules involves jumping between adsorption sites [84].

In a liquid-saturated pore two different regions can be distinguished: a bulk region and pore surface [85,86]. In the bulk region, the liquid behaves as a bulk liquid, which fills the majority of the pore space. In this case, pore diffusion predominates, i. e., the diffusive migration of the molecules is according to their concentration gradient, with no interaction with the solid surface. At the pore surface, where the adsorption at the solid surface takes place, the diffusion paths are limited and surface diffusion occurs.

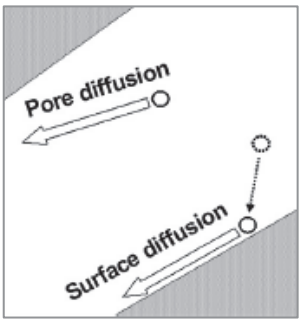

Figure 22 – Intraparticle pore space: pore diffusion and surface diffusion [85]

The relation between adsorption and surface diffusion is shown in Figure 23 [85]. As adsorption is an exothermic process, when a molecule is adsorbed at the solid surface from the bulk phase, it releases energy – heat of adsorption, Q_{st}. By getting over the activation energy E_s, which is smaller than the heat of adsorption, the molecule adsorbed can then migrate. Under surface diffusion conditions the desorption process does not occur.

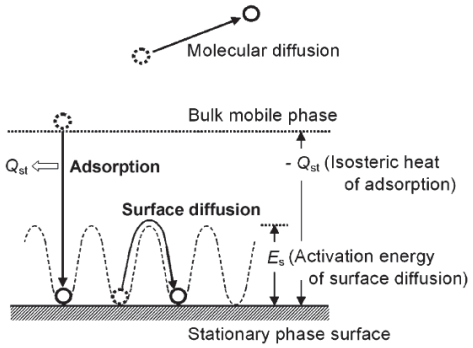

Figure 23 – Adsorption and surface diffusion [85]

The importance of surface diffusion for the total diffusive flux depends on the adsorbate-adsorbent interactions, temperature, thickness of the adsorbed layer and initial solution concentration [86]. Despite that the mobility in the adsorbed phase is slight, the concentration of molecules is higher. So that, when the thickness of the adsorbed layer is considerable, surface diffusion has a significant contribution for the total diffusive flux. As diffusion is an activated process, it may be described by Arrhenius equation [85]. Furthermore, contribution of surface diffusion decreases as temperature rises [84].

Concerning surface diffusion coefficients they can be determined from the concentration of active element in solution and by measuring adsorption isotherms [86].

Diffusion in porous media can be studied by NMR and many other techniques, see Figure 24.

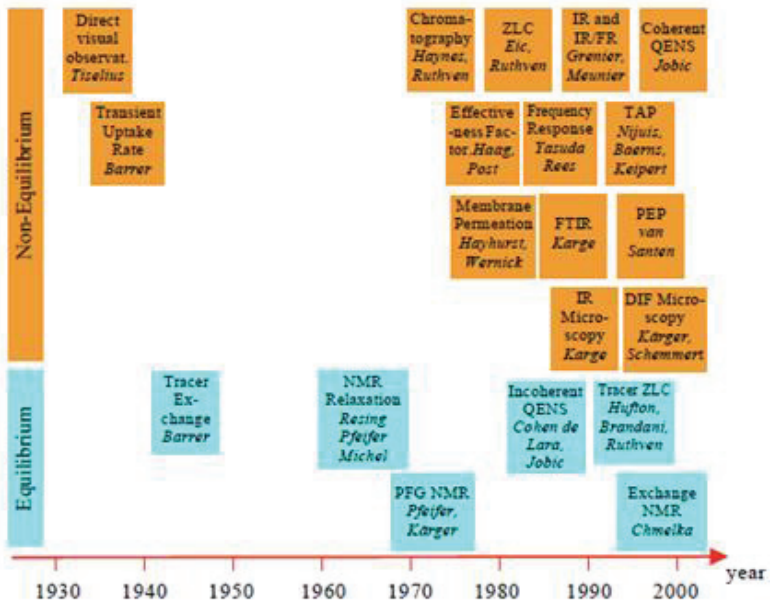

Figure 24 – Evolution of different techniques to study diffusion in equilibrium and non-equilibrium situation

In case of porous medium, an effective diffusion coefficient D_e must be used instead of the molecular diffusion coefficient D to take into account the structure and geometry of the porous network. Typically, the cross-sectional areas of pores are not uniform in size and the porous space is tortuous and interconnected [80]. Generally, the solid/fluid heterogeneous medium is considered as a pseudo-homogeneous medium [81]. Thereby, the cross sectional area takes into account the porosity ε of the medium and the diffusion path is rectified by a tortuosity factor τ. This factor considers that the diffusion path is no longer a straight line, but a non-linear path that is defined by the porous structure. The tortuosity takes into account the porous orientation and the connectivity for instance. Based on Fick's law (Eq. 19), the following expression relates the free molecular diffusion coefficient D with the effective diffusion coefficient D_e. Indeed, D_e will be smaller than D.

$$D_e = \frac{\varepsilon}{\tau} D \qquad \textbf{Eq. 21}$$

However, this expression is valid only for porous media with a narrow pore size distribution and in cases where there is no surface diffusion. For a broad pore size distribution, the effective diffusion coefficient should take into account both Knudsen and bulk diffusion contributions.

2.2.3. *Chemical phenomenon: adsorption and/or precipitation*

2.2.3.1. *Adsorption phenomenon*

Adsorption can be described as the interaction between molecules in a fluid phase (adsorbate) and a surface (adsorbent) [87]. An adsorption layer of the adsorbate on the surface of the adsorbent is then formed.

Adsorption is a spontaneous process, which means that $\Delta G<0$, where ΔG is the Gibbs free energy variation during adsorption. Besides, there is also a decrease in the number of degrees of freedom, as the adsorbed molecules can only move over the surface, so $\Delta S<0$, where ΔS is the variation of entropy during adsorption. As a result, the variation of enthalpy ($\Delta H=\Delta G+T\Delta S$) is always negative: adsorption is an exothermic process and the quantity of adsorbed molecules decreases as the temperature rises [87].

Depending on the type of forces involved, there are two different kinds of adsorption: physical adsorption and chemical adsorption.

Physical adsorption involves weak intermolecular forces, namely van der Waals forces and is similar to a condensation process. **Electrostatic interactions** should be considered. Moreover, the amount of surface charges precisely balances the amount of charged metal complexes in a region adjacent to the solid surface [88].

For a gas adsorbate phase, the heat of adsorption is small and is of the same order of the condensation heat, ΔH=2.1-20 kJ/mol (while for a liquid adsorbate phase is $\Delta H<50$ kJ/mol) [87]. In physical adsorption, there are no chemical changes in the adsorbed molecule. In this case, monolayer or multilayer formation can occur and the adsorption strength decreases as the number of layers increases (see Figure 25). Furthermore, this process is rapid, non-activated, non-specific and reversible. Its contribution is significant at relatively low temperatures [84].

Chemical adsorption involves the formation of a chemical bond (covalent bond) between the adsorbate molecule and the surface of the adsorbent [84]. This phenomenon is also known as **hydrolytic adsorption**. Chemical adsorption is related with surface complexation, site binding and

triple layer models [88]. As a result, the heat of adsorption for a liquid adsorbate phase is ΔH>60-450 kJ.mol^{-1} [87].

In contrast with physical adsorption, chemical adsorption may be an irreversible process and the formation of only a monolayer is observed (see Figure 25). Chemical adsorption is highly specific, which means that adsorption only happens in active adsorption sites. It is an activated process and is favoured at higher temperatures than physical adsorption. This is the reason why at low temperatures, this process may be slow.

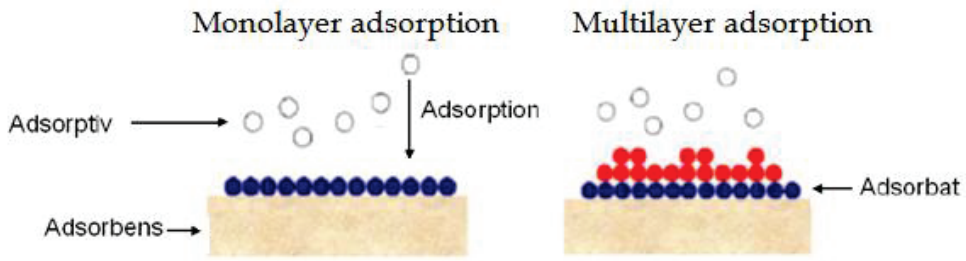

Figure 25 – Formation of a monolayer (either chemical or physical adsorption) and multilayer (physical adsorption) [89]

Figure 26 describes different mechanism of adsorption referred above: electrostatic adsorption and hydrolytic adsorption [90].

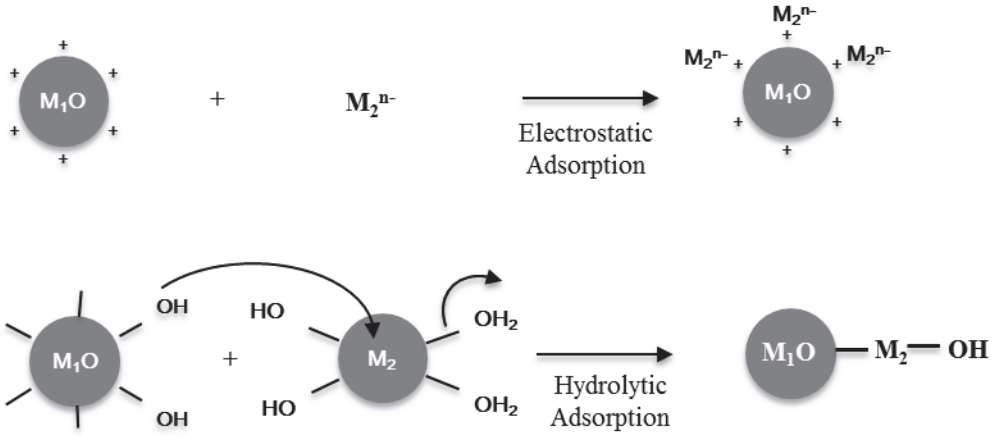

Figure 26 – Different types of specific adsorption [90] (a) Electrostatic adsorption –if the surface charge is of opposite sign to that of the metal complex (b) Hydrolytic adsorption - surface reaction by covalent bond between a surface site (S-OH or S-O$^-$) and a metal complex

2.2.3.1.1. Adsorption Isotherms

The quantitative treatment of physical and chemical adsorption is done by means of equilibrium adsorption isotherms [87]. They represent the amount of adsorbed molecules by a surface, at equilibrium as a function of the chemical potential (concentration for ideal liquids, partial pressure for ideal gases), at constant temperature. In the following paragraphs are presented some models used to describe adsorption isotherms.

The equilibrium physical adsorption isotherms have been classified by Brunauer, Emmett and Teller into five different isotherm types (I-V) [91]. Nowadays, six different types (I-VI) of equilibrium adsorption isotherms are accepted [92], as shown in Figure 27. Each isotherm is associated to a certain mechanism.

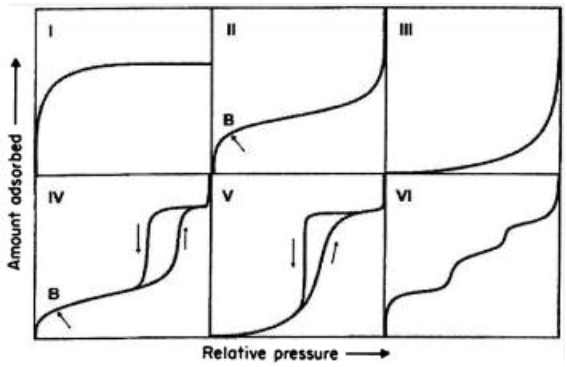

Figure 27 – Classification of equilibrium adsorption isotherms [92]

Isotherm I corresponds to adsorption on microporous materials, which have small external surfaces. This type of isotherms are characterized by a plateau and when p/p_0 tends to 1, the amount adsorbed approaches to a limiting value. This isotherm also represents reversible chemical adsorption (Langmuir model), wherein the limiting value corresponds to the formation of a monolayer – surface saturation.

Isotherm II and III are typically for adsorption in multilayers. They correspond to non-porous solids and macroporous. Point B in isotherm II corresponds to the beginning of multilayer adsorption.

Isotherm IV and V are associated with capillary condensation on mesoporous. They are also characterized by an hysteresis phenomenon, which is due to different saturation pressures during condensation and evaporation of the liquid present in the pores.

Isotherm VI corresponds to stepwise multilayer adsorption on non-porous solid.

Isotherms III and V are not much frequent. They are associated with weak interactions between the adsorbate and the adsorbent.

A final remark is that for low surface coverage, isotherms have a linear form (the amount adsorbed is proportional to the relative pressure) – Henry's law domain.

Henry isotherm is the simplest model used in adsorption and is valid for uniform surfaces and low concentrations. It considers that there is a linear relation between fluid phase and adsorbed phase concentrations [84]. Moreover, according to this model, there are no interactions between molecules of the adsorbat and there is no saturation of the adsorbent.

$$q = K \times c \quad \textbf{Eq. 22}$$

Where, q and c are the concentration in the adsorbed phase and liquid phase (expressed as molecules or moles per unit volume), respectively, and K is Henry's constant.

Langmuir model [93] is the most widely used model in the quantitative treatment of adsorption/desorption, mainly due to its simplicity. It is based on the following assumptions:

1. Adsorbed molecules have no mobility
2. Each adsorption site adsorbs only one molecule
3. Energy of adsorption is the same for all adsorption sites, which means that heat of adsorption is the same for all adsorption sites and independent on the quantity of adsorbed molecules
4. There is no interaction between adsorbed molecules
5. The maximal adsorbed amount corresponds to the formation of a monolayer

Considering an adsorption site X and a given component A in a liquid phase (considered as an ideal solution), which is adsorbed in X (see Eq. 23).

$$A + X \leftrightarrow AX \quad \textbf{Eq. 23}$$

At equilibrium, adsorption rate (r_a) and desorption rate (r_d) are the same. Representing the fraction of covered surface by θ, the following equations may be written:

$$r_a = r_d \quad \textbf{Eq. 24}$$

$$k_a(1-\theta)C_A = k_d\theta \quad \textbf{Eq. 25}$$

Where, k_a and k_d correspond to the kinetic constants of adsorption and desorption phenomena, respectively. These can be obtained by Arrhenius law.

From Eq. 25 the following relation can be drawn, which represents Langmuir isothermal (see Eq. 26):

$$\theta = \frac{KC_A}{1 + KC_A} \quad \textbf{Eq. 26}$$

Where, $\theta = n^a/n_m^a$, n^a is the adsorbed quantity and n_m^a is the monolayer adsorbed quantity (kg.m^{-3} of solid), $K = k_a/k_d$ is the equilibrium adsorption constant and C_A is the concentration of the solute in the solution (kg.m^{-3} of solution).

Nevertheless, when the adsorption reaction is irreversible, the adsorption phenomenon is then treated as a chemical reaction between the molecule in the fluid phase and the active site.

2.2.3.1.2. Adsorption of Transition Metal Ionic Species (TMIS)

The TMIS includes here Mo, Co and Ni, whose speciation in solution has already been discussed in section 2.1. To understand the adsorption mechanism of these species onto the surface of alumina, three different regions must be considered [17]:

- Electrolytic solution, which contains the free ionic species of the active element (for instance, Co) as well as water molecules and other ions necessary to the preparation step (for instance, NO_3^- ions).
- Oxide support surface, which is generally covered with hydroxyl (OH) surface groups. These correspond to acid or basic Brønsted sites, depending on pH of the medium.
- Interfacial region, for which different models have been suggested. These models take into account ionic species inside the interface, distribution of the charge and variation of the potential from the surface of the support up to the bulk solution. Between them, Stern model and Three Layer Model (TLM) are well accepted among the scientific community (for further details see [15]). According to the Three Layer Model (TLM), the interface region comprises three regions: compact layer, diffuse layer and bulk solution [15], as shown in Figure 28. In the compact layer, two layers of water are formed: a primary layer of water molecules in contact with the surface and a second layer. Part of the electrolyte ions can interact closely with the surface sites forming ion-pairs (specific adsorption), which corresponds to the inner Helmholtz plane (IHP). Non-specifically absorbed metal ionic species (ions of the precursor salt) are electrostatically retained after the secondary water layer, forming the outer Helmholtz plane (OHP) of the interfacial model as well as in diffusive layer. The OHP is at the front of the diffuse layer.

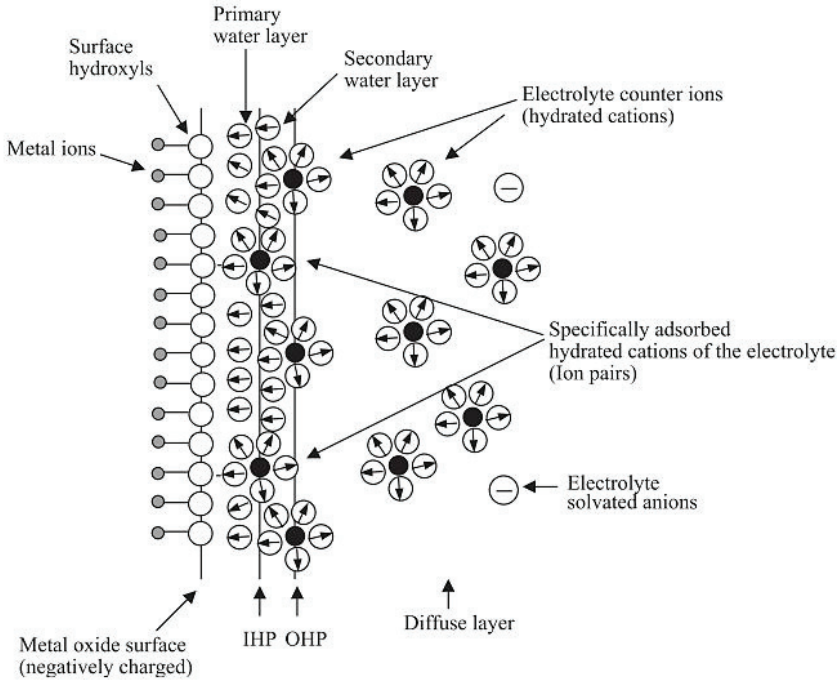

Figure 28 – Schematic picture of the interface region [17]

There are different modes of deposition on the support surface, such as [15]:

1. Electrostatic adsorption
2. Electrostatic adsorption through ion pair formation in the outer plane of the compact layer
3. Electrostatic adsorption through ion pair formation in the inner plane of the compact layer
4. Retention in the compact layer of the interface exclusively through hydrogen bond formation
5. Formation of inner sphere surface complexes
6. Surface or interface oligomerization, polymerization and precipitation
7. Surface dissolution of the support and formation of mixed solid phases

Among them, the first two modes are considered as non-specific electrostatic adsorption. While modes 3 to 5 are considered as specific adsorption.

The adsorption Ni^{2+} and more particularly Co^{2+} species on the surface of catalytic supports has been an issue of study [94–102]. According to O. Clause et al. [97], three main phenomena occur in the surface oxide/liquid interface:

- Adsorption of ions
- Dissolution of alumina, which is the lowest step
- Precipitation of the cations released from the support with metal ions in solution

Various authors [94,95] state that Co^{2+} adsorption is an endothermic process, which means that for a given pH, the adsorption constant increases with temperature. Besides, according to these authors,

there is also a range of pH (pH=5/6-7.5/8), for which adsorption is favoured. Above a pH of 8, precipitation of $Co(OH)_2$ occurs, hindering adsorption. Moreover, for higher temperatures, the adsorbed cobalt reacts with alumina surface forming compounds like spinel $CoAl_2O_4$ and aluminates.

The formation of inner-sphere Co(II) complexes has also been reported [96] as well as the formation of surface co-precipitates with Al(III) ions [97]. This last observation shows that alumina should not be considered as an inert support, as it will be discussed later in section 2.2.3.2. These studies were carried out using either Co^{2+} amine complexes or aqua complexes.

Vakros et al. [103] studied the impregnation of cobalt-supported γ-alumina catalysts by diffuse reflectance spectroscopy. The formation of inner-sphere complexes, resulting from the adsorption of $[Co(H_2O)_6]^{2+}$ ions on the interface developed between the surface of the γ-alumina particles, was confirmed by a peak centered at approximately 585 nm. This peak is attributed to the exchange of one aqua ligand with one Al_xOH_y negatively charged group, which results in the formation of Co^{2+} surface complexes.

Adsorption of Mo species on alumina has also been studied, using AHM as precursor. For an acidic pH, polymeric Mo species predominate and electrostatic adsorption of $Mo_7O_{24}^{6-}$ was reported on unsaturated Al^{3+} sites [104] as well as its slow diffusion. For a basic pH, MoO_4^{2-} ions predominate and can be not only electrostatically adsorbed on alumina surface depending on its surface charge, but can also react with the neutral surface hydroxyls.

The control of the proton sites concentration can be made by regulating the pH and temperature of the impregnation solution or by adding ions such as Na^+, Li^+ or F^- to the support. Adsorption of Mo can be increased by either decreasing the pH, adding Na^+ to support or increasing temperature. The best way to achieve the maximum Mo adsorption is to increase the temperature, since adding Na^+ to the support leads to the formation of sodium molybdate, which is an inactive catalytic species [105].

Bergwerff et al. [4] studied the impregnation of an acidic ammonia heptamolybdate solution over alumina support. Raman spectroscopy was used to study pore-volume impregnation inside alumina pellets. They reported on the strong interaction between $Mo_7O_{24}^{6-}$ and alumina, which resulted in a slow transport of these species towards pellet center. Moreover, the formation of $Al(OH)Mo_6O_{18}^{3-}$ was observed near support surface. Bergwerff et al. [28] also performed Raman studies in CoMo based catalysts supported on alumina. Pore-volume impregnation was carried out and Raman analyses were done after impregnation. HPA species were used as precursor. They reported on the disintegration of $H_2PMo_{11}CoO_{40}^{5-}$ complex as a result of reaction of phosphate with alumina's hydroxyl groups, forming $AlPO_4$ phase. Therefore, $Mo_7O_{24}^{6-}$ and $Co(H_2O)_6^{2+}$ were formed and they diffuse towards the center of the pellet. They also found that diffusion of Mo species is slower than the diffusion of Co species. They concluded that the deposition of HPA in catalyst pellet is not uniform. Figure 29

illustrates the distribution of Mo and Co species over alumina pellet. This study evidences the strong affinity of phosphorus with the oxygen of the support.

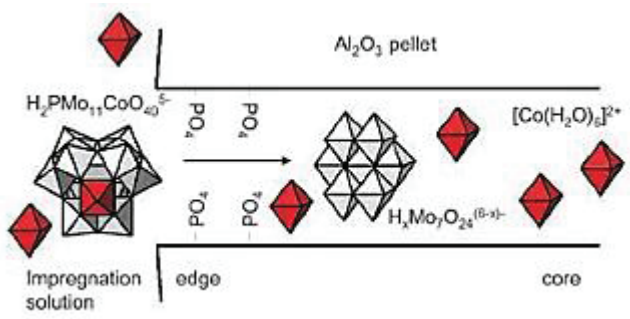

Figure 29 - Distribution of Mo and Co species over alumina pellet after impregnation with HPA species $H_2PMo_{11}CoO_{40}^{5-}$ containing solution [28]

W. Cheng [31] also reported on the adsorption of HPA containing phosphorus into alumina. The decomposition of pentamolybdodiphosphate into phosphate and molybdate when contacting with alumina was observed thanks to NMR spectroscopy. A competitive adsorption between phosphate and molybdate in alumina was also reported.

Finally, the impact of several parameters (pH, PZC, ionic strength) can be used to determine how a transition metal is deposited at the interface developed between itself and the support. Some examples are listed below, for further details see [15]. Nevertheless, these examples are only appropriate for aqueous media and when performing impregnation in excess.

- Determination of the extent of adsorption at various pH and constant initial concentration and ionic strength
- Determination of adsorption edges by varying ionic strengths
- Determination of the modification of pH during adsorption
- Determination of PZC in the presence or not of transition metal

2.2.3.2. *Other phenomena: polymerization, precipitation and dissolution of the support*

Other phenomena like **acid-base reactions** at the surface and in solution, **dissolution of alumina support** or **precipitation** can take place [15]. Indeed, these reactions are due to the acidity of the solution, which may alter the alumina properties (whose dissolution occurs below pH of 4) and also to the rising of the pH of the solution, which occurs when the acidic impregnation solution penetrates into the pores of alumina (PZC approximately equals to 8).

2.2.3.2.1. Buffer effect and dissolution of alumina support

An example of the buffer effect of alumina can be demonstrated with Mo/γ-Al_2O_3 system [106], using ammonium heptamolybdate $(NH_4)_6Mo_7O_{24}$ as precursor. $Mo_7O_{24}^{6-}$ anions are stable in an acidic medium (pH of 2-5), thus when putting in contact with the support, the pH of the solution inside the pores tends to rise towards a value of 8-9, consistent with the PZC of alumina.

According to Kim et al. [107], the local pH depends on the PZC of the support, the coverage of Mo species and the number of NH_4^+ or H^+ counter ions of the negative complexes. Moreover, molybdenum complexes ($Mo_7O_{24}^{6-}$), present in a solution with pH equal to 3.5, strongly interact with alumina surface. This can be explained as alumina has a PZC approximately 6-7. Therefore, for an acidic solution, alumina is positively charged.

Bergwerff et al. [4] also reported on the influence of the pH and its relation with PZC, for Mo systems. For a solution pH close to the PZC of alumina (approximately 8), only MoO_4^{2-} is present and hence, the interaction between Mo ions and surface of alumina is not significant. Therefore, Mo ions are transported with the convective flow of the water phase through the pore space. On the other hand, for a pH lower than 8, the transport of Mo anions is slow, since the interaction between these anions and alumina is enhanced (adsorption of Mo anions on alumina surface).

Moreau et al. [108] also studied the influence of pH impregnation of an Anderson-type HPA, $H_4Co_2Mo_{10}O_{38}^{6-}$ over alumina. This work correlates the surface density of Mo atoms and the pH with Mo species present. For surface densitites between 2.5 and 3.8 Mo atoms nm^{-2}, MoO_4^{2-} condense into $Mo_7O_{24}^{6-}$, which are then adsorbed via electrostatic interactions with alumina. Preferential adsorption of MoO_4^{2-} resulted in a decrease of the pH, allowing the dimers to be preserved. On the other hand, for surface densitiy lower than 2.5 Mo atoms nm^{-2}, decomposition of the HPA into monomolybdates MoO_4^{2-} and Co^{2+} was reported. This occurred due to an increase of pH by alumina buffering effect.

Alumina dissolves in highly acidic impregnation solutions and a fraction of dissolved aluminum may be reabsorbed during impregnation or drying [109]. This phenomenon was reported during the preparation of alumina-supported nickel catalysts [110].

The dissolution of alumina may be explained by a modification of its solubility due to the presence of TMIS. For instance, the formation of an inner-sphere complex on the support surface may improve the dissolution of the support by weakening the Al-O bonds [15]. This enables the detachment of surface Al^{3+} ions from the support lattice, which is the limiting step. As it was already mentioned, the adsorption of the Mo-oxo species on γ-alumina was also found to promote its dissolution [45]. Besides, the additive chosen might also affect the support dissolution from a kinetically and thermodynamically point of view. For instance, the adsorption of a ligand with affinity for aluminum

ions on its surface facilitates the detachment of Al from the support lattice, which enhances alumina dissolution from a kinetically point of view [137]. Thermodynamically, the formation of ligand-aluminum complexes in solution increases the dissolution of metal oxides, by consuming Al ions in solution.

For instance, the formation of Anderson type alumino heteropolymolybdate requires the dissolution of the support [45], as already explained in section 1.3.1 (page 15). The same observation has been reported by Bergwerff et al. [15].

2.2.3.2.2. Polymerization

Transition metals adsorbed at the interface can react to form oligomeric or polymeric species [15]. For instance, transition metals may be retained in the compact region of the interface only by hydrogen bonds, forming inner-sphere complexes. As a result, during drying these complexes may become destabilized, which favours their polymerization promoted by surface H^+ ions.

Dimerization is favoured by the release of protons, so that is promoted with relatively high positive charge. The referred protons are then transferred to the bulk solution. The formation of oligomeric species is depicted in Figure 30. One Co unit of the dimmer species binds to one already existing inner-sphere surface complex by a hydrogen bond, while the other unit forms a surface coordinative bond by exchanging one water ligand with one surface oxygen.

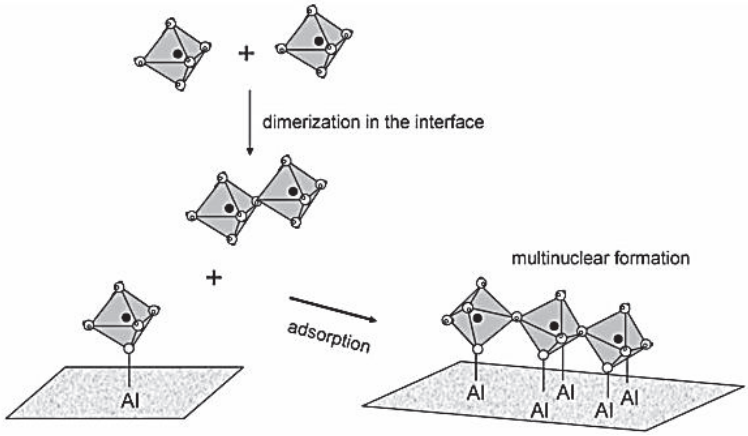

Figure 30 – Formation of oligomeric species [15]

Spanos et al. [105] reported the formation of oligomers after adsorption of molybdates on the surface of γ-alumina. Indeed, $Mo_xO_y^{z-}$ were adsorbed on the IHP of the compact layer in the interface region. As a result of their interactions, oligomers were formed. Moreover, this polymeric species are deposited on the surface during drying step.

2.2.3.2.3. Surface precipitation

Surface precipitation can be interpreted as phenomenon between bulk deposition and adsorption (Figure 31) [15]. When the concentration of negatively charged groups (Al_xOH_y), both Co units of the dimmer form hydrogen bonds with the already formed two-dimensional multinuclear inner-sphere complexes.

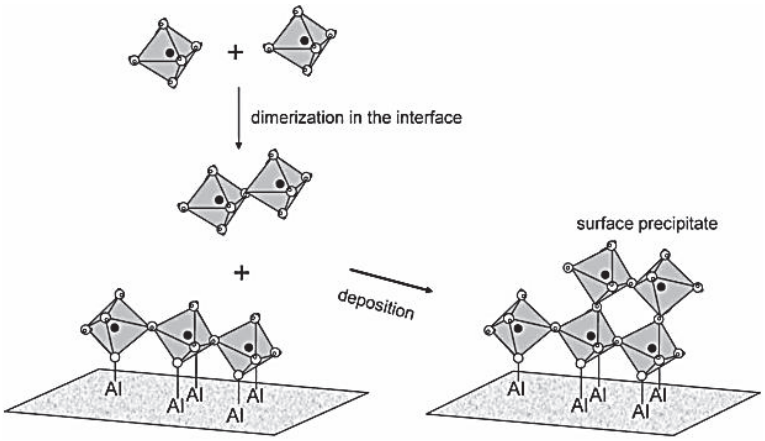

Figure 31 – Surface precipitation [15]

Besides, supports can act as a reagent and the formation of hydrotalcite-type coprecipitates involving Al(III) ions from the support surface is one of the evidences. The formation of these phases occurs either by a surface reaction or by support dissolution, followed by recombination with metal ions in the solution and re-precipitation. This fact was reported during the impregnation of γ-Al_2O_3 with Ni^{2+}, Zn^{2+} and Co^{2+} ions under mild conditions, i.e. pH close to the PZC (point of zero charge) and ambient temperature [97,111–113].

2.3. Mathematical models to describe impregnation process

Among the literature, several models have been developed to describe either dry or wet impregnation (the last one concerns impregnation in diffusional conditions). Concerning dry impregnation, two main approaches are often used to describe the capillary stage. These are based on either the Washburn equation [114] or Dracy's law [115]. In particular, Vincent et al. [114] developed a single-pore model for time-dependent flow of one-component impregnation of a catalyst pellet. This model takes into account the existence of capillary forces, which are described by Washburn equation, mass transfer across the liquid-solid interface based on Fickian diffusion and adsorption, which is responsible for removal of the metal precursor from solution. The latter was described by the Langmuir model. A good agreement between the predictions based on the model and laboratory experiments was obtained. Additionally, adsorption capacity was found to be the most important parameter to regulate the distribution profile.

Different improvements have been made to the Vincent et al. model. For instance, Komiyama et al. [116] expanded the Washburn equation to three dimensions. Therefore, an evaluation of the effect of the geometry on the imbibition front velocity for impregnation of γ-alumina spheres using $NiCl_2$ solution was performed. Aditionally, Kulkarni et al. [117] extended the Vincent et al. [114] model to the case where co-impregnation is performed. They considered two species competing for the same surface sites, which was described through a competitive Langmuir adsorption model. They also reported on the importance of the adsorption kinetics to obtain a good agreement between the experimental results and the model equation. Zhang et al. [118] proposed an equation that establish the critical parameters that affect the extent of metal penetration during imbibition. Parameters such as the solution viscosity, surface tension, support geometry, pore size and immersion time were considered. The validity of this model was demonstrated through experiments with silica as support and nickel nitrate as metal precursor. A mathematical model for dry impregnation of Ni/Al_2O_3 catalysts proposed by Assaf et al. [119] and based on Vincent et al. model has already been developed. They reported on the influence of concentration of impregnation solution and the time of contact as the two main parameters that define the distribution profiles.

Wet impregnation is usually described based on diffusion-adsorption model [120]. This model can be also applied for a multicomponent system by considering a competitive adsorption based on Langmuir model [121] [122].

To summarize all data given in the literature, different phenomena must be taken into account for both dry and wet impregnation. In the first period of dry impregnation, imbibition takes place due to the capillary action, which is usually described based on Washburn model. Besides this convective flow, diffusion and adsorption of the solute by the pore walls also occur. These phenomena are often described as a diffusion-adsorption model, in which diffusion is defined by Fick's law, while adsorption is described thanks to Langmuir model.

2.4. Conclusion

Impregnation, which determines the final dispersion and the chemical structure of the metallic species on the support **is governed by two main phenomena: transport (diffusion or convection) and surface interaction (adsorption or irreversible chemical reaction).**

By revising all the data given in the literature, the parameters that influence these physicochemical phenomena can be divided into two main groups. The ones related with the diffusivity of ions of the impregnation solution within the oxide support, which concerns pore space geometry (tortuosity, connectivity and porosity). While the second group regards the main parameters that influence the interactions between metal complex with support. These ones can be listed as follows:

- **Local metal concentration,** which influences the nature of species deposited in the support.
- **PZC** influences the electrostatic interaction metal/support.
- **pH,** which impacts not only the final metal distribution obtained, but also the nature of species deposited on the support. It has also an impact in metal adsorption, since it determines the sign of the global surface charge and the number of charged sites. Moreover, it influences the dissolution of the oxide support both thermodynamically and kinetically [25]. Additionally, it controls the solubility of the oxide support: its dissolution is more important when the pH of the solution departs from the PZC [135]. It also allows selection of the most abundant metal complex from those coexisting at the same pH and it controls the amount of monomer produced in the solution upon oxide support dissolution.
- **Ionic strength,** which influences the surface charge. The surface charge increases with the ionic strength: at low ionic strengths the surface groups mostly interact with each other; at high ionic strengths the surface groups are more reactive, since interactions between each other decrease. As a result, egg-shell catalysts will be favoured.
- **Additive Nature,** which has a strong influence in the nature and the strength of the metal-surface support interaction
- **Counter-ions,** whose choice is made so as to achieve a soluble precursor salt and easily transformed one into an oxide or metallic phase upon heating. In HDT catalysts, the most used precursors are metal nitrates ($M(NO_3)_x.yH_2O$, where M=Ni,Co) and Mo salts in their ammonium or protonic form are used (e.g., $(NH_4)_6Mo_7O_{24}$, $(NH_4)_2Mo_2O_7$, H_2MoO_4).
- **Competitive ions,** which determines the macroscopic distribution of the metal on the support. Certain additives act by a competition effect on adsorption as well as by a pH effect. An increase in the pH decreases the exchange capacity of alumina, causing a more uniform occupation of the surface by a metallic complex. Through a careful selection of both metal precursors and competitors, a large number of metal distribution profiles on the support surface between the periphery and the grain center are obtained, depending on the strength of their interaction with the support, Figure 32 [21], [22].

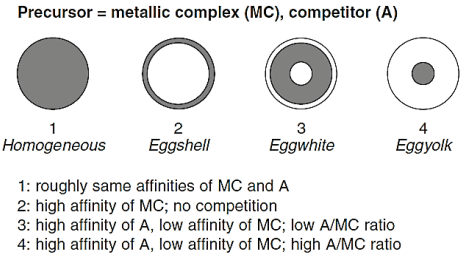

Figure 32 - Distribution profiles of the active phase [22]

According to the literature, different analytical techniques can be used in order to characterize either impregnation solution or oxide catalysts. Such techniques can give information about some of the

physicochemical phenomena occurring during the impregnation step and the impact of each parameters described above. Some of these techniques are discussed in the next part.

3. Towards the comprehension of the impregnation step: suitable analytical techniques

In order to well understand the phenomena occurring during impregnation step, it is of crucial importance to monitor the impregnation with analytical techniques that are able to:

- Identify the metals on the support with the best spatial resolution and low acquisition times. Examples of application of the most suitable characterization techniques to monitor the transport of metals during impregnation are described in part 3.1.
- Characterize the parameters that may influence the impregnation with the best spatial resolution and low acquisition times. Some examples of how to achieve such a characterization are reviewed in part 3.2.

3.1. Local characterization of impregnation: monitoring of the metals

3.1.1. *Magnetic Resonance Imaging (MRI)*

One of the most promising techniques to monitor *in-situ* the impregnation step of supported catalysts is Magnetic Resonance Imaging (MRI), due to its non-invasive and non-destructive character. This technique is based on Nuclear Magnetic Resonance (NMR) principles. As NMR, MRI can also provide information concerning chemical structure and composition of metal species and mass transport, but with spatial resolution of the order of tens or hundreds of microns [123]. Image acquisition can be less than a second to hours.

In the literature [124,125], there are two main approaches to monitor the transport of metals in a porous support:

- Indirect approach - Mapping the distribution of a solute within a porous support by detection of the NMR signal of the solvent (usually water)

Paramagnetic and diamagnetic species, such as Ni^{2+}, Co^{2+} and Mo^{6+} are used in this approach, since they influence the ^{1}H MRI signal as image contrast agent. These species induce a modification in the relaxation times of the solvent, leading to relaxation-weighted images. Some examples are listed below.

Lysova et al. [7,8] studied the distribution of paramagnetic Co^{2+} complexes inside $Co/\gamma\text{-}Al_2O_3$ catalyst extrudates with 3.85 mm diameter. The BET surface area of the support was 149 m^2/g and the pore volume was 0.39 mL/g. The mean pore diameter was defined as 8 nm. They performed a pore-volume impregnation with 0.20M Co^{2+} solution, using cobalt nitrate as metal precursor.

An example is given in Figure 33, where images were collected by performing a spin-echo experiment, with a spatial resolution of 139 µm × 231 µm. The red color corresponds to a low ^{1}H MRI signal intensity (indicating the presence of Co^{2+} ions), whereas the blue color corresponds to a high ^{1}H MRI signal intensity (indicating the absence of Co^{2+} ions). A uniform distribution was achieved after 160 minutes. One of the limitations of this study is the lack of information about the impact of the acquisition technique's parameters and the type of contrast obtained (either T_1 or T_2 contrast).

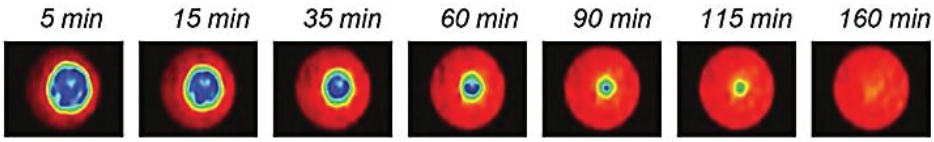

Figure 33 - 2D ^{1}H MRI of a γ-Al_2O_3 extrudate in transversal section with a spatial resolution of 139 µm×231 µm after impregnation with an aqueous solution containing 0,2M Co^{2+}. The red color corresponds to a low ^{1}H MRI signal intensity (indicating the presence of Co^{2+} ions), whereas the blue color corresponds to a high ^{1}H MRI signal intensity(indicating the absence of Co^{2+} ions) [7]

Furthermore, Lysova et al. [8] studied the transport of Mo ions into a γ-alumina support after impregnation with a 2M $(NH_4)_6Mo_7O_{24}$ solution. γ-Al_2O_3 pellets (12 mm long and 3.20-3.85 mm in diameter) with a BET surface area of 184 m^2/g and a pore volume of 0.48 mL/g were used. The impregnation step was followed using an inversion-recovery preconditioning, with a resolution of 139 µm × 231 µm. The transport of $Mo_7O_{24}^{6-}$ within alumina pellet is slow, as these species are progressively transformed into MoO_4^{2-} due to the buffer effect of alumina. Therefore, the monomeric Mo species interact with the OH groups of alumina surface. Nevertheless, once more the impact of the support properties on the transport of Mo, especially the textural properties is not so well understood.

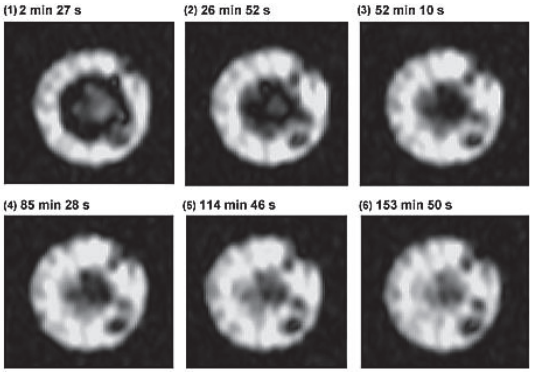

Figure 34 - 2D ^{1}H MRI images showing the dynamics of the impregnation of a γ-Al_2O_3 support body with a 2.0M aqueous solution of $(NH_4)_6Mo_7O_{24}$ (pH 5.5) detected using the pulse sequence with inversion-recovery preconditioning with the recovery delay of 130 ms. The acquisition time of each 2D image is 4 min 53 s and spatial resolution is 139 µm×231 µm. The time corresponding to the middle of the acquisition period is shown for each image [8].

Espinosa-Alonso et al. [126] studied the impregnation step of Ni/γ-Al_2O_3 hydrogenation catalysts by applying a similar approach. γ-Al_2O_3 extrudates (12 mm long and 3,85 mm in diameter) with a BET surface area of 145 m^2/g and a pore volume of 0.36 mL/g were used. Impregnation solutions ranging from 0.1 to 1.0 M Ni^{2+} were prepared using $Ni(NO_3)_2 \cdot 6H_2O$ as metal precursor. Images were collected using a spin-echo sequence either in T_1 or T_2 contrast, with a spatial resolution of 140 μm × 230 μm. According to this study, the adsorption of $[Ni(H_2O)_6]^{2+}$ on the alumina surface is limited. One may consider this result quite surprising taking into account some works in the literature that reported on the interaction between nickel and surface of alumina [127]. One can consider that the impact of the support and solution properties in the transport phenomena is not so well understood.

Nowacka et al. [128] showed that, in the absence of nickel ions, the water protons (^1H) present in a γ-alumina support already experience a T_1 of the order of the hundreds of milliseconds. This can be explained due to the impact of paramagnetic impurities present in the support. For this study, trilobe pellets with 1.2–1.4 mm diameter and 5–6 mm length were used. The BET surface of the support was 200–250 m^2/g and the pore volume was 0.7-0.9 mL/g. The mean pore diameter was defined as 8-11 nm. Moreover, they monitored the impregnation of the alumina pellets with a $Ni(NO_3)_2 \cdot 6H_2O$ aqueous solutions at varying Ni^{2+} concentration (between 0.05 and 0.3 M). For that purpose, they performed a Single Point Imaging sequence in T_1 contrast with a resolution of 78 μm × 78 μm. They reported that already at a concentration as low as 0.05 M Ni^{2+}, a homogeneous ion distribution was achieved. For nickel concentrations higher than 0.2 M, a uniform ion distribution is almost instantaneous obtained.

- Direct approach (in cases where the NMR signal is strong enough) - Tracking directly the NMR signal of the solute or the adsorbate molecules

Lysova et al. [5] studied the transport of $H_xPO_4^{(3-x)-}$ into a γ-Al_2O_3 pellet after it was immersed in a 0.76 M aqueous solution of H_3PO_4 thanks to ^{31}P NMR. Images were collected using a spin-echo sequence with a spatial resolution of 172 μm × 371 μm. At the beginning of the experiment ^{31}P is only detected near the outside of the pellet as shown in Figure 35. A uniform distribution of phosphate inside the pellet was achieved after about 14h of impregnation.

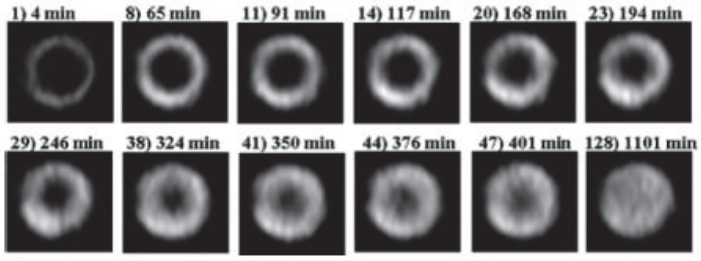

Figure 35 - Impregnation of γ-Al_2O_3 pellet, which was first saturated with water and then immersed in a 0,76M aqueous solution of H_3PO_4 - ^{31}P images obtained by a spin-echo sequence with a spatial resolution of 172 μm×371 μm [5]

Nevertheless, even though it is a promising technique, MRI has a few limitations concerning monitoring the transport of fluids in porous materials, which are listed below [129].

- Spatial resolution given by each voxel corresponds to a large number of pores, since pores dimension is usually too small. Therefore, each voxel corresponds to a NMR average signal. The spatial resolution is dependent on the technical constraints (mainly gradients' intensity), but also on a compromise with the time resolution.
- Relaxation times (T_1 and T_2) can be reduced by the presence of paramagnetic species, interactions between fluid molecules and pores walls. Shorter relaxation times can limit the achievable space resolution.
- When paramagnetic or ferromagnetic compounds are present, magnetic susceptibilities at the interface liquid/solid can cause large local gradients. Therefore, a liquid phase in a porous medium can be influenced by these gradients, leading to image distortion and shortening of T_2^* (overall relaxation time that governs the decay of transverse magnetization, further details are given in Chapter II). This leads to a fast FID (free induction decay), hindering the achievement of a NMR signal. Moreover, shorter FID leads to broad spectral lines.
- Temperature is an important parameter that influences the measured signal, since it affects the probe tuning/matching.
- MRI experiments in porous media are limited by signal-to-noise ratio (SNR), which is affected by the amount of liquid in a porous sample. SNR determines the achievable space resolution and the image acquisition time. For instance, lower spatial resolution (larger voxel size and slice thickness) gives a higher SNR.
- In MRI experiment there is always a delay between signal excitation and detection, of the order of 50 μs to 10 ms, depending on the imaging method. However, the relaxation times of a liquid in small pores can be even shorter, leading to a rapid FID, which makes difficult to obtain an NMR signal.

MRI technique is usually complemented with other characterization techniques as Raman and UV-Visible spectroscopies. Examples are given in paragraphs 3.1.2 and 3.1.3, respectively.

3.1.2. *Raman spectroscopy*

Raman spectroscopy is a vibrational technique, which can be used to determine the chemical nature of the Raman active species in the catalyst pellet. It provides information about the nature of the species, their crystallinity and the spatial distribution of phases through a sample. Typically, the resolution is in the order of 1-2 μm. Unlike MRI, Raman is an invasive and destructive technique [68], since catalysts must be bisected before measurements using a kind of a razor blade. To avoid artifacts, the sliced surface must be smoothed. Yet, this interruption of the preparation process might influence the

representativeness of the analysis. Moreover, the sample might be or not submitted to a thermal treatment.

In the case of HDT catalyst, this technique is widespread used to study Mo based catalysts supported on alumina because of the strong signal of molybdenum species in the form of molybdates or heteropolycompounds [3,4,58,130]. Since alumina exhibits a weak Raman signal, the Raman spectra only divulge the bands of Mo surface species that have great response coefficients [131,132]. Table 1 gathers some characteristic Raman vibrational bands of molybdate species [107,133].

Table 1 – Raman frequencies (cm^{-1}) of molybdate species [107,133]. υ corresponds to stretching vibrations and δ states for bending vibrations of either the terminal M=O groups or the internal Mo-O bonds.

Vibration	Species			
	$(NH_4)_6Mo_7O_{24}.4H_2O$	$Mo_7O_{24}^{6-}$	$Mo_8O_{26}^{4-}$	MoO_4^{2-}
υ_s (Mo=O)	931	943	965	897
υ_{as} (Mo=O)	879	903	925	837
δ (Mo=O)	354	362	370	317
υ (Mo-O-Mo)	-	564	860	-
δ (Mo-O-Mo)	217	219	230	-

In the case of HPA, there are three types of M-O bonds in all HPA structures, each of one having its own IR/Raman vibrational band [134]:

- Terminal bonds M-O_t (1000-900 cm^{-1})
- M-O_b bonds (M-O-M) (850-550 cm^{-1})
- M-O_c bonds (M-O(H)-M) (below 600 cm^{-1})

For instance, the work of Bergwerff et al. [28] can be considered one of the greatest examples using Raman spectroscopy as local characterization. As it was already mentioned in section 2.2.1 (page 39), this work concerns Raman spectroscopy studies in CoMo based catalysts supported on alumina. Indeed, they were able to obtain the distribution of Mo and Co species over alumina pellet (see Figure 29).

Recently, Gibson et al. [135] also performed an *in-situ* study about the impregnation of γ-alumina with a Mo(P) solution using a combination of X-Ray absorption Tomography and Diagonal Offset Raman Spectroscopy. This combined method provided the same nature of information as MRI, but additionally it provided chemical speciation information, which was obtained in a non-invasive way.

3.1.3. *UV-Visible spectroscopy*

UV-Visible spectroscopy gives qualitative and quantitative information about coordination environment of the metal ion as well as its electronic state. The bands of UV-Visible are characteristic of the local environment of the element (its symmetry, degree of oxidation, spin state). It is usually applied to characterize the impregnation solution (by operating in absorption mode) and the dried catalyst (by operating in diffuse reflectance mode).

For instance, UV-Visible is often applied to impregnation solutions containing either Co or Ni. According to Vakros J et al. [103], the characteristic band of Co^{2+} in solution is 515 nm, while for Ni^{2+} are 655 and 718 nm. Besides, this technique was also was applied to monitor the metal-ion speciation of catalyst precursors along the catalyst body on Ni/γ-Al_2O_3 system [136].

3.1.4. *Electron Probe Microanalysis (EPMA)*

The distribution of the elements deposited over support pellet can be obtained by Electron Probe Microanalysis (EPMA), which is a local elemental analysis [137]. It has a depth resolution that may vary from a few tenths of a micrometer to several micrometers and a voxel resolution of 1 µm. Detection limits between 100 to 500 ppm on a single analysis point are described.

As principal drawback, EPMA technique is a destructive analysis, since the catalysts must be bisected before measurements. The preparation of the samples is then done by polishing. Additionally, the sample must be pre-thermal treated (drying or calcination), which may induce several transformations, such as precursor's decomposition and formation of new surface species. Moreover, it is performed under secondary vacuum, which makes it non-suitable for moist samples. Finally, it is not sensible to the chemical environment of the analyzed element.

3.1.5. *Laser-induced breakdown spectroscopy (LIBS)*

Laser-induced breakdown spectroscopy (LIBS) is a technique that allows one to obtain *in-situ* quantitative elemental analysis [138]. It is based on atomic emission spectroscopy, which uses highly energetic laser pulses to induce sample excitation. Moreover, it can be either a qualitatively technique (i.e., to give information of the presence of particular elements) or a quantitatively one, in which the relative amount of different elements in the sample is quantified from the processing of the acquired spectra. It has a depth spatial resolution from 10 to 15 µm and a voxel resolution approximately of 2 µm. Moreover, no sample preparation is necessary, which is one of the main advantages of LIBS comparing to EPMA. An extended review concerning application of LIBS in for chemical mapping of materials can be found in [139]. Recently, LIBS method has been applied to characterize palladium-based porous alumina catalysts [140].

3.2. Characterization of descriptors that influence the impregnation step

The parameters that most influence the interactions between metal complex with support have been referred in section 2.4 (page 46). In the following paragraphs, there are some examples of suitable techniques to characterize some of these parameters.

3.2.1. *Local metal concentration*

The measurement of the local concentrations of elements can be achieved by EPMA for calcined samples. Quantitative analysis on bulk (non-porous) sample leads to a relative trueness of about 2% and relative precision lower than 1% for major elements [137]. On porous samples, trueness can strongly vary with the pore size, from 2% for true mesoporous sample to tens of percent in the presence of high macroporosity.

Also, relaxation-weighted images of the solvent obtained by MRI can reflect the local concentration of the solute. Bergwerff [58] obtained a correlation between ^{1}H MRI signal intensity of water and the Co^{2+} concentration in the impregnation solution. This calculus was based on the hypothesis that the Co^{2+} concentration of impregnation solution corresponds to the Co^{2+} amount on the support, for an excess impregnation. For impregnation solutions with Co^{2+} concentrations higher than 0.3 M, the NMR-signal became too low. One of the drawbacks of this approach is that it does not take into account the impact of the metal ion concentration and the nature on the relaxation times of the proton. Indeed, it considers that the impact of the metal ion in relaxation times of the proton is uniform. Thus, the relation between ^{1}H MRI signal intensity and concentration of metal ion precursor is not yet so well understood.

3.2.2. *pH*

Among the literature, there are not many studies concerning the measurement and control of the pH inside the pore system. Indeed, one of the main limitations of measuring the pH inside the pore system is to achieve a spatial resolution characteristic of the pores dimension in order to have a local measurement.

Nevertheless, pH characterization can be done by NMR Chemical Shift. For instance, the information about chemical shift obtained using ^{31}P NMR spectroscopy can be used to determine pH [141]. One of its main applications is the measurement of the intracellular pH. This method is based on the difference of 2.4 ppm between chemical shift of HPO_4^{2-} and $H_2PO_4^{-}$. As soon as there is a rapid exchange between these two forms, the average chemical shift is measured, which gives information about their relative concentrations [142]. Another solution might be to measure the pH by proton Chemical Shift Imaging. So far these studies concern more biological systems [143]. Nevertheless, it

can be limited by the presence of paramagnetic ions which can modify the apparent chemical shift of the phosphorus species.

3.2.3. *Additive Nature*

UV-Visible [58] and, in a few cases, Raman spectroscopies [4,7,60,68,130,144] can be used to determine different molecular structures of the complexes formed between the metal precursor and the additive.

Characterization of citric acid in solid state and in solution have already been performed by Raman spectroscopy [58,145]. In solution, Raman peaks between 1600 and 1350 cm^{-1} are usually ascribed to symmetric and anti-symmetric stretching vibrations of carboxylate group, ($\nu_s COO^-$) and ($\nu_{as} COO^-$), respectively. Vibrations mode $\nu_{as} COO^-$ are expected to appear at higher wavenumbers than $\nu_s COO^-$ [58]. While vibration modes approximately at 1720 cm^{-1} are characteristic of (ν COOH). Indeed, these Raman wavenumbers are of main interest since it allows one to identify the presence of citric acid or totally deprotonated citrate (absence of Raman peak at 1720 cm^{-1}). Additionally, C-O-H deformation is usually found between 1200 and 1050 cm^{-1}. CH_2 scissoring bands and H-C-H deformation bands (CH_2 wagging) are found in the region between 1350 and 1150 cm^{-1}. The region between 1100 and 700 cm^{-1} is characteristic of mainly C-C vibrations. Table 2 gathers the characteristic Raman peaks and vibrational assignment of citric acid.

Table 2 – Characteristic Raman peaks and vibrational assignment of citric acid in aqueous solution [58,145]

Raman bands (cm^{-1})	Assignments
1721 (disappears for pH > 6)	ν(COOH)
1430	Symmetric COO stretch
1392	CH_2 scissors
1292	CH_2 wag
1196	C-O-H deformation
941 (disappears for solution pH > 6)	C-C symmetric stretch
933	OH out-of-plane bend
816 (disappears for solution pH > 6)	Asymmetric COO deformation
701	C=O stretching
677	COO deformation

Besides, MRI can also give information about the interaction between the additive either with metal precursor or the support surface. Some examples are gathered bellow.

A.A. Lysova et al. [8] reported on the distribution of citrate inside an alumina pellet by monitoring the ^{1}H MRI signal. Furthermore, A.A. Lysova et al. [7] also studied the influence of adding citrate to cobalt-based catalysts supported on alumina, once more by monitoring the ^{1}H MRI signal (see Figure 36) with a spatial resolution of 139 μm × 231 μm. The BET surface area of the support was 149 m^2/g and the pore volume was 0.39 mL/g. The mean pore diameter was defined as 8 nm. The cobalt concentration in the impregnation solution was 0.2 M, the Co:Citrate ratio was in the range of 1:0 to 1:5 and the pH of the impregnation solution was in the range of 1 to 10. A competitive adsorption between the metal-ion precursor and citrate could be controlled by varying the pH and the citrate concentration in the impregnation solutions. For acidic solutions, they concluded that a higher concentration of citrate in the impregnation solution corresponded to a faster transport of Co^{2+} complexes For a pH higher than 5, a slow transport of Co^{2+} ions was reported, due to a strong interaction between $[Co(Cit)(H_2O)_3]^{2-}$ and the alumina surface.

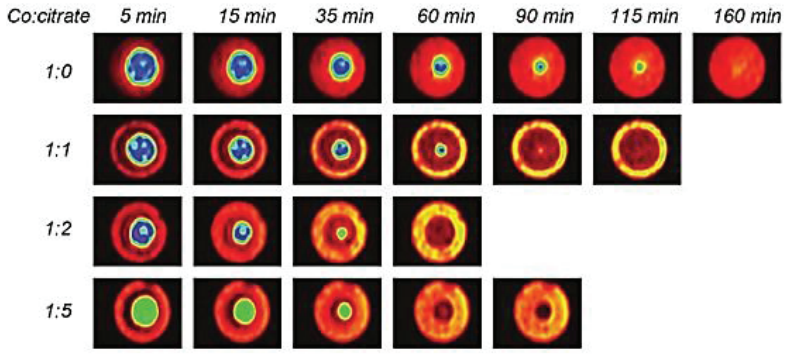

Figure 36 - 2D ^{1}H MRI of a γ-Al_2O_3 extrudate in transversal section with a spatial resolution of 139 μm×231 μm after impregnation with an aqueous solution containing 0,2M Co^{2+} and different Co^{2+}/citrate ratio. The red color corresponds to a low ^{1}H MRI signal intensity (short relaxation time T_2) (i.e., high concentration of Co^{2+} complexes), whereas blue color corresponds to a high ^{1}H MRI signal intensity (long relaxation time T_2) (i.e., low concentration of Co^{2+} complexes) [7]

In the same study, UV-Vis spectroscopy was also used in order to determine the nature of the Co^{2+} complexes present in the extrudates.

Impregnation of γ-Al_2O_3 support bodies with a solution containing Ni^{2+}-EDTA [126] was also studied through MRI. Once more the approach of monitoring the ^{1}H MRI signal of the water solvent to deduce the distribution of complexes of Ni was applied. γ-Al_2O_3 extrudates (12 mm long and 3.85 mm in diameter) with a BET surface area of 145 m^2/g and a pore volume of 0.36 mL/g were used. Impregnation solutions with 0.1 M Ni^{2+} (Ni:EDTA ratio of 1:1) and 0.6 M Ni^{2+} (Ni:EDTA ratio of 6:1) were studied. Images were collected using a spin-echo sequence either in T_1 or T_2 contrast, with a spatial resolution of 140 μm × 230 μm. They concluded that when the stoichiometric ratio was used, a uniform distribution of metal ion was obtained. The use of lower ratios leads to a Ni^{2+} egg-shell distribution, with EDTA ligand acting as linker between Ni^{2+} and the alumina surface. For a Ni:edta

ratio of 6:1, the macrodistribution of Ni could be controlled depending on the pH. Thus, a Ni^{2+} egg-white macrodistribution was obtained at a pH equal to 1, whereas at a pH equal to 6 a Ni^{2+} egg-shell distribution was obtained.

In addition to MRI measurements, UV-Vis micro-spectroscopy was also used in order to localize $[Ni(H_2O)_6]^{2+}$ and $[Ni(EDTAH_x)]^{(2-x)-}$. $[Ni(H_2O)_6]^{2+}$ was found to be along the cross section of the extrudate, after 2h of impregnation, whereas Ni^{2+}-EDTA remained in the edge of the extrudate.

Finally, EPMA technique is not very suitable in the presence of organic additives, due to their sensitivity to the thermal treatment. Therefore, the preparation of the sample constitutes one of the major difficulties.

3.3. Conclusion

Several studies prove that MRI is a suitable technique to monitor *in-situ* the transport of metals in a porous medium, since it is a non-destructive technique and allows low acquisition times (to the order of seconds to several minutes) [8,126,128]. So far, the spatial resolution in the image plane is approximately 140 μm by 230 μm [8,126,128], which constitutes a limitation since information is obtained only at a macroscopic level. Recently Gédéon et al. [128] improved the spatial resolution to 78 μm by 78 μm.

Besides, in MRI studies, the impact of transport, surface interaction and local metal concentration on the sequence parameters (namely, relaxation times) is not so well understood. Furthermore, absolute quantitative characterization is not performed.

Usually, MRI studies are complemented with other techniques, such as Raman and UV-Visible spectroscopies, which give information about the chemical nature of the different species present in the catalyst pellet. One of the drawbacks of these techniques is that catalysts must be bisected before measurements, which results in a modification of the equilibrium of impregnation. Besides, a thermal treatment may be required, which induces several transformations.

With respect to the descriptors that influence the impregnation step, different techniques can be applied. Image processing of MRI seems to be a promising approach to obtain quantitative information about local metal concentration. Information about the pH can be obtained through ^1H MRI Chemical Shift, while information about additive nature can be provided by either UV-Visible or Raman spectroscopy.

4. Conclusion of the bibliographic study and strategy of the thesis

The objective of this work is to characterize the impregnation step of molybdenum based catalysts supported on γ-alumina promoted either by Co or Ni, in the presence of phosphorus and/or organic additives, such as citric acid. The aim is to identify the key descriptors and improve the impregnation step. This bibliographic study is mostly focused on the description of different phenomena that take place during impregnation step and on the most suitable analytical techniques to characterize them.

The different phenomena that take place during impregnation step are:

- Transport by capillarity, which can be described by Darcy's law or Poiseuille state. Nevertheless, as it is a very fast phenomenon, it cannot limit transport of solution containing the active precursors through the porous space.
- Transport by diffusion, which can be described by Fickian diffusion.
- Surface interaction, which comprises adsorption (usually described by Langmuir treatment or by a chemical reaction in the cases of irreversible adsorption), dissolution of the support and/or precipitation.

The transport by diffusion is dependent on the molecular diffusion coefficient of the different chemical species in the liquid phase. According to Fick's law, the driving force for diffusion increases with the chemical species concentration in solution. Additionally, the effective diffusion coefficient is also dependent on textural properties of the support, such as pore size, porous volume, connectivity and tortuosity of the porous network.

Concerning surface interaction (either adsorption on support surface or precipitation of the chemical species present in solution), several factors should be taken into account. First, the properties of the impregnation solution, such as the concentration of metallic precursors and additive, the pH and the ionic strength influence the speciation in solution and in the support and consequently, the final metal distribution profile. Second, the nature of support surface and more precisely, the density of OH groups are critical, since they determine the interaction between the surface and the metallic precursor. In the particular case of alumina, its surface is covered with hydroxyl groups (Al-OH), which may exhibit either Lewis and Brønsted basicity or Brønsted acidity. Their proportions are determined by the pH of the solution.

The challenge in this thesis is to accurately describe the physical (transport by capillarity and diffusion) and chemical (evolution of chemical species, adsorption and/or precipitation) phenomena involved in the impregnation step. More precisely, it comprises to spatially monitor the metal species in the aqueous impregnation solution as a function of time without modifying the equilibrium of impregnation and with spatial resolution and time resolution suitable with the this step.

Recently, MRI has been applied to monitor *in-situ* the impregnation step of supported catalysts, since it is a non-invasive and non-destructive technique [5–8,68,126,128]. Moreover, the characteristics times of impregnation are accessible by MRI, yielding spatial resolution of approximately 140 μm by 230 μm [128]. The order of magnitude of the spatial resolution achieved so far constitutes a limitation, since information only at a macroscopic level is obtained. Recently Gédéon et al. [128] obtained a spatial resolution of 78 μm by 78 μm, but improvements can still be achieved. An indirect MRI approach has been used to monitor de transport of paramagnetic species, such as Ni^{2+} (depending on the chemical environment) and Co^{2+} and diamagnetic species, such as Mo^{6+} . These species induce a change in the relaxation times of the protons, leading to relaxation-weighted images. Besides, this approach has also been applied to cases where impregnation is performed in the presence of organic additives. Nevertheless, these studies concern only the transport of monometallic solutions. Indeed, MRI technique can be a very promising technique if it enables to monitor the transport of a complex impregnation solution as a function of textural and surface properties of the support.

In addition, Raman spectroscopy has been widely used to study molybdenum solutions and molybdenum based catalysts supported on alumina because of the strong signal of these species [3,4,58,130]. Unlike MRI, Raman spectroscopy is an invasive technique, since catalysts must be bisected before measurements in order to obtain information within the pellet. Raman spectroscopy allows identification of the chemical nature of the species either in solution or in the support. Additionally, Raman mapping can give access to the chemical nature of molybdenum species with a spatial dimension on the bisected pellet. This chemical study can be carried out by modifying parameters such as the pH of the impregnation solution and the concentration of the metal species.

To conclude, **in order to identify and describe the physicochemical descriptors that govern the transport of the metallic precursors within the porosity of the support, the strategy of this thesis is implemented into three steps:**

1. **Implementation and application of the MRI technique** to monitor the impregnation of simple solutions, *i.e.*, monometallic solutions composed either by Ni or Co, eventually in the presence of citric acid. The main challenge of this step is to improve the spatial resolution so far achieved in the literature in order to obtain local information. Yet, this can be hindered by the presence of paramagnetic elements at high concentrations. Besides, a quantitative approach based on MRI and EPMA techniques is also evaluated in order to obtain local information about the metal concentration. MRI and Raman Imaging techniques are then applied to study the impact of solution properties on the impregnation of monometallic solutions.
2. **Study of the phenomena involved in impregnation of HDT catalysts.** More precisely, the impact of phosphorus on the transport of Mo, a possible competitive adsorption between P, Co

and Mo and finally the impact of a citric acid are studied. The characterization tools developed with impregnation with monometallic solutions are extended to more complex impregnation solutions. At this stage, one should be able to distinguish the different contributions of the different elements of the impregnation solution on the MRI images.

3. **Development of an impregnation model** to describe the transport by capillarity and by diffusion as well as to take into account the adsorption on alumina surface. The validation of this model is made based on the MRI results of impregnation with monometallic solutions.

Chapter II – Experimental procedure

In the first part of this chapter, the catalyst preparation, which concerns the choice of the metallic precursors, additives and the support as well as the impregnation method is described. In the second part, a detailed description of MRI and Raman Imaging is given as well as a brief explanation concerning the application of Electron Probe Microanalysis. At the end, the procedure of image processing for both MRI images and Raman images is explained.

1. Catalyst preparation

1.1. Preparation of the impregnation solutions

Impregnation solutions have been prepared by dissolving the proper amount of metal precursor (and additive when needed) in water in order to obtain the desired concentration of the precursor. The following compounds have been used:

- Nickel nitrate ($Ni(NO_3)_2.6H_2O$) of 98.5 wt.% purity (Sigma-Aldrich, CAS number 13478-00-7)
- Cobalt nitrate ($Co(NO_3)_2.6H_2O$) of 98.0 wt.% purity (Alfa Aesar, CAS number 10026-22-9)
- Ammonium heptamolybdate ($(NH_4)_6Mo_7O_{24}$) of 100 wt.% purity (VWR BDH Prolabo)
- Phosphoric acid (H_3PO_4) of 85.0 wt.% purity (Sigma-Aldrich, CAS number 7664-38-2)
- Citric acid ($C_6H_8O_7$) of 99.5 wt.% purity (Sigma-Aldrich, CAS number 77-92-9)
- Oxygen peroxide (H_2O_2) of 30 wt.% of purity, which is needed to increase AHM solubility in water)
- Sodium hydroxide (NaOH) solution of 46/51 wt.% purity (Fisher Chemical, CAS number 215-185-5), which is used to adjust solution pH

1.1.1. Monometallic solutions preparation

Simple solutions, *i.e.*, monometallic solutions composed either by Ni or Co in the presence or not of a citric acid have been prepared.

Nickel and cobalt solutions have been prepared by varying the concentration of the nitrate metallic precursor, with solution pH ranging from 5 to 6. Table 3 and Table 4 gather the concentration of nickel and cobalt solutions, respectively. Moreover, it has been experimentally verified that there is no evolution of the solution pH after contact with the alumina pellet.

Table 3 – Nickel concentration in impregnation solutions

$[Ni^{2+}]$ (M) in impregnation solution	**wt% Ni^{2+} in impregnation solution**
0.05	0.29
0.06	0.35
0.07	0.40
0.08	0.46
0.09	0.51
0.10	0.57
0.11	0.63
0.20	1.11
0.30	1.17

Table 4 – Cobalt concentration in impregnation solutions

$[Co^{2+}]$ (M) in impregnation solution	**wt% Co^{2+} in impregnation solution**
0.05	0.29
0.08	0.46
0.09	0.52
0.10	0.57
0.11	0.63
0.20	1.11

Different citric acid (CA) solutions in the absence of nickel have been prepared. Besides, the solution pH has also been varied by adding NaOH. The composition of citric acid solutions is gathered in Table 5.

Table 5 – Composition of citric acid solutions used. In H_3Cit, Cit corresponds to $C_6H_5O_7$.

[H_3Cit] (M)	Solution pH		
0.2	1.9	5.1	11.9
0.4	1.7		
0.8	1.5		

To study the impact of presence of an additive in impregnation, citric acid has been added to different Ni solutions by co-impregnation. Different nickel concentrations have been tested, with different CA:Ni molar ratios above and below the stoichiometry ratio needed to form a nickel-citrate complex (1:1). Table 6 gathers the composition of Ni-CA solutions.

Table 6 - Composition of nickel and citric acid solutions.

[Ni^{2+}] (M)	CA:Ni (molar)	[CA] (M)	Solution pH
0.05	0.4	0.02	2.4
0.05	1	0.05	2.1
0.05	1.2	0.06	1.7
0.05	4	0.2	1.4
0.2	0.4	0.08	2.1
0.2	1	0.2	1.9
0.2	1.2	0.24	1.1
0.2	4	0.8	< 1.1

Besides, the pH of nickel-CA solutions has also been modified by adding NaOH. Table 7 gathers the composition of impregnation solutions used.

Table 7 - Composition of Ni-CA impregnation solutions used. Cit corresponds to $C_6H_5O_7$.

[Ni^{2+}] (M)	CA:Ni (molar)	[CA] (M)	Solution pH
0.05	1.2	0.06	8
0.2	1.2	0.24	6

1.1.2. Bimetallic solutions preparation

For preparation of a classical HDT catalyst, impregnation solutions have been prepared based on molybdenum, cobalt (or nickel), phosphorus and/or citric acid. Table 8 gathers the composition of the different solutions prepared. The applied P:Mo ratio corresponds to 0.4 (molar), while cobalt is added

in a Co:Mo ratio equal to 0.3 (molar). Concerning citric acid, CA:Mo ratios ranging from 0.2 to 1 have been used. Once again, it has been experimentally verified that there is no evolution of the solution pH after contact with the alumina pellet.

Table 8 - Composition of molybdenum solutions in the presence of metal promotor and additives

Solution	[Mo] (M)	[P] (M)	[Co] (M)	[CA] (M)	pH
Mo	0.8	-	-	-	6.0
MoP	0.8	0.32	-	-	2.0
CoMo	0.8	-	0.24	-	5.0
CoMoP	0.8	0.32	0.24	-	2.0
NiMo	0.8	-	0.24	-	5.0
NiMoP	0.8	0.32	0.24	-	2.0
MoCA	0.8	-	-	0.16	3.7
MoCA	0.8	-	-	0.80	1.7
CoMo-CA	0.8	-	0.24	0.32	1.8
CoMoP-CA	0.8	0.32	0.24	0.32	1.3
CoMoP-CA	0.8	0.32	0.24	0.16	<1.3
CoMo-PCA	0.8	0.32	0.24	0.56	<1.3

1.2. Support properties

A pre-shaped γ-Al_2O_3 is in the form of trilobal extrudate, with 1.2-1.3 mm diameter and 3-6 mm of length is used as support. This support is characterized by a monomodal pore size distribution centered about 9 nm. The main characteristics of γ-Al_2O_3 support are gathered in Table 9.

Table 9 - Characteristics of γ-Al_2O_3 support. Hg porosimetry are used to determine porosity (ε), pore volume and mean pore size (d_{pore}), while N_2 adsorption-desorption is used to determine the specific surface area (S_{BET}).

Support	Porous Distribution	S_{BET} (m^2/g)	d_{pore} (nm)	$V_{mesoporous}$ (cm^3/g)	$V_{macroporous}$ (cm^3/g)	ε	Shape
γ-Al_2O_3	Monomodal (Mesoporous)	260	9	0.6	0.01	0.65	Trilobal extrudate

1.3. Impregnation methods

Two different impregnation methods (method A and B) have been performed in order to put in evidence the different phenomena that take place during this preparation step. The γ-Al_2O_3 support is

not submitted to any pre-treatment in any of the methods. Therefore, porosity of alumina is totally hydrated.

- Method A – Standard impregnation

Standard impregnation method consists in contacting for 30s one γ-Al_2O_3 pellet with the impregnation solution, being the excess solution removed by a wiping to avoid artifacts in MRI images. The sample is then introduced in a capillary tube with 1.7 mm diameter ø and then in a 5 mm ø thick wall NMR tube having a heavy wall thickness of a 1.4 mm. The capillary tube allows one to ensure that the sample is vertically positioned and parallel to the z direction of the main magnetic field and the z gradient of imaging. The preparation method is schematically shown in Figure 37.

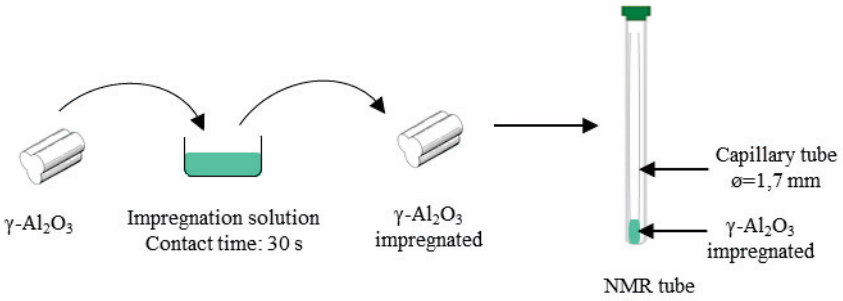

Figure 37 – Preparation method A: impregnation with no thermal pretreated support – standard impregnation (closest of the traditional incipient wetness impregnation)

By performing this method, the aim is to be as close as possible to wetness incipient impregnation method, which is usually carried out to prepare HDT catalysts. Besides, the aim of this preparation method is also to put in evidence the **capillary transport**. In this work, this method is performed to study the impact of solution properties on the impregnation step. Thus, it is referred as standard impregnation. This preparation method has already been performed in the literature by Lysova et al. [8].

- Method B - Diffusional impregnation

In order to study impregnation in **diffusional conditions**, γ-Al_2O_3 pellet is first saturated with water (same solvent as the impregnation solution). After that, preparation method A is performed. Figure 38 shows a schematic picture of this preparation method.

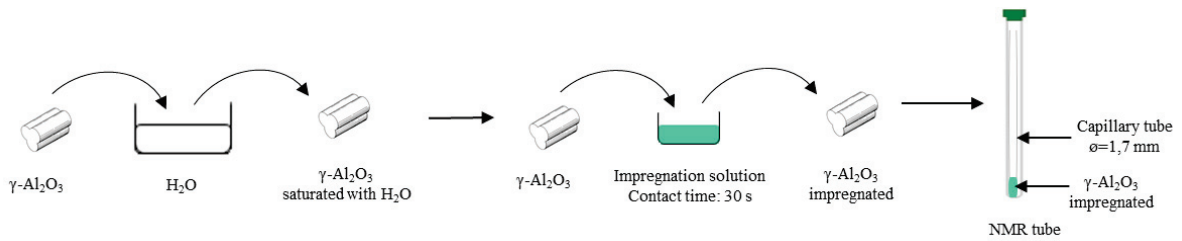

Figure 38 - Preparation method B: diffusional impregnation no thermal pretreated support

2. Characterization techniques

2.1. Magnetic Resonance Imaging technique

2.1.1. *Theoretical nuclear magnetic resonance (NMR) principles*

Magnetic Resonance Imaging (MRI) is based on nuclear magnetic resonance (NMR) principles. All nuclei with an odd atomic number have a fundamental quantum mechanical property called spin, which confers an intrinsic magnetic moment to the nucleus. The nuclear magnetic resonance phenomenon occurs when the nuclei of atoms are immersed in a static magnetic field and exposed to a second oscillating magnetic field. In the absence of an external magnetic field, the spin directions of all atoms are random. When placed in an external magnetic field, the spins align with the external field. There are two possible orientations with respect to the external field: parallel (more stable position) and antiparallel (less stable). To obtain a NMR (or MRI) signal, transitions must be induced between these two energy levels. In the specific case of MRI, the MRI signal of the nucleus is spatially visualized.

In this study, a focus is set on the proton signal as a function of its chemical environment. Indeed, MRI experiments applied in catalysis are based on the impact of metal ion, phosphorus or citric acid on ^{1}H signal of water present in the porosity of the support. The most suitable way to visualize metal precursor or additive transport in the porosity is based on their impact on the proton relaxation properties.

In this part, a focus on the description of the physical properties of nuclei and their impact on the MRI images is presented.

Relaxation is the phenomenon in which spins release the energy received from a radiofrequency (RF) pulse and return to equilibrium along z direction. This relaxation process enables to observe the NMR phenomenon.

In an NMR experiment, the magnetization vector $\vec{M}$ is a result of the sum of all the contributing magnetic moments $\overrightarrow{\mu_i}$ of the individual nuclei. Relaxation phenomena represent the return to the equilibrium state of $\vec{M}$ along the applied magnetic field ($\overrightarrow{B_0}$) as a function of time. They depend on the energy transfer to the environment (also called lattice) and the interactions with other spins. These two processes, associated to the spin-lattice relaxation so called longitudinal relaxation T_1 and to the spin-spin relaxation so called transverse relaxation T_2 are responsible for the loss and the broadening of the NMR signal, respectively (see Figure 39).

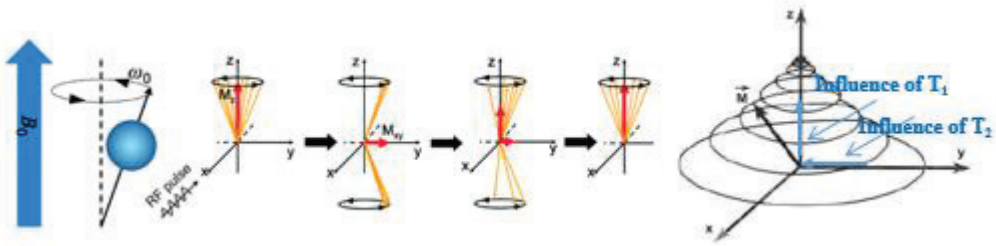

Figure 39 - Initially, the net magnetization vector is collinear to B_0. The action of the excitation pulse (a r.f. pulse, in this case a π/2 pulse) deviates M from its equilibrium position and it starts to precess around B_0 at the Larmor frequency. As a result of this excitation pulse, M is rotated to lie along the y-axis in the x-y plane [142]

The magnetization is given by the following Bloch equation (see Eq. 27) [146]:

$$\frac{d\vec{M}}{dt} = \gamma\left(\vec{M} \wedge \vec{B}\right)_{x,y} - \frac{\overrightarrow{M_{x,y}}}{T_2} - \frac{\overrightarrow{M_z} - \overrightarrow{M_o}}{T_1} \qquad \textbf{Eq. 27}$$

The solution for motion for the longitudinal nuclear magnetization, $M_z(t)$ simplifies to Eq. 28.

$$M_z(t) = M_0\left(1 - e^{-t/T_1}\right) \qquad \textbf{Eq. 28}$$

While for transversal magnetization $M_{xy}(t)$ is given by Eq. 29.

$$M_{xy}(t) = M_0\left(e^{-t/T_2}\right) \qquad \textbf{Eq. 29}$$

M_{xy} describes a spiral in xOy plane. Its rotation around xOy plan induces a magnetic field or a RF wave. This signal is called Free Induction Decay (FID) and is collected by a coil, which is located in the xOy plane. When M_{xy} is directed to the coil, the signal is positive, and on the contrary, it is negative. Between these two positions, the signal decreases exponentially, as described by Figure 40.

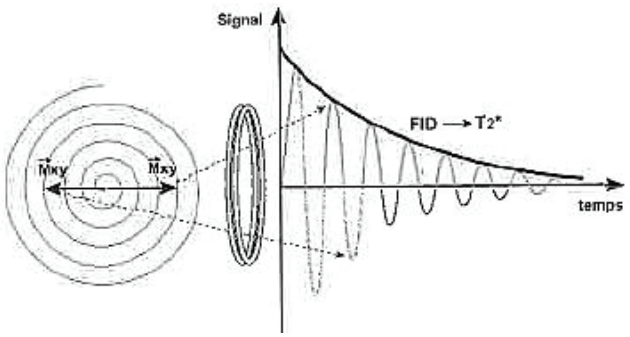

Figure 40 - Free Induction Decay FID, where T_2^* represents the overall relaxation time that governs the decay of transverse magnetization. T_2^* takes into account the effect of the non-homogeneities of molecular origin and those of the field B_0. T_2^* is smaller than T_2. [147]

2.1.2. *Basis of MRI*

The challenge in MRI characterization is to localize strictly the NMR signal in the three direction xyz [147] during a dynamic phenomenon, such as the transport of metal precursors through a porous system. Spatial and time resolved information needs to be encoded into the NMR signal. Hence, spatial location of the signal is done by applying magnetic field gradients along x, y and z axis.

Under a static magnetic field B_0, spins precessed at the Larmor frequency, given by $\omega_0 = \gamma B_0$, where ω_0 is the angular velocity linked to the precession frequency υ_0, γ is the gyromagnetic ratio and B_0 is the magnetic field.

A variation of the effective magnetic field B_{eff} ($B_{eff} = B_0(1-\sigma)$, where σ is the shielding constant) leads to a variation of ω_0 as a function of spin position. So that, ω_0 can be described as a measurement of the position and the velocity of the spin. In MRI experiments, these variations in magnetic field are induced by using magnetic field's gradients along the x, y and z axis. The effective magnetic field felt by spins is linearly increased in the direction of the applied gradient [147].

2.1.2.1. *Imaging Gradient Principle*

The simplest imaging sequence consists of a π/2 selective RF (radiofrequency) pulse and the three gradients pulses, which are described in Figure 41. Using a **slice gradient** G_s, along the z direction, one can select a volume of interest at a particular z position.

After the selection of the slice the other two dimensions along the y and x axis must be encoded to produce a two-dimensional image, by applying a **phase-encoding gradient** $G_ø$, and a **frequency-encoding gradient** G_f.

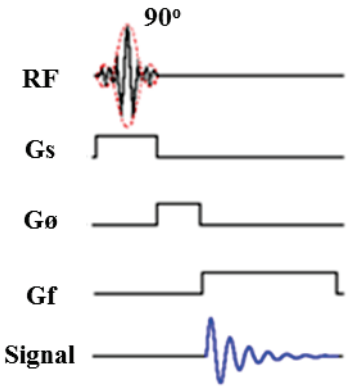

Figure 41 – Principle of a MRI sequence

The application of three gradients during a MRI sequence can be described as follows:

- Slice selection gradient (G_s)

This gradient is applied during 90° RF selective pulse. At this point, a slice has been chosen along Z axis. The π/2 RF selective pulse is applied at a frequency ω_s with an excitation bandwidth of $\pm\Delta\ \omega_s$. This RF pulse allows one to flip spin magnetization of protons into the transverse plane (xOy), see Figure 42. Only protons precessig at frequencies between $\omega_s+\Delta\omega_s$ and $\omega_s-\Delta\omega_s$ are affected and give an NMR signal. The choice of the slice-select direction dictates the orientation of the image: axial, sagittal or coronal.

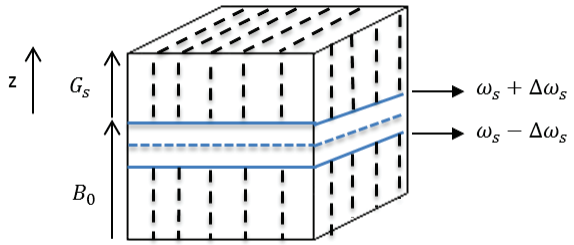

Figure 42 – Slice selection during MRI experiment - effect of G_s gradient to spin magnetization

The slice thickness (ST) corresponds to the volume where protons are affected by the RF pulse and is defined as the ratio of the RF pulse frequency bandwidth $2\Delta\omega_s$ and the value of the slice gradient G_s (see Eq. 30) [146]:

$$ST = \frac{2\Delta\omega_s}{\gamma G_s} \qquad \textbf{Eq. 30}$$

Where, γ is the gyromagnetic ratio.

Slice thickness ST can be adjusted by the RF selective pulse bandwidth and the strength of the slice gradient.

- Phase-encoding gradient ($G_ø$)

The phase encoding gradient ($G_ø$), which is schematically applied along Y axis, is used to assign a specific phase angle to the transverse magnetization vector depending on its location. The net effect of G_ϕ is to introduce a spatially dependent phase shift into the acquired signal [146]. The effective magnetic field felt by spins depends on their position and the precession frequency is given by Eq. 31.

$$\upsilon = \frac{\gamma}{2\pi}(B_0 + yG_ø) = \upsilon_0 + \frac{\gamma}{2\pi}.yG_ø \qquad \textbf{Eq. 31}$$

- Frequency-encoding gradient (G_f)

Finally, a frequency-encoding gradient (G_f) is schematically applied along x direction. In contrast to G_ϕ, G_f is turned on during data acquisition. That is why it is also called read gradient. Under the influence of this gradient, spins will precess at different frequencies [146]. The effective magnetic field felt by spins depends on their x position and the precession frequency is given by Eq. 32.

$$\upsilon = \frac{\gamma}{2\pi}\left(B_0 + xG_f\right) = \upsilon_0 + \frac{\gamma}{2\pi}.xG_f \qquad \textbf{Eq. 32}$$

The spatial phase encoding and frequency encoding gradient can be described by drawing a matrix, as schematized in Figure 43: spins in the same line, *i.e.* at the same i position along y direction, will all have the same phase ϕ; each column corresponds to spins resonating at the same frequency. Hence, magnetization vector of each spin at a xy position into the matrix is characterized by its own phase and frequency.

Moreover, using this simple MRI sequence image acquisition is done line by line (see Figure 43). For each line, phase-encoding and frequency-encoding gradient are applied. The phase-encoding one is increment vertically, while frequency-encoding one is incremented horizontally. The time between each line, *i.e.*, each cycle is called the repetition time (TR) [147].

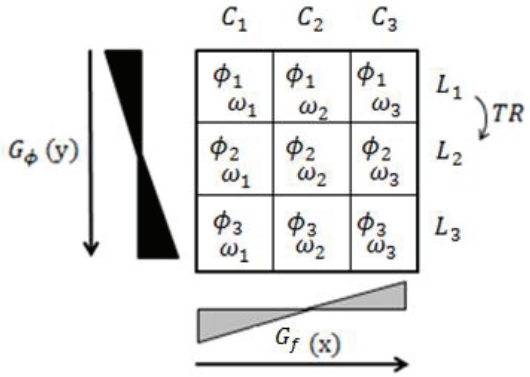

Figure 43 – Each spin is located in a certain line and column of the matrix, depending on its phase and frequency: spin with coding ($\boldsymbol{\phi_1, \omega_1}$) is located in pixel of first line and first column (L1,C1) and so on [147]

Data from MRI experiments is stored in the so-called **k-space** or Fourier plane [148]. k-space is a grid of raw data, whose main axes are k_x and k_y. Both axes represent spatial frequencies in the x and y directions, instead of positions.

Therefore, the acquired k-space data must be converted into real images in spatial domain. Usually, decoding of spatial information is done by a double inverse Fourier Transform, in the frequency encoding direction (along x direction in this chapter) to extract the frequency domain information and

then in the phase encoding direction (along y direction) to extract information about the locations in the phase encoding gradient direction.

2.1.2.2. *Sequences of NMR imaging*

A number of MRI sequence are reported in literature and they are usually optimized for biological systems. In this part, the description of some of MRI sequences is presented.

2.1.2.2.1. Combined T_1&T_2 Measurement by RARE MRI Sequence

RAREVTR (Rapid Acquisition with Relaxation Enhancement with variable repetition time TR) sequence allows one to measure simultaneously the T_1 and T_2 relaxation times. It is based on multiple-echoes sequence [149]. These multiple spin echoes are generated using the CPMG (Carr-Purcell-Meiboom-Gill) sequence [150,151], which is the reference sequence to measure the T_2 relaxation time, with slice selective RF pulses. Additionally, by varying the repetition time TR, RAREVTR sequence allows one to measure also the T_1 relaxation time.

A $\pi/2$ pulse is first applied simultaneously with the slice gradient (G_s), after which a train of π pulses is applied to refocus the spins, leading to the echo formation, as described in Figure 44. A phase encoding gradient ($G_Ø$) follows each π pulse, after which the frequency encoding gradient (G_f) is applied and the acquisition of the signal occurs. For each echo, $G_Ø$ is different, which is why, for a single TR, multiple k-space lines can be acquired at once.

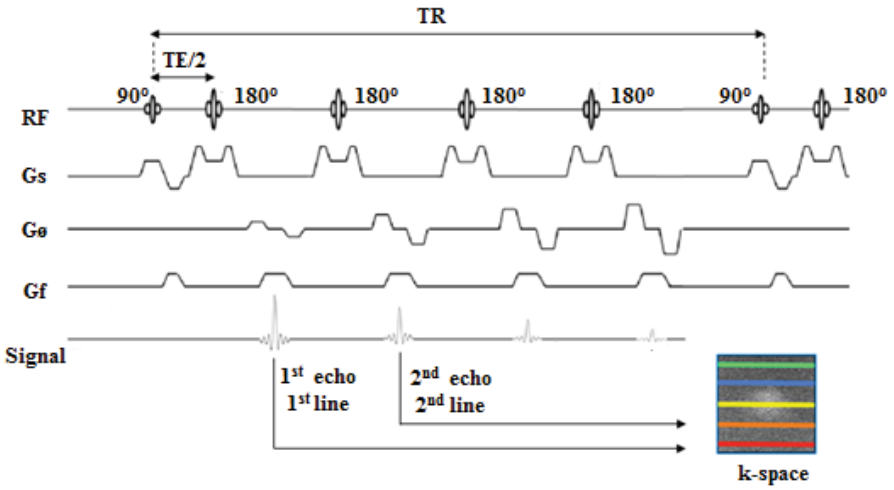

Figure 44 – RARE sequence

In RAREVTR sequence, T_1 is also measured by a saturation-recovery method (variable TR), while T_2 is measured by a multi-echo CPMG sequence (variable TE). A list of repetition time and echo time are defined to, respectively, fit T_1 and T_2 according to Eq. 33 and Eq. 34. For each repetition time the number of echoes defined is performed.

$$M_z(t) = M_0\left(1 - e^{-TR/T_1}\right) \quad \textbf{Eq. 33}$$

$$M_z(t) = M_0 e^{-TE/T_2} \quad \textbf{Eq. 34}$$

Where, $M_z(t)$ is the signal intensity at a certain (TR, TE) and M_0 is the equilibrium signal.

2.1.2.2.2. Imaging by Single Point Imaging (SPI) sequence

In SPI sequence, an impulsion with α angle ($\alpha < \pi/2$) is applied after the gradients are turned on (see Figure 45). The detection of the signal (which is only one point) is done after an encoding time (t_p). All spatial information is obtained using phase-encoding gradients. The gradients of the three directions (x, y and z corresponding to G_f, $G_ø$ and G_s, respectively) are applied at the same time during the duration of the sequence. As a result, the encoding time is determined by the extent of the FID. The value of the applied gradient is incremented after each repetition (i.e., after each TR).

Since the detection of the signal is acquired at a constant time interval after the pulse, there is no information on spectral evolution. It means that, there is no frequency encoding, and therefore the SPI images are not influenced by distortions due to the magnetic field inhomogeneity and susceptibility variations.

So that, SPI is not influenced by T_2^* (parameter T_2^* takes into account the non-homogeneities of the field), since the magnetization is measured as a function of applied gradient and not as a function of time [152]. This sequence will then give information in T_1 weighted.

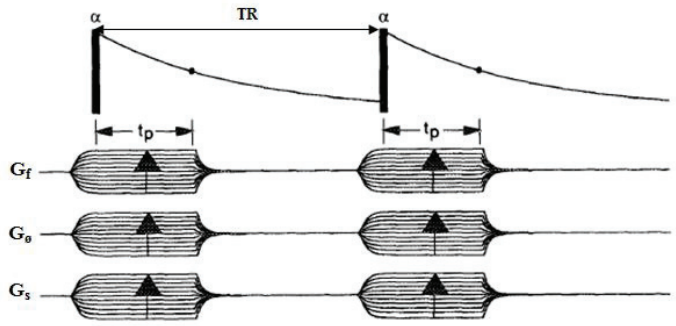

Figure 45 – Single Point Imaging sequence [153]

Nevertheless, the execution of this sequence might be delicate due to the following reasons:

- Slice selection might be difficult due to very small T_2 relaxation times
- Phase encoding is done in three directions. Therefore, the experience must be repeated for each gradient value to properly sample the signal in the three dimensions, which increases the acquisition time.

The signal I measured after each RF pulse is given by Eq. 35 [153]:

$$I = I_0 K \quad \textbf{Eq. 35}$$

Where I_0 is the signal that would be measured immediately following a 90° pulse and K is defined according to Eq. 36:

$$K = e^{-t_p/T_2^*} G\left(\frac{TR}{T_1}, \alpha\right) \quad \textbf{Eq. 36}$$

Where t_p corresponds to the encoding time, T_2^* corresponds to the transverse relaxation and $G(TR/T_1, \alpha)$ describes the signal attenuation from the Ernst-angle excitation pulse, α (see Eq. 37).

$$G = \frac{1 - E}{1 - E^2}\sin(\alpha) \quad \textbf{Eq. 37}$$

Where

$$\cos(\alpha) = E = e^{-TR/T_1} \quad \textbf{Eq. 38}$$

In Eq. 38 TR corresponds to the repetition time and T_1 corresponds to the longitudinal relaxation.

2.1.2.2.3. Imaging by spin-echo sequence

In a spin-echo sequence three different gradients are also applied: slice-selection gradient (G_s), a phase-encoding gradient ($G_ø$) and a frequency-encoding gradient (G_f). As schematized in Figure 46, two radiofrequency pulses are applied: a 90° pulse, which creates the detectable magnetization and a 180° rephasing pulse. Repetition time (TR) determines the recuperation of the longitudinal magnetization, while the Echo-time (TE) determines the time at which the signal is measured. Relation between these parameters is given by Eq. 39:

$$M_z(t) = M_0\left(1 - e^{-TR/T_1}\right)e^{-TE/T_2} \quad \textbf{Eq. 39}$$

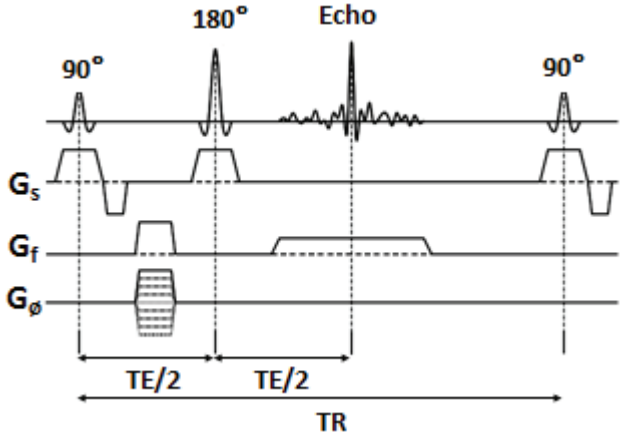

Figure 46 - Spin echo sequence for MRI experiments, in which three gradients are applied: slice-selection gradient (G_s), a phase-encoding gradient ($G_ø$) and a frequency-encoding gradient (G_f). TR corresponds to Repetition Time, while TE to echo-time (adapted from [147])

2.1.2.3. *Contrast in MRI*

In MRI, the contrast corresponds to the conversion of the NMR signals (magnetization) in a grayscale (black: weak signal; white: strong signal). This contrast results from the differences of relaxation times (T_1 and T_2) as well as the proton density (ρ). Indeed, chemical species of the impregnation solution induce a perturbation on the ^1H MRI signal of water protons inside the porosity of the support. They influence the relaxation times of proton, by decreasing/increasing the T_1 and T_2 relaxation times.

2.1.2.3.1. T_1 contrast experiments - Influence of the repetition time (TR)

In Figure 47 the comparison between the evolution of NMR signal as a function of time for two materials (A and B) having different T_1 is shown. For a long TR, the longitudinal magnetization of both materials has time to recover its initial level: it is not possible to distinguish the two materials by their T_1. For a small TR the material with the smallest T_1 (A) recovers faster and will have the strongest signal (white imaging in a grayscale) - T_1 contrast [147]. Thus, to have a **T_1 contrast**, both following factors should be met:

1. Small TR
2. Small TE, in order to minimize the T_2 contrast

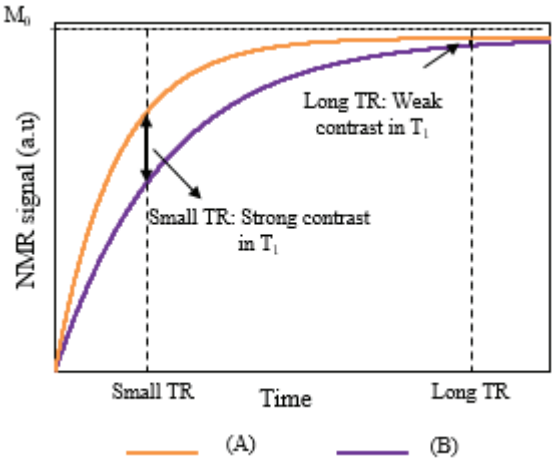

Figure 47 – Comparison between two materials (A and B) having different T_1. For a long TR, the longitudinal magnetization of both materials has time to recover its initial level: it is not possible to distinguish the two materials by their T1. For a small TR the material with the smallest T1 (A) recovers faster - T1 contrast (adapted from [147])

2.1.2.3.2. T_2 contrast experiments- Influence of the echo time (TE)

Figure 48 schematizes the evolution of the NMR signal as a function of time for two materials (A and B) having different T_2. For a small TE, the difference in the decrease of the transversal magnetization

of the two materials does not have time to express itself. For a long TE, the transversal magnetization of material with the highest T_2 (B) will decrease more slowly and will have the strongest signal - T_2 Contrast [147]. Thus, to achieve a **T_2 contrast** following parameters must be implemented:

1. Long TR, in order to minimize the T_1 contrast
2. Long TE

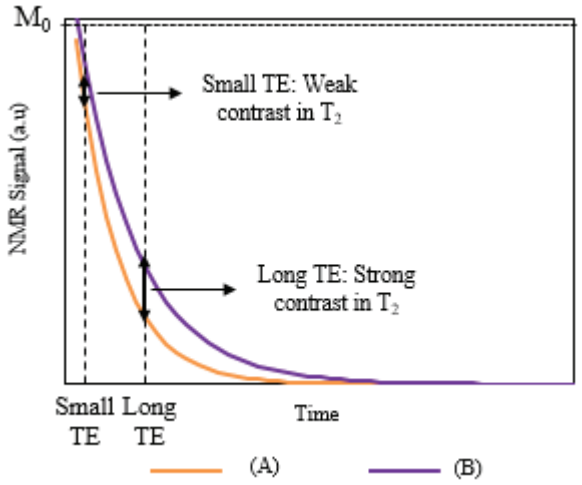

Figure 48 – Comparison between two materials (A and B) having different T_2. For a small TE, the difference in the decrease of the transversal magnetization of the two materials does not have time to express itself. For a long TE, the material with the highest T2 (B) decreases more slowly -T_2 Contrast [147]

2.1.2.3.3. Proton density (ρ) contrast experiments

In order to achieve a **proton density (ρ) contrast, the following** parameters must be used:

1. Long TR, in order to minimize the T_1 contrast
2. Small TE, in order to minimize the T_2 contrast

In this way, T_1 and T_2 contrasts are minimized and a proton density (ρ) contrast is obtained. The differences in the proton density will lead to differences in M_{zo} vectors in the equilibrium and consequently, differences in the signal.

2.1.2.4. *Geometry of MRI images*

The geometry of MRI images is based on two main concepts: field of view (FOV) and matrix size image, which are based in voxels and pixels. Voxel represents the elementary volume of the sample, whose signal intensity is reported to the corresponding pixel (picture element) in the image (Figure 49).

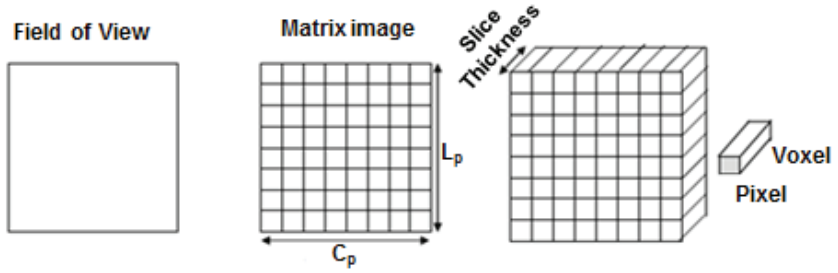

Figure 49 - Field of view (FOV), matrix image, voxel and pixel [147]

FOV represents the real dimensions of slice (width and height) and matrix image size determines the number of rows (L_p) and the number of columns (C_p) [147]. Pixel size is determined by FOV and matrix size as it will be explained in the following paragraphs.

MRI is mainly used for medical application, in which the sample is horizontally positioned and is parallel to the z direction of the magnetic field and the z direction of imaging. In the present study, the sample is vertically positioned, which means that the gradient-coordinate system (xyz) undergoes a few exchanges as schematized in Figure 50 (B), which has the same dimensions of Figure 50 (A). In these figures, FOV read corresponds to field of view in reading direction, FOV P_1 is the field of view in phase direction and FOV P_2 corresponds to the slice thickness.

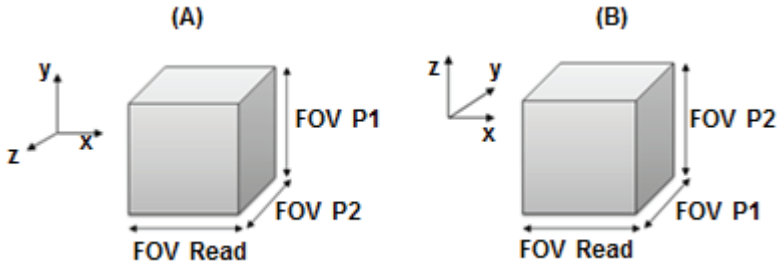

Figure 50 – Gradient-coordinate system (xyz) of (A) medical application (sample horizontal positioned) and (B) present study (sample vertical positioned)

As already explained, images obtained by MRI can be visualized as a matrix. Therefore, for a 3D experiment, three dimensions are defined: Matrix Read×Matrix P_1×Matrix P_2. Beyond them, only Matrix P1 and Matrix P2 will contribute to the acquisition time. Matrix Read corresponds to the number of columns, while Matrix P_1 to the number of lines. Matrix P_2 defines the number of images obtained (each one corresponding to a certain slice).

2.1.3. *Experimental Apparatus*

MRI experiments have been performed on a Bruker Avance 400MHz spectrometer, which produces a homogeneous and stable superconducting magnetic field $\overrightarrow{B_0}$ (9.4 T). This spectrometer is equipped with a specific device for MRI experiments, which consists of a 5mm imaging probe (Micro5) and xyz

gradient amplifiers (850×850×850 G/cm), which allow to select the voxels of interest. The experiments have been carried out at a temperature regulated at 17° C. To avoid the overheating of the imaging probe, the coil is cooled by a flow of water, whose temperature is adjusted by a thermostatic bath. Lastly, Paravision 5.1 software has been used for MRI images acquisition and processing. TopSpin 3.2 software has been used to optimization of NMR sequence parameters.

2.2. Raman spectroscopy and Raman Imaging (Streamline mode)

2.2.1. *Basis of Raman Spectroscopy*

Raman spectroscopy is a vibrational spectroscopy based on Raman effect. This means that the acquired spectrum results from the inelastic scattering of a monochromatic light by the sample [154].

Indeed, when a sample is submitted to monochromatic light of a frequency υ_0, there are two possible scenarios: the great majority of the photons are elastically scattered, *i.e.,* without energy exchange (known as Rayleigh scattering), while the other part (about one over 10 millions) are inelastically scattered. In this last scenario, either a vibration can be excited (Stokes band) or a vibrational excited mode in the sample is de-excited (Anti-Stokes band). These different scattering processes are schematized in Figure 51.

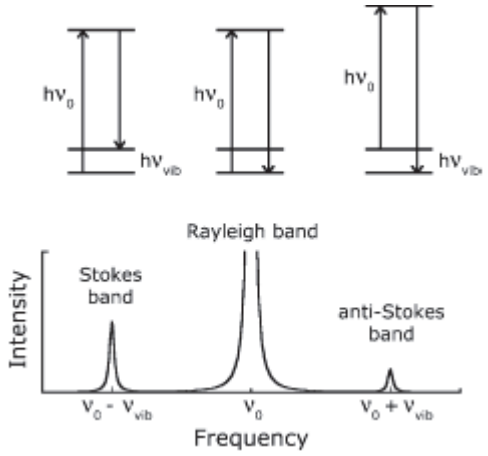

Figure 51 – Scheme of the elastic (or Rayleigh) and inelastic scattering processes [154]

If a molecule is excited from its ground state to an unstable state with an energy $h\upsilon_0$ and then returns to the ground state, no energy is exchanged between the molecule and light (photons): this phenomenon is responsible for the Rayleigh band. If the molecule instead of going back to its ground state, returns to the first vibrational level with frequency υ_{vib}, it takes energy from the photon equals to $h\upsilon_{vib.}$ Thus, scattered light has an energy equal to $h(\upsilon - \upsilon_{vib})$: it is called the Stokes band. The reverse case is when the molecule is excited, this time, from the first excited vibrational state to an unstable state with an energy $h\upsilon_0$ and then it returns back to ground state by transferring a certain amount of

energy $h\upsilon_{vib}$ to the photon: it is called the Anti-Stokes band. As the number of vibrational excited molecules is governed by Boltzmann's law, at room temperature the anti-Stokes band has a lower intensity than Stokes band.

The main differences between Raman and Infrared spectroscopy concern the physicochemical phenomena responsible for the signals of each technique. Indeed, a vibrational mode is IR active if there is a variation of the molecular dipole moment induced by the corresponding atomistic movement. On the other hand, a vibrational mode is Raman active if the atomistic movement induces a variation of the molecular polarizability. Because variations of polarity and polarizability are not incompatible, some vibrations can be IR-active and Raman-active.

2.2.2. *Experimental apparatus*

A Raman spectrometer consists of:

- A monochromatic light source, usually a laser
- A microscope to focus the light on the sample and collecting the scattered light
- A spectrometer that contains a filter (dielectric filters) to remove the Rayleigh scattering and a diffraction grating to split the Raman scattered light into component wavelengths
- A detector, which is normally a CCD camera
- A computer for acquisition and processing spectral data

Raman spectroscopy has been performed using a Renishaw inVia Raman microscope in backscattering configuration and an excitation line of 532 nm provided by a double frequency Nd-YAG laser equipped with EasyConfocal Renishaw device, a dielectric filter and an holographic grating with 2400 lines/nm which allows an optimal spectral resolution around 0.9 cm^{-1}. Wire 4.1 software is used for spectra acquisition.

Concerning measurements of impregnation solutions, Raman spectra have been acquired from 60 to 1300 cm^{-1} and the laser beam is focused with a wide-angle 50x objective resulting in a spot size of approximately 1µm. The laser power used is 1.7 mW and the exposure time is set to 10 seconds.

For characterization of the impregnated catalysts, the innovative Streamline Raman mode has been applied, which enables Raman cartography with a spatial dimension on the bisected pellet. Raman spectra from 140 to 1260 cm^{-1} have been recorded in the bisected pellet, using a 20x objective. The laser power used is 3.5 mW. Streamline [155] mode has been used to generate rapidly high definition 2D chemical images by illuminating with a line of a laser light rather than a spot. Exposure time is defined to 60 seconds and no thermal treatment has been carried out. The spatial resolution of each pixel is around 16.2 µm × 16.2 µm. It is worth noticing that for each streamline analysis, a surface

map is defined to prevent from focalization issues and get information about the whole intensities of the spectra when needed.

2.3. Electron Probe Microanalysis (EPMA)

EPMA measurements, which allows one to localize and to carry out a semi-quantification of the elements, have been performed on a JEOL JXA 8100 electron microprobe at 20 kV and 200 nA. Before EPMA measurements, catalysts have been calcined at 450°C for 2h. Concerning EPMA sample preparation, catalysts are embedded in a prepolymerized epoxy resin and polished to their diameter. A carbon coating is deposited at the surface of each sample.

Nickel, cobalt, phosphorus and aluminum concentrations are quantified using the Kα lines and molybdenum with Lα line. For P Kα, an overlap correction with the Mo *Ll* line has been performed. Under these conditions, detection limits are 380 ppm for Mo, 160 ppm for Ni, 100 ppm for Co and 4 ppm for P.

The average distribution profile along the cross section has been recorded by measuring between three to five different profiles along different 3-fold symmetry axes of the pellets. The analysis step is approximately 50 µm, excluding the cases where the metal is in an egg-shell profile. For these ones, an analysis step of 10 µm in each side of the crust is set.

2.4. Image Processing

The study concerning image processing and analysis of both MRI images and Raman images (Streamline maps) has been done in collaboration with M. MOREAUD from IFPEn (Mechatronics, Computer Science and Applied Mathematics Division).

INDIGO, a proprietary IFPEn software platform has been used for data processing.

The mean penetration depth of metal ions (and additive) is measured on both MRI images and Streamline Raman maps whose resolution is numerically increased in the orthogonal plane (x, y) to, respectively, 14 µm x 14 µm (or 11 µm x 11 µm) and 8 µm x 8 µm by means of high quality spline interpolation [156]. The noise contained in the images is then reduced by a local adaptive filter, a flowing bilateral filter [157], which maintains strong transitions in the image. The area corresponding to the penetration of impregnation solution is obtained by image segmentation with an automatic threshold calculated on the histogram by interclass variance maximization [158]. This procedure has the benefit to be no user dependent. The measure of the mean penetration depth is obtained with the same procedure from [159]. A medial axis is calculated by a morphological watershed from two markers defined as the core and the outside of the catalyst respectively, and propagated on distance function from these two markers. The mean thickness of the penetration, but also the minimum,

maximum, and standard deviation, are then obtained from the previous distance function by crossing the points of the medial axis. The different steps of the procedure are illustrated Figure 52.

Figure 52 – Example of processing and analysis of MRI image. From left to right : initial image (resolution 47 µm ×47 µm), increase of resolution by numerical interpolation (resolution 14 µm × 14 µm), automatic segmentation, distance function calculation (red to yellow colors) and medial axis extraction (blue color)

Chapter III – Implementation and application of MRI and Raman Imaging techniques to characterize the impregnation step

In the first part of this chapter, the methodology developed to implement and validate the MRI technique to the characterization of impregnation is described.

Secondly, the combination of MRI and Raman Imaging characterization is applied to study the impregnation of γ-alumina with a simple solution, i.e., a monometallic solution composed by nickel, eventually in the presence of citric acid. The impact of the solution properties (metal ion concentration, viscosity and pH) on the impregnation is investigated. At the end, the application of MRI is extended to study the impact of the metal ion concentration on the impregnation of cobalt based catalysts.

1. Implementation and optimization of MRI technique to catalyst characterization

As described in the Chapter I, MRI technique has already been used to monitor the impregnation step of monometallic solutions through an **indirect MRI approach**. This approach is based on the influence of paramagnetic (Ni, Co) or diamagnetic species (Mo) on the NMR signal of the proton of the solvent. The same approach can also be applied to localize phosphorus (P) species and organic additives, such as citric acid.

In the present study, the transport of metal ions and additives inside γ-alumina has been monitored by measuring the ^{1}H MRI signal of water inside the porosity of the support. Indeed, after impregnation, there is a rapid imbibition of water by the pores, which results in a uniform water distribution throughout the pellet. Thus, the paramagnetic/diamagnetic effect of metal on the ^{1}H MRI signal is used to visualize its distribution on the porous support.

Different protons can contribute to the ^{1}H MRI signal (see Figure 53):

1. Water protons confined into the porosity of alumina, which are also referred to "free water".
2. Water protons adsorbed at the monolayer, whose relaxation times are less than 1 ms [160–163]. These water molecules are characterized by their random motion at the monolayer and they can also interact with other molecules external to the monolayer [164,165]
3. Protons form the hydroxyl groups that cover the support surface, whose relaxation times are lower than 1 ms [160].

Figure 53 – Different types of H_2O protons present in the alumina support (adapted from [160])

The relaxation rate $R_{1,2}$ is a result of the intrinsic contribution of the different protons. This effect can be mathematically expressed according to Eq. 40 [160,166]:

$$\frac{1}{T_{1,2}} = \frac{f_b}{T_{1,2b}} + \frac{f_s}{T_{1,2s}} + \frac{f_{OH}}{T_{1,2OH}} \qquad \textbf{Eq. 40}$$

Where

$1/T_{1,2}$ represents the relaxation rate,

$T_{1,2}$, $T_{1,2b}$ represents the relaxation times T_1 and T_2 of the water confined into the porosity of alumina,

$T_{1,2s}$ represents the relaxation times T_1 and T_2 of the water adsorbed at the monolayer,

$T_{1,2OH}$ represents the relaxation times T_1 and T_2 of protons from the surface hydroxyl groups,

f_b, f_s, f_{OH} represents water fraction, respectively, confined into the porosity of alumina, adsorbed at the monolayer and in surface hydroxyl groups ($f_b + f_s + f_{OH} = 1$).

In the current NMR experiments, the protons of surface OH groups are not detected, and therefore their signal is considered as negligible [160]. Concerning the protons adsorbed at the monolayer, their signal might be detected but not in the conditions of the MRI experiments chosen for the present work. **Therefore, the ^{1}H MRI signal measured during this work is referred to the water molecules confined into the porosity of alumina.**

The choice of the MRI pulse sequences and parameters to study paramagnetic/diamagnetic systems are highly dependent on the relaxation times (T_1 and T_2). This dependence is widely used in order to induce contrast in MRI images, which enables to distinguish between different elements in impregnation solution. The following paragraphs describe the procedure to measure the relaxation times and the choice of the most suitable pulse sequence to follow the transport of each metal ions inside the porosity.

1.1. Optimization of NMR sequence parameters

As performed in classical NMR experiments, two different parameters related with the NMR sequence have been optimized: the length of the RF pulse and the power level. The optimization of these parameters has been performed thanks to TopSpin 3.2 software.

A single pulse sequence is applied, as described in Figure 54. In this figure, d_1 (usually $d_1 \approx 5T_1$) represents the relaxation delay and p1 states for the pulse length. The pulse length strongly depends on the transmitter power level (parameter pl1) and probe design.

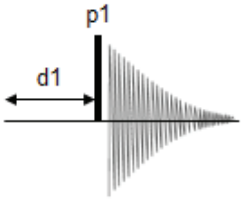

Figure 54 – zg pulse program, where d_1 represents the relaxation delay and p1 states for the pulse length (adapted from [167])

The optimal parameters for a 90° excitation pulse and for a 180° refocusing pulse are gathered in Table 10.

Table 10 – Optimal parameters for an excitation pulse of 90°, obtained by Topspin 3.2

Pulse (°)	Power level - pl1 (dB)	Pulse length - p1 (µs)
90	-6.8	22.5
180	-6.8	45

These optimal parameters have been defined in each MRI sequence used. Nevertheless, Paravision 5.1 sofware (used for MRI images acquisition) performs intrinsic adjustments to calibrate the RF selective pulses that the user cannot control. For this reason, it is not possible to ensure that these parameters have been in fact recognized by the MRI software.

1.2. Measurement of relaxation times and choice of MRI sequence

Relaxation times have been measured simultaneously by applying a RAREVTR sequence in the following systems:

- γ-alumina only impregnated with water
- γ-alumina impregnated with a 0.05M [Ni^{2+}] solution
- γ-alumina impregnated with a 0.05M [Co^{2+}] solution
- γ-alumina impregnated with a 0.8M [Mo^{6+}] solution
- γ-alumina impregnated with a 4 v/v% [H_3PO_4] solution
- γ-alumina impregnated with a 0.2 M [CA] solution

All these samples have been prepared by impregnation in excess in order to maximize signal to noise (S/N) ratio. This method consists in putting several γ-Al_2O_3 pellets in the NMR tube and then adding the impregnation solution with the desired Ni concentration. Impregnation volume added is approximately 2 mL, which is larger than pore volume (ratio between solution volume and pore volume is approximately 3.3).

The experimental conditions applied are gathered in Table 11, where FOV represents the real dimensions of the slice (width and height) and matrix image size determines the number of rows (L_p or N_p) and the number of columns (C_p or N_f). Both of them determine the spatial resolution of the image, i. e., the size of the pixel.

Table 11 – Experimental conditions of RAREVTR sequence

Parameters	Values
Excitation pulse (°)	90 (1000 µs at 15.4 dB)
Refocusing pulse (°)	180 (748.8 µs at 6.8 dB)
Repetition time list – TR (ms)	5000 – 3000 – 1500 – 1000 – 750 – 500 – 396.69 – 396.69
Echo time list – TE (ms)	4.5 – 9 – 13.5 – 18 – 22.5 – 27 – 31.5 – 36
TE effective 1 (ms)	4.5
TE effective 2 (ms)	9
Number of Echoes	8
FOV Read × FOV P_1 (mm)	6×6
Spatial resolution (mm/pixel)	0.047×0.047
Slice Thickness – ST (mm)	6
Matrix (number of points)	128×128
Total scan time	26 min 45 s

For each experiment, eight images are obtained for each value of TR. As an example, Figure 55 shows the image corresponding to the first TR and the first echo (TR=5000ms, TE=4,5ms) of the case of Ni/ γ-Al_2O_3.

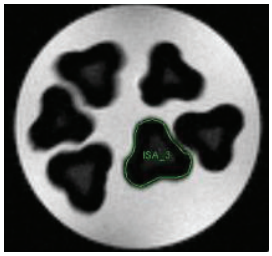

Figure 55 – Results obtained for RAREVTR sequence for several pellets have been impregnated with nickel solution. Both images correspond to TR=5000ms and TE=4.5ms

The image in Figure 55 is in proton density contrast, since a high TR and small TE have been applied, which means that images are little influenced by T_1 and T_2. Therefore, regarding one alumina pellet, the dark area corresponds to a low NMR signal (low proton density), while the area more bright corresponds to a high MRI signal (high proton density). Nevertheless, the contrast obtained is weak. Using Paravision 5.1 software, a region of interest (ROI) is selected, as shown in Figure 55, for which an averaged value of relaxation time is calculated.

T_1 and T_2 measurements have been done by fitting Eq. 33 and Eq. 34, respectively. The corresponding curves are in Figure 56. The T_1 curve is not well adjusted to the data points due to the short value of T_1. A qualitative value of T_1 is then determined.

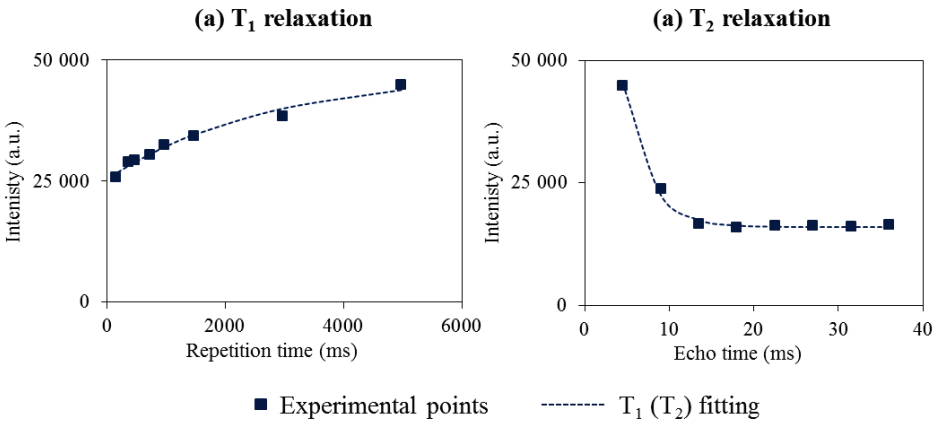

Figure 56 – (a) T_1 and (b) T_2 fitting for Ni/γ-alumina

The relaxation times obtained are summarized in the following table.

Table 12 – Relaxation times of the proton obtained in the presence or not of contrast agents. Measurements have been performed at the equilibrium stage of impregnation (after approximately 15h)

System	Relaxation times (ms)	
	T_1	T_2
H_2O/γ-alumina	372	3.9
Ni/γ-alumina	<15	2.8
Co/γ-alumina	<15	3.5
Mo/γ-alumina	667	4.2
H_3PO_4/γ-alumina	935	7.7
CA/γ-alumina	468	3.8

The short relaxation times found for the proton in the absence of any metal ion (in the order of dozens milliseconds) results from the water interactions with the porous surface and also from the traces of paramagnetic elements, such as iron (Fe) resulting from the preparation of alumina. These results are in good agreement with the study of Gédéon et al. [128].

In the presence of nickel and cobalt ions, the T_2 relaxation time of the proton is even further decreased, which evidences their paramagnetic behaviour as already reported by Espinosa-Alonso [126]. On the contrary, the presence of molybdenum, phosphorus and citric acid leads to an increase in the relaxation times of the proton. This result, which has been already reported by Lysova et al. [8], might evidence the diamagnetic character of these species. The results obtained are determinant for the choice of the MRI sequence, as explained in the next section.

1.3. Monitoring the impregnation step: choice of MRI sequence

Numerous MRI sequences have been used to monitor the impregnation step. Among them spin-echo based sequences, whose principle has been already described in section 2.1.2.2 (page 80) are the most common ones [5,7,8,126]. Nevertheless, the short value of T_2 obtained in the case of Ni and Co, suggests that spin-echo based sequences are not suitable to study the transport of these metal ions through alumina. Indeed, this sequence requires a stabilization time between pulses and a preparation time for gradient encoding. This stabilization time can lead to signal losses or even to a complete decay of the signal before its acquisition.

Thus, one alternative is to use other kind of sequences for which the impact of relaxation phenomena is less important. One of these sequences in the Single Point Imaging (SPI), which is successfully applied for systems with T_2 relaxation times very small (milliseconds or dozen of milliseconds), such as liquid samples in small pores [153]. Furthermore, SPI does not require a long gradient-stabilization time (hundreds of microseconds), so that the influence of the transversal relaxation time is minimized. Other advantages of SPI are as follows: SPI is not influenced neither by the different chemical shifts nor by the different magnetic susceptibilities nor by non-homogeneities of B_0. **For all these reasons, SPI is the method of choice to monitor impregnation step of Ni(Co) based catalyst. On the contrary, since there are not constraints in relation to value of T_2 in the case of Mo, P and citric acid, transport of these species within the porosity of the support is followed by applying a spin-echo sequence.**

A description of the parameters used in spin-echo and SPI sequences adapted for the systems in study is given in the following paragraphs.

1.3.1. *Follow the transport of a one- paramagnetic component solution by applying Single Point Imaging (SPI) sequence*

The methodology performed to adapt the MRI technique to follow the transport of a one-paramagnetic component solution during impregnation of a porous support has been developed by monitoring the transport of Ni^{2+} into the porosity of γ-alumina. The applied SPI sequence parameters are gathered in Table 13. The same approach has been then extended to the case of Co/γ-Al_2O_3 catalysts.

Due to the value of the repetition time (TR) applied, which is lower than T_1 relaxation time of protons near nickel ions, the MRI images are in T_1 contrast. Moreover, the choice of an excitation pulse of 90° and a small TR aims to improve T_1 contrast. Besides, a low time acquisition is preferred instead of a high spatial resolution (which implies higher acquisition times) in order to dynamically follow the impregnation step. Images have been recorded each hour for all nickel concentrations, apart from cases of 0.2 and 0.3M [Ni^{2+}]. In these last ones, images have been acquired every 10 min and 5 min, respectively, since the transport of Ni is very fast at these concentrations.

Table 13 – Sequence parameters for SPI sequence

Parameters	Values
Excitation pulse (°)	90 (22.5 μs at 6.8 dB)
Repetition time - TR (ms)	10-30[1]
Encoding time - t_p (μs)	200
FOV Read × FOV P_1 × FOV P_2 (mm)	3×3×1
Resolution Read × Resolution P_1 × Resolution P_2 (mm/pixel)	0.047×0.047×0.125
Slice Thickness – ST (mm)	1
Matrix Read × Matrix P_1 × Matrix P_2 – N	64×64×8
Total scan time for image	10min 55s
Excitation pulse (°)	200

[1] For the cases of 0.2 and 0.3 M [Ni^{2+}], TR has been set to 10ms in order to decrease the total scan time, since the transport of Ni ions is too fast in the referred cases. For the case of Co, TR has been increased to 30 ms to improve S/N.

The pulse length used (22.5 μs for 90° excitation pulse) is higher than the one suggested by the literature [153], which is obtained by Eq. 41:

$$t_{pul} \leq \frac{2t_p}{n} \qquad \textbf{Eq. 41}$$

Where, t_p corresponds to the encoding time and n number of samples of k-space.

If the pulse length is too long, then blurry images can be obtained, especially at the edges and a resolution less than the one expected can be also found [153]. For this reason, an experiment with a pulse length of 6.3 µs (limiting value of Eq. 41) and a power level of -3 dB has been performed. No significant differences have been observed between these images and the ones with the parameters of Table 13.

Figure 57 shows two examples concerning the ^{1}H MRI images acquired in γ-alumina pellets over impregnation time with a 0.06M [Ni^{2+}] and 0.2M [Ni^{2+}] solutions. These images are in T_1 contrast, which exhibits the ^{1}H signal influenced by Ni^{2+} ions in the neighbourhood of the proton water molecules. As a consequence, the dark area corresponds to a low concentration of metal ion (T_1 longer - small ^{1}H signal intensity), while the bright area corresponds to a higher concentration of these ions (T_1 shorter - high ^{1}H signal intensity). Initially, paramagnetic ions are only observed close to the edges of the pellet, while water molecules are rapidly transported into the entire pellet due to the capillary forces developed by the pore system. As time elapses, an evolution of the bright area is observed, which corresponds to a progression of Ni^{2+} ions inside γ-alumina. In these examples, a non-uniform ^{1}H MRI signal is observed in the entire pellet even after several hours of impregnation in the case of 0.06M [Ni^{2+}], which is interpreted as non-homogeneous metal ion profiles. On the contrary, for a 0.2M [Ni^{2+}] solution, a homogeneous metal profile is observed.

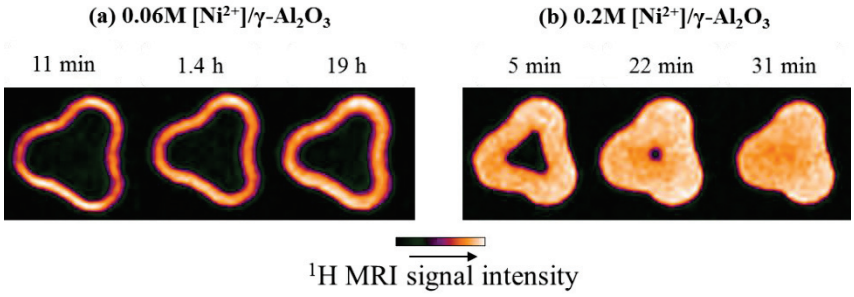

Figure 57 – ^{1}H MRI images corresponding to transport of (a) 0.06 M [Ni^{2+}] and (b) 0.2 M [Ni^{2+}] solution within the porosity of a γ-Al_2O_3 pellet obtained by a SPI sequence (FOV=3×3×1 mm; Spatial resolution= 47×47×125 µm/pixel; Matrix=64×64×8)

1.3.2. *Follow the transport of a two or more components solution by applying the spin-echo sequence*

Impregnation step of γ-alumina with Ni-CA solution has been used to adapt the ^{1}H MRI technique to follow the transport of two or more components solution through the catalyst support during the impregnation step.

When citric acid is added to a nickel solution, different impacts in the relaxation times of proton are observed. Citric acid increases the relaxation times of the proton, while nickel has an opposite behaviour (see Table 12, page 97). By applying the spin-echo MRI sequence, one can distinguish between these elements by choosing the appropriate sequence parameters, namely the repetition time, TR and the echo time, TE. Table 14 gathers the spin-echo sequence parameters applied. Once more, to dynamically follow the transport of impregnation within the porosity, images have been acquired every 30 minutes.

Table 14 – Sequence parameters of spin-echo sequence

Parameters	Values
Excitation pulse (°)	90 (100 µs at 9.9 dB)
Refocusing pulse (°)	180 (200 µs at 9.9 dB)
Repetition time - TR (ms)	500
Echo time - TR (ms)	2.2
FOV Read × FOV P_1 × FOV P_2 (mm)	2.5×2.5×8
Resolution Read × Resolution P_1 × Resolution P_2 (mm/pixel)	0.039×0.039×0.125
Slice Thickness – ST (mm)	8
Matrix Read × Matrix P_1 × Matrix P_2 – N	64×64×8
Total scan time for each image	17min 04s

Based on parameters gathered in Table 14, a contrast in MRI image either in T_1 or T_2 can be obtained. Figure 58 shows the comparison between the evolution of the ^{1}H MRI signal as a function of time for protons in the presence or not of the solution precursors (Ni and citric acid), which are characterized by different T_1. For the TR chosen (equal to 500 ms), the longitudinal magnetization (M_z) of protons near Ni has time to recover until its initial level: it is not possible to distinguish between protons in absence and in presence of Ni by their T_1. On the contrary, for the same TR, it is possible to distinguish between protons in absence and in the presence of citric acid, since a small TR comparing

to its T_1 is applied. Thus, protons with higher T_1 (near citric acid) recover later and will have a weaker signal intensity - T_1 contrast.

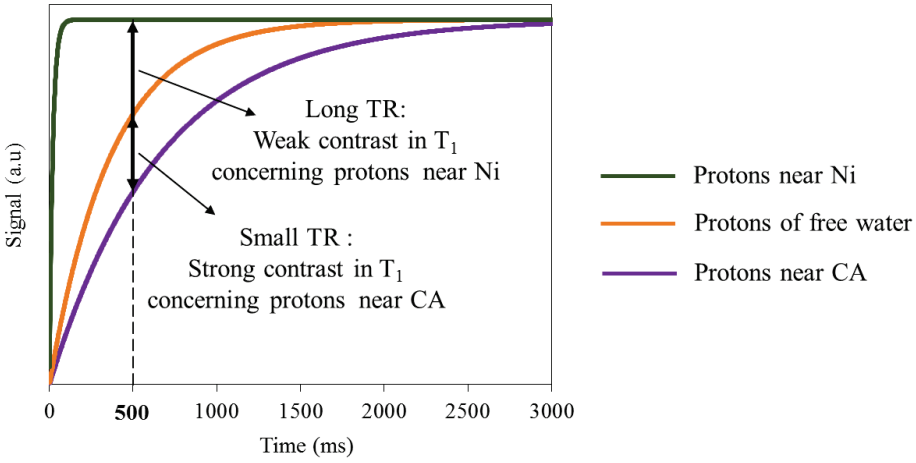

Figure 58 - Comparison between protons having different T_1. Protons near citric acid are distinguished by a T_1 contrast.

Figure 59 illustrates the comparison between the evolution of ^{1}H MRI signal as a function of time for protons in the presence or not of the solution precursors (Ni and citric acid), which are characterized by different T_2. For the TE applied (equal to 2.2 ms), differences in the decrease of the transversal magnetization (M_{xy}) of protons with or without citric acid do not have time to express themselves. On the contrary, for the same TE, differences between protons in absence and in the presence of Ni ions can be visualized. Indeed, a higher TE comparing to the T_2 of protons near Ni is applied. Thus, protons near Ni have smaller T2 and consequently, they decrease faster, which gives weaker signal intensity - T_2 contrast.

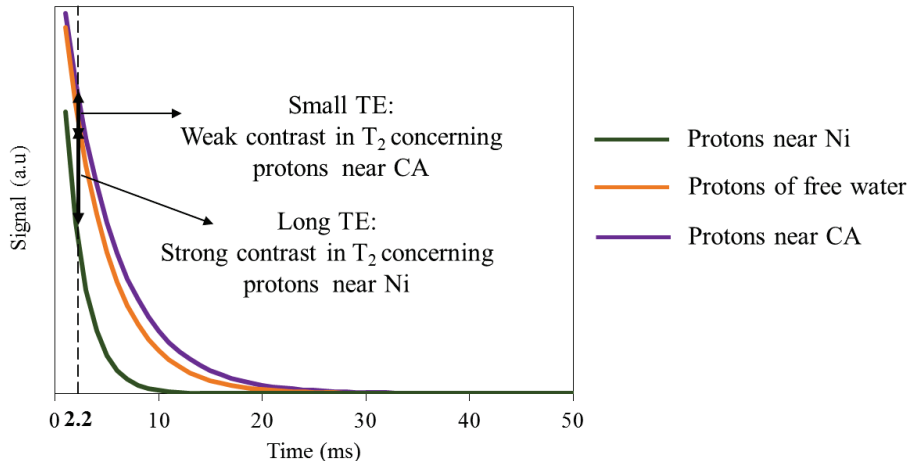

Figure 59 - Comparison between protons having different T_2. Protons near Ni will be distinguished by a T_2 contrast.

To conclude, by applying a T_1 contrast, it is possible to observe protons near citric acid, while a T_2 contrast allows one to observe protons close to nickel. Both elements contribute to a decrease in the ^{1}H MRI signal, however the effect of nickel is stronger due to its paramagnetic effect, which leads to an almost absence of ^{1}H MRI signal. An example of a MRI image with two contrasts is shown in Figure 60.

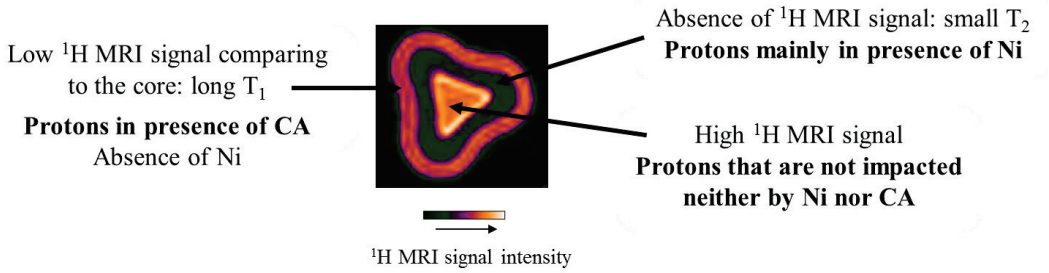

Figure 60 – ^{1}H MRI image recorded on a γ-Al_2O_3 pellet impregnated with Ni citrate solution (FOV=2.5×2.5×8 mm; Spatial resolution= 39×39×100 µm/pixel; Matrix=64×64×8)

The same approach is applied for the case of CoMo(P) solutions: protons near Mo(P) are observed thanks to a T_1 contrast, while protons near Co are observed thanks to a T_2 contrast. As nickel ions, cobalt also leads to an almost absence of ^{1}H signal.

1.4. Validation of MRI technique to characterize the impregnation step: comparison with EPMA characterization

In order to validate this indirect MRI approach, one have to be sure that the observed signal of the proton actually corresponds to the signal of protons in the neighborhood of nickel ions. To this end, the average radial intensity profiles (I_0) of MRI images and the average EPMA concentration profiles have been compared. One can assume that the calcination step performed to obtain EPMA profiles do not influence the repartition of the metal.

Besides, the aim is also to obtain a quantitative relation between the pixel intensity of MRI images and the local metal concentration, which is obtained thanks to EPMA characterization. Indeed, a correlation between the pixel intensity of ^{1}H MRI images and the concentration of the metal ion in the impregnation solution has already been obtained in the literature [6,8,126]. However, this hypothesis does not take into account the impact of metal ion concentration and nature on the relaxation times of the proton. Indeed, it considers that the impact of metal ion in relaxation times of the proton is uniform.

To extract quantitative information from the MRI images, ParavisionMatLab tool provided by Bruker has been used. The aim is to obtain information about the intrinsic adjustments carried out by Paravision 5.1 software, such as threshold, individual scaling of each image (Visu Core Data Slope parameter), smoothing and artifacts reduction filters. These treatments induce changes in the intensity observed and hinder an absolute comparison between the experiments.

First, the software ImageJ is used to export MRI image data into 16bit.tiff files. From these data, INDIGO software is then used to calculate on each image the radial intensity profiles as a function of the distance from the edge of the support. For each distance, a minimum, a maximum and an average intensity are computed, and provide associated profiles. In this study, the intensity profiles obtained by INDIGO are referred as the apparent intensity (I) profiles as they do not take into account neither relaxation times dependence nor normalization carried out by Paravision software. Figure 61 shows an example of the apparent intensity of a MRI image corresponding to a γ-alumina impregnated with a 0.06M [Ni^{2+}] solution.

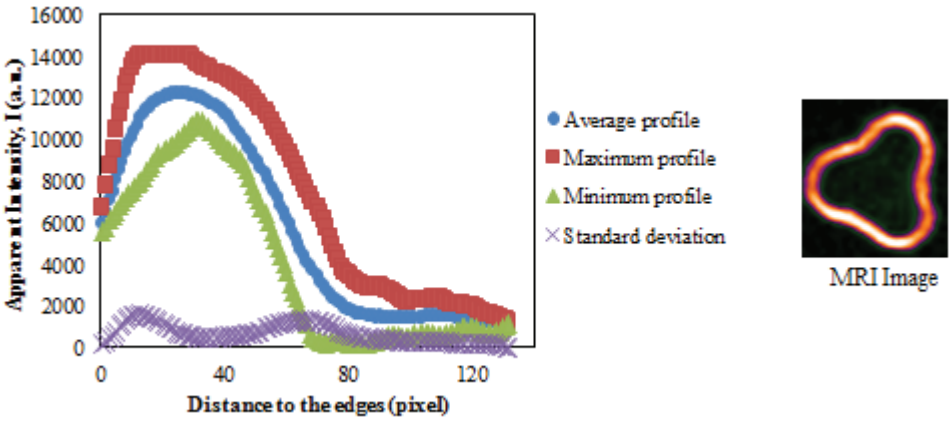

Figure 61 – Apparent intensity profile as a function of the distance to the edges in pixel: example of a Ni solution concentration of 0.06M [Ni^{2+}]

These apparent intensity profiles (I) are corrected with K factor (see Eq. 35) in order to take into account the relaxation times dependence. They are also corrected by the scaling factor of each image applied by Paravision software (Visu Core Data Slope parameter). The mathematical equation to obtain average radial intensity profiles (I_0) is shown in Eq. 42.

$$I_0 = \frac{I \times Scaling\ factor}{K} \qquad \textbf{Eq. 42}$$

Figure 62 shows the comparison between average EPMA concentration profiles and radial average intensity profiles I_0 obtained for the example cases given in Figure 57.

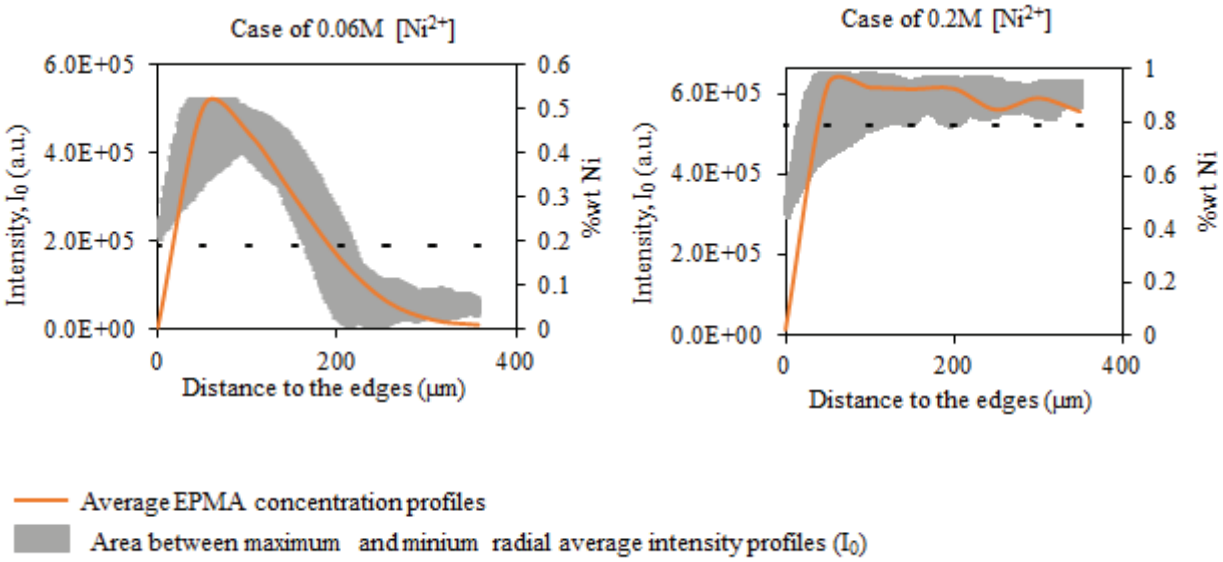

Figure 62 - Comparison between average EPMA concentration profiles (Spatial resolution 50 µm) and radial average intensity profiles I_0 obtained by Indigo© (Spatial resolution 14µm/pixel). Shaded area delimits the maximum and minimum radial average intensity profiles (I_0). Standard deviation concerning concentration profiles is also presented.

The shaded area observed in Figure 62 delimits the maximum and minimum radial average intensity profiles (I_0) measured by MRI image processing. The ^{1}H MRI intensity and the average EPMA nickel concentration profiles (wt% Ni^{2+}) are in good agreement. Indeed, both techniques show the presence of nickel ions in the same positions of the catalyst pellet regarding to the spatial resolution of each technique. Hence, a direct correlation between the ^{1}H MRI intensity and the concentration of Ni^{2+} (wt%) ion is verified. Slight differences may be observed due to signal to noise ratio of MRI images, since the sensitivity of MRI technique is lower than EPMA

Based on the linear relation observed between ^{1}H signal intensity and concentration of metal ion, MRI signal intensity is normalized to the maximum and minimum of metal concentration obtained by EPMA. Figure 63 shows the comparison between the normalized intensity profiles I_0 and average EPMA profiles. This semi-quantitative approach shows that the local nickel concentration can be obtained through MRI technique in a non-invasive way by measuring the intensity profiles of MRI images recorded at equilibrium state. Additionally, it can give information about gradient concentrations, which can be related to diffusion and surface interaction phenomena.

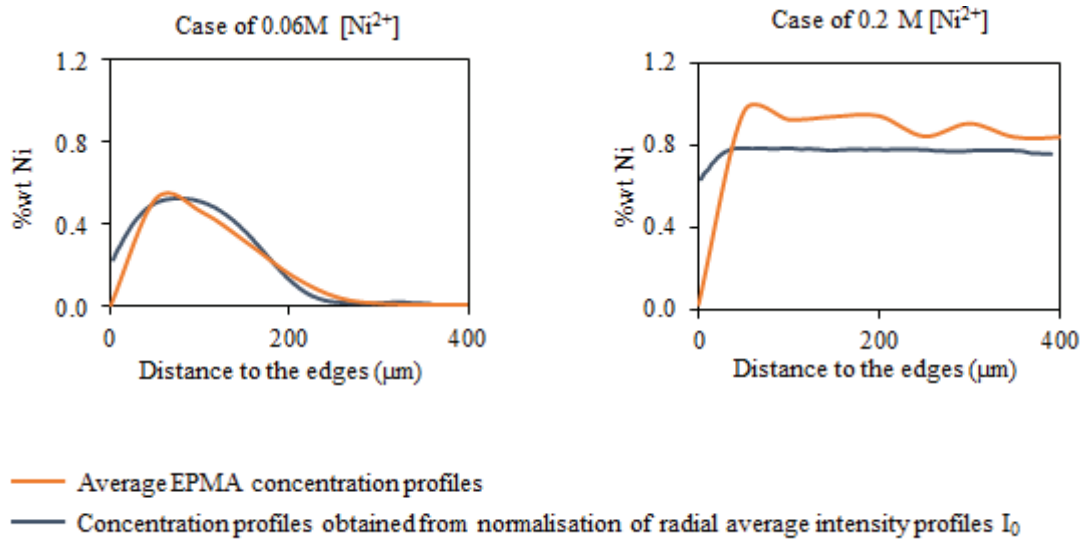

Figure 63 - Comparison between average EPMA concentration profiles and concentration profiles obtained from normalization of radial average intensity profiles I_0

MRI technique has been implemented and optimized to monitor the impregnation step of a monometallic solution using the SPI sequence and of a multi-component solution using the spin-echo sequence. An indirect MRI approach is used, which enables to obtain information about the spatial distribution of the different elements present in impregnation solution by measuring the proton MRI signal. An improvement of spatial resolution to 39×39µm has been achieved. The methodology has been validated through a comparison with EPMA distribution profiles, which enables to obtain a direct correlation between ^{1}H MRI intensity and concentration of Ni^{2+} (wt%) ion within the pellet.

2. Application of MRI and Raman Imaging to characterize the impregnation step of a simple case

MRI technique has been applied to monitor the impregnation step of a simple case, *i.e.*, nickel based catalyst in the presence or not of citric acid. The challenge of this study is to describe the transport of the metal ion through the support porosity as a function of capillarity, Fickian diffusion and surface interaction. The impact of the solution properties, such as metal ion concentration, viscosity (by adding citric acid) and the pH is evaluated. Additionally, Raman Imaging characterization has also been performed at the end of impregnation in order to obtain spatial information concerning citrate speciation in the oxide catalyst. The standard impregnation method (method A, see Figure 37 in Chapter II page 71) has been performed.

Finally, this approach is extended to the case of cobalt based catalysts.

2.1. First simple case: impregnation with a nickel aqueous solution

2.1.1. *Impact of metal ion concentration*

Different concentrations of Ni^{2+} in impregnation solution ranging from 0.05 to 0.30 M, which corresponds to a Ni^{2+} weight percent (wt%) of 0.25 up to 1.39 in the final catalysts have been prepared. For this range of metal weight fractions and considering γ-Al_2O_3 used (see Table 9 in Chapter II, page 70), the surface density of metal ions ranges from 0.09 to 0.53 Ni atoms/nm^2 in the final catalysts.

The MRI images corresponding to the time right after impregnation and the measurement at equilibrium (set to the time for which there is no variation of the metal distribution profile) are presented in Figure 64.

For low nickel concentrations (0.05 and 0.06M [Ni^{2+}]), which corresponds to, respectively, 0.09 Ni atoms/nm^2 and 0.10 Ni atoms/nm^2 in the final catalyst, extreme egg-shell profiles are obtained. This fact indicates that an interaction between metallic precursor and the γ-alumina surface cannot be neglected. For impregnation solutions with Ni^{2+} concentration higher than 0.1M (0.21 Ni atoms/nm^2 in the final catalyst), the distribution of metal ion tends to uniformity. These distribution profiles have also been verified by EPMA on calcined samples at 450°C.

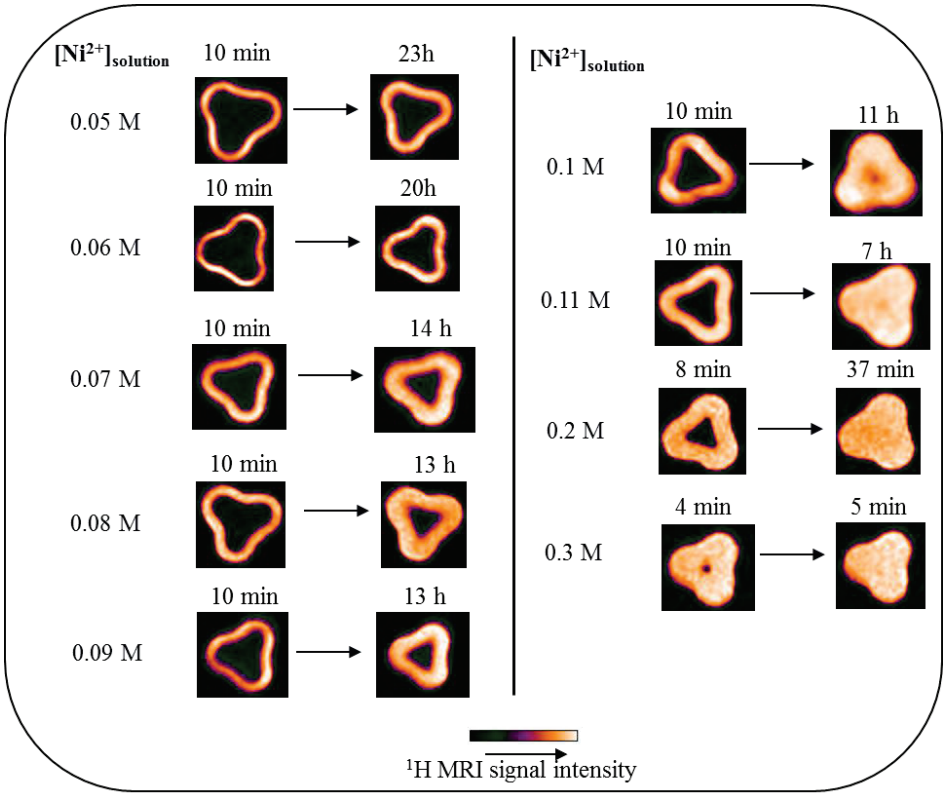

Figure 64 – Impact of [Ni^{2+}] in impregnation solution on the distribution profile of Ni^{2+} ions inside γ-alumina: ^{1}H MRI images recorded right after impregnation and at equilibrium (set to the time for which there is no variation of the metal distribution profile) using a SPI sequence (FOV=3×3×1 mm; Spatial resolution= 47×47×125 µm/pixel; Matrix=64×64×8)

As expected, the transport of Ni^{2+} ions is favoured by high metal concentrations in impregnation solution. Indeed, higher metal ion concentrations increase the driving force for diffusion, according to Fick's law [80]. These MRI experiments allows one to suggest that:

- First the capillary flow and diffusion transport the water solvent together with the metal ions into the empty pores. This observation remains in agreement with the study of Espinosa et al. [6,126].
- The interactions between the metals ion and the support surface are not negligible as they seem to hamper the transport of the metal ions through the porous support, in contrast with Espinosa's work [126]. Such surface interaction can be a result of hydrolytic adsorption (through the formation of covalent bonds) or even precipitation.

2.1.1.1. *Diffusion and adsorption characterization by a semi-quantitative MRI approach*

The transport of nickel ions within the porous space is evaluated thanks to the penetration distance of the front of metal ions. This parameter is referred to as the average thickness and it has been measured thanks to Indigo IFPEn software, as described in Chapter II (see section 1.4 in page 103). The

evaluation this parameter is directly related with the physicochemical phenomena involved in impregnation step: molecular diffusion and surface interaction.

The results concerning the evolution of the average thickness as a function of time are in Annex A (page 229). Based on these measurements, Figure 65 shows a relation between the metal ion concentration and the time to achieve a crust thickness chosen of 370 µm. Nickel concentrations lower than 0.06M [Ni^{2+}] have not been considered in these calculations, since at equilibrium, the crust thickness is less than 370 µm.

According to these measurements, for low Ni^{2+} concentrations in solution, it takes a longer time to achieve the 370 µm distance from the edge of the pellet. One can remark that to achieve the distance of 370 µm a difference of almost sixteen hours is observed between the 0.07M [Ni^{2+}] and 0.1M [Ni^{2+}] cases. These results suggest again that diffusion in the fluid phase is hindered by a surface interaction phenomenon.

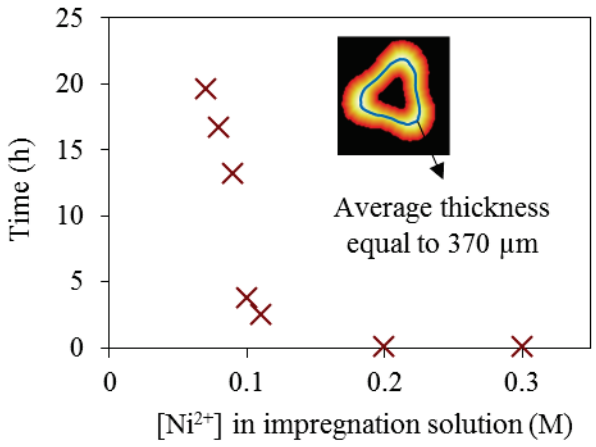

Figure 65 - Time to achieve a mean penetration depth equal to 370 µm as a function of metal concentration in impregnation solution

Many PFG-NMR (Pulsed Field Gradient-Nuclear Magnetic Resonance) studies [168–171] allow one to estimate the self-diffusion coefficient of a solute in the porosity of a support of the order of 10^{-9}-10^{-10} m^2/s assuming no interactions with the surface.

Based on the MRI results, one can estimate the self-diffusion coefficient of Ni^{2+} ions in the porosity of γ-Al_2O_3 support using a roughly approximation given by Eq. 43 [172].

$$t \approx \frac{d^2}{2D} \qquad \textbf{Eq. 43}$$

Where, D is the self-diffusion coefficient ($m^2.s^{-1}$), d represents the mean distance travelled by nickel ions (m) and t stands for time (s).

For example, for the case of 0.07M [Ni] experiment, one can remark that almost 20 hours are needed to cover 370 µm within the catalyst pellet (see Figure 65). The experimental estimated diffusion coefficient (thanks to Eq. 43) of order of magnitude of 10^{-13} m^2/s is much smaller than the expected diffusion coefficient of a liquid phase of 10^{-10} m^2/s [173]. A surface interaction mechanism can be then suggested as a predominant phenomenon in the transport of Ni^{2+} ions inside the porosity of γ-Al_2O_3.

To conclude, transport of nickel ions is governed by a competition between diffusion and surface interaction. One can assume that this interaction consists in a hydrolytic adsorption, which hinders the transport by diffusion resulting in non-uniform Ni^{2+}.

2.1.1.2. *Discussion: impact of metal ion concentration on impregnation of Ni/ γ-Al_2O_3 catalysts*

A qualitative analysis of the MRI experiments allows one to describe the transport of nickel ions inside γ-alumina as a function of three different phenomena: capillarity, diffusion and surface interaction. Among them, capillarity is the fastest phenomenon, since right after impregnation, water is already present in the entire porosity. One can assume that capillarity is not the limiting step of transport of metal ions through γ-alumina. Thus, a competition between diffusion and surface interaction is indicated. Moreover, the estimated diffusion coefficient of the protons near Ni^{2+} of order of 10^{-13} m^2/s also corroborates this fact.

Diffusion is highly dependent on the metal concentration, while surface interaction is highly dependent on the solution pH. Indeed, this parameter impacts the nature of Ni species in solution and also the state of surface (nature of OH groups and their surface density).

Starting from nickel nitrate precursor ($Ni(NO_3)_2$) and in an acidic medium (pH < 6), the thermodynamic species in solution are Ni^{2+} aqua complexes $[Ni(H_2O)_6]^{2+}$, for a Ni-solution concentration of 0.5M [74] as depicted in Figure 66.

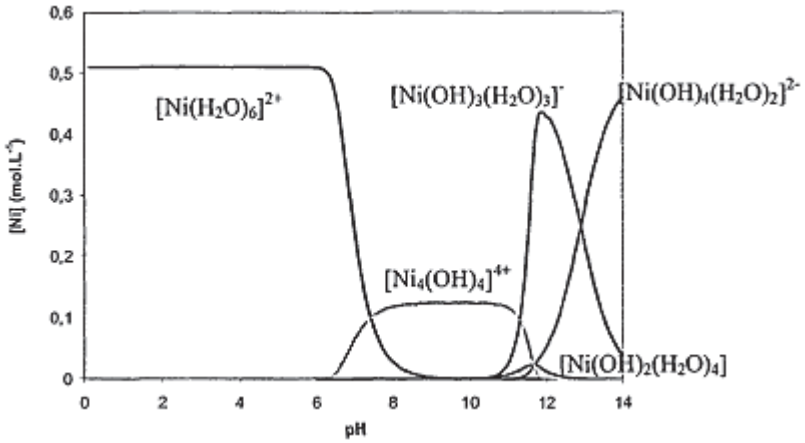

Figure 66 - Predictions of hydrolysis products of Ni(II) species in 0.5M [Ni] aqueous solution and I=1.3M as a function of pH [74]

In basic medium, $[Ni(H_2O)_6]^{2+}$ can undergo the following hydrolysis [75]:

$$[Ni(H_2O)_6]^{2+} + H_2O \leftrightarrow [Ni(H_2O)_5(OH)]^{+}(aq) + H_3O^{+} \quad \textbf{Eq. 44}$$

$$[Ni(H_2O)_6]^{2+} + 2H_2O \leftrightarrow [Ni(H_2O)_4(OH)_2](aq) + 2H_3O^{+} \quad \textbf{Eq. 45}$$

$$[Ni(H_2O)_6]^{2+} + 3H_2O \leftrightarrow [Ni(H_2O)_3(OH)_3]^{-}(aq) + 3H_3O^{+} \quad \textbf{Eq. 46}$$

The neutral complex ($[Ni(OH)_2(H_2O)_4](aq)$), which is stable for pH between 10.5 and 12.5, is the precursor of the solid phase with the composition $Ni(OH)_2$ (s). Besides, for Ni^{2+} concentrations higher than 0.1M, the $[Ni_4OH)_4]^{4+}$ polymer can also be found in solution, before the precipitation of $Ni(OH)_2$ [75]. Nevertheless, in acidic medium, the dissolution of this solid phase may take place, according to the equilibrium in Eq. 47:

$$Ni(OH)_{2(s)} + 2H^{+} \leftrightarrow [Ni(H_2O)_6]^{2+} + 2H_2O \quad \textbf{Eq. 47}$$

In the present work, impregnation solutions with metal ion concentrations varying from 0.05 to 0.3 M (corresponding to solutions pH from 5 to 6) have been prepared. According to Figure 66, the formation of a solid Ni phase is not favoured is in these conditions. Therefore, only the aqua complexes of metal species $[Ni(H_2O)_6]^{2+}$ are present in solution.

Upon impregnation with an acidic solution, the surface charge of γ-alumina is slightly positive as a result of protonation of the hydroxyl groups. In these conditions, an electrostatic repulsion between the positively charged metal ion complexes ($[Ni(H_2O)_6]^{2+}$ and the protonated OH groups occurs. In contrast, ions of the precursor salt (NO_3^-) are electrostatically retained at the interface metal/support. However, as a result of the buffering effect of alumina, the pH of the solution inside the pores tends to rise towards a value of 8, according to the PZC of support (approximately 8-8.5). This behaviour results in the formation of either surface neutral (AlOH) or negatively (AlO^-) OH groups.

Consequently, nickel ions might be adsorbed by exchanging one or more water ligands of the $[Ni(H_2O)_6]^{2+}$ with the surface oxygen atoms of the negatively charged group (AlO^-). Consequently, inner-sphere Ni(II) complexes are formed, following an hydrolytic adsorption mechanism [96,98,99,103,174]. Moreover, deprotonation reaction of one adjacent neutral hydroxyl group occurs in order to stabilize Ni^{2+} ions through the formation of ion-pairs (Ni^{2+}-O^-Al) [98]. Different studies in the literature have reported that the adsorption of nickel is indeed increased from a pH 6 to 8 [94,95,175].

Figure 67 depicts the mechanism of hydrolytic adsorption of Ni^{2+} on γ-alumina.

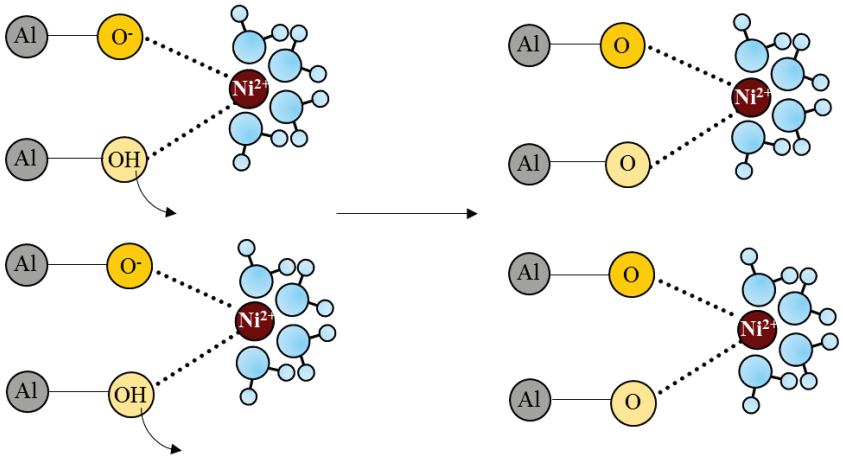

Figure 67 – Mechanism of hydrolytic adsorption of Ni^{2+} in γ-alumina (adapted from [3,98])

The maximum amount of Ni that can be adsorbed on γ-Al_2O_3 is related to the density of OH surface groups and their nucleophilic character.

According to Digne et al. [176], γ-alumina surface exhibits a preferentially exposed (110) surface with a surface OH coverage of approximately 11.8 OH/nm^2 at 573K, whereas the (100) plane of γ-alumina exhibits a surface coverage of 8.8 OH/nm^2 at the same temperature. In the present study, OH surface should be even higher as impregnation step has been performed in an aqueous medium and at ambient temperature. Therefore, the density of Ni atoms (between 0.09 and 0.44 Ni atoms/nm^2) is always lower than the OH surface coverage. These observations suggest a selective affinity of nickel ions for the γ-alumina OH sites depending on their nucleophilic character. A similar behaviour has already been reported in the literature [177] considering impregnation of palladium based catalysts supported on alumina.

The MUSIC model proposed by Hiemstra et al. [178,179] enables to identify the nature of the different OH groups depending on their coordination with Al. For a pH approximately equal to 8, negatively charged OH groups ($[(Al_{Oh})OH_2]^{-0.25}$) and neutral ($[(Al_{Oh})_2OH]$) predominate in the (110) surface of γ-alumina, even if some protonated OH groups are still present ($[(Al_{Oh})OH_2]^{+0.5}$) [180,181].

As already mentioned, among the different OH groups, only deprotonated and neutral OH groups contribute to the adsorption of metal ions.

To conclude, initially in the impregnation solution, Ni^{2+} is in the form of aqua complexes, $[Ni(H_2O)_6]^{2+}$. In the form of $[Ni(H_2O)_6]^{2+}$, one can assume that nickel ions first interact with the most reactive basic or neutral OH sites via an hydrolytic adsorption mechanism (see Eq. 48) [7].

$$[Ni(H_2O)_6]^{2+} + xAl_sOH \leftrightarrow [(Al_sO)_xNi(H_2O)_{6-x})]^{(2-x)+} + xH^+ \qquad \textbf{Eq. 48}$$

Figure 68 shows a schematic picture of the phenomena that take place in the interface region during impregnation of γ-alumina with a nickel solution based on the Three Layer Model [15]. One can assume that initially, titration of the most reactive OH basic and neutral sites with metal ions occurs through a hydrolytic adsorption mechanism in the inner Helmholtz plane (IHP). This is indeed the case of low Ni concentrations in solution (0.05M and 0.06M [Ni]), which explains the extreme egg-shell distribution profiles obtained. For higher Ni concentrations in solution, the remaining nickel ions can be electrostatically adsorbed in the less reactive OH basic sites (having a weaker nucleophilic character) in the outer Helmholtz plane (OHP). Those nickel ions can migrate via a surface diffusion mechanism. In the diffusive layer, $[Ni(H_2O)_6]^{2+}$ ions diffuse according to their concentration gradient (diffusion in the fluid phase). Consequently, homogenous distributions are obtained for Ni^{2+} concentrations in the impregnation solution equal or higher than 0.11M.

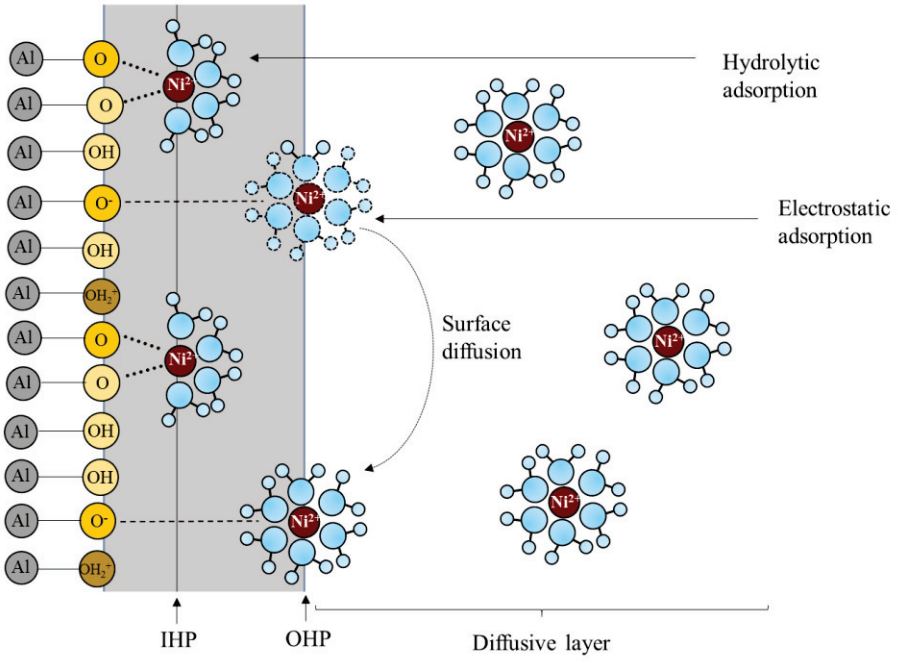

Figure 68 – Schematic picture about phenomena that take place in the interface region during impregnation of γ-alumina with nickel solution: diffusion, surface diffusion and surface interaction (electrostatic interaction and hydrolytic adsorption) using Three Layer Model (adapted from [3,15,98])

2.1.2. *Impact of organic additives: addition of citric acid to a nickel solution*

The study concerning the influence of citric acid in impregnation of nickel based catalysts is divided into two steps.

First of all, impregnation of γ-alumina with a citric acid solution is investigated. The impact of citric acid concentration and solution pH are evaluated. The aim is to understand the interactions between citrate and γ-alumina upon impregnation, which can help in understanding a more complex system, namely nickel-citrate. For reasons of clarity of the manuscript, this study is not shown. To sum up the conclusions obtained, two different phenomena are responsible for the transport of citrate species during impregnation: capillarity and Fickian diffusion. Surface interaction must also be taken into consideration, which is highly dependent on pH. For solutions pH lower than PZC of γ-alumina, adsorption is favoured over diffusion phenomenon. Indeed, either electrostatic or covalent interactions take place. The latter one occurs via the carboxylate groups of deprotonated citrate and the positive/neutral OH surface groups, according to Eq. 49 and Eq. 50. Moreover, for low citric acid concentrations in solution (for instance, 0.2M [CA], which corresponds to 0.45 CA molecules/nm^2 in the final catalyst), egg-shell distribution profiles of citrate species are obtained.

$$HCit^{2-} + Al - OH_2^+ \leftrightarrow Al - CitH_2 + H_2O \quad \textbf{Eq. 49}$$

$$Cit^{3-} + Al - OH \leftrightarrow Al - Cit^{2-} + OH^- \quad \textbf{Eq. 50}$$

For solutions pH higher than PZC of support and regardless the concentration in solution, interaction between the deprotonated citrate and the deprotonated alumina surface are negligible (repulsive electrostatic interaction), which leads to uniform profiles.

Secondly, the impregnation of nickel based catalysts is carried out in the presence of citric acid. The impact of the following solution properties are analyzed: citric acid concentration (CA:Ni ratio) and solution pH in order to study, respectively, the buffer effect of citrate and a possible complexation of nickel ions by citrate. The first property has been analyzed for two different nickel concentrations in solution (0.05M and 0.2M [Ni^{2+}]). Since the same conclusions are obtained for both cases, only the case of 0.05M [Ni^{2+}] is given as example.

2.1.2.1. *Effect of CA:Ni ratio in impregnation solution*

Figure 69 shows the time-resolved ^{1}H MRI images during impregnation of γ-alumina with a 0.05M [Ni^{2+}] solution, in which the CA:Ni ratio ranges from 0.4 to 4. At the initial stage of impregnation, ^{1}H MRI signal is very intense near the core, which suggests that hardly citrate ions and nickel ions are transported together with the capillary flow of water. This is indeed observed for all the cases studied, which suggests that interactions between metal ion and additive should not be negligible. Moreover, as

the CA:Ni ratio is increased, an evolution of the thickness layer close to the edges of the support (orange colour) is also observed, which corresponds to the presence of citrate. Likewise, an increase in the diameter of the inner front (magenta colour - low ^{1}H MRI signal) is also observed, which corresponds to the presence of nickel ions. For CA:Ni ratios equal or lower than 1.2, this inner front does not progress for impregnation times higher than 15h, which results in an egg-white distribution of nickel ions. For higher CA:Ni ratios, the formation of an egg-yolk distribution of nickel is rather observed for the same time of impregnation. Egg-shell profiles of citrate are obtained, regardless the concentration used.

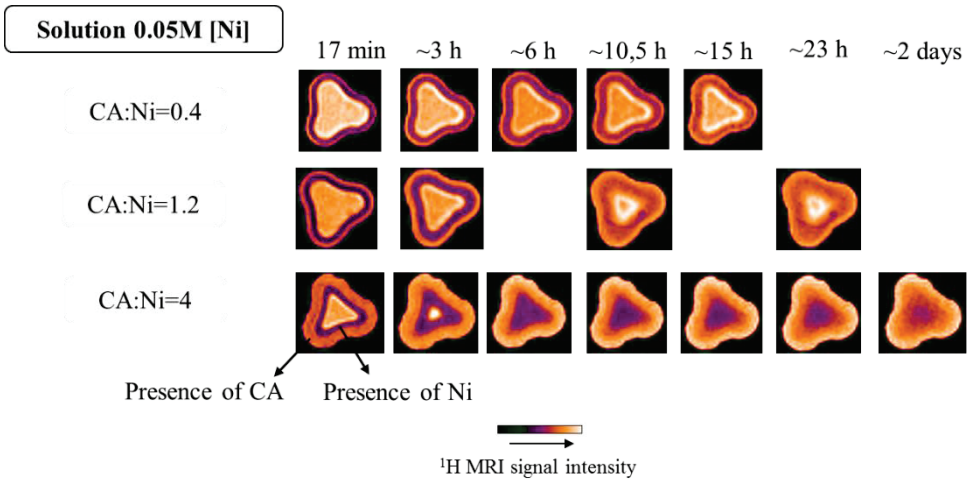

Figure 69 – Impact of CA:Ni ratio for a 0.05M [Ni] solution in the distribution profile of Ni^{2+} ions inside γ-alumina: ^{1}H MRI images recorded at different times during impregnation using a spin-echo sequence (FOV=2.5×2.5×8 mm; Spatial resolution= 39×39×100 µm/pixel; Matrix=64×64×8)

Apparently, when citric acid is added to the impregnation solution, nickel ions penetrate further into the support upon impregnation (see Figure 64 and Figure 69). This fact suggest that adsorption of metal ion is somewhat hindered by the presence of organic additive. A competitive adsorption mechanism between citrate ions and nickel ions on the alumina surface is then indicated.

Figure 70 (a) shows the resulted Raman spectra obtained at different positions within a bisected γ-alumina pellet impregnated with a 0.05M [Ni^{2+}] solution with a CA:Ni molar ratio of 4. To obtain information about a possible interaction between citrate and nickel ions, Raman spectroscopy has also been applied to characterize a γ-alumina pellet impregnated with the same concentration of citric acid (0.2M) in the absence of nickel (see Figure 70 (b)). Despite the Raman band at 1049 cm^{-1} ascribed to nitrate ions, the resulting Raman bands are similar in both cases. The high intense peaks at 980 cm^{-1} and 1505 cm^{-1} come from the support preparation (see Annex B). The band at 1417 cm^{-1} is ascribed to the stretching vibrations of carboxylate group $\nu_s(COO^-)$ [58]. Besides, the Raman band at 1723 cm^{-1} can be attributed either to vibration mode νCOOH [145] or to support preparation (see Annex B).

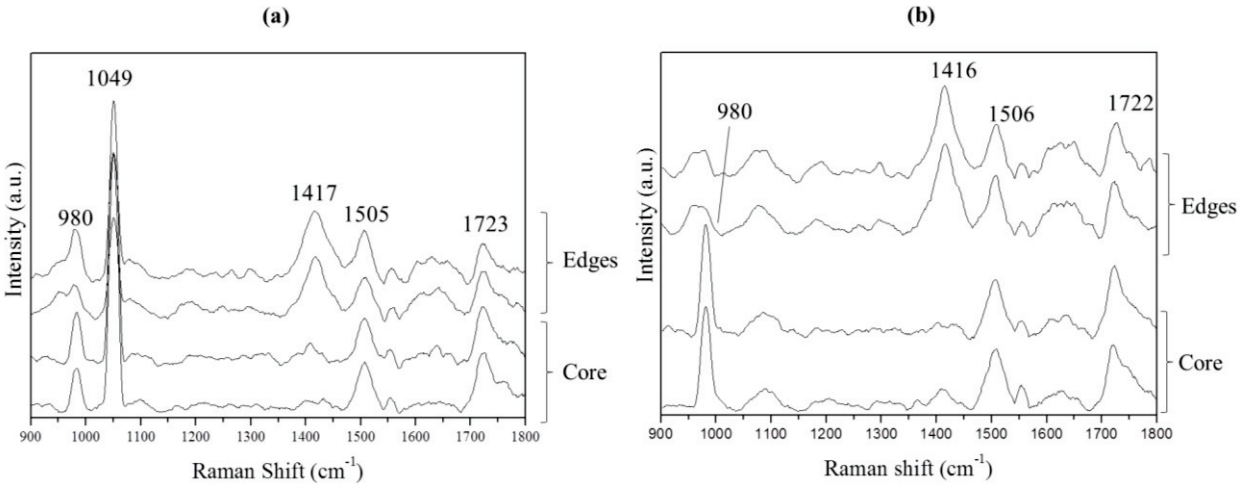

Figure 70 - Raman spectra recorded at different positions within a γ-alumina pellet impregnated with (a) 0.05 M [Ni] solution with CA:Ni of 4 at equilibrium (b) 0.2 M [CA] at equilibrium

The similarities of the spectra of both figures suggest that there are no interactions between citrate ions and nickel ions and therefore, no nickel-citrate complex is formed upon impregnation. Therefore, the Raman band at $\nu_s(COO^-)$ 1417 cm^{-1} in Figure 71 (a) can be ascribed to free citrate, i.e., not coordinated to nickel ions [58,67]. A Raman cartography concerning the intensity at 1417 cm^{-1} indicates a higher intensity near the edges, which can be interpreted as an egg-shell distribution of citrate (see Figure 71).

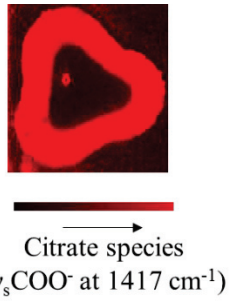

Figure 71 – Streamline Raman image recorded in a γ-alumina pellet impregnated with 0.05 M [Ni] solution with CA:Ni of 4 at equilibrium with a spatial resolution of 16.2 µm × 16.2 µm: cartography of intensity at 1417 cm^{-1} ($\nu_s COO^-$)

Figure 72 shows the comparison between MRI and Raman Imaging results. Both images show a higher signal intensity near the edges, which corresponds to the presence of citrate. Further quantitative analysis concerning the measurement of citrate crust thickness shows that the same thickness is observed in both profiles.

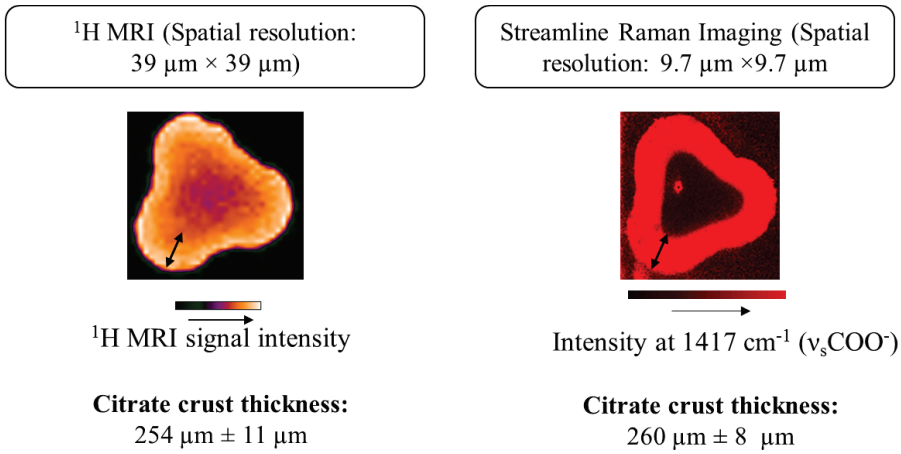

Figure 72 - Comparison between ^{1}H MRI and Streamline Raman Imaging: images recorded in a γ-alumina support impregnated with 0.05M [Ni] solution with CA:Ni=4 at equilibrium. Crust thickness has been measured by Indigo©.

To summarize, regardless the CA:Ni molar ratio in solution and under acidic solution pH (pH < 2.4), $[Ni(H_2O)_6]^{2+}$ complexes and citric acid (H_3Cit) are expected in the impregnation solution (according to Figure 9 in Chapter I, page 21). A competitive adsorption between citrate and nickel ions is suggested, which results in an increase of transport rate of Ni ions through the porosity. An egg-shell distribution of citrate not coordinated to nickel ions is obtained, which indicates a preferential adsorption of citrate on γ-alumina. A covalent interaction between citrate and γ-alumina is then expected. Nickel ions remain in the form of $[Ni(H_2O)_6]^{2+}$ complexes inside the porosity, which are either in egg-yolk or egg-white distributions. Under extreme acidic pH, the interaction citrate/γ-alumina is favoured over complexation of nickel by citrate.

2.1.2.2. *Effect of solution pH: complexation of nickel ions by citrate*

Two different nickel solutions with a CA:Ni molar ratio of 1.2 have been prepared: one with 0.05M [Ni^{2+}] pH 8 and another one with 0.2M [Ni^{2+}] pH 6.

Impregnation of γ-Al_2O_3 with a 0.05M [Ni^{2+}] solution (CA:Ni equal to 1.2, pH 8) has been followed by ^{1}H MRI. The same MRI sequence parameters (repetition time, TR and echo time, TE) used in case of acidic solutions have been applied. Yet, the resulted MRI images have a weaker contrast (see Figure 73), which makes difficult the interpretation of the results. Additionally, the modification of the contrast obtained already suggests the deposition of different species in the support. Indeed, based on the speciation diagram in Figure 9 (page 21), formation of a nickel-citrate complex ($NiCit^-$) is expected. Besides, citrate not coordinated to metal ions can also be present, since CA:Ni molar ratio

used is higher than stoichiometry one. Citrate is assumed to be totally deprotonated (Cit^{3-}) regarding solution pH.

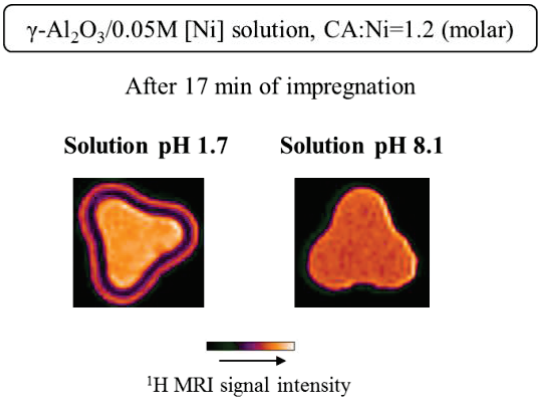

Figure 73 - Impact of pH of a 0.05M [Ni] with CA:Ni=1.2 impregnation solution on the distribution profiles inside γ-alumina: ^{1}H MRI images recorded 17min after impregnation (using a spin-echo sequence in T_1 contrast (FOV=2.5×2.5×1 mm; Spatial resolution= 39×39×100 µm/pixel; Matrix=64×64×8; TR=500ms; TE=2.2ms).

To improve the contrast and the comprehension of MRI images, different TR values have been tested, maintaining the same TE in order to enhance the contrast of protons near citric acid. The additive can be either in a citrate form (Cit^{3-}), coordinated to nickel ions or in the neighbourhood of nickel ions. Results are gathered in Figure 74.

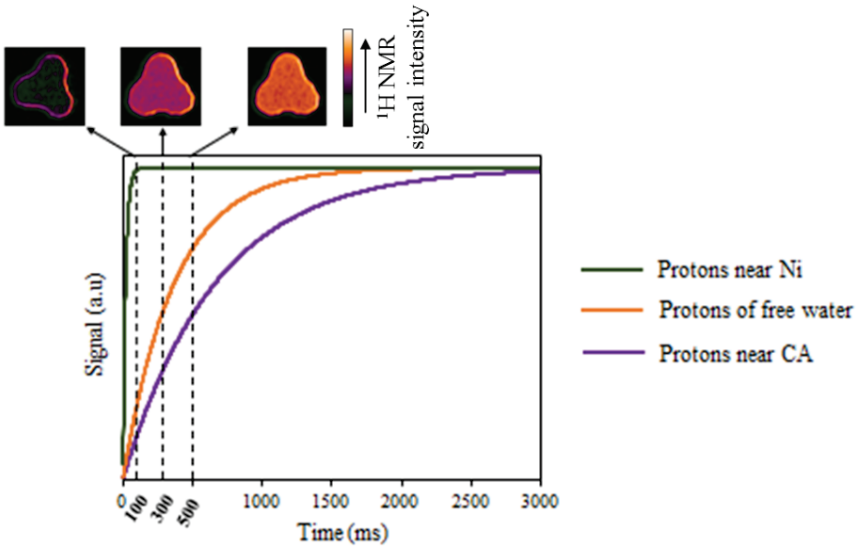

Figure 74 – Impact of repetition time (TR) in contrast obtained: ^{1}H MRI images recorded in a γ-alumina pellet impregnated with 0.05M [Ni] with CA:Ni=1.2 solution pH 8 using a spin-echo sequence (FOV=2.5×2.5×1 mm; Spatial resolution= 39×39×100 µm/pixel; Matrix=64×64×8)

Different hypotheses can be made based on Figure 74 as follows:

- For long TR (500 ms), no contrast between the protons near citric acid and protons of free water is observed. One can conclude that this MRI image corresponds to a proton density

contrast, which explains the low contrast observed. Yet, for acidic solutions, this value of TR is the optimal to give the best contrast concerning protons near citric acid. The modification of this contrast suggests that the relaxation times of the protons near citric acid are also modified because the organic additive might be in a complex form with Ni or in the neighbourhood of the metal ions.

- For intermediate TR (300 ms), the contrast in MRI image is improved as a decrease in ^{1}H MRI signal near the core is observed. Apparently, a decrease in TR leads to a destructive effect on ^{1}H MRI signal of protons of free water, which enables to clarify the regions where citric acid might be found.
- For small TR (100 ms), a strong contrast is observed in MRI image. Once again, with an even smaller TR, ^{1}H MRI signal of protons of free water vanishes. Thus, it is possible to distinguish between these protons and the ones near citric acid. An optimal T_1 contrast concerning protons near citric acid is visualized. For this reason, this value of TR has been used to dynamically follow impregnation step.

One can then assume that citric acid and nickel ions are located near the edges. Different hypotheses concerning the speciation of citric acid and nickel ions inside the catalyst can be considered. Either this crust corresponds to citrate in the neighbourhood of nickel ions or citrate coordinated to nickel ions ($NiCit^-$, for instance). The proximity between citrate and nickel can induce a modification in nickel paramagnetism, which can explain the modification of relaxation times of the proton near citric acid and therefore a different contribution to ^{1}H MRI signal.

Figure 75 gathers different ^{1}H MRI images obtained at different times of impregnation with solution pH 8. ^{1}H MRI images do not show any differences comparing the beginning and end of the experience. An interaction between nickel/citrate ions with γ-alumina surface must take place.

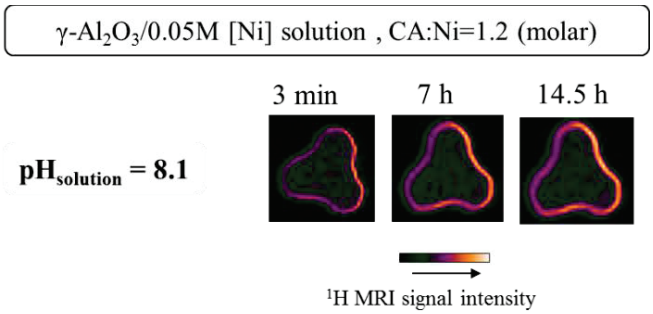

Figure 75 – ^{1}H MRI images recorded at different times of γ-alumina impregnation with a 0.05M [Ni] with CA:Ni=1.2 pH 8.1 using a spin-echo sequence (FOV=2.5×2.5×1 mm; Spatial resolution= 39×39×100 µm/pixel; Matrix=64×64×8; TR=100 ms)

The resulted Raman spectra acquired in different positions of the catalyst pellet are shown in Figure 76 (a). The vibration modes $\nu_s(COO^-)$ at 1416 cm^{-1} and 1435 cm^{-1} are ascribed to citrate. Raman

cartography concerning $\nu_s(COO^-)$ at 1416 cm^{-1} (see Figure 76 (b)) indicates that citrate is mainly present near the edge of support.

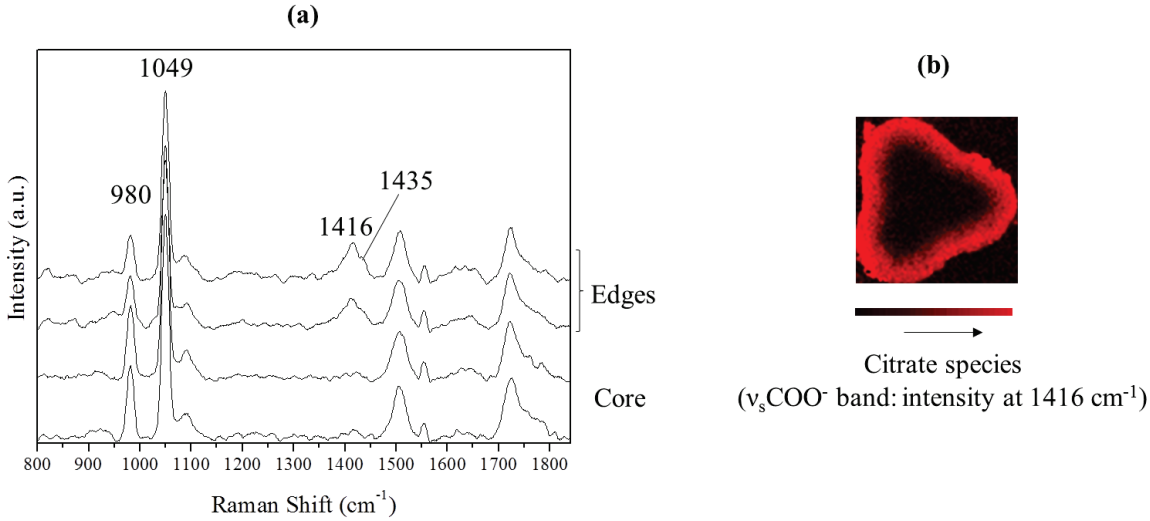

Figure 76 - (a) Raman spectra recorded at different positions within a γ-alumina pellet impregnated with 0.05 M [Ni] solution with CA:Ni of 1.2 pH 8 at equilibrium (b) Streamline Raman image of the same pellet with a spatial resolution of 16.2 µm × 16.2 µm: cartography of intensity at 1416 cm^{-1} (ν_sCOO^-)

For a solution 0.05M [Ni^{2+}] with a CA:Ni molar ratio of 1.2 and pH 8, $NiCit^-$ and Cit^{3-} are formed in solution (according to Figure 9 in Chapter I, page 21). Upon impregnation, citrate and/or a nickel-citrate complex nickel ions are located near the edges. Near the core, a nickel (citrate)-free region is indicated. No modification of distribution profile is observed during impregnation, which suggests a covalent interaction between citrate and/or nickel-citrate complex and the support surface.

The same study has been performed using the same CA:Ni ratio (1.2), but with a higher concentration of nickel (0.2M [Ni^{2+}]) and a solution pH equal to 6. To begin with MRI experiments, the same parameters used for the solution but in acidic conditions (study not shown) have been applied in the present case. The comparison between them is gathered in Figure 77. The contrast observed for basic solution is very weak. Indeed, this issue has already been observed in the earlier case for a Ni^{2+} concentrations of 0.05M. The modification of the MRI image contrast is in line with modification of species in solution: for acidic solution, Ni ions are present in the form of $[Ni(H_2O)_6]^{2+}$ and citric acid is in a protonated form (H_3Cit). As solution pH is increased, $Nicit^-$, $Ni(HCit)(Cit^{3-})$ and Cit^{3-} are expected in solution, according to Figure 9 in page 21. Additionally, the important decrease in ^1H MRI signal near the edges can be attributed to the presence of nickel ions. Indeed, these metal ions are known to decrease relaxation times of the proton; which results in a decrease of the intensity observed.

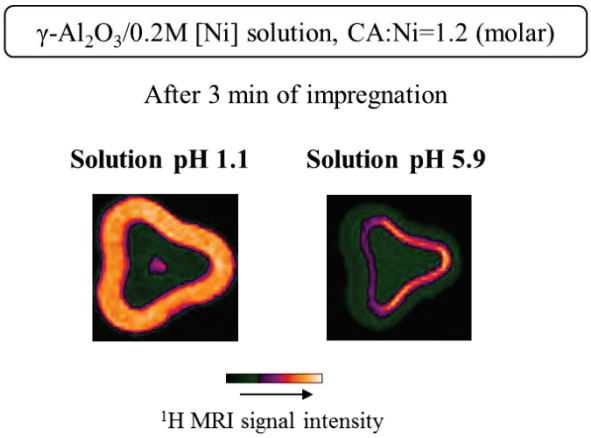

Figure 77 - Impact of pH of a 0.2M [Ni] with CA:Ni=1.2 impregnation solution on the distribution profiles inside γ-alumina: ^{1}H MRI images recorded 3min after impregnation (using a spin-echo sequence in T_1 contrast (FOV=2.5×2.5×1 mm; Spatial resolution= 39×39×100 µm/pixel; Matrix=64×64×8; TR=100ms; TE=2.2ms).

To clarify the contrast of MRI images, different sequence parameters (namely TR) have been verified, as shown in Figure 78. Once again, the aim of varying the TR is to influence the contrast of protons near citric acid. Different assumptions can be done to understand the results:

- For low TR (100 ms), no contrast between protons near citric acid/nickel and protons of free water is observed. As for the case of solution 0.05M [Ni] with CA:Ni=1.2 pH 8, this low contrast is attributed to a proton density contrast.
- For high TR (300 ms), ^{1}H MRI signal near the core is increased, which suggests that this region corresponds to a nickel-citrate free region. Once again, this fact does not hinder that low quantities of nickel/citrate can be found near the core. MRI contrast seems to be enhanced with this value of TR. Thus, impregnation has been followed using this a TR equal to 300 ms.

According to these results, one can assume that citric acid and nickel are mainly present near the edges. In particular, citric acid in the form of Cit^{3-} or coordinated to nickel ions (such as, $Nicit^{-}$, $Ni(HCit)(Cit^{3-})$) are considered. The latter hypothesis seems to be quite suitable, since it can explain the modification of ^{1}H MRI signal intensity near the edges. One can consider that these nickel-citrate complexes have a paramagnetic behaviour, which contributes to a decrease in the intensity observed. The region near the core can be ascribed to a nickel-citrate free region.

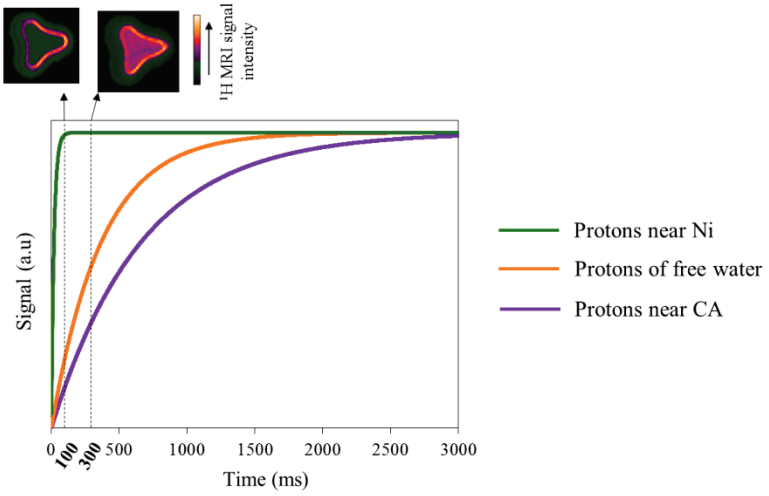

Figure 78 - Impact of repetition time (TR) in contrast obtained: ^{1}H MRI images recorded in a γ-alumina pellet impregnated with 0.2M [Ni] with CA:Ni=1.2 solution pH 6 using a spin-echo sequence (FOV=2.5×2.5×1 mm; Spatial resolution= 39×39×100 µm/pixel; Matrix=64×64×8)

Figure 79 shows ^{1}H MRI images acquired at different times during impregnation. Even after several days of impregnation, no significant modifications of the distribution profile are observed.

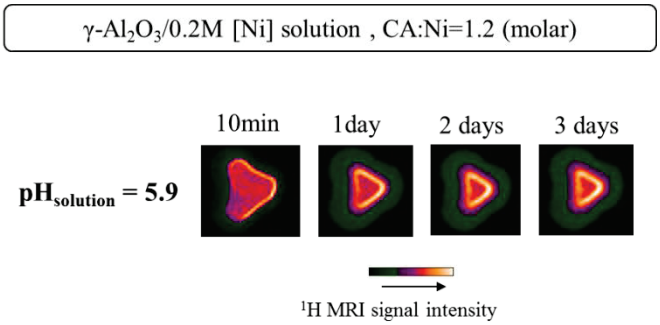

Figure 79 – ^{1}H MRI images recorded at different times of γ-alumina impregnation with a 0.2M [Ni] with CA:Ni=1.2 pH 5.9 using a spin-echo sequence (FOV=2.5×2.5×1 mm; Spatial resolution= 39×39×100 µm/pixel; Matrix=64×64×8; TR=300 ms)

Raman spectroscopy characterization of the same catalyst pellet is shown in Figure 80. The Raman band of interest, $\nu_s(COO^-)$ at 1413 cm^{-1} corresponding to citrate, appears to be uniformly distributed over the entire pellet. A Raman cartography of the intensity of this band reveals a homogeneous distribution (see Figure 80 (b)). The presence of Cit^{3-} near the core is not suggested by the MRI image in Figure 79. One can conclude that the sensibility of the MRI technique is lower than Raman spectroscopy, which means that it may exists a critical value for which MRI does no longer detect the presence of organic additive.

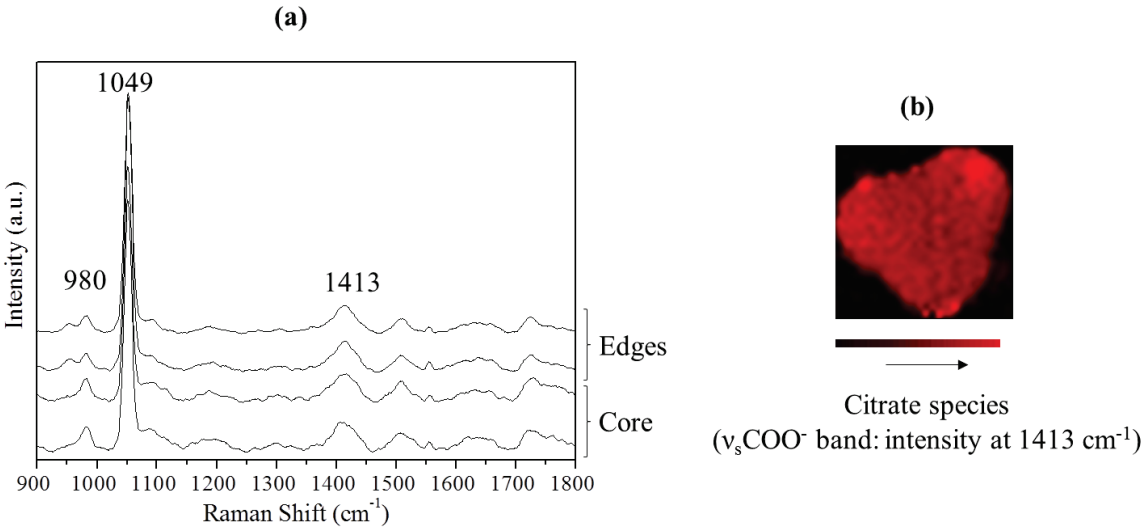

Figure 80 - (a) Raman spectra recorded at different positions within a γ-alumina pellet impregnated with 0.2M [Ni] solution with CA:Ni of 1.2 pH 5 at equilibrium (b) Streamline Raman image of the same pellet with a spatial resolution of 39 µm × 39 µm: cartography of intensity at 1413 cm^{-1} ($\nu_s COO^-$)

To summarize, the impregnation solution of 0.2M [Ni] (CA:Ni=1.2, pH 5) contains initially $Nicit^-$, $Ni(Hcit)(Cit^{3-})$ and Cit^{3-} (see Figure 9 in Chapter I, page 21). Upon impregnation, the formation of a crust near the edges can be ascribed to a nickel-citrate complex or citrate in the neighbourhood of nickel ions. Near the core, a nickel-free region is indicated by the higher ^1H MRI signal intensity than in the edges. Besides, citrate seems to be uniformly distributed through the entire pellet. No important modifications of distribution profile are observed as impregnation evolves, which suggests a covalent interaction between metal-additive complex and the support surface.

2.1.2.3. *Discussion: impact of citric acid on impregnation of Ni/ γ-Al_2O_3 catalysts*

One of the purposes to use citric acid as an additive in the preparation of a hydrotreatment catalyst is to decrease the interactions between the metallic precursors and the support upon impregnation. Moreover, it is also suitable to coordinate cobalt and/or nickel with citric acid in order to delay their sulfidation. The results obtained above can give new insights into the role of citric acid during the impregnation step as a function of metal ion concentration, additive concentration and solution pH. Revising all data in the literature concerning the application of citric acid, several phenomena can be anticipated:

- Under extreme acidic conditions (pH lower than 3), no complexation between nickel ions and citrate is expected in impregnation solution [7,70,71]. This is explained by the protonation of

carboxylate functions of citric acid, which do not favour the complexation reaction. Moreover, for these conditions, a preferential adsorption of citrate on alumina surface is expected, which results in egg-shell profiles of citrate and either egg-yolk or egg-white profiles of the metal ion [7].

- For higher pH (approximately to 5-6), complexation of nickel ions by citrate can take place [7,70]. For instance, coordination of cobalt ions is proposed to take place through two carboxylate groups and the hydroxyl group of citrate [7]. Besides, interactions between the metal-additive complex and the surface of the support are expected and can hindered the diffusion phenomenon. For instance, egg-shell profiles of the metal-organic additive complex can be even obtained [7].

First of all, the effect of CA:Ni molar ratio (ranging from 0.4 to 4) in acidic impregnation solutions (pH=1-2.4) with 0.05M [Ni^{2+}] has been considered. Only nickel aqua complexes $[Ni(H_2O)_6]^{2+}$ and citric acid mainly in the protonated form (H_3Cit) are expected in the impregnation solution. No nickel citrate complex should be formed in solution. These conclusions are in good agreement with Bentaleb et al. [71]. The authors verified that citric acid does not act as a complexing agent to an important extent when it is only introduced as an additive into the nickel nitrate solutions, and only causes a pH decrease.

The results show that regardless CA:Ni ratio used in impregnation solution, egg-shell distributions of citrate are obtained. Given that the solution pH is lower than 2 and assuming that presence of citrate can counteract the buffer effect of γ-alumina, one can assume that the increase in solution pH is not enough to give rise to completely deprotonated citrate (Cit^{3-}). Therefore, citric acid is assumed to be in the form of either H_2Cit^- or Cit^{2-} inside the porosity, which implies a local pH between 3-4 [7]

The egg-shell distribution of citrate even after several hours of impregnation can only be explained by a covalent interaction. Adsorption of citrate takes place either in positive or neutral charged OH surface sites of γ-alumina, according to Eq. 49 (page 128). Besides, electrostatic interactions between deprotonated citrate and positively charged OH surface sites occurs.

When there is no complexation with citrate, nickel ions remain in the form of aqua complexes inside the pores. Additionally, the presence of citrate can counteract the buffer effect of γ-alumina in some extent, which means that pH values characteristic of precipitation of nickel ions are not achieved (see Figure 66). Egg-yolk or egg-white profiles concerning nickel ions are obtained, depending on CA:Ni ratio in impregnation solution. This behaviour is totally different for the cases where citrate is absent. To remind, for very low nickel concentrations in solution (0.05M), egg-shell profiles are rather obtained. Apparently, transport rate of nickel ions is increased in the presence of citrate. As discussed earlier for impregnation with nickel solutions, $[Ni(H_2O)_6]^{2+}$ ions can adsorb on the OH surface sites

(see Eq. 48, page 113). Therefore, a competitive adsorption between citrate and nickel ions takes place during impregnation of γ-alumina. As nickel ions are found more towards the core of the pellet for smaller impregnation times in the presence of citrate, one can conclude that a preferential adsorption of citrate on γ-alumina surface is highlighted.

To go further in this interpretation, the density of both acid functions and nickel atoms should be evaluated. When 0.05M [Ni^{2+}] impregnation solutions are used, the density in nickel atoms in the catalyst corresponds to 0.09 Ni atoms/nm^2. While the density of acid functions ranges from 0.04 to 0.43 CA molecules/nm^2. As already mentioned, γ-alumina surface OH coverage is of approximately 11.8 OH/nm^2 at 573K for (110) plane, whereas the (110) plane of γ-alumina exhibits a surface coverage of 8.8 OH/nm^2 at the same temperature [176]. Since citrate molecules and nickel atoms adsorb in the same active sites (OH neutral groups), one can conclude that the presence of citrate decreases the number of available sites for Ni^{2+} ions. However, there is a large excess of OH sites in relation to overall of citrate molecules and nickel atoms. Hence, the fact that adsorption of metallic ions is limited when organic additive is present can be a result of steric hindrance induced by citrate. Indeed, adsorption of citrate can block the neighbouring available OH sites due to steric reasons. Towards the core, where hardly citrate should be presented, adsorption of $[Ni(H_2O)_6]^{2+}$ can take place. These results and mechanism proposed are in good agreement with the literature [7,71].

Figure 81 shows a schematic picture of the phenomena that take place in the interface region during impregnation of γ-alumina with an acidic (pH lower than 2.4) 0.05M [Ni^{2+}] nickel solution with CA:Ni ranging from 0.4 to 4 . Citrate is assumed to be in the form of H_2Cit^- or $HCit^{2-}$, for the reasons already explained.

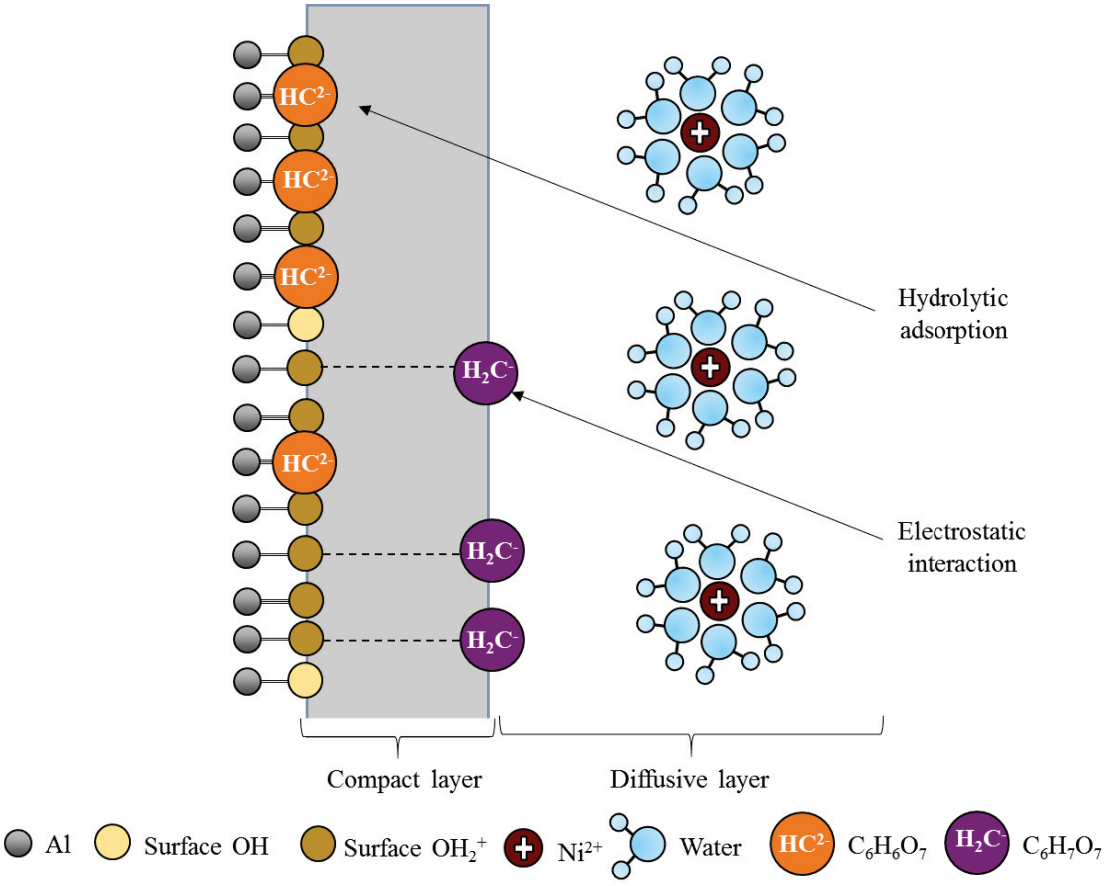

Figure 81 - Proposition of different phenomena that take place at the surface of γ-alumina near the edges upon impregnation 0.05M [Ni] solutions with CA:Ni molar ratio ranging from 0.4 to 4. Very acidic solution pH (lower than 2.4) explains why the surface is mainly positively charged. Citrate is assumed to be in the form of H_2Cit^- or $HCit^{2-}$, which can interact in an electrostatic way with support or form a covalent bond. Near edges, nickel ions are not expected to be adsorbed. (Adapted from [3,15])

As second point of this study, the impact of an increase of solution pH has been considered. The aim is to promote the formation of a nickel-citrate complex and to verify its impact in the final distributions profiles.

In a 0.05M [Ni^{2+}] solution with CA:Ni molar ratio equal to 1.2 and pH of 8, the formation of a nickel-citrate complex is expected according to Eq. 51 [182]. Besides, citrate not coordinated to metal ions can also be present, since CA:Ni molar ratio used is higher than stoichiometry one. Citrate is assumed to be totally deprotonated (Cit^{3-}) regarding the solution pH.

$$Ni^{2+} + Cit^{3-} \leftrightarrow NiCit^{-} \qquad \textbf{Eq. 51}$$

An egg-shell distribution of nickel-citrate complexes and/or citrate is obtained. Additionally, since the solution pH is close to PZC of γ-alumina, no important modification of the solution pH inside the pores is expected. Thus, the same species in solution should also be present inside the porosity.

For this value of pH, the support surface mainly consists of neutral OH surface sites, even if some negatively OH surface sites should also be considered. Therefore, electrostatic repulsion between nickel-citrate complex and negatively OH surface sites is expected. Because an egg-shell profile of these complexes is obtained even after several days of impregnation, a hydrolytic adsorption between $NiCit^-$ and OH neutral surface sites must be assumed (see Eq. 52). These results seem to be in good agreement with the literature [7].

$$[Ni(Cit)(H_2O)_3]^{2-} + xAl_sOH \leftrightarrow [(Al_sO)_xNi(Cit)_{3-x})]^{(2+x)-} + xH^+ \qquad \textbf{Eq. 52}$$

A schematic representation of phenomena that take place at the interface region between impregnation and surface is in Figure 82.

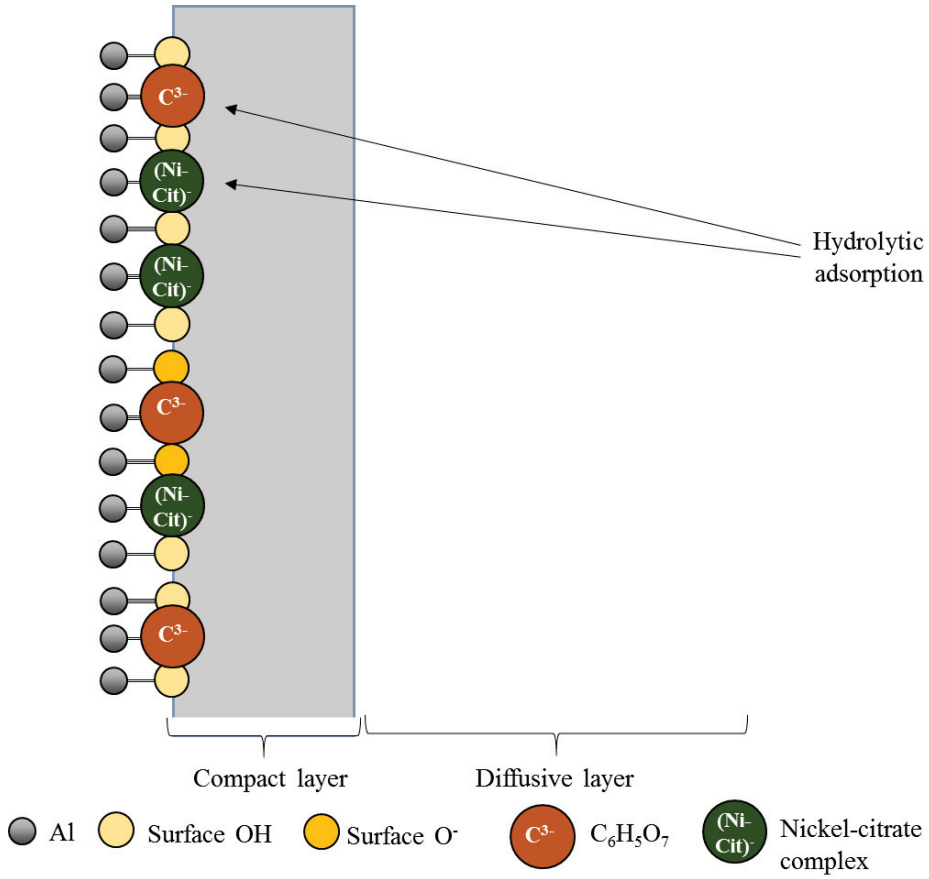

Figure 82 - Proposition of different phenomena that take place at the surface of γ-alumina near the edges upon impregnation 0.05M [Ni] solution with CA:Ni 1.2. Solution pH 8 explains why the surface is mainly neutral charged. Citrate is assumed to be in the form of citrate (Cit^{3-}) and in a nickel-citrate complex, which can interact form a covalent bond with support. Near edges, nickel-citrate complex is adsorbed in a covalent way. (Adapted from [3,15])

When a 0.2M [Ni] solution with CA:Ni equal to 1.2 and pH of 6 is used, the formation of nickel-citrate complexes can occur. In particular, the presence of $NiCit^-$ (see Eq. 51), NiHCit (see Eq. 53) and $Ni(HCit)(Cit^{3-})$ (see Eq. 54) is expected [182].

$$Ni^{2+} + HCit^{2-} \leftrightarrow NiHCit \qquad \textbf{Eq. 53}$$

$$NiHCit + Cit^{3-} \leftrightarrow Ni(HCit)(Cit^{3-}) \qquad \textbf{Eq. 54}$$

An egg-shell profile concerning nickel-citrate complex is established, while citrate ions are present in the entirely pellet

For a solution pH of 6, the surface of γ-alumina should be positively and neutral charged (OH_2^+ and OH surface sites, respectively). Citrate can be adsorbed (electrostatic or covalent interactions) in OH surface groups, as already mentioned. Hydrolytic adsorption of nickel-citrate complex can also take place in the same OH surface sites, as expressed in Eq. 52.

In the absence of citrate, a uniform profile has been obtained for the same nickel concentration (0.2M, see Figure 64). Apparently, an interaction between $[Ni(H_2O)_6]^{2+}$ ions and γ-alumina surface is favoured when nickel ions are in the form of a nickel-citrate complex. This can be explained taking into account the work of Bergwerff et al. [7]. Coordination of nickel ions by citrate might contribute to an easier exchange between the remaining water ligands and OH surface sites.

A schematic representation of phenomena that take place at the interface region between impregnation and surface is in Figure 83.

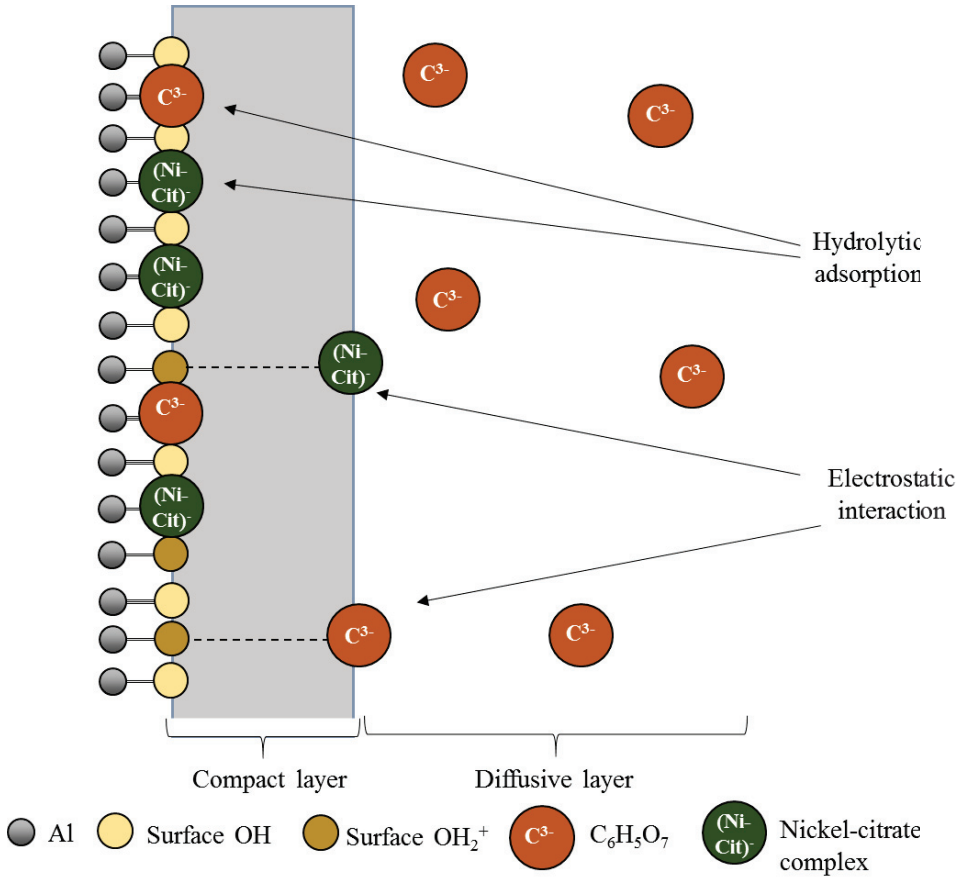

Figure 83 - Proposition of different phenomena that take place at the surface of γ-alumina near the edges upon impregnation 0.2M [Ni] solution with CA:Ni 1.2. Acidic solution pH 6 explains why the surface is positively and neutral charged. Citrate is assumed to be in the form of free citrate (Cit^{3-}) and in a nickel-citrate complex, which can interact in an electrostatic way with support or form a covalent bond. Near edges, nickel-citrate complex is adsorbed in a covalent and electrostatic way. (Adapted from [3,15])

To conclude, the influence of citric acid in the impregnation step of nickel based catalysts has been studied thanks to a MRI and Raman Imaging techniques. ^{1}H MRI enables to follow the impregnation at different points in time, while Raman Imaging has been performed to obtain information about nature of species deposited in the support.

The results obtained can highlight two different roles of citrate:

- Adsorption of citrate limits in a high extent the interaction between nickel ions and OH surface sites of γ-alumina. Two factors are responsible for this behaviour. First, adsorption of citrate and nickel ions takes place in the same OH surface sites. A preferential adsorption of citrate is then highlighted. Second, adsorption of citrate can block the neighbouring available OH sites due to steric reasons. As a result, egg-shell profiles of citrate are obtained, while nickel ions are found in either egg-yolk or egg-white profiles depending on CA:Ni ratio.

- When complexation reaction between citrate and nickel takes place, a hydrolytic adsorption of metal-additive complex on the surface is suggested. Therefore, egg-shell distributions of nickel-citrate complex are obtained.

To conclude, by varying the pH and citric acid loading in impregnation solution, it is possible to control the profile of nickel ions desired and nature of species. The main conclusions are depicted in Figure 84.

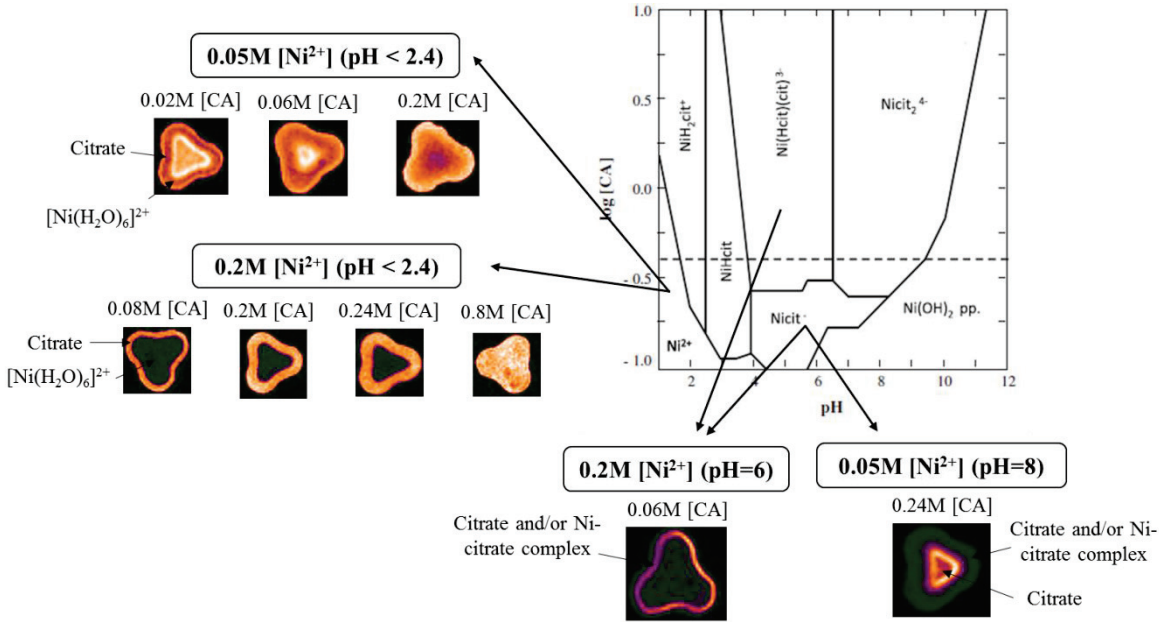

Figure 84 – Final distribution of citrate and Ni ions as a function of citric acid concentration, Ni concentration and solution pH.

2.1.3. *Conclusion on impact of solution properties*

Two different parameters related with solution properties have been investigated: metal ion concentration and presence of citric acid in impregnation solution.

Impregnation of nickel ions is governed by a competition between diffusion and surface interaction phenomena, which is strongly dependent on metal ion concentration. For low nickel concentrations (0.05 M [Ni]), extreme egg-shell distributions profiles are obtained, which indicate a strong surface interaction. On the contrary for higher nickel concentrations (for instance, higher than 0.11M [Ni]), uniform profiles are obtained. A mechanism to explain these different metal profiles is suggested as follows.

In the first 30 seconds of impregnation, which corresponds to the contact time between impregnation solution and support, impregnation solution is transported through the porosity by the action of capillary forces and diffusion. Simultaneously, metal precursor is removed from the solution through

an adsorption mechanism. It is indeed this strong surface interaction that explains why nickel ions are not transported together with the water flow. Once the support is withdrawn from the solution, transport is only done by diffusion. At the same time adsorption takes place. Two different phenomena should be considered based on a selective affinity of nickel ions for the γ-alumina OH sites depending on their nucleophilic character. For low nickel concentrations (0.05M [Ni]), titration of the most reactive OH groups occurs. These interactions involves an hydrolytic adsorption, which explains the egg-shell distribution profiles even after several days of ageing or even after a thermal treatment. For higher nickel concentrations, once titration of the most reactive OH groups by nickel ions has occurred, the remaining nickel ions in the fluid phase in the form of $[Ni(H_2O)_6]^{2+}$ can be electrostatically adsorbed in the less reactive OH groups at the surface of alumina. Those adsorbed nickel ions may be transported through a surface diffusion mechanism, which can explain the long impregnation times needed to obtain a homogenous metal distribution inside the pellet.

By adding citrate to a nickel solution, either egg-yolk or egg-white nickel profiles are obtained depending on the nickel concentration in the impregnation solution. In general, adsorption of citrate limits in a high extent the interaction between nickel ions and OH surface sites of γ-alumina, which results in a faster transport of metal ions towards the core. On the contrary, by increasing solution pH in order to promote the complexation reaction between citrate and nickel takes place, a higher affinity with surface is observed. Hence, egg-shell distributions of nickel-citrate complex are obtained.

2.2. Second simple case: extension to the case of Co

Besides nickel, cobalt is widely used as metal promotor for hydrotreatment catalysts. Therefore, the same MRI approach has been performed to study the impregnation of γ-alumina with a Co solution. The main difficulty in the implementation of this approach concerns the stronger paramagnetic behaviour of cobalt, which also results in small relaxation times (T_1 and T_2) of proton. Therefore, Single Point Imaging sequence has once more been performed to overcome these constraints.

It has also been verified that when the standard impregnation method (method A) is performed with cobalt solutions containing other elements (metal precursors and/or additives), no contrast in MRI images is obtained either with SPI or spin-echo sequences, which hinders to distinguish between different compounds. Indeed, cobalt is known to contribute to a short T_2 value of neighbouring water protons, which implies a destructive of ^{1}H MRI signal. To overcome this difficulty, impregnation with solutions containing Co has been performed in diffusional conditions meaning that the support is pre-saturated with water. The aim is to, in some extent, dilute this destructive effect of cobalt on ^{1}H MRI signal. Indeed, it has been verified for the case of nickel solutions (study not shown for reasons of clarity of the manuscript) that the only difference concerning standard impregnation method (method A) and diffusional impregnation (method B) concerns the transport rate. In diffusional impregnation, no capillary action occurs, which means that the driving force is only the concentration gradient. Therefore, no changes in phenomena concerning surface interaction are expected.

2.2.1. *Impact of metal concentration*

The impact of cobalt concentration on the impregnation step has been studied. Different concentrations of cobalt in impregnation solution ranging from 0.05 to 0.2 M, which corresponds to a metal weight percent (wt%) of 0.25 up to 0.96 in the final catalyst have been tested. ^{1}H MRI images are gathered in Figure 85. As for the case of nickel, MRI images have been obtained in T_1 contrast, which means that the dark area corresponds to a low concentration of metallic ion (T_1 longer - small ^{1}H signal intensity), while the bright (orange) region corresponds to a higher concentration of these ions (T_1 shorter - high ^{1}H signal intensity). One can remark a lower signal to noise ratio comparing to Ni case. This fact is explained due to a higher paramagnetic behaviour of Co ions.

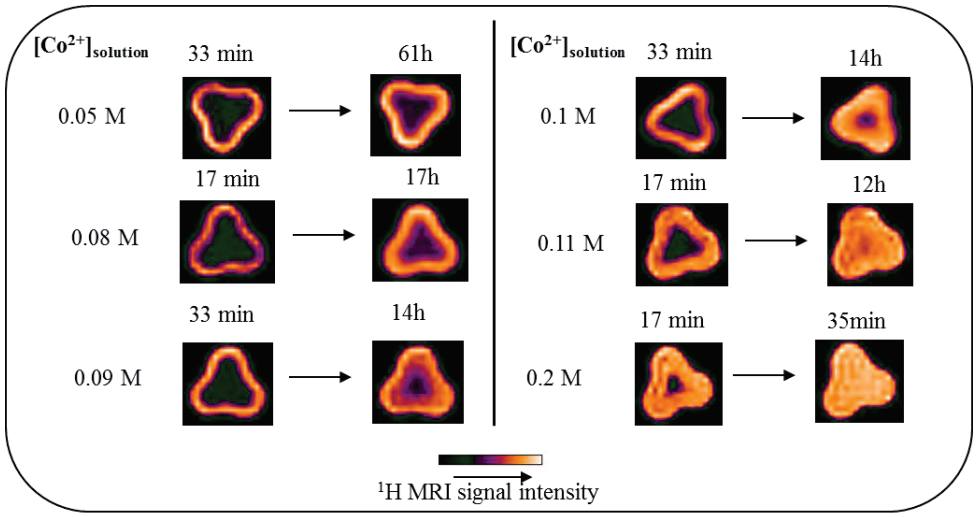

Figure 85 - Impact of $[Co^{2+}]$ in impregnation solution on the distribution profile of Co^{2+} ions inside γ-alumina: ^1H MRI images recorded right after impregnation and at equilibrium (set to the time for which there is no variation of the metal distribution profile) using a SPI sequence (FOV=2.5×2.5×8 mm; Spatial resolution= 78×78×100 µm/pixel; Matrix=32×32×8)

These results are similar to the ones obtained with Ni solution. Homogenous distributions of Co ions are only obtained for concentrations higher than 0.1M. One can conclude that the same physicochemical phenomena described for the case of impregnation with Ni solutions are valid in the case of Co solutions.

2.2.2. *Conclusion*

To summarize, impregnation of cobalt based catalysts is governed by capillarity, diffusion and surface interaction (formation of inner-sphere Co complexes through hydrolytic adsorption). As described for Ni impregnation study, a competition between diffusion and surface interaction mainly governs impregnation.

3. Conclusion

In this chapter, the implementation and validation of the MRI technique to monitor the impregnation has been shown. This methodology enables spatial and time-resolved characterization of the impregnation step.

The MRI technique has been adapted to characterize the impregnation step using monometallic solutions composed either by nickel or cobalt in the presence or not of citric acid. To follow the transport of a one-paramagnetic component solution, MRI time-resolved images have been recorded by applying the SPI sequence. When the impregnation solution is composed at least of two elements, an innovative MRI approach has been implemented to monitor the impregnation step. By applying the spin-echo sequence, it is possible to induce two different contrasts in the MRI image in order to distinguish the different species deposited onto the support. An improvement of spatial resolution to 39 µm×39 µm has been achieved (so far, standard spatial resolution is 78 µm × 78 µm [128]). This MRI methodology has been validated through a comparison between intensity profiles of MRI images and the EPMA concentration profiles, which enables to obtain a direct correlation between ^{1}H MRI intensity and concentration of the metal ion within the pellet. Finally, Raman Imaging has also been used in order to obtain information about the nature of the organic species inside the support with a spatial resolution of 16.2 µm × 16.2 µm.

Second, the MRI-Raman Imaging characterization methodology has been applied to study the phenomena that take place during the impregnation of a simple solution and the impact of the solution properties.

Impregnation step of γ-alumina with a nickel solution is governed by capillarity, diffusion and surface interaction. The capillary action is almost an instantaneous process. MRI results demonstrates that impregnation is governed by a competition of diffusion of nickel ions in liquid phase and adsorption at the surface. A selective affinity of nickel ions for the γ-alumina OH sites depending on their nucleophilic character has been highlighted. The same conclusions can be drawn for the impregnation of cobalt based catalysts.

The addition of citrate to a nickel solution at pH in range of 1.4 to 2.4 lead to a faster transport of nickel ions towards the core of the support. A competitive adsorption mechanism between citrate and nickel ions is highlighted. A higher affinity between citrate and alumina is indicated rather than a complexation of citrate to nickel ions. A different behaviour is observed when solution pH is increased to 6 and even to 8. In these conditions, complexation of citrate to nickel ions is favoured, which results in an increase of the interactions between the negatively charged nickel-citrate complex and the

protonated support surface. This study demonstrates that it is possible to control the metal distribution profile by choosing the appropriate CA:Ni ratio and solution pH.

Chapter IV – Towards the real case of HDT catalysts: comprehension of impregnation step

In this chapter, MRI has been applied for the first time to monitor *in-situ* the distribution and the nature of molybdenum, cobalt and phosphorus with or without citric acid during the impregnation step. Raman Imaging (Streamline mode) yields complementary spatial information about molybdenum speciation through a Raman mapping of specific Mo species.

The impact of metal concentration in solution on the impregnation of molybdenum catalysts is first evaluated through MRI. For reasons of clarity of the manuscript, this study is not present. As demonstrated in the case of nickel based catalysts (in Chapter III), the higher is the concentration of the metal ion, the faster is the transport of the impregnation solution through the porosity. For a certain molybdenum concentration, the impact of phosphorus on the distribution profiles of a molybdenum based oxide catalyst is investigated. A possible competitive adsorption between the metal species and phosphorus on the surface of alumina is evaluated.

The influence of the metal promotor (either cobalt or nickel) on the impregnation of molybdenum based catalyst in the presence or not of phosphorus is also investigated. The final distribution profiles and nature of Mo species are evaluated.

In the third part of this chapter, an example concerning the impact of citric acid as an additive on the impregnation of CoMoP/γ-Al_2O_3 catalysts is evaluated. The physicochemical phenomena that occur during impregnation are then studied.

1. Study of the impregnation of γ-Al_2O_3 with Mo(P) solution: impact of phosphorus

1.1. Characterization of Mo(P) impregnation solutions by Raman spectroscopy

As mentioned in Chapter II, two different Mo impregnation solutions with a concentration of 0.8M [Mo] (corresponding to 1.6 Mo atoms/nm^2 in the final catalyst) supported on γ-alumina have been prepared: an impregnation solution without phosphorous (pH 6) and other with phosphorus, P:Mo molar ratio of 0.4 (pH 2). This ratio corresponds to the one required to the formation of a Strandberg-type heteropolyanion based on molybdenum, $P_2Mo_5O_{23}^{6-}$ [39].

Each solution has been characterized by Raman spectroscopy. Figure 86 (a) gathers the Raman spectrum of a 0.8M [Mo] solution. Raman peaks at 938 cm^{-1} and 895 cm^{-1} are, respectively, assigned to the symmetric $\nu_s(MoO_{2t})$ and asymmetric $\nu_{as}(MoO_{2t})$ stretching vibrations of $Mo_7O_{24}^{6-}$ anions in solution [183]. The weaker band at 357 cm^{-1} is related to its bending modes $\delta(MoO_{2t})$ [183]. In the presence of P (see Figure 86 (b)), Mo is in the form of $H_2P_2Mo_5O_{23}^{4-}$ complexes (Strandberg heteropolyanion) as indicated by Raman bands at 942 cm^{-1} $\nu_s(MoO_{2t})$ and 390 and 369 cm^{-1} $\delta(MoO_{2t})$ [4]. Besides, part of phosphorus is in the form of free phosphates, which is indicated by the Raman peak at 1018 cm^{-1}.

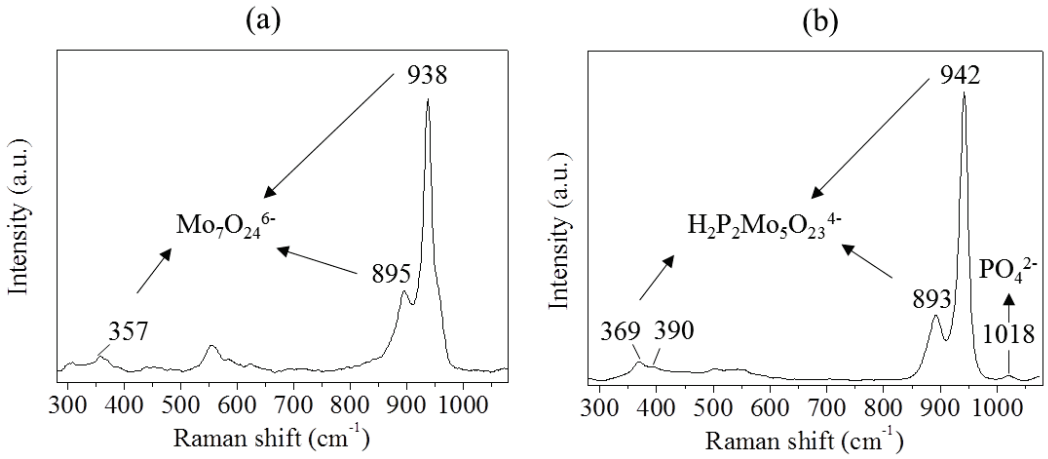

Figure 86 - Raman spectrum for (a) 0.8M [Mo] solution at pH 6 and (b) 0.8M [Mo] with P:Mo=0.4 (molar) at a pH of 2

1.2. Monitoring the impregnation of γ-Al_2O_3 with Mo(P) solution: MRI and Raman Imaging characterizations

1.2.1. *Impregnation of γ-alumina with Mo solution*

^{1}H MRI images obtained during impregnation of γ-alumina extrudate with 0.8 M [Mo] solution are presented in Figure 87. The preparation method has been performed according to the standard impregnation method (method A).

The presence of Mo ions results in an increase of the relaxation times of water protons, which is in good agreement with the work of Lysova et al. [8]. Thus, as the ^{1}H MRI images are in T_1 contrast (value of TR and TE are lower than T_1 and T_2, respectively), the low ^{1}H MRI signal (magenta color) corresponds to the presence of Mo-complexes. In contrast, a high ^{1}H MRI signal (white color) implies the absence of Mo-complexes.

After impregnation there is a rapid imbibition of water due to capillary action of the porous space, which results in a uniform distribution of the solvent throughout the pellet. Initially, ^{1}H signal is very intense in the core, which is consistent with a Mo-free region. As time elapses, changes in ^{1}H signal intensity are observed towards the core, which corresponds to the transport of Mo species. After approximately 5h, the ^{1}H signal distribution is almost uniform, which indicates a homogeneous distribution of the metal species. The image obtained after 5h corresponds then to the equilibrium state. Besides, for this time of impregnation, one can notice slight differences in signal intensity, which implies that different types of Mo-complexes are deposited onto the support.

Furthermore, one can roughly estimate the self-diffusion coefficient of Mo ions in the porosity of γ-Al_2O_3. According to MRI results, Mo ions need almost 5h to cover 530 µm within the catalyst pellet (value obtained through Indigo IFPEn software). Applying once again the relation given in Eq. 43 [172] (page 109), a diffusion coefficient of the order of magnitude of 10^{-12} m^2/s is obtained. This value is indeed much smaller than the expected diffusion coefficient of a liquid phase of 10^{-9}-10^{-10} m^2/s [168–171], which suggests the presence of a surface adsorption mechanism that hinders diffusion.

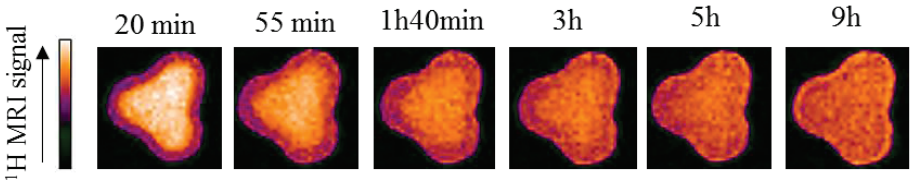

Figure 87 – Monitoring transport of a 0.8 M [Mo] solution within the porosity of a γ-Al_2O_3 pellet: ^{1}H MRI images recorded at several times during impregnation using a spin-echo sequence (FOV=2.5×2.5×8 mm; Resolution= 39×39×100 µm/pixel; Matrix=64×64×8)

Figure 88 presents the Raman spectra recorded at different positions along the cross-section of the same Mo/γ-Al_2O_3 catalyst at the equilibrium state of impregnation. Different Mo species are observed: the ν(MoO_{2t}) vibration mode at 940 cm^{-1} and δ(MoO_{2t}) at 355 cm^{-1} reveal the presence of $Mo_7O_{24}^{6-}$ in electrostatic interaction with alumina. The δ (MoO_{2t}) peaks at 328 cm^{-1} and ν(MoO_{2t}) peaks at 920 cm^{-1} (and also at 896 cm^{-1}) can be attributed to monomolybdates in electrostatic and covalent interaction with alumina, respectively [184]. Moreover, the formation of an Anderson–type alumino heteropolymolybdate ($[Al(OH)_6Mo_6O_{18}]^{3-}$ denoted by $AlMo_6$) can be assigned by ν(Al-O) peaks at 565 cm^{-1} and ν(MoO_{2t}) at 903 cm^{-1} and 946 cm^{-1} [3,183].

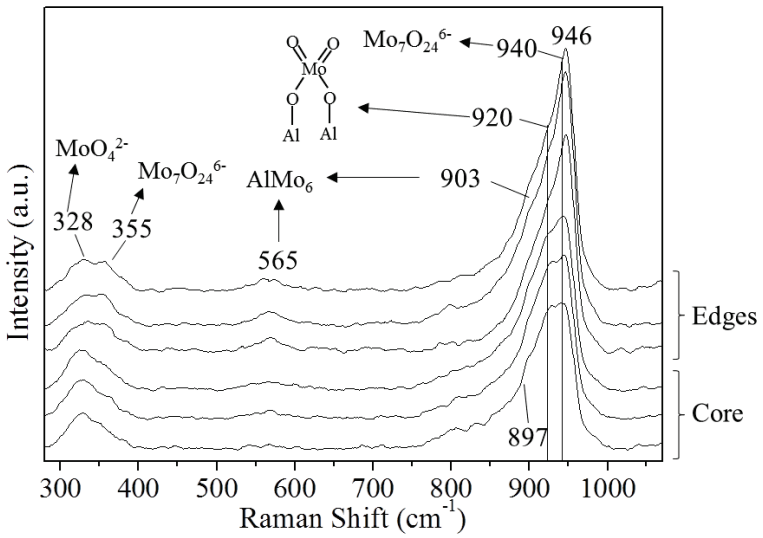

Figure 88 – Streamline Raman spectra recorded at different positions within a γ-alumina pellet impregnated with 0.8 M [Mo] at equilibrium

Based on the spectra showed in Figure 88, Figure 89 shows the spatial distribution of $Mo_7O_{24}^{6-}$ ions (δ(MoO_{2t}) band corresponding to the intensity at 355 cm^{-1}, see Figure 89 (a)) and the repartition of $AlMo_6$ over the pellet (ν(Al-O) band corresponding to the intensity at 565 cm^{-1}, see Figure 89 (b)). For both of them, a higher concentration is found near the edges. In Figure 89 (c), one can also observe a higher concentration of MoO_4^{2-} near the core, as indicated by the ratio between the intensity at 355 cm^{-1} and 328 cm^{-1}, which corresponds to the proportion of $Mo_7O_{24}^{6-}$ in relation to MoO_4^{2-}.

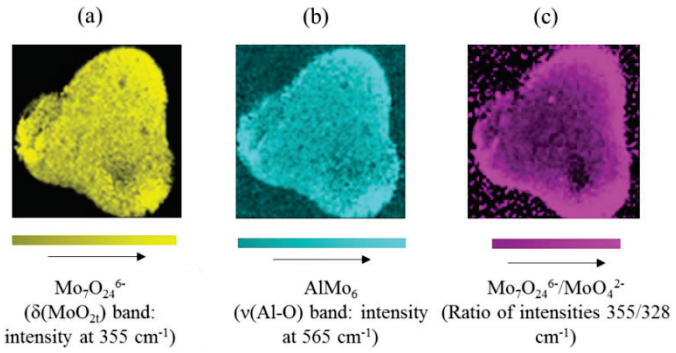

Figure 89 –Raman cartography images of γ -alumina impregnated with 0.8 M [Mo] obtained at equilibrium with a spatial resolution of 16.2 µm × 16.2 µm (a) repartition of $Mo_7O_{24}^{6-}$ over the pellet ($\delta(MoO_{2t})$ at 355 cm^{-1}) (b) repartition of $AlMo_6$ over the pellet (ν(Al-O) at 565 cm^{-1}) (c) proportion between $Mo_7O_{24}^{6-}/MoO_4^{2-}$ over the pellet (obtained through the ratio between $\delta(MoO_{2t})$ at 355 cm^{-1} and 328 cm^{-1})

1.2.2. *Impregnation of γ-alumina with MoP solution*

To begin with study of impregnation with a MoP solution, ^{1}H MRI has been first applied to monitor the impregnation step of γ-alumina with 0.76 M [H_3PO_4] solution. As discussed in Chapter II, the presence of phosphorus leads to an increase in relaxation times of proton. Figure 90 shows the ^{1}H MRI images recorded at different times of impregnation. As for the case of Mo, images have been acquired in T_1 contrast, which means that the low ^{1}H MRI signal (in green) corresponds to the presence of phosphorus.

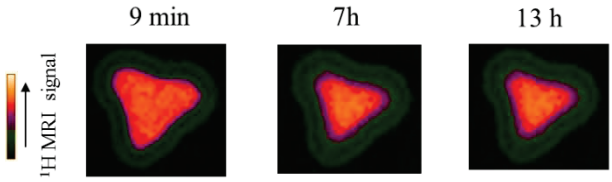

Figure 90 - Monitoring transport of a 0.76 M [H_3PO_4] solution within the porosity of a γ-Al_2O_3 pellet: ^{1}H MRI images recorded at several times during impregnation using a spin-echo sequence (FOV=2.5×2.5×8 mm; Resolution= 39×39×100 µm/pixel; Matrix=64×64×8)

For this H_3PO_4 concentration, a phosphorus egg-shell distribution is observed after 13h of impregnation. This egg-shell profile corresponds to approximately 86 µm thickness as measured through Indigo IFPEn software. Based on these data, a self-diffusion coefficient of order of magnitude of 10^{-14} m^2/s is estimated once again thanks to Eq. 43 [172] (page 109). As observed in the case of Mo, this value suggests that diffusion of phosphorus is limited by a surface adsorption phenomenon. Indeed, adsorption of phosphorus on the support surface has already been reported by Bergwerff et al. [58].

T_1-weighted ^1H MRI images corresponding to the transport of MoP solution inside γ-alumina as a function of time are illustrated in Figure 91.

Initially, MRI shows that Mo and P species are located at the edges of the support due to the low ^1H MRI signal observed (magenta color). The high signal intensity in the core is attributed to free water protons. As time elapses, the progression of the low ^1H MRI signal front is observed, which corresponds to the transport of impregnation solution. After 9 hours, there are no variations in the distribution profile, although differences in the signal intensity evidence a non-uniform distribution of Mo and P species. The slight low NMR signal intensity observed near the edges of the pellet suggests an overconcentration of P species like in the case of H_3PO_4 transport described above.

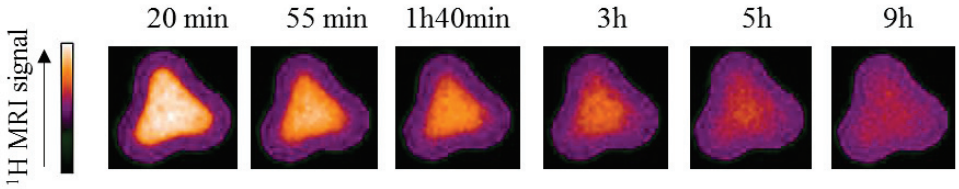

Figure 91 - Monitoring transport of a 0.8 M [Mo] solution with P:Mo=0.4 molar within the porosity of a γ-Al_2O_3 pellet: ^1H MRI images recorded at several times during impregnation using a spin-echo sequence (FOV=2.5×2.5×8 mm; Resolution= 39×39×100 µm/pixel; Matrix=64×64×8)

Figure 92 shows the Raman spectra recorded at different positions of the same MoP/γ-Al_2O_3 catalyst at equilibrium (corresponding to 18h after impregnation). Neither the P-based heteropolyanions nor free phosphates present in impregnation are observed in the impregnated catalyst. Furthermore, the presence of $Mo_7O_{24}^{6-}$ (ν(MoO_{2t}) at 943 cm^{-1} and 357 cm^{-1}) and MoO_4^{2-} (δ(MoO_{2t}) at 328 cm^{-1}), in electrostatic interaction with γ-alumina is similar to Mo/γ-Al_2O_3 study (see Figure 88). Moreover, the formation of $AlMo_6$ is indicated by Raman band ν(Al-O) at 565 cm^{-1} and also by the slight contribution of the ν(MoO_{2t}) band at 946 cm^{-1}. Nevertheless, in the presence of P, there are less MoO_4^{2-} species in covalent interaction with alumina (slightly contribution of ν(MoO_{2t}) at 920 cm^{-1}).

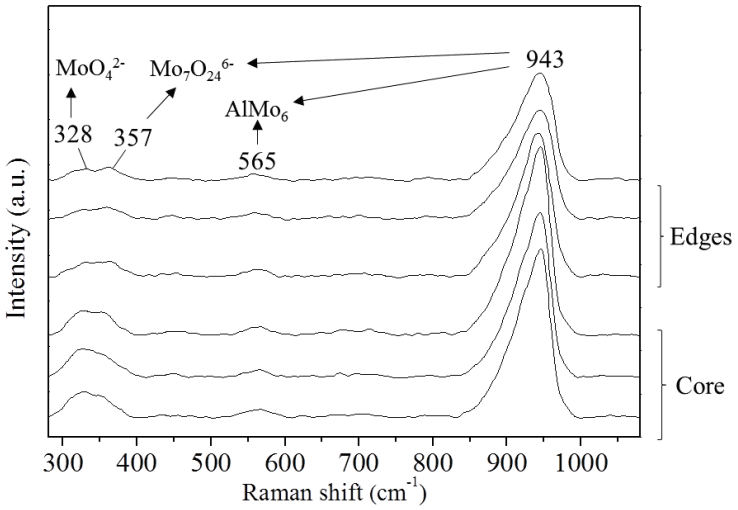

Figure 92 - Streamline Raman spectra recorded on γ-alumina impregnated with a solution of 0.8 M [Mo] with P:Mo=0.4 molar at equilibrium

Figure 93 presents the Streamline Raman images obtained based on the Raman spectra of Figure 92. The first one shows the repartition over the pellet of MoO stretching vibrations (maximum of the intensity between 920 and 946 cm^{-1} (see Figure 93 (a)), the second one the repartition of $AlMo_6$ (ν(Al-O) at 565 cm^{-1}, see Figure 93 (b)) and the last one is the image corresponds to the ratio between intensity at 355 cm^{-1} and 328 cm^{-1}, see Figure 93 (c)).

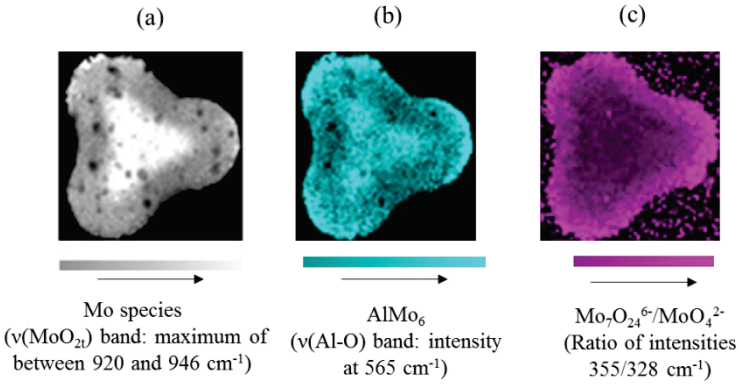

Figure 93 - Streamline Raman images of γ-alumina impregnated with 0.8 M [Mo] with P:Mo=0.4 molar obtained at equilibrium with a spatial resolution of 16.2 µm × 16.2 µm (a) repartition of Mo-O stretching (corresponding to the large Raman band between 920 and 946 cm^{-1}) (b) repartition of $AlMo_6$ over the pellet (intensity at 565 cm^{-1}) (c) proportion between $Mo_7O_{24}^{6-}/MoO_4^{2-}$ over the pellet (obtained through the ratio between intensity at 357 cm^{-1} and 328 cm^{-1})

These images confirm an overconcentration of molybdenum species near the core of the pellet. More precisely, a higher concentration of MoO_4^{2-} in relation to $Mo_7O_{24}^{6-}$ is indicated near the core (see Figure 93 (c)). Additionally, Figure 93 (b) shows a higher concentration of $AlMo_6$ near the edges of

the support. These results suggest a gradient of pH within the catalyst, since the Mo polymerization degree depends on the pH.

1.3. Discussion: description of physicochemical phenomena during impregnation of Mo(P)/γ-Al_2O_3 catalyst

As for the previous case of impregnation with Ni(Co) solutions, MRI results allow one to describe the transport of molybdenum ions as a function of capillarity, diffusion and surface interaction. It has been demonstrated that capillarity cannot be the limiting step of impregnation, since it is an instantaneous process.

According to MRI results, a uniform distribution of Mo-complexes through γ-alumina is only observed after 5h of the initial contact between the support and the impregnation solution. A roughly estimation of the self-diffusion coefficient indicates a diffusion coefficient of the order of magnitude of 10^{-12} m^2/s, which suggests that the diffusion of molybdenum species is hindered by metal-support interactions. This fact is indeed confirmed by Raman spectra obtained at equilibrium, which show MoO_4^{2-} in covalent interaction with the support. Several parameters such as the nature of surface OH groups of γ-alumina, speciation and pH of impregnation solution can explain these metal/support interactions.

As mentioned in Chapter III, the surface of γ-alumina can be described using the Digne's model [176]. The hydroxyl surface density can be estimated to around 11.8 OH/nm^2 after a thermal treatment at 573K. As a consequence, the total amount of OH groups at the surface of γ-Al_2O_3 in aqueous conditions is larger than the density in Mo atoms in the final catalyst (equal to 1.6 Mo $atoms/nm^2$). Moreover, as the distribution of Mo species is homogeneous approximately after 5 hours, one can conclude that a selective adsorption of Mo ions in the OH surface groups occurs.

Once more, based on the MUSIC model proposed by Hiemstra et al. [178,185], it is possible to identify the nature of different OH groups as function of their electronegativity. At the pH of the impregnation solution (approximately 6) and considering the (110) surface of γ-alumina as mainly exposed, OH groups are either positively charged ($[(Al_{Td})OH_2]^{+0.75}$ and $[(Al_{Oh})OH_2]^{+0.5}$) or neutral ($[(Al_{Oh})_2OH]$) [180,181]. Raman spectroscopy shows that $Mo_7O_{24}^{6-}$ ions predominate in solution. Therefore, in the early moments of impregnation, one can conclude that the ^1H MRI signal ring observed near the edges of support (see Figure 87) corresponds to the presence of $Mo_7O_{24}^{6-}$ at the neighbourhood of free water molecules confined into the porosity. Thus, an electrostatic interaction between the negatively charged Mo species and positively charged OH groups is expected, which led to a slow diffusion of the $Mo_7O_{24}^{6-}$ front [104].

A higher concentration of $Mo_7O_{24}^{6-}$ in electrostatic interaction with alumina near the edges is maintained at equilibrium, as demonstrated by Raman image in Figure 89 (a). This observation suggests a lower local pH than the pH of the solution. This fact supports the presence of an Anderson-type heteropolyanion (HPA) ($[Al(OH)_6Mo_6O_{18}]^{3-}$ ($AlMo_6$) observed at the same position of $Mo_7O_{24}^{6-}$ (see Figure 89 (b)). Indeed, the formation of this HPA, which is favoured in acidic medium (see Eq. 55) results from the dissolution of alumina due to interactions with Mo species, as demonstrated by Carrier et al. [45]. The interaction with Mo species enhance the dissolution rate by labilizing the Al-O lattice bonds.

$$12Mo_7O_{24}^{6-} + 7Al_2O_3 + 27H_2O + 30H^+ \rightarrow 14[Al(OH)_6Mo_6O_{18}]^{3-} \quad \textbf{Eq. 55}$$

Besides, Raman spectra also shows that the final impregnated catalyst contains MoO_4^{2-} ions in electrostatic and covalent interaction with the alumina support, at equilibrium stage. This observation reflects the buffering effect of alumina. Part of $Mo_7O_{24}^{6-}$ ions are progressively transformed into MoO_4^{2-} towards the core of the support due to an increase of the pH of the solution inside the porosity (see Eq. 56). Indeed, Figure 89 (c) shows that proportion $Mo_7O_{24}^{6-}$ / MoO_4^{2-} is more important near the edges.

$$Mo_7O_{24}^{6-} + 8OH^- \leftrightarrow 7MoO_4^{2-} + 4H_2O \quad \textbf{Eq. 56}$$

The increase of the pH towards the core of the support has also an impact in the OH groups at the surface of alumina. For basic pH, even if some protonated OH surface groups are still present in the (110) surface of γ-alumina ($[(Al_{Oh})OH_2]^{+0.5}$), negatively charged OH groups ($[(Al_{Oh})OH_2]^{-0.25}$) and neutral ($[(Al_{Oh})_2OH]$) predominate [180,181]. $Mo_7O_{24}^{6-}$ and MoO_4^{2-} ions can be electrostatically retained on alumina surface, but hydrolytic adsorption only occur between MoO_4^{2-} ions and neutral surface hydroxyls, according to Eq. 57 [4,184]:

$$2Al_sOH + MoO_4^{2-} \leftrightarrow (Al_s)_2MoO_4 + 2OH^- \quad \textbf{Eq. 57}$$

Figure 94 schematizes the different interaction between molybdenum ions and OH surface sites. The interactions between $Mo_7O_{24}^{6-}$ and surface of alumina are involved in the formation of $AlMo_6$.

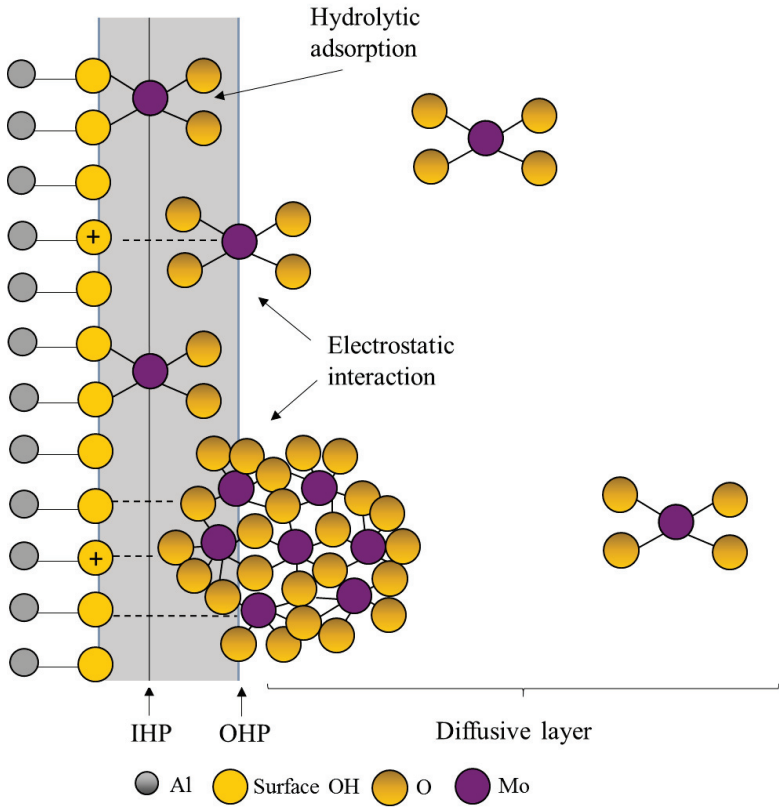

Figure 94 - Schematic picture using Three Layer Model about phenomena that take place in the interface region at equilibrium of impregnation of γ-alumina with 0.8M [Mo] solution: diffusion and surface interaction (electrostatic interaction and hydrolytic adsorption) (adapted from [3,15])

MRI results show that a homogeneous distribution of Mo species is obtained after several hours of impregnation, which results from a competition between diffusion transport and interaction with the alumina surface. According to Raman spectroscopy results, this homogeneity is only relative: polymeric Mo ions and $AlMo_6$ are mainly present near the edges of the support, which suggests a lower local pH, whereas monomeric Mo ions in electrostatic and covalent interactions with the support are mainly observed near the core

When phosphorus is added to a molybdenum solution, in the initial stages of impregnation, there is once again the capillary flow that transports water through the porous medium. The low ^{1}H MRI ring observed in Figure 91 suggests that part of the dissolved precursors in solution stays behind due to interactions with the support.

As shown by Raman spectroscopy, part of phosphates in the impregnation solution is present as free phosphate and in the form of Strandberg heteropolyanion ($H_2P_2Mo_5O_{23}^{4-}$). Several studies reported that free phosphates react with hydroxyl groups of alumina (see Eq. 58), which leads to the formation of either linear polyphosphate chains due to the interaction of adjacent phosphorus molecules [25] or an

amorphous $AlPO_4$ layer [4,29–31]. Moreover, this strong affinity contributes to a higher concentration of the additive near the external surface of catalyst. This is in good agreement with the slight high MRI signal intensity observed near the core of the pellet after 9h of impregnation (see Figure 91) and the high intensity of characteristic Mo-O stretching in Raman cartography also near the center of catalyst (see Figure 93 (a)).

$$Al_sOH + HPO_4^{2-} + H^+ \leftrightarrow Al_sHPO_4^- + H_2O \qquad \textbf{Eq. 58}$$

Moreover, reaction in Eq. 58 leads to a decrease in free phosphates, which influences the stability of P-type heteropolyanion according to following reaction [4].

$$7P_2Mo_5O_{23}^{6-} + 15H_2O \leftrightarrow 5Mo_7O_{24}^{6-} + 14HPO_4^{2-} + 16H^+ \qquad \textbf{Eq. 59}$$

As a consequence of the decomposition of HPA, $Mo_7O_{24}^{6-}$ is formed, according to the Raman spectra (see Figure 92). As described for the impregnation of Mo based catalysts, $Mo_7O_{24}^{6-}$ interacts electrostatically with positive surface hydroxyls of alumina. Apparently the adsorption of $Mo_7O_{24}^{6-}$ on alumina leads to the formation of $AlMo_6$ mostly near the edges of the support (see Figure 93 (b)). Once more, this observation indicates a lower local pH near the edges of the support. The fact that MoO_4^{2-} is also observed in Raman spectra at equilibrium reflects once more the buffering effect of γ-alumina. Indeed, as $Mo_7O_{24}^{6-}$ species progress towards the core of the support, they are transformed into MoO_4^{2-}. One can conclude that pH towards the core is increased at least up to 6, which corresponds to the pH for which monomeric species are formed departing from an initial 0.8M [Mo] concentration in solution [3]. In the presence of P, hardly MoO_4^{2-} species in covalent interaction with the support are observed. This suggests a titration of neutral OH groups by phosphorus, which lead to the diffusion of monomeric Mo species towards the core of the support interacting only electrostatically with γ-alumina. The results indicate a preferential adsorption of phosphorus species on γ-alumina surface in relation to Mo monomers. Figure 95 describes the proposed surface interaction phenomena that take place during impregnation of γ-alumina with MoP solution.

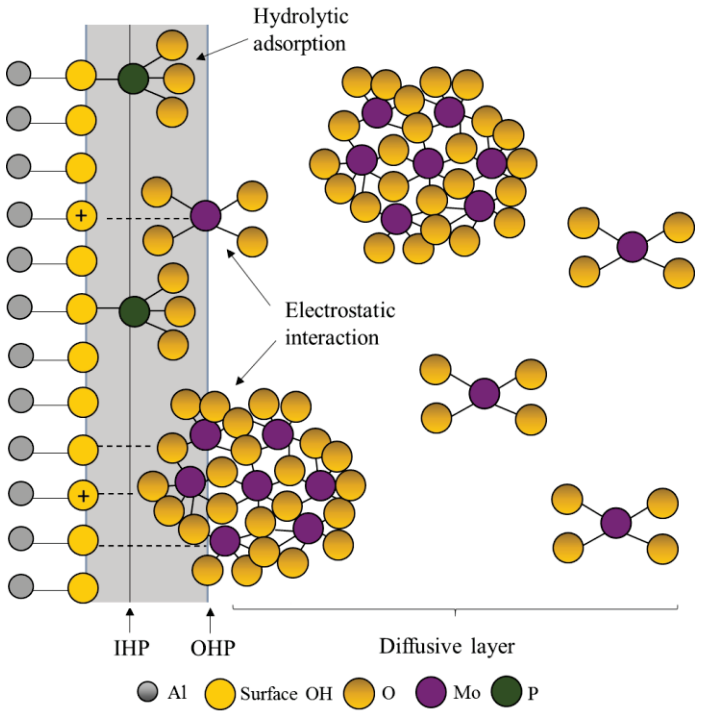

Figure 95 - Schematic picture using Three Layer Model about phenomena that take place in the interface region at equilibrium of impregnation of γ-alumina with 0.8M [Mo] and P (with P/Mo=0.4 molar) solution: diffusion and surface interaction (electrostatic interaction and hydrolytic adsorption) (adapted from [3,15])

In the presence of P, a preferential adsorption of phosphorus on γ-alumina surface is suggested, which results in the decomposition of Strandberg HPA and an egg-white distribution of Mo species. Besides, almost no Mo species in covalent interaction with γ-alumina are found.

1.4. Conclusion on the impact of phosphorus

To conclude the study of the Mo(P)/γ-Al_2O_3 impregnation, Figure 96 shows the comparison between the ^{1}H MRI and Raman Imaging results at the equilibrium state of impregnation and the EPMA distribution obtained after a thermal treatment at 450°C. Concerning MRI results, the two images show differences in ^{1}H MRI signal intensity, which evidences that different types of Mo-complexes are deposited in the support body (*i.e.*, different impacts on relaxation times).

The buffer effect of γ-alumina is proposed to explain the evolution of Mo species in the catalyst support. In a Mo/γ-Al_2O_3 catalyst, $Mo_7O_{24}^{6-}$ anions are found in the entire support in electrostatic interactions with γ-alumina, even if a slightly higher concentration of these species near the edges is indicated. $AlMo_6$ is found in positions associated to a higher concentration of $Mo_7O_{24}^{6-}$. In contrast, MoO_4^{2-} ions are mainly present in covalent interaction with alumina near the core.

When P is present, Raman spectroscopy shows that the Strandberg heteropolyanion initially present in impregnation solution is no longer observed in impregnated support at equilibrium. Moreover, almost no Mo species in covalent interaction with the support are observed.

Besides, even after a thermal treatment, the distribution profiles are maintained. For the case of impregnation with a Mo solution, a uniform distribution is obtained. While for the case of impregnation with a MoP solution, a higher concentration of Mo near the core and a higher concentration of P near the edges are maintained. The good agreement between the techniques proves the representativeness of the MRI-Raman Imaging characterization methodology.

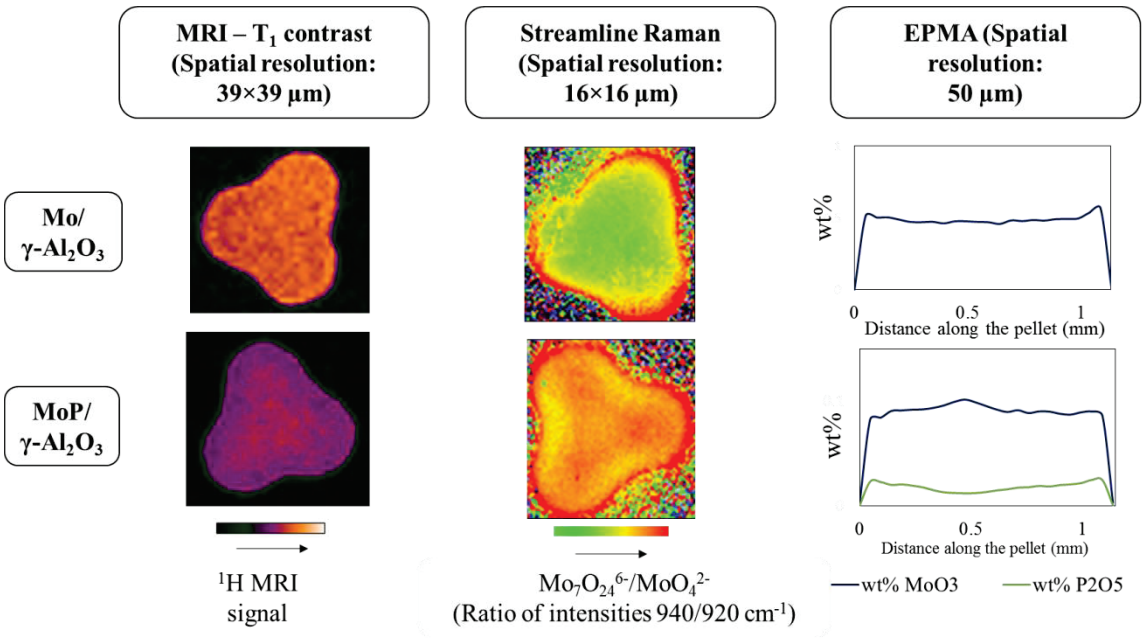

Figure 96 - Comparison MRI, Raman Imaging and EPMA – Case of Mo(P)/γ-Al_2O_3 catalyst

In conclusion, information obtained by MRI and Raman Imaging enables to better understand the different interactions of Mo and P with γ-alumina. The comparison between these two techniques highlights a competitive adsorption between phosphates and molybdates ions and a stronger affinity of phosphates to γ-alumina, which remain in satisfactory agreement with the literature [21,22]. In the presence of phosphorus, an egg-white distribution of Mo species is rather obatined and almost no Mo species in covalent interactions with the support are observed.

2. Influence of the nature of metal promotor on the impregnation step of HDT catalysts: Ni or Co

This part is focused on the potential impact of the nature of metal promotor (Ni or Co) on Mo distribution in a Co(Ni)MoP/γ-Al_2O_3 catalyst. The impregnation method has been conducted in diffusional conditions (method B), *i.e.*, support is first saturated with water for the reasons already explained in Chapter III. Only the study concerning the CoMoP/γ-Al_2O_3 catalyst is presented for reasons of clarity of this manuscript.

2.1. Characterization of CoMo(P) impregnation solutions by Raman spectroscopy

Two different Mo impregnation solutions with a concentration of 0.8M [Mo] have been prepared: a Mo solution in the presence of (Co:Mo ratio of 0.3, pH 5) and in the presence of P (P:Mo ratio of 0.4, pH 2). Once again, the P:Mo ratio used corresponds to the one required to the formation of a Strandberg-type heteropolyanion based on molybdenum, $P_2Mo_5O_{23}^{6-}$ [39]. No Anderson-type HPA containing Co should be formed, since it requires specific synthesis conditions with a redox reaction [186].

Figure 97 (a) shows the Raman spectrum obtained for the CoMo solution. The Raman band at 1047 cm^{-1} is ascribed to the presence of nitrate ions, which results from the precursor of Co. One can observe that the most intense stretching vibration mode $\nu_s(MoO_{2t})$ observed in the case of Mo at 938 cm^{-1} (see Figure 86 (a)) is shifted to a value of 955 cm^{-1} when Co is added (see Figure 97 (a)). This shift to a higher wavenumber might be a result of the protonation of $Mo_7O_{24}^{6-}$ to $H_xMo_7O_{24}^{(6-x)-}$ polyanions according to Eq. 60 [187], which is in good agreement with the decrease of the solution pH to a value of 5 when Co is added.

$$7MoO_4^{2-} + (8+x)H^+ \leftrightarrow H_xMo_7O_{24}^{(6-x)-} + 4H_2O \qquad \textbf{Eq. 60}$$

When P is added to a CoMo solution, Raman spectrum in Figure 97 (b) yields the characteristic $\nu_s(MoO_{2t})$ vibrations of $H_2P_2Mo_5O_{23}^{4-}$ (Strandberg heteropolyanion) at 942 cm^{-1} and $\delta(MoO_{2t})$ modes at 390 and 369 cm^{-1}. Besides, the Raman band corresponding to nitrate ions (1047 cm^{-1}) is once more observed. Raman spectra of MoP (see Figure 86 (b)) and CoMoP (see Figure 97 (b)) solutions are similar, which suggest that there is no modification in MoP speciation when cobalt is added. Indeed, due to the phosphorus concentration in impregnation solution ([0.3M]), it is not surprising that Co ions remain in the form of aqua complexes, $[Co(H_2O)_6]^{2+}$ [28].

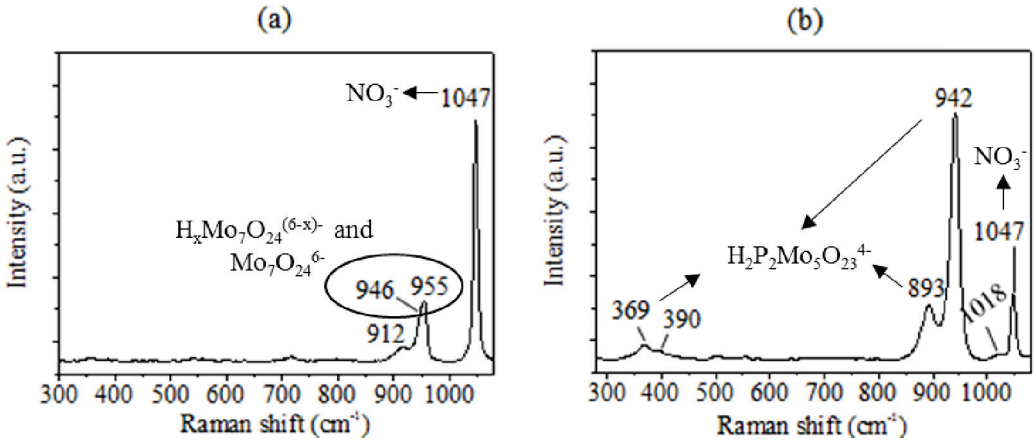

Figure 97 - Raman spectrum for (a) 0.8M [Mo] solution with Co:Mo=0.3 (molar) at a pH 5 and (b) 0.8M [Mo] solution with Co:Mo=0.3 (molar) and P:Mo=0.4 (molar) at a pH 2

2.2. Monitoring the impregnation of γ-alumina with CoMo(P) solution: MRI and Raman Imaging characterizations

^{1}H MRI has been applied to follow the impregnation step of γ-alumina with CoMo(P) solutions. To remind, the presence of ions such as cobalt, molybdenum or phosphorus influence the relaxation times of proton. On one hand, the presence of molybdenum and phosphorus induce an increase in T_1 and T_2 parameters. On the other hand, Co induces a decrease in relaxation times of the proton. Indeed, this different contribution of the elements present in impregnation solution has already been explained for nickel-citric acid solutions (see Chapter III, section 1.3.2, page 101). The same approach is valid for the present case. Then, by applying spin-echo sequence, it is possible to distinguish between Mo(P) and Co, by choosing the appropriate sequence parameters (TR and TE). In this way, a contrast in MRI image either in T_1 or T_2 can be obtained.

Protons near Mo(P) are observed thanks to a T_1 contrast, while protons near Co are observed thanks to a T_2 contrast. All elements contribute to a decrease in ^{1}H MRI signal, however a stronger impact of cobalt is observed due to its paramagnetism, which leads to an almost absence of ^{1}H signal.

2.2.1. *Impregnation of γ-alumina with CoMo solution*

Figure 98 shows the ^{1}H MRI images corresponding to the transport of a CoMo solution during the impregnation of γ-alumina. Initially, only the core is observed, since all the paramagnetic Co ions must be near the edge of the support. Indeed, the strong paramagnetic behaviour of Co explains the destructive effect observed on ^{1}H MRI signal, which can also hide the signal of the protons near Mo. Additionally, the high ^{1}H signal in the core of the pellet indicates the absence of Mo in this region. The

formation of a sharp ring of weak ^{1}H signal near the edge of the pellet is observed from 1h40 min of impregnation. This suggests the presence of mainly Mo near the support surface, while Co ions penetrate further in the support, which corresponds to the absence of signal in the ring surrounding the pellet's core. After a long period of impregnation (11h), non-uniform ^{1}H signal through the pellet is observed.

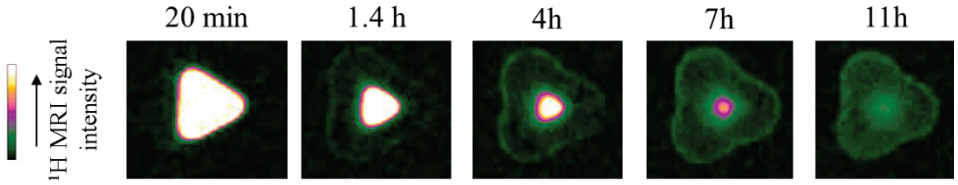

Figure 98 - Monitoring transport of a 0.8 M [Mo] solution with Co:Mo=0.3 molar within the porosity of a γ-Al_2O_3 pellet: ^{1}H MRI images recorded at several times during impregnation using a spin-echo sequence (FOV=2.5×2.5×8 mm; Resolution= 39×39×100 µm/pixel; Matrix=64×64×8)

Figure 99 shows the Raman spectra of the cross section of the same catalyst pellet at the equilibrium state. Mo species are mainly in the form of MoO_4^{2-} in covalent ($\nu(MoO_{2t})$ peak at 920 cm^{-1}) and electrostatic ($\delta(MoO_{2t})$ peak at 323 cm^{-1}) interactions with γ-alumina. Besides, a slight contribution of $\nu(MoO_{2t})$ peak at 940 cm^{-1} also indicates the presence of deprotonated heptamolybdates ($Mo_7O_{24}^{6-}$) in electrostatic interaction with the support.

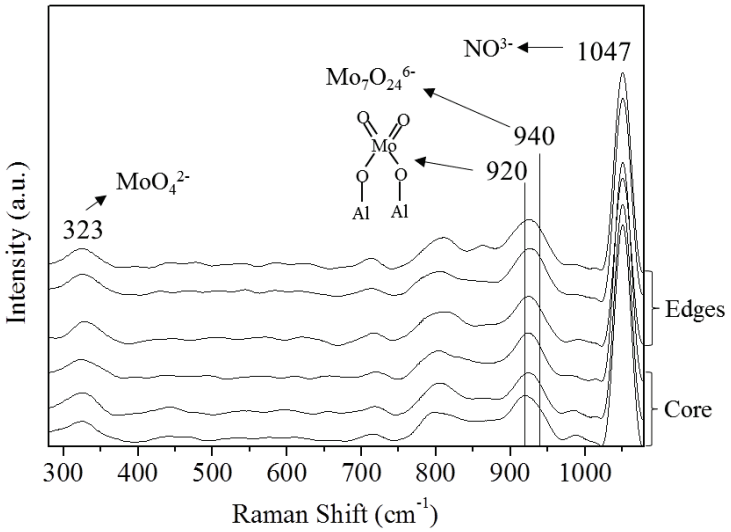

Figure 99 - Streamline Raman spectra recorded on γ-alumina impregnated with 0.8 M [Mo] and Co:Mo=0.3 (molar) at equilibrium

Figure 100 shows the Raman cartographies based on Figure 99. MoO stretching vibrations (maximum of intensities between 920 and 940 cm^{-1}) are more intense near the edges (see Figure 100 (a)), while MoO_4^{2-} species in electrostatic interaction with the support are uniformly distributed through the

catalyst pellet (see Figure 100 (b)). Yet, a higher concentration of MoO_4^{2-} in covalent interaction with γ-alumina is observed near the edges of the support (see Figure 100 (c)).

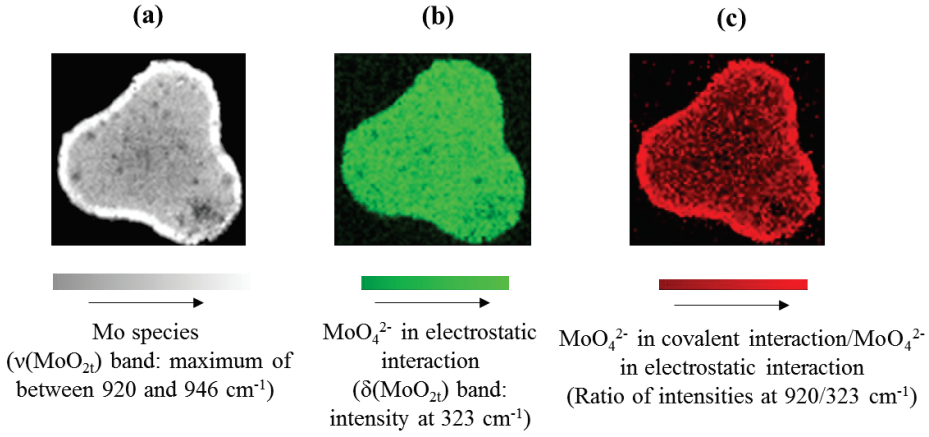

Figure 100 - Streamline Raman images of γ-alumina impregnated with 0.8 M [Mo] with Co:Mo=0.3 molar obtained at equilibrium with a spatial resolution of 16.2 µm × 16.2 µm (a) repartition of Mo species (corresponding to maximum of $\nu(MoO_{2t})$ between 920 and 940 cm^{-1}) (b) repartition of MoO_4^{2-} in electrostatic interaction with Al ($\delta(MoO_{2t})$ at 323 cm^{-1}) (b) proportion between MoO_4^{2-} in covalent and electrostatic interaction with Al (obtained through the ratio between at $\nu(MoO_{2t})$ at 920 cm^{-1} and $\delta(MoO_{2t})$ at 323 cm^{-1})

Figure 101 shows the comparison of the Mo crust thickness observed in both MRI and Raman images at equilibrium. A good agreement between the two techniques concerning a high local concentration of Mo ions near the edges is obtained regarding to the spatial resolution of each technique.

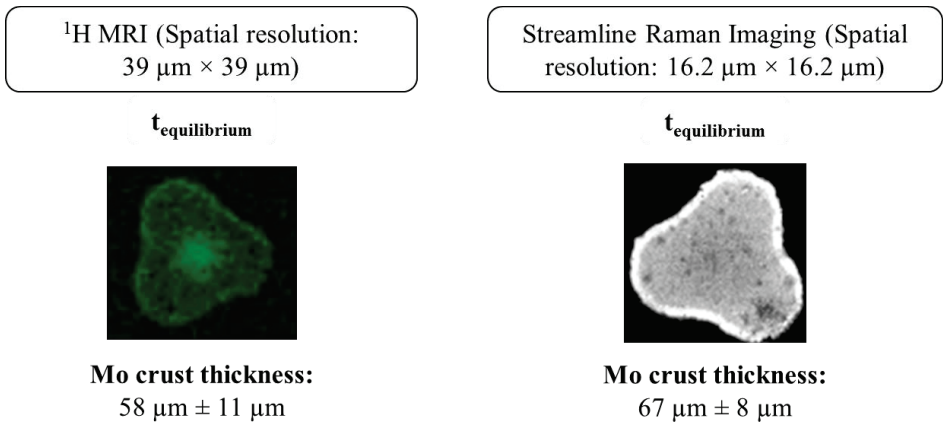

Figure 101 – Comparison between ^1H MRI and Streamline Raman Imaging: images recorded in a γ-alumina support impregnated with 0.8M [Mo] solution with Co:Mo=0.3 at equilibrium. Crust thickness of Mo ions has been measured by Indigo©, which increases resolution of both MRI and Raman image in the orthogonal plane (x, y) to 11 µm x 11 µm and 8 µm x 8 µm, respectively, by means of high quality spline interpolation.

To conclude, MRI and Raman Imaging results demonstrate that:

- **At the beginning of impregnation, information obtained through MRI indicates that Co ions are found near the edges of the support.**
- **As impregnation evolves, MRI images show that the ring near the pellet's core starts to decrease, which corresponds to the progression of Mo and Co ions**
- **At equilibrium, no significant differences are observed. A thickness crust of 58 µm ± 11 µm and 67 µm ± 11 µm is obtained, respectively, for MRI and Raman image, which corresponds to a higher concentration of Mo species. Additionally, a slight lower ^{1}H MRI signal intensity seems to be in an egg-yolk profile, which can correspond to the repartition profile of cobalt ions.**

2.2.2. *Impregnation of γ-alumina with CoMoP solution*

Figure 102 shows the ^{1}H MRI images recorded during the impregnation of γ-alumina with a CoMoP solution. MRI images are similar to the ones concerning impregnation with a CoMo solution. The main difference in relation to Figure 98 is that right after the initial impregnation, a ring with weak ^{1}H signal is observed near the edges. This crust might correspond to the presence of either P or Mo, but also indicates the absence of Co. Moreover, the presence of P induces a faster transport of Mo through the core of the support as a uniform ^{1}H signal distribution is obtained after 8 hours.

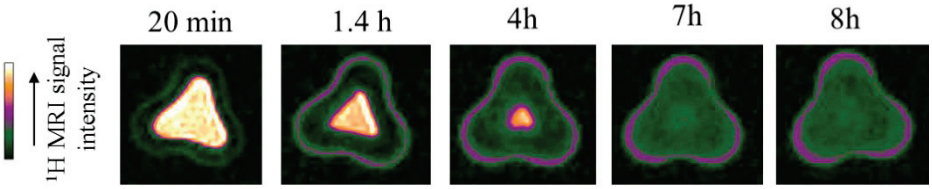

Figure 102 - Monitoring transport of a 0.8 M [Mo] solution with Co:Mo=0.3 molar and P:Mo=0.4 molar within the porosity of a γ-Al_2O_3 pellet: ^{1}H MRI images recorded at several times during impregnation using a spin-echo sequence (FOV=2.5×2.5×8 mm; Resolution= 39×39×100 µm/pixel; Matrix=64×64×8)

In the present case, Raman spectroscopy analyses have been performed at different times of impregnation in order to compare with the MRI images. The hypothesis made for this comparison is that once the pellet is bisected to perform Raman spectroscopy measurements, impregnation finishes, *i.e.*, the transport of the metal ions and/or additive through the porosity ends. The first MRI and Raman spectroscopy measurement do not correspond exactly to the same time. For MRI, the first measurement ends after 17 minutes of impregnation due to sequence acquisition time, while for Raman spectroscopy it is obtained after 5 minutes. These 5 minutes are considered to be representative

of the first point measured during acquisition time of MRI sequence. Indeed, almost 5 minutes are needed to perform impregnation and to prepare the sample in order to start the MRI experiment.

Figure 103 gathers the Raman spectra acquired at different positions along the cross-section of catalyst pellet after 5 minutes of impregnation. Raman bands at 932 cm^{-1} $\nu_s(MoO_{2t})$ and 370 and 395 cm^{-1} $\delta(MoO_{2t})$ are ascribed to the presence of a Strandberg HPA. Besides, the presence of nitrates is once more observed (peak at 1047 cm^{-1}).

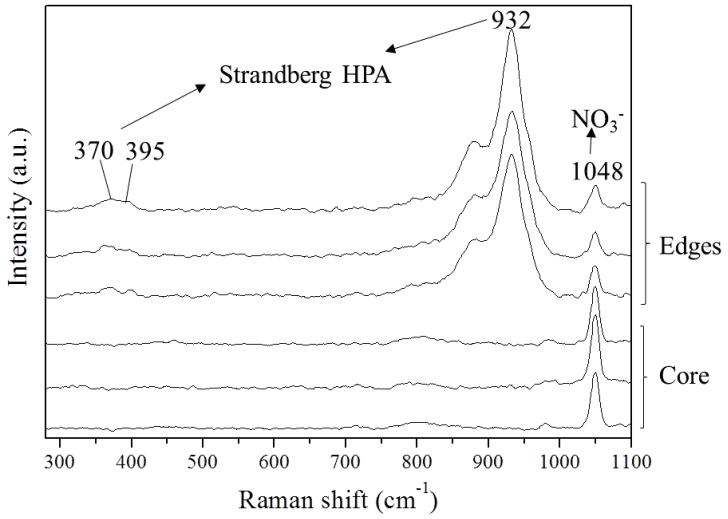

Figure 103 – Streamline Raman spectra recorded on γ-alumina impregnated with 0.8 M [Mo] and Co:Mo=0.3 (molar) and P:Mo=0.4 (molar) right after initial impregnation (≈5 min)

Raman images based on the spectra of Figure 103 are shown in Figure 104. MoO streching vibrations characteristic of Strandberg HPA ($\nu(MoO_{2t})$ at 932 cm^{-1}) yields an egg-shell distribution profile (see Figure 104 (a)). Besides, nitrate ions are observed mainly near the core (see Figure 104 (b)).

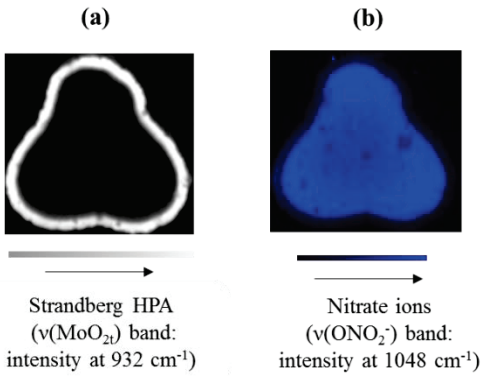

Figure 104 - Streamline Raman images of γ-alumina impregnated with 0.8 M [Mo] with Co:Mo=0.3 molar and P:Mo=0.4 molar obtained after 5 minutes of impregnation with a spatial resolution of 16.2 µm × 16.2 µm (a) repartition of Mo species ($\nu(MoO_{2t})$ at 932 cm^{-1}) (b) repartition of nitrate ions over the pellet ($\nu(ONO^-_2)$ cm^{-1})

Figure 105 shows the comparison between the MRI and Raman images observed at the beginning of impregnation. Almost the same crust thickness near the edges is measured in both images: 68 µm ± 11 µm for MRI image and 72 µm ± 8 µm in Raman image, which is ascribed to the presence of either Mo and/or P. The good coherence concerning the crust thickness proves the validity of the hypotheses made to perform the comparison between the two techniques. Once the pellet is bisected to perform Raman spectroscopy analyses, impregnation finishes and there are no significant differences after 5 or 17 minutes of impregnation, due to the slow transport observed. Therefore, one can conclude that the same thickness obtained by two techniques indicates that Mo and P ions are transported together in the in the form of a HPA in the beginning of impregnation.

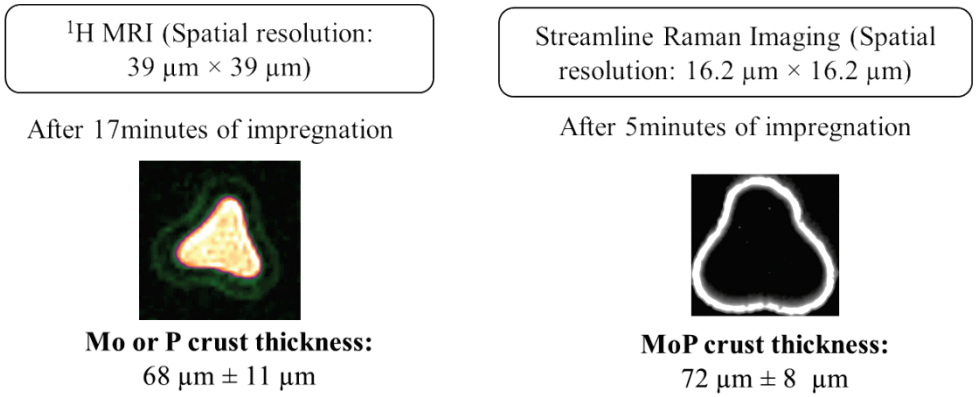

Figure 105 - Comparison between ^{1}H MRI and Streamline Raman Imaging: images recorded in a γ-alumina support impregnated with 0.8M [Mo] solution with Co:Mo=0.3 and P:Mo=0.4 (molar) at initial time of impregnation (after 17 minutes for MRI images and after 5 minutes for Raman cartography image). Crust thickness of MoP ions has been measured by Indigo©.

Figure 106 gathers Raman spectra obtained after 5h of impregnation. A modification of Raman bands is observed comparing to initial stage of impregnation. The broad feature at 939-942 cm^{-1} indicates either the presence of Strandberg HPA (whose bending bonds $\delta(MoO_{2t})$ are observed at 395 and 370 cm^{-1}) or $Mo_7O_{24}^{6-}$ ions. Besides, MoO_4^{2-} ions in electrostatic ($\delta(MoO_{2t})$ at 320 cm^{-1}) and covalent interaction ($\nu(MoO_{2t})$ at 920 cm^{-1}) with support are also observed.

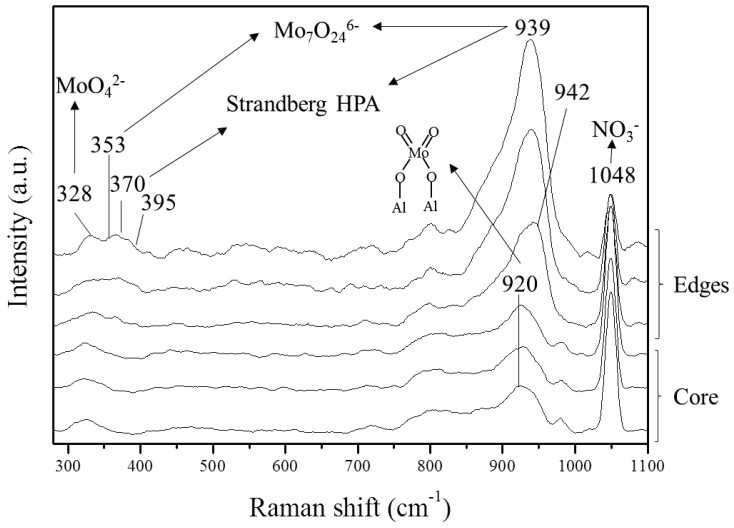

Figure 106 - Streamline Raman spectra recorded on γ-alumina impregnated with 0.8 M [Mo] and Co:Mo=0.3 (molar) and P:Mo=0.4 (molar) right after 5h of impregnation (Spatial resolution: 16.2 µm × 16.2 µm)

Figure 107 (a) shows a higher intensity of MoO stretcheting vibrations $\nu(MoO_{2t})$ at 939 cm^{-1} near the edges, which is ascribed to a higher concentration of either $Mo_7O_{24}^{6-}$ or Strandberg HPA. This result suggests a low local pH, since $Mo_7O_{24}^{6-}$ ions are favoured for pH lower than 6 [3]. Near the core, a higher intensity of MoO bending vibrations $\delta(MoO_{2t})$ at 328 cm^{-1} indicates a higher concentration of MoO_4^{2-} in electrostatic interaction with the support (see Figure 107 (b)). This observation suggests then a higher pH near the core because for pH higher than 8, formation of MoO_4^{2-} takes place [58].

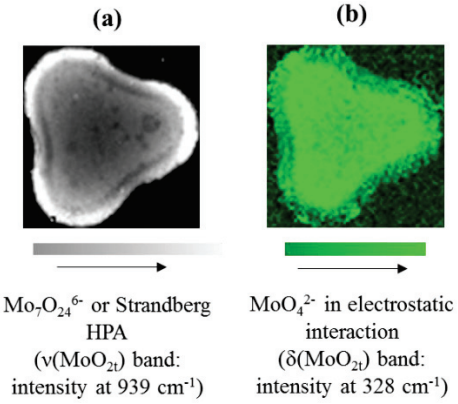

Figure 107 - Streamline Raman images of γ-alumina impregnated with 0.8 M [Mo] with Co:Mo=0.3 molar and P:Mo=0.4 molar obtained after 5h of impregnation with a spatial resolution of 16.2 µm × 16.2 µm (a) repartition of $Mo_7O_{24}^{6-}$ or Strandberg HPA over the pellet ($\nu(MoO_{2t})$ at 939 cm^{-1}) (b) repartition of MoO_4^{2-} over the pellet ($\delta(MoO_{2t})$ at 328 cm^{-1})

After 5 hours of impregnation, no significant changes in the crust thickness observed in both MRI and Raman images are noticed (see Figure 108) comparing to initial time of impregnation. One can conclude that Mo and P ions travel together as impregnation carries on.

Figure 108 - Comparison between ^{1}H MRI and Streamline Raman Imaging: images recorded in a γ-alumina support impregnated with 0.8M [Mo] solution with Co:Mo=0.3 and P:Mo=0.4 (molar) after 5h of impregnation. Crust thickness of MoP ions has been measured by Indigo©.

Raman spectra obtained at equilibrium (see Figure 109) show the presence of $AlMo_6$ (ν(Al-O) at 585 cm^{-1} and ν(MoO_{2t}) 946 cm^{-1}), which has not been observed in the former spectra. Additionally, the bending modes δ(MoO_{2t}) at 395 and 370 cm^{-1} are no longer observed, which indicates the decomposition of Strandberg HPA during impregnation. Mostly $Mo_7O_{24}^{6-}$ ions (ν(MoO_{2t}) at 940 cm^{-1} and δ(MoO_{2t}) at 353 cm^{-1}) and MoO_4^{2-} ions (ν(MoO_{2t})) at 920 cm^{-1} and δ(MoO_{2t})) at 320 cm^{-1}) are observed. In the presence of phosphorus, Raman spectra show a mixture of $HMo_7O_{24}^{5-}$ and $Mo_7O_{24}^{6-}$ (Raman bands corresponding to ν(MoO_{2t}) between 939 and 946 cm^{-1}) and MoO_4^{2-} mostly near the core (higher intensity of ν(MoO_{2t}) at 920 cm^{-1}), contrary to what is observed in Figure 99.

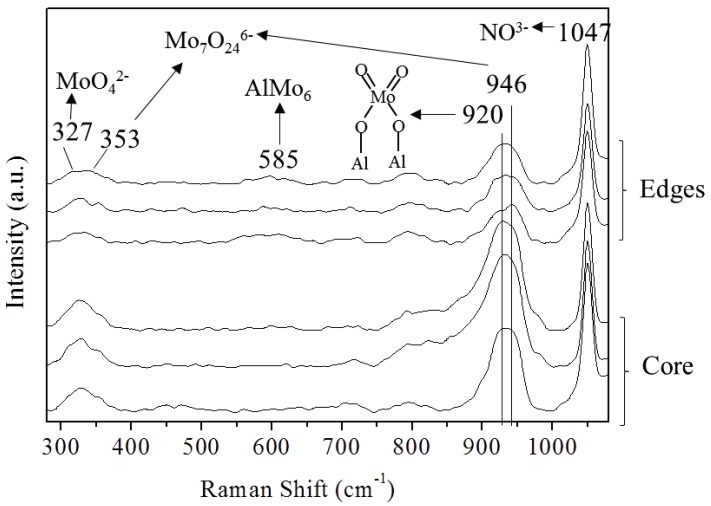

Figure 109 - Streamline Raman spectra recorded on γ-alumina impregnated with 0.8 M [Mo] and Co:Mo=0.3 (molar) and P:Mo=0.4 (molar)right after 5h of impregnation (Spatial resolution: 16.2 µm × 16.2 µm)

A higher intensity of MoO stretching vibrations ν(MoO_{2t}) (maximum of intensity between 920 and 946 cm^{-1}) is observed near the core (Figure 110 (a)). MoO_4^{2-} ions in electrostatic interactions with support are mainly observed near the core as indicated by the higher intensity of MoO bending

vibrations $\delta(MoO_{2t})$ at 327 cm^{-1}, see Figure 110 (b). Besides, a higher intensity of ν(Al-O) at 585 cm^{-1} near the edges is observed, which corresponds to the formation of $AlMo_6$ (see Figure 110 (c)).

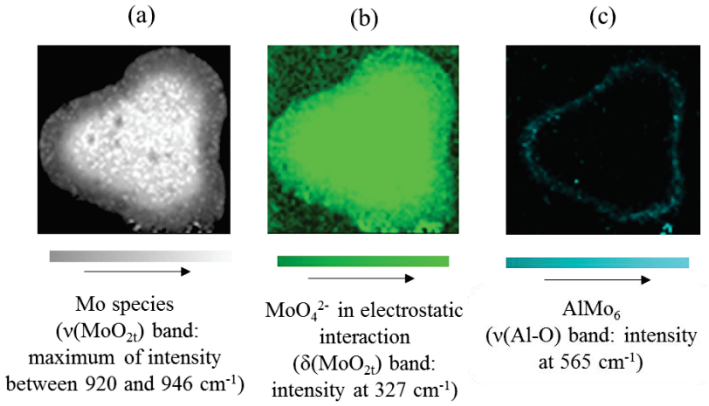

Figure 110 - Streamline Raman images of γ-alumina impregnated with 0.8 M [Mo] with Co:Mo=0.3 molar obtained at equilibrium with a spatial resolution of 16.2 µm × 16.2 µm (a) repartition of Mo-O stretching (corresponding to the large Raman band between 920 and 946 cm^{-1}) (b) repartition of MoO_4^{2-} in electrostatic interaction with Al (intensity at 327 cm^{-1}) (c) repartition of $AlMo_6$ over the pellet (intensity at 585 cm^{-1})

The comparison of the results obtained through the different techniques at equilibrium is shown in Figure 111. ^{1}H MRI results suggest an egg-yolk distribution of Mo ions, which is proved by Raman Imaging. Yet, differences in the Mo yolk thickness are observed. In MRI image is not straightforward to distinguish between Mo and P, which might induce an overestimation of Mo yolk crust.

Figure 111 - Comparison between ^{1}H MRI and Streamline Raman Imaging: images recorded in a γ-alumina support impregnated with 0.8M [Mo] solution with Co:Mo=0.3 at equilibrium. Crust thickness of Mo ions has been measured by Indigo©

To summarize, results obtained above enable the following interpretations:

- **At the beginning of impregnation, almost the same crust thickness is observed by both techniques (68 µm ± 11 µm for MRI image and 72 µm ± 8 µm for Raman cartography image). This crust is ascribed to the presence of both Mo and P ions. Co ions penetrate further in throughout pellet.**
- **After 5h of impregnation, almost the same crust thickness is observed in both ^{1}H MRI and Raman images. A higher concentration of Mo and P ions is found near the edges, even if certain Mo species are already observed towards the core as well Co ions.**
- **At equilibrium, information obtained through two techniques indicate an egg-shell distribution of P, while Mo and Co are found in an egg-yolk profile.**

2.3. Discussion: description of physicochemical phenomena during impregnation of CoMo(P)/γ-Al_2O_3 catalyst

Impregnation of γ-alumina with a CoMo(P) solution has been conducted in diffusional conditions, *i.e.*, without capillary action. For this reason, only diffusion and surface interaction phenomena govern the transport of metal precursors through the support.

In the case of impegnation with a CoMo solution, initially, the impregnation solution contains a mixture of $Mo_7O_{24}^{6-}$ and $H_xMo_7O_{24}^{(6-x)-}$ polyanions, while cobalt ions are in the form of aqua complexes ($[Co(H_2O)_6]^{2+}$).

Upon contact with an acidic solution, the OH surface groups of alumina are either positive ($[(Al_{Td})OH_2]^{+0.75}$ and $[(Al_{Oh})OH_2]^{+0.5}$) or neutral ($[(Al_{Oh})_2OH]$) charged [180,181]. As a result, in the early moments of impregnation, $H_xMo_7O_{24}^{(6-x)-}$ polyanions can be electrostatically retained at the positive OH groups of alumina surface. At the same time, $[Co(H_2O)_6]^{2+}$ complexes are also retained near the edges of the support through interactions with neutral OH groups, as already reported in Chapter III.

As impregnation carries on, the solution pH tends to rise inside the porosity as a result of the buffer effect of γ-alumina. The modification of the acidity of the medium can explain the different Mo speciation in solution and deposited in the support. Part of $H_xMo_7O_{24}^{(6-x)-}$ and $Mo_7O_{24}^{6-}$ give rise to MoO_4^{2-} according to Eq. 56. This last phenomenon has already been observed in impregnation carried out with a Mo solution. Besides, it has been explained that an increase in the pH also changes the nature of the OH sites, leading to negatively charged OH groups ($[(Al_{Oh})OH_2]^{-0.25}$) [180,181].

Therefore, MoO_4^{2-} can interact either in an electrostatic way with the negatively OH groups or be chemically adsorbed in neutral OH groups. At equilibrium, MoO_4^{2-} in electrostatic interaction with surface is uniformly distributed in the entire support. Furthermore, formation of Al-Mo complexes (in this case, $(Al_s)_2MoO_4$) is more important near the edges, as demonstrated by Raman cartography in Figure 100 (b).

The interaction between Co ions and the neutral and deprotonated groups of γ-alumina [96,98,99,103,174] explains the several hours needed to observe Co ions near the core of the pellet. Additionally, a preferential adsorption of Mo ions is indicated, as these species mainly remain near the edges of the pellet, while Co ions travel through the support.

Figure 112 shows different phenomena at interface region between the metal precursors and the support surface.

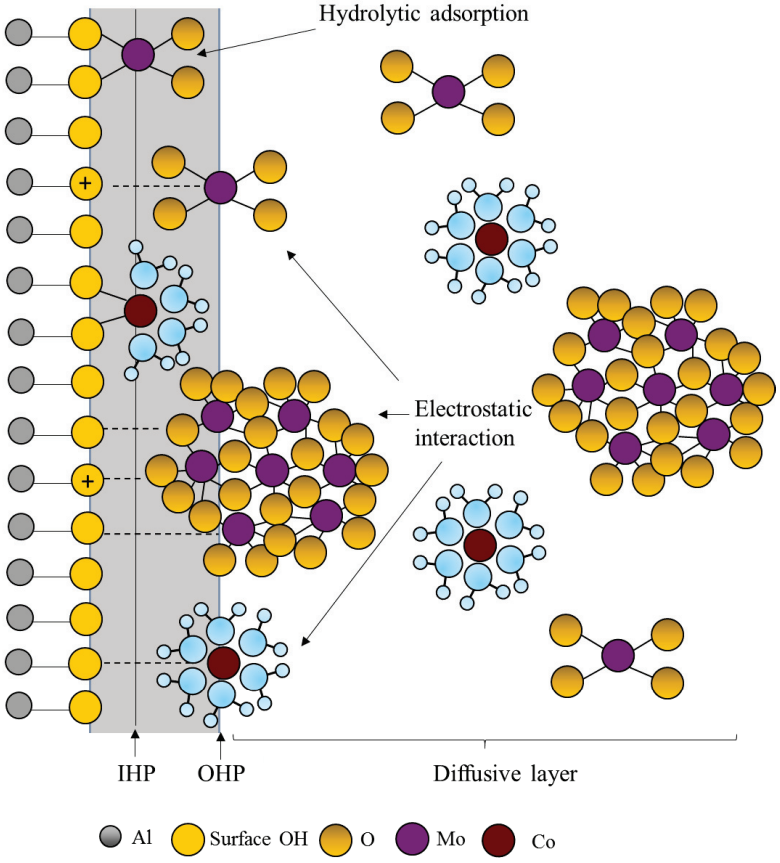

Figure 112 - Schematic picture using Three Layer Model about phenomena that take place in the interface region at equilibrium of impregnation of γ-alumina with 0.8M [Mo] and Co (Co:Mo=0.3 molar) solution: diffusion and surface interaction (electrostatic interaction and hydrolytic adsorption) (adapted from [3,15])

When Co is used as metal promotor, Mo species in covalent interaction with γ-alumina are observed more towards the edges. An egg-shell distribution of Mo species is obtained, while Co ions are in an egg-yolk repartition.

When phosphorus is used a third element in impregnation, Mo and P are in the form of a Strandberg heteropolyanion in the impregnation solution, while cobalt ions remains in the form of $[Co(H_2O)_6]^{2+}$.

At the beginning of impregnation, phosphorus tends to be adsorbed in the OH neutral groups, according to Eq. 58. As already explained, Co^{2+} ions are also expected to react with the same OH neutral groups. The fact that these ions are observed in the core of the pellet in a shorter time when P is added suggests a competitive adsorption between the additive and the metal promotor. One can consider that the available OH adsorption sites near the edges are decreased and so that Co^{2+} ions can progress towards the core of the support. A preferential affinity of γ-alumina to phosphorus rather than to cobalt is highlighted.

Moreover, the interaction between phosphorus and γ-alumina surface through a hydrolytic adsorption mechanism explains why Strandberg HPA is no longer observed in Raman spectra recorded at equilibrium (see Figure 109). The decomposition of this complex has already been observed in the case of impregnation with a MoP solution. Thus, one can conclude that phosphates mainly remain in interaction with γ-alumina near the edges.

Additionally, the formation of $AlMo_6$ is only observed at equilibrium in an egg-shell distribution. Two reasons can explain the presence of this Anderson-type HPA only at the equilibrium stage. First, the presence of P near the edges contributes to a low local pH. And second, the decomposition of Strandberg HPA leads to the formation of $Mo_7O_{24}^{6-}$ according to Eq. 59. These anions are electrostatically retained in protonated OH sites of alumina, which favours the reaction described in Eq. 55.

At equilibrium, there is a higher concentration of Mo species near the core of the pellet as already observed in the case of MoP catalyst (see Figure 93 (a)). Moreover, monomeric Mo species are found in covalent and electrostatic interaction with γ-alumina. As already explained in the previous cases, this fact reflects the buffering effect of alumina. Towards the center of the pellet, polymeric Mo species are transformed into MoO_4^{2-}, which can interact either in an electrostatic or covalent way with γ-alumina. Monomeric Mo in electrostatic interaction are mainly observed towards the core, according to the Raman image at equilibrium (see Figure 110 (b)). It is worth mentioning that almost no Mo species in covalent interactions with support are observed in the case of impregnation with a MoP solution. Unlike the case of MoP/γ-Al_2O_3 catalyst, phosphorus seems to be mainly present near the edges of the support, almost like in an egg-shell profile in the CoMoP/γ-Al_2O_3 catalyst. Therefore, a

small quantity of phosphorus is transported through the core of the pellet. In this way, the quantity of the additive present near the core of the support is not enough to counteract the buffering effect of alumina, leading to an increase in the pH inside the porosity and therefore to the formation of MoO_4^{2-}.

Figure 113 sums up the different surface interaction described above at the interface region for impregnation at equilibrium.

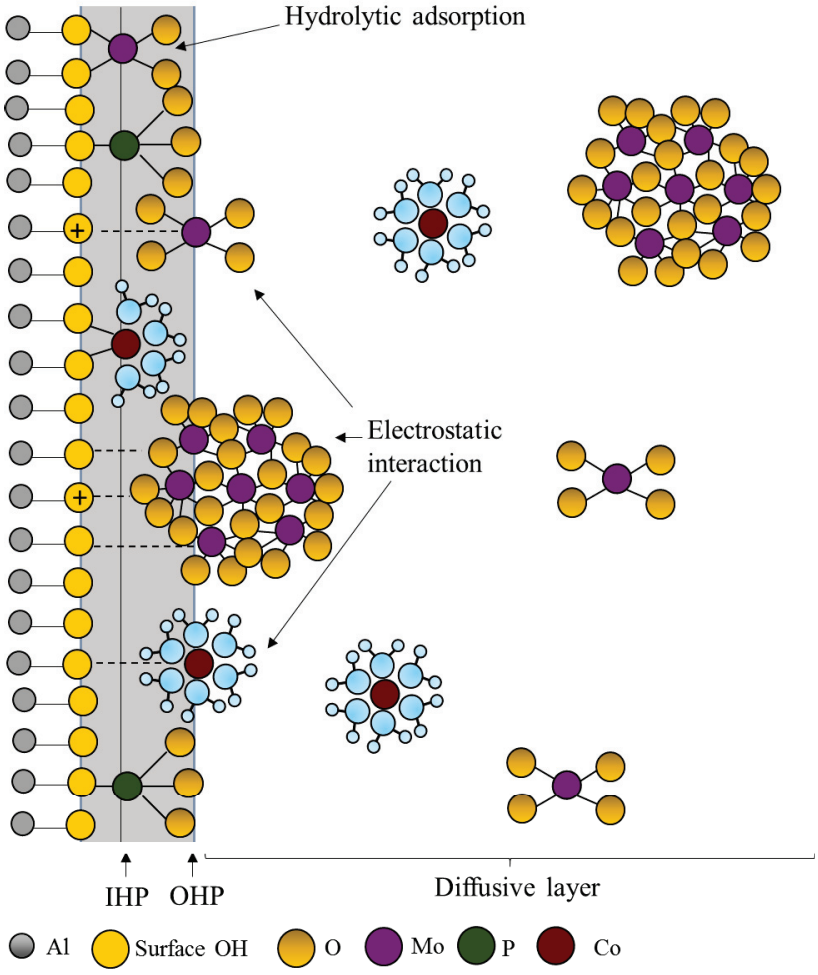

Figure 113 - Schematic picture using Three Layer Model about phenomena that take place in the interface region at equilibrium of impregnation of γ-alumina with 0.8M [Mo] and P (with P:Mo=0.4 molar) and Co (Co:Mo=0.3 molar) solution: diffusion and surface interaction (electrostatic interaction and hydrolytic adsorption) (adapted from [3,15])

In the presence of P, a preferential adsorption to P is observed rather than to Co, which leads to the decomposition of Strandberg HPA during impregnation. and less quantity of Mo species in covalent interactions with γ-alumina are found comparing to CoMo/γ-Al_2O_3 catalyst.

To conclude, Figure 114 shows the comparison between MRI and Raman Imaging results concerning impregnation of CoMo(P)/γ-Al_2O_3 catalyst at equilibrium. Besides, the EPMA distribution profiles obtained after calcination are also shown.

The information obtained through the different techniques is complementary. In the absence of P, the results point out an egg-shell distribution of Mo species, which are either in the form of MoO_4^{2-} or $Mo_7O_{24}^{6-}$. Distribution profiles obtained by EPMA after a calcination step also confirm a more important presence of Mo and Co near the outer surface of the support.

In the presence of phosphorus, a higher quantity of Mo and Co is transported towards the core of the support, while phosphorus remains in an egg-shell profile.

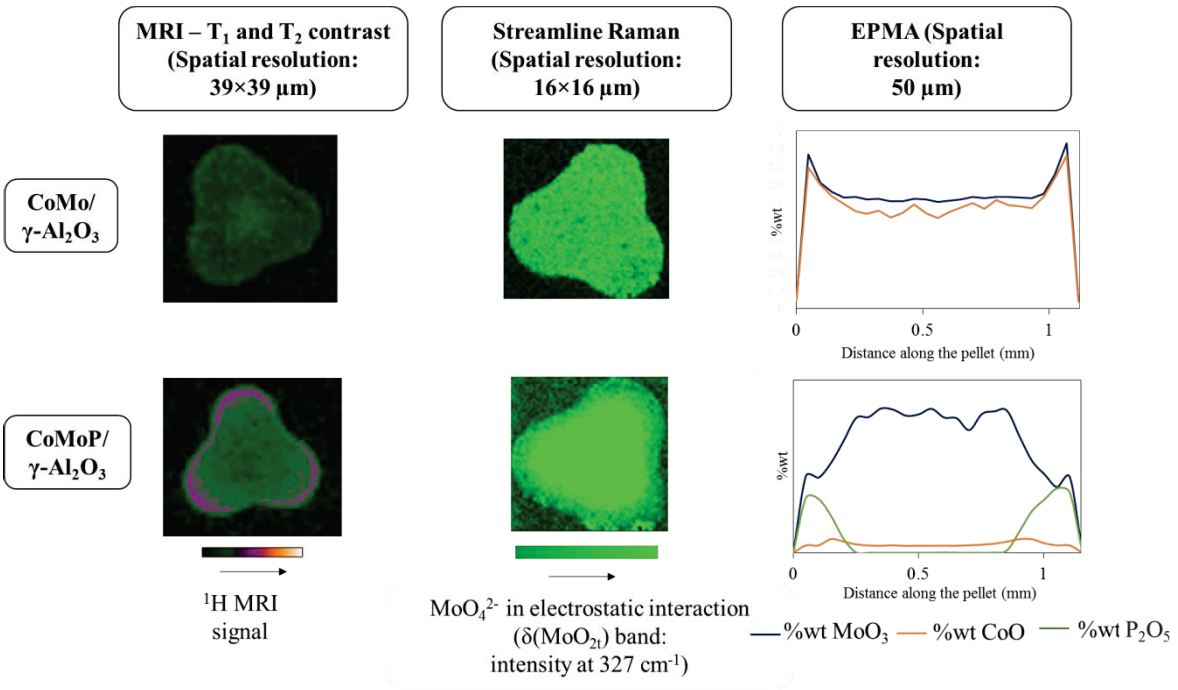

Figure 114 - Comparison MRI, Raman Imaging and EPMA for CoMo(P)/ γ-Al_2O_3 catalysts at equilibrium

These results put in evidence a higher affinity of γ-alumina to phosphorus, which mainly remains at the edges of the pellet. For this reason, decomposition of HPA occurs as impregnation progresses. Besides, the presence of phosphorus contributes to a lower local pH comparing to a CoMo catalyst, which in a certain way can counteract the buffer effect of alumina. For this reason, a less quantity of monomeric Mo species is found in the presence of P. Besides, Co ions are known to react with the neutral and deprotonated OH surface groups, forming inner-sphere complexes that can hinder the diffusion of the metal promotor.

2.4. Conclusion on the influence of the metal promotor nature

Figure 115 shows the comparison concerning impregnation of Co(Ni)Mo/γ-Al_2O_3 catalyst at equilibrium. The differences observed in ^{1}H signal intensity are related with stronger paramagnetic behaviour of Co comparing to Ni. Egg-yolk distributions of Mo species are obtained using either Co or Ni. Moreover, it has been verified by Raman spectroscopy that the nature of the metal promotor does not influence the Mo speciation (study not shown).

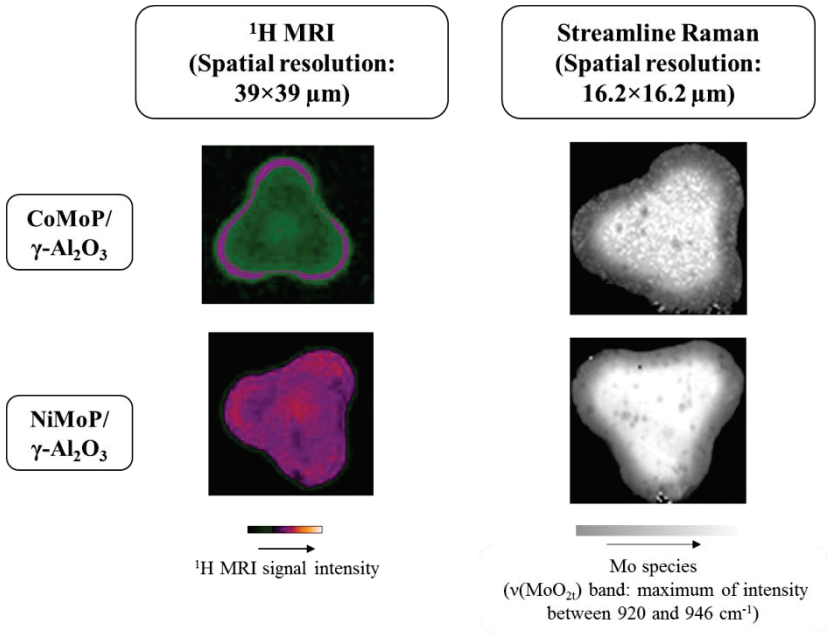

Figure 115 - Comparison between CoMoP and NiMoP cases: comparison MRI, Raman Imaging and EPMA techniques

The nature of the metal promotor does not change the behaviour of impregnation of Mo based catalysts. When P is present, decomposition of Strandberg HPA is observed upon impregnation either in the presence of Ni or Co. Mo species are found mostly near the core, while P remains in an egg-shell profile due to a hydrolytic adsorption mechanism. Indeed, the similarity between Ni and Co impregnation has already been reported in Chapter III.

3. Example of the impact of an organic additive: citric acid

In Chapter III, the effect of citric acid on the impregnation of nickel based catalysts has been studied. To go further in understanding the role of citric acid in impregnation of HDT catalyst, this study has been extended to a classical HDT catalyst (CoMo(P)/γ-Al_2O_3).

Firstly, the effect of citric acid (CA) on a Mo based catalyst has been evaluated through MRI and Raman Imaging techniques. For reasons of clarity of the manuscript this study is not shown. To summarize, impregnation solutions have been prepared by co-impregnation. Impregnation step has been carried out according to standard impregnation method (method A). Two different molar ratios CA:Mo in solution have been tested in order to investigate a possible complexation of Mo by citrate in order to form $Mo_4(Cit)_2O_{11}^{4-}$ complex. Therefore, CA:Mo ratio is varied between 0.2 (below stoichiometric ratio of CA to Mo) to 1 (above stoichiometric ratio of CA to Mo). As conclusion, ^{1}H MRI images suggest that uniform profiles are obtained for impregnation with Mo-citric acid solutions, regardless the CA:Mo ratio used. The main difference concerns the transport rate, which can be explained based on the Mo speciation. For CA:Mo equal to 1, Mo-citrate complex is deposited in the support, which results in electrostatic interactions with the surface. For CA:Mo equal to 0.2, a preferential adsorption to citrate ions than to polymeric/monomeric Mo ions seems to occur.

Secondly, the same MRI-Raman Imaging methodology has been applied in the presence of cobalt and phosphorus. To help in the interpretations, the impact of citric acid has been first evaluated in the case of a CoMo/γ-Al_2O_3 catalyst. Once again, for reasons of clarity of the manuscript this study is not presented. To summarize, ^{1}H MRI images suggest that citrate ions remain in an egg-shell profile, while Mo and Co ions are found near the core. Moreover, Raman spectroscopy shows the decomposition of Mo-citrate complex upon contact with the support. A preferential adsorption to the organic additive on the γ-alumina surface in relation to either Mo or Co ions is highlighted. Finally, the impact of CA:Mo ratio in the impregnation of CoMoP/γ-Al_2O_3 catalyst has been evaluated. Different ratios above and below the stoichometric one required to form $Mo_4(Cit)_2O_{11}^{4-}$ complex have been tested. Impregnation has been carried out in diffusional conditions (method B). Only the example concerning CA:Mo molar ratio of 0.7 in the impregnation solution is shown in the following paragraphs.

3.1. Characterization of CoMo(P)-CA impregnation solution by Raman spectroscopy

Impregnation solution with a concentration of 0.8M [Mo] in the presence of Co (Co:Mo equal to 0.3 molar), P (P:Mo equal to 0.4 molar) and CA (CA:Mo equal to 0.7 molar) has been prepared. Solution pH is lower than 1.3. Further information is given in Table 8 in Chapter II in section 1.1.2 page 69.

Figure 116 shows the Raman spectrum obtained for the impregnation solution. The vibration modes $\nu_s(MoO_{2t})$ at 944, 903 and 861 cm^{-1} and $\delta(MoO_{2t})$ at 343, 375 and 383 cm^{-1} are ascribed to a $Mo_4(Cit)_2O_{11}^{4-}$ complex. Besides, the vibration modes ν_sCOO^- (1408 cm^{-1}) and νCOOH (1720 cm^{-1}) result from the presence of citrate.

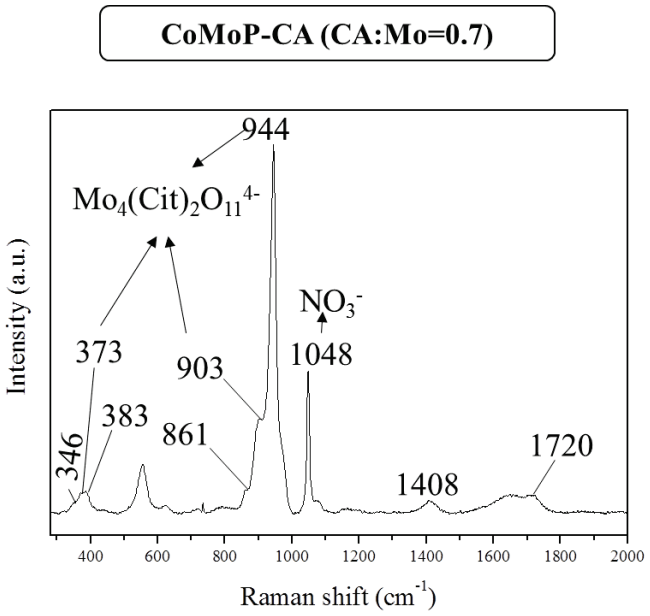

Figure 116 - Raman spectra for 0.8M [Mo] with Co:Mo=0.3 (molar) and P:Mo=0.4 (molar) and CA:Mo=0.7 (molar) solution at a pH lower than 1.3

3.2. Monitoring the impregnation of γ-alumina with CoMoP-CA solution: MRI and Raman Imaging characterizations

Figure 117 shows the ^1H MRI images recorded during impregnation of γ-Al_2O_3 with a CoMoP-CA solution (CA:Mo of 0.7 molar). The low ^1H signal intensity observed near the core suggests the presence of mainly cobalt ions. Almost after one hour of impregnation, this front of low ^1H signal achieves the pellet's core, which suggests a faster transport of Co^{2+} ions than in the previous cases. Besides that, a crust with a higher ^1H signal intensity near the edges is maintained through the impregnation process, which is attributed to the presence of either citrate, phosphorus or a Mo complex.

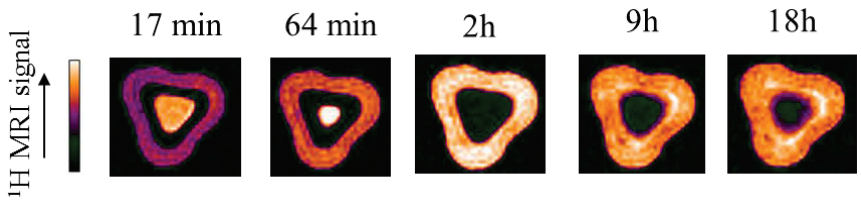

Figure 117 - Transport of a 0.8 M [Mo] with Co:Mo=0.3 and and P:Mo=0.4 molar and CA:Mo=0.7 molar solution within the porosity of a γ-Al_2O_3 pellet by a spin-echo sequence (FOV=2.5×2.5×8mm; Spatial resolution: 39 × 39 × 125 µm/pixel; Matrix=64×64×8)

Figure 118 shows the Raman spectra acquired in the bisected catalyst after 5 minutes of impregnation. The vibration modes ν(MoO_{2t}) at 944, 901 and 861 cm^{-1} are characteristic of $Mo_4(Cit)_2O_{11}^{4-}$ complex [4]. The bending modes δ(MoO_{2t}) are observed at 390, 378 and 340 cm^{-1}. Besides, ν(MoO_{2t}) at 956 cm^{-1} is also observe. One can conclude that a mixture of $Mo_4(Cit)_2O_{11}^{4-}$ and $H_2Mo_7O_{24}^{4-}$. Presence of citrate is ascribed by ν(COO^-) at 1410 cm^{-1}.

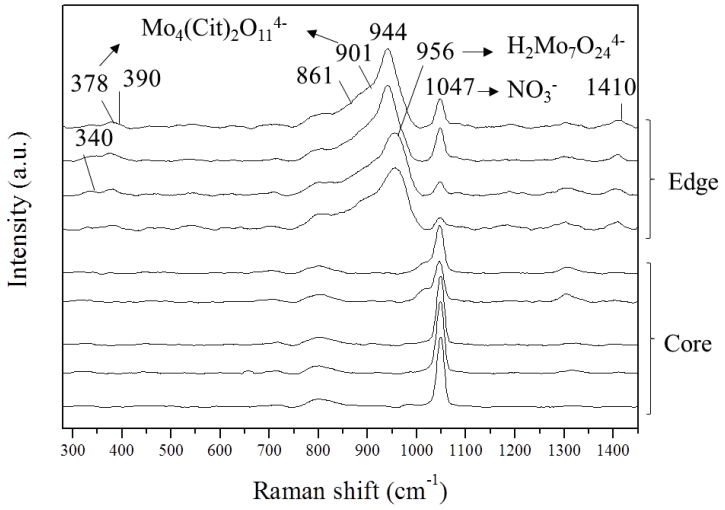

Figure 118 – Streamline Raman spectra were recorded on γ-alumina impregnated with 0.8 M [Mo] and Co:Mo=0.3 (molar) and CA:Mo=0.7 and P:Mo=0.4 molar after 5min of impregnation (Spatial resolution: 16.2 µm × 16.2 µm)

As already observed for the latter cases, right after the initial impregnation an egg-shell distribution of both Mo species (see Figure 119 (a)) and citrate (see Figure 119 (b)) is observed according to Raman images.

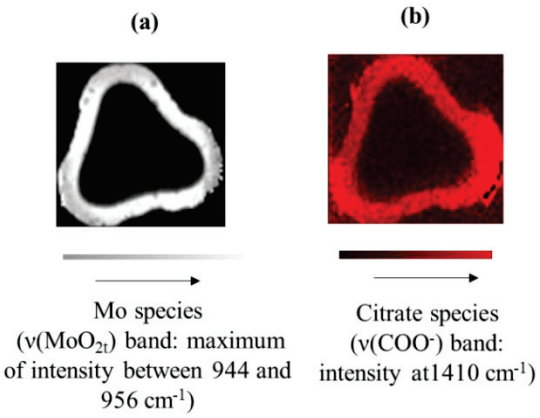

Figure 119 - Streamline Raman images of γ-alumina impregnated with 0.8 M [Mo] with Co:Mo=0.3 molar, P/Mo=0.4, CA:Mo=0.7 molar obtained at equilibrium with a spatial resolution of 16.2 µm × 16.2 µm (a) repartition of MoO stretches (corresponding 943-953 cm^{-1}) (b) repartition of citrate over the pellet (intensity at 1410 cm^{-1})

Figure 120 gathered the Raman spectra obtained after 5 hours of impregnation. Due to the large Raman bands observed, it is not straightforward to identify the different Mo-species. The broad feature between 935 and 950 cm^{-1} can be ascribed to either $H_xP_2Mo_5O_{23}^{(6-x)-}$ or different protonated forms of polymolydbates ($H_xMo_7O_{24}^{(6-x)-}$). Mo-citrate complex, which is observed in the first instants of impregnation is no longer present as indicated by the shift of the main Raman band ($\nu_s(MoO_{2t})$) to higher wavenumber values. Raman band at 1410 cm^{-1} ($\nu_s(COO)$), which is characteristic of citrate is once again observed.

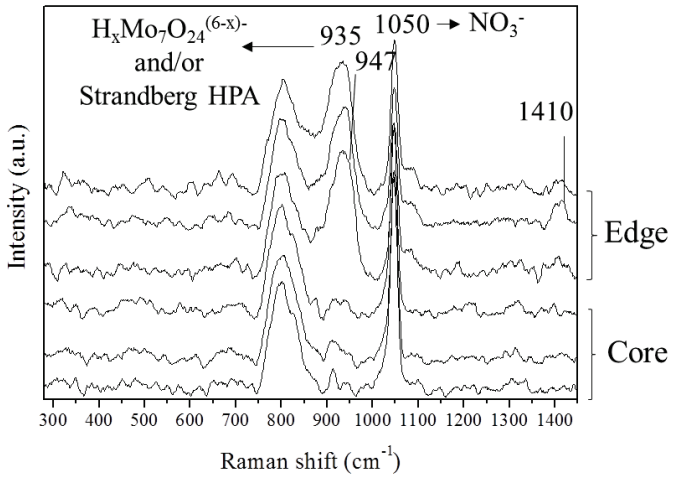

Figure 120 - Streamline Raman spectra were recorded on γ-alumina impregnated with 0.8 M [Mo] and Co:Mo=0.3 (molar) and CA:Mo=0.7 and P:Mo=0.4 molar after 5h of impregnation

A Raman image has been obtained concerning the MoO strething vibrations (maximum of intensity between 935 and 960 cm^{-1}, see Figure 121 (a)). Results demonstrate that no Mo-species are present in the core of the support. Citrate is also found near the edges (see Figure 121 (b)). One can remark that

these observations are in good agreement with MRI image obtained for the same time of impregnation (see Figure 117): the high ^{1}H signal near the edges indicates the presence of either Mo(P) and/or citrate, while near the core the absence of ^{1}H signal suggests a local high concentration of Co.

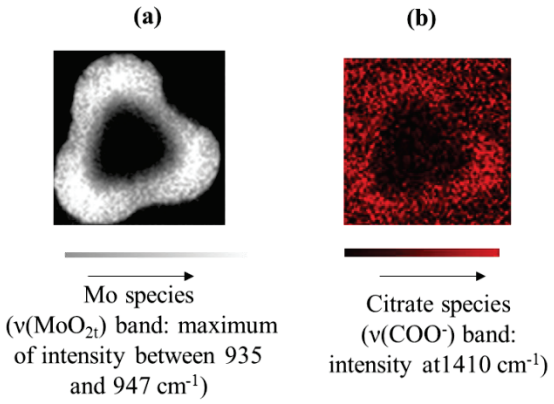

Figure 121 - Streamline Raman images of γ-alumina impregnated with 0.8 M [Mo] with Co:Mo=0.3 molar, P/Mo=0.4, CA:Mo=0.7 molar obtained after 5h of impregnation with a spatial resolution of 16.2 µm × 16.2 µm (a) repartition of MoO stretches (corresponding 935-960 cm^{-1}) (b) repartition of citrate over the pellet (intensity at 1410 cm^{-1})

At the equilibrium state, the Raman band observed at 971 cm^{-1} indicates the formation of $H_2PMo_{11}CoO_{40}^{5-}$. Once again, a mixture of $H_xP_2Mo_5O_{23}^{(6-x)-}$ and $H_xMo_7O_{24}^{(6-x)-}$ can be ascribed due to the large Raman band between 932 and 955 cm^{-1}. Raman band at 1410 cm^{-1} ($\nu_s(COO)$) is once again observed.

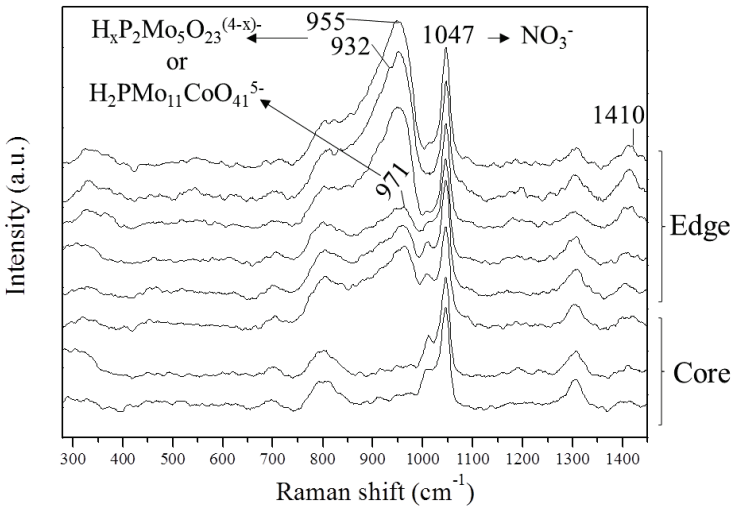

Figure 122 – Streamline Raman spectra were recorded on γ-alumina impregnated with 0.8 M [Mo] and Co:Mo=0.3 (molar) and CA:Mo=0.7 and P:Mo=0.4 molar at equilibrium (Spatial resolution: 16.2 µm × 16.2 µm)

Raman cartography shows that the intensity of 932 cm^{-1} is more intensity near the edges, while the intensity at 971 cm^{-1} is more intense towards the core (see Figure 123 (a) and (b)). One can conclude that the formation of $H_2PMo_{11}CoO_{40}^{5-}$ takes place towards the core, while Strandberg HPA is mainly near the edges. Citrate is still in an egg-shell distribution (see Figure 123 (c)).

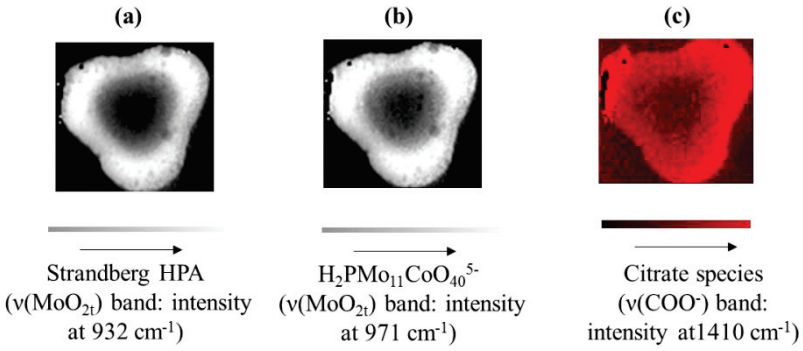

Figure 123 - Streamline Raman images of γ-alumina impregnated with 0.8 M [Mo] with Co:Mo=0.3 molar, P/Mo=0.4, CA:Mo=0.7 molar obtained at equilibrium with a spatial resolution of 16.2 µm × 16.2 µm (a) repartition of Stranbderg HPA (intensity at 932 cm^{-1}) (b) repartition of $H_2PMo_{11}CoO_{40}^{5-}$ (intensity at 971 cm^{-1}) (c) repartition of citrate over the pellet (intensity at 1410 cm^{-1})

To sum up, the following interpretations can be made according to MRI and Raman Imaging results:

- **At the beginning of impregnation, the MRI image show a crust near the edges, which is also observed in Raman Streamline images. This crust can be assigned to the presence both citrate, Mo and P near the edges of support. Additionally, as for the CoMoP case, the fact that ^1H signal is visualized in this crust indicates the absence of Co ions.**
- **After almost 2h of impregnation, Mo(P) ions and citrate are still in an egg-shell distribution. Concerning Co, MRI images indicates an egg-yolk distribution of cobalt aqua complexes. After this time, no significant differences are observed as impregnation evolves.**

3.3. Discussion: description of physicochemical phenomena during impregnation of CoMoP-CA/γ-Al_2O_3 catalyst

Impregnation solution CoMoP-CA contain a Mo-citrate complex. Upon impregnation, support surface is mainly positively charged as solution pH is lower than PZC of γ-alumina.

Right after initial impregnation a mixture of Mo-citrate complex and $H_2Mo_7O_{24}^{4-}$ is initially deposited on the catalyst. As impregnation evolves, an evolution of Mo speciation also occurs. At equilibrium, Mo-species are present has either $H_xP_2Mo_5O_{23}^{(6-x)-}$ or different protonated forms of polymolydbates ($H_xMo_7O_{24}^{(6-x)-}$). The formation of an $H_2PMo_{11}CoO_{40}^{5-}$ is also suggested.

The decomposition of Mo-citrate complex present in initial stages of impregnation highlights two different facts. On one hand, there is a strong affinity of citrate to alumina. On the other hand, a possible competitive adsorption between phosphorus and citrate on alumina surface is observed.

To understand this phenomenon, surface OH groups of alumina (which is considered equal to 11.8 OH/nm^2 at 573K [176]) and total amount of citric acid and phosphorus should be evaluated. The density in citric acid molecules in the final catalyst is approximately of 2.3 CA molecules/nm^2, while the density of phosphorus atoms is 0.2 P atoms/nm^2. As already explained, citrate and phosphorus are known to react in the same type of OH surface groups of alumina support. Therefore, the larger excess of citrate used has apparently prevented the adsorption of P near the edges of the support. A higher affinity of alumina to citrate rather than to phosphorus is then highlighted. Consequently, the ratio of P:Mo is high enough to prevent the decomposition of Strandberg HPA. Moreover, the citrate can also contribute to counterbalance the buffering effect of alumina, which also contributes to the stabilization of Strandberg HPA.

At equilibrium,the formation of $H_2PMo_{11}CoO_{40}^{5-}$ is observed more towards the core. This behaviour had already been observed by Bergwerff et al. [144], who proposed an explanation based on a concentration gradient of P through the catalyst pellet. Indeed, towards the core of the support there is less quantity of citrate, which favours the adsorption of phosphorus. Consequently, decomposition of Strandberg HPA occurs has P:Mo is not high enough to stabilize the HPA, allowing the formation of $H_2PMo_{11}CoO_{40}^{5-}$.

In Figure 124, an illustration concerning the different interactions that can take place at the interface between impregnation solution and surface of alumina for the case of CA:Mo=0.7 is presented. Only the Strandberg HPA and polymolydbates are considered, since it is the formation of $H_2PMo_{11}CoO_{40}^{5-}$ is not fully understood.

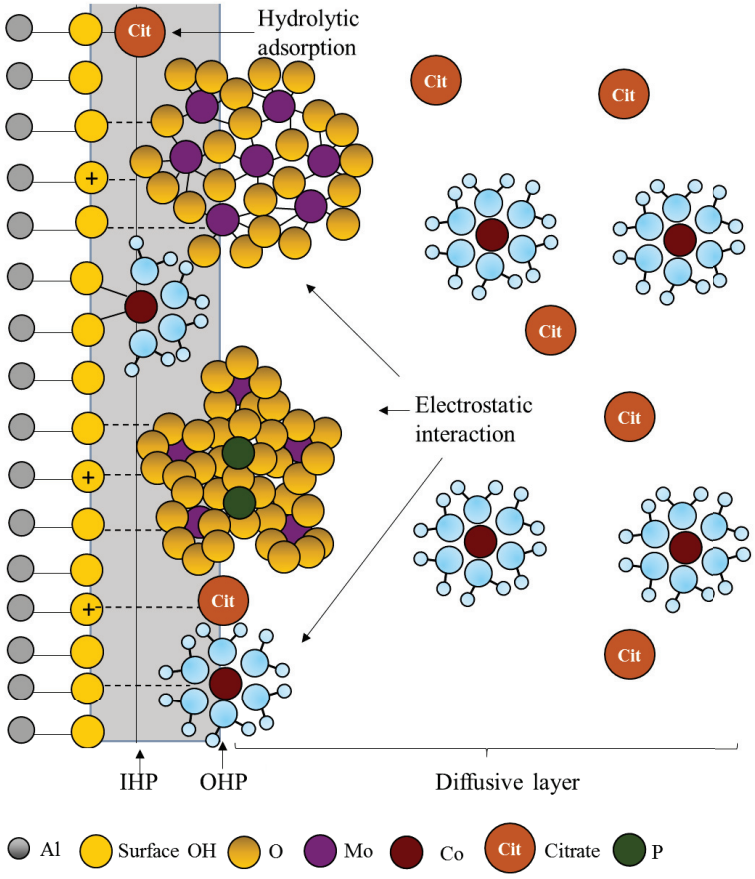

Figure 124 - Schematic picture using Three Layer Model about phenomena that take place in the interface region at equilibrium of impregnation of γ-alumina with 0.8M [Mo], P (P:Mo=0.4), Co (Co:Mo=0.3 molar) and CA (with CA:Mo=0.7 molar) solution: diffusion and surface interaction (electrostatic interaction) (adapted from [3,15])

3.4. Conclusion of the impact of an organic additive

The effect of citrate strongly depends on CA:Mo ratio used in the impregnation solution. For CA:Mo ratio of 0.2 (below the stoichiometric one), both MRI and Raman Imaging suggests a higher concentration of Mo-species near the core of the support at the end of the impregnation (see Figure 125). One may conclude that citrate and phosphorus remains at the edges of the catalyst body as a result of strong chemical interactions with the support. Moreover, Raman Imaging allows one to identify either $H_xMo_7O_{24}^{6-}$ or MoO_4^{2-} in electrostatic interaction with the support. No evidences of a CoMo-citrate complexes are observed. One can consider that the metal promotor ions remain in the form of $Co[H_2O]_6^{2+}$ that can interact with the support.

On the contrary, for CA:Mo ratio of 0.7 (higher than stoichiometric one), both characterization techniques show a small quantity of Mo-complexes in the core of the support ((see Figure 125). This fact suggests then an egg-yolk distribution of Co^{2+} ions as illustrated in MRI images. Besides,

molybdenum is found in the form of a $H_xP_2Mo_5O_{23}^{(6-x)-}$ or $H_2PMo_{11}CoO_{40}^{5-}$ or even protonated polymolydbates.

Apparently, the presence of citrate in the impregnation of a CoMoP catalyst contributes to enhance the promoting effect of Co, as a close interaction between metal promotor and Mo is observed. Apparently, Mo ions are more likely to be in an egg-shell distribution either or not in interaction with P (depending on CA:Mo ratio).

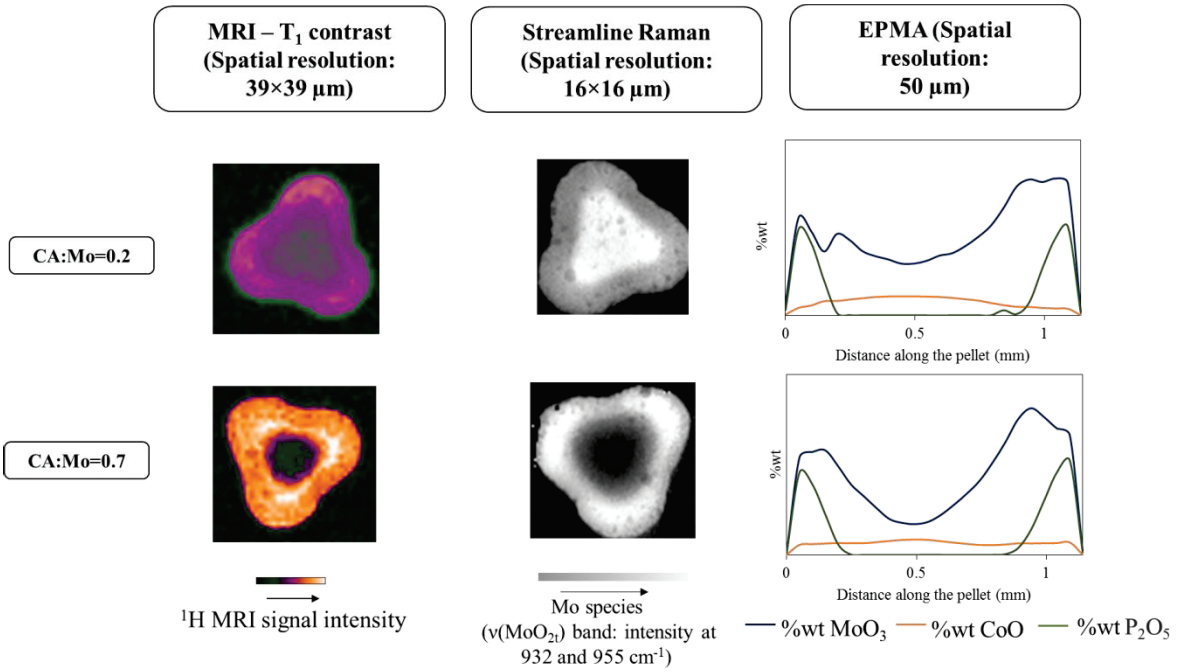

Figure 125 - Comparison MRI, Raman Imaging and EPMA for CoMoP-AC case: different CA:Mo ratios in impregnation solution were used. Time 16h is considered as the equilibrium state.

4. Conclusion

In previous studies concerning the impregnation step of hydrotreatment catalysts, Raman spectroscopy has been predominantly performed. Besides, UV-Visible, IR and electron probe microanalysis are often applied as complementary techniques. One of the drawbacks of these methods is that catalysts must be bisected before measurements, which may result in a modification of the equilibrium of impregnation. For this reason, non-invasive techniques, which the best spatial resolution and low acquisition times are required to study the preparation of heterogeneous catalysts.

This study demonstrates the high potential of Magnetic Resonance Imaging as a new tool to monitor *in-situ* the impregnation step of multimetallic catalysts, such as real hydrotreatment catalysts. MRI not only gives information about spatial distribution of all metal precursors inside the catalyst support, but also suggests different interactions between each precursor and the support. Moreover, the application of Raman Imaging provides information about the nature of Mo species and their location.

Impregnation of γ-alumina with a Mo solution is governed by a competition between diffusion and an interaction with the OH surface groups of γ-alumina. Moreover, different Mo-complexes are deposited in the support body. A higher concentration of $Mo_7O_{24}^{6-}$ and $AlMo_6$ is found near the edges, while MoO_4^{2-} in covalent interaction with alumina is predominantly observed near the core. In the presence of phosphorus, a Strandberg heteropolyanion is formed in impregnation solution, whose decomposition occurs upon impregnation. Moreover, almost no Mo species in covalent interaction with the support are observed in the presence of P.

When Co is added to a Mo solution, a higher concentration of Mo-complexes in covalent interaction with the support is found near the edges. A simultaneous transport of cobalt and Mo ions is observed. This effect is not verified in the presence of P. The additive contributes to a low pH, which in some way delays the formation of Mo in covalent interaction with the support, contributing to a faster transport of Mo ions. Indeed, Mo species are found near the core of the support after 7h of impregnation when P is present and 11h after impregnation in the absence of P. A favoured adsorption of phosphorus in relation to Mo or Co ions is clearly observed. Therefore, impregnation of a CoMoP catalysts results in an egg-yolk profiles of Mo, an egg-yolk or egg-white profile of Co and an egg-shell profile of P. An identical behaviour is observed when nickel is used as metal promotor.

When the impregnation of a CoMoP/γ-Al_2O_3 is carried out in the presence of citrate, the effect of the organic additive strongly depends on CA:Mo ratio used in impregnation solution. Mo ions are in an egg-shell distribution either or not in interaction with P for a CA:Mo molar ratio of 0.2. Co ions can be in the form of aqua complexes in an egg-yolk distribution or in the form of $H_2PMo_{11}CoO_{41}^{5-}$ HPA, for

a CA:Mo ratio of 0.7. This last observation can indeed improve the proximity between Mo and Co ions. No evidences of a CoMo-citrate complexes are observed at the equilibrium state of impregnation.

This approach allows one to obtain *in-situ* information about the distribution of different elements within the catalyst pellet, but also to obtain information about metal speciation at the end of impregnation. These information contribute to further understand the interactions between different precursors and support that can hinder diffusion process during impregnation. Therefore, this approach enables a better control of the impregnation step and therefore of the distribution profile of active phase, which has an impact on the catalytic performance.

Chapter V - Rationalization of the impregnation step

In this chapter, a mathematical model to rationalize the impregnation step and to identify the most important descriptors that influence the final metal distribution profile is put forward. This impregnation model takes into account different physicochemical phenomena that occur during this step: capillarity, diffusion and surface interaction (adsorption). Additionally, this model is sensitive to the solution properties (presence of an organic additive) and the impregnation method (dry or diffusional impregnation).

The MRI experiments present in Chapter III concerning the impregnation of monometallic (nickel) solutions eventually in the presence of citric acid are used to validate this model. A brief summary of these experimental results is given in the following paragraphs.

First, the impact of the metal ion concentration on the impregnation step has been studied. Different nickel solutions concentrations (0.05 to 0.30 M, which corresponds to a metal weight percent (wt% Ni) of 0.25 up to 1.39 in the final nickel-based catalysts) with pH ranging from 5 to 6 have been prepared. According to these results, transport of nickel ions within γ-alumina depends on different phenomena: capillarity, diffusion and surface interaction. One can assume that capillarity is an instantaneous process and therefore is not the limiting step of impregnation. The estimated diffusion coefficient of the order of magnitude of 10^{-13} m^2/s suggests a competition between diffusion and adsorption. A mechanism of hydrolytic adsorption between nickel aqua complexes in solution ($[Ni(H_2O)_6]^{2+}$) and the neutral OH surface sites is proposed. Moreover, a selective affinity of nickel ions for the γ-alumina OH sites depending on their nucleophilic character has been suggested.

When impregnation of nickel catalysts is carried out in the presence of citric acid in acidic conditions (pH lower than 2.4), adsorption of citrate limits in a high extent the interaction between nickel ions and the OH surface sites. A competitive adsorption mechanism has been suggested, since adsorption of citrate and nickel ions takes place on the same OH surface sites.

1. Modeling of the impregnation step

The impregnation model developed in the current work has been done in collaboration with J.-M. SCHWEITZER from IFPEn (Process Design and Modeling Division).

1.1. Physicochemical phenomena

This impregnation model takes into account different physicochemical phenomena: **capillarity, bulk diffusion, surface diffusion and surface interaction (adsorption)**, as schematized in Figure 126. Capillarity is characterized by the penetration rate of liquid ($\vec{v}$), diffusion in the fluid phase (bulk diffusion) is characterized by the effective diffusion coefficient (D_e), surface diffusion is described by the surface diffusion coefficient (D_s) and adsorption is characterized by the reaction kinetic constant (k).

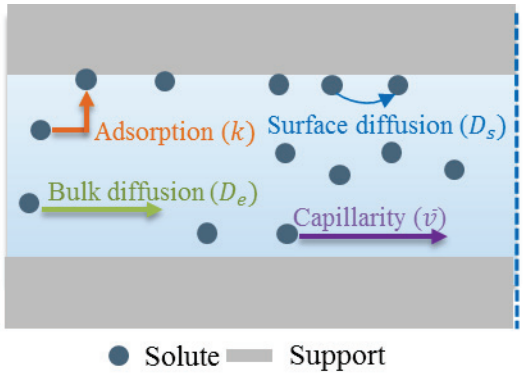

Figure 126 – Schematic representation of physicochemical phenomena taken into account by the model

1.1.1. *Capillary suction model*

Upon dry impregnation, the replacement of the fluid inside the pore space by impregnation solution takes place through the action of capillary forces.

The evolution of the distance travelled by the liquid into the pore (z) as a function of time (t) depends on three different forces:

- Capillary force, $\vec{F}_{capillary}$,
- Friction force , $\vec{F}_{friction}$,
- Gravity force, $\vec{P}$, which is negligible compared to the first ones [188].

To obtain z(t), the Washburn model [189] is widely used in the literature. A detailed description of how to obtain z(t) based on this model is given in Annex C. The Washburn model is valid for low Reynolds number ($Re < 1$) and viscous fluid. It is also assumed that the flow of the impregnation

solution in the pore is characterized by Poiseuille's law. Therefore, the small inertia effects are neglected. According to the Washburn model, the following momentum balances can be written:

$$\frac{d(m.\vec{v})}{dt} = \vec{F}_{capillary} + \vec{F}_{friction} = 0 \quad \textbf{Eq. 61}$$

$$2 \cdot \pi \cdot R_{pore} \cdot \gamma \cdot cos\theta - 8 \cdot \pi \cdot \mu \cdot z.\bar{v} = 0 \quad \textbf{Eq. 62}$$

Where, m corresponds to mass (kg), $\bar{v}$ is the average flow velocity (m.s^{-1}) , t stands for time (s), R_{pore} is the pore radius (m), γ is the interfacial tension, θ is the wetting angle (^{o}) and μ is the dynamic viscosity of the fluid (Pa.s).

All calculations made and assuming that $z(t = 0) = 0$, the distance z (m) that the impregnation solution travels into the pore is given by:

$$z = \sqrt{\frac{R_{pore} \cdot \gamma \cdot cos\theta}{2 \cdot \mu} \cdot t} \quad \textbf{Eq. 63}$$

The capillary flow of water is simulated using Eq. 63 and the result is shown in Figure 127. One can observe that after 5 seconds, water is already present in the entire porosity, which is in good agreement with the literature [77].

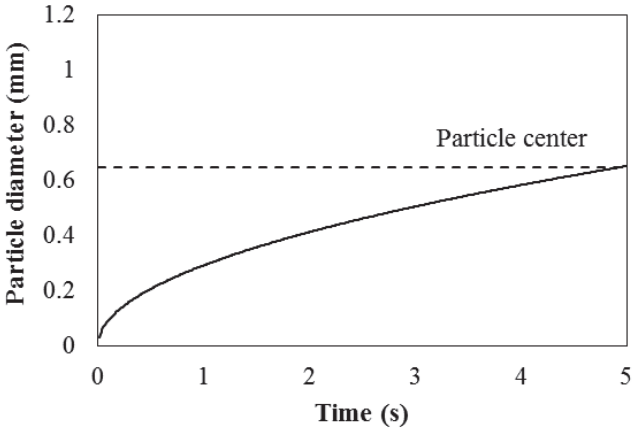

Figure 127 – Evolution of advancing front of water calculated thanks by Eq. 63

1.1.2. *Transport by diffusion*

Mass transport by diffusion is described by Fick's law, which has been described in detail in Chapter I, section 2.2.2.2, page 30. Fick's First Law is defined in Eq. 19 (page 31). In this equation, the diffusion coefficient D corresponds to the effective diffusion coefficient D_e, which takes into account the structure and geometry of the porous network.

Besides the diffusion of the metal ions in the fluid phase, surface diffusion might also be considered. The latter is responsible for the transport of the adsorbed molecules through the adsorbed layer on the solid surface [84] and is characterized by a surface diffusion coefficient, D_s.

1.1.3. *Surface interaction: adsorption phenomenon*

It is assumed that the adsorption of the nickel aqua complexes, $[Ni(H_2O)_6]^{2+}$ takes place via two OH surface sites through an irreversible reaction. This reaction can be written as follows (see Eq. 64).

$$Ni^{2+} + 2 * \overset{k_1}{\rightarrow} Ni *_2 \qquad \textbf{Eq. 64}$$

Where * represents the active site (in this case, an OH group), Ni* represents the adsorbed nickel molecule and k_1 is the kinetic constant.

The reaction rate is then given by the following equation.

$$r_1 = k_1[Ni^{2+}][q_*]^2$$
$$r_1 = k_1\left[C_{Ni}^p\right][q_t - C_{Ni}^*]^2 \qquad \textbf{Eq. 65}$$

Where r_1 is the reaction kinetic rate ($mol.kg^{-1}.s^{-1}$), k_1 is the reaction kinetic constant ($m^3.mol^{-1}.s^{-1}$), C_{Ni}^p is the nickel ions concentration ($mol.m^{-3}$) in the fluid phase, q_* is the concentration of active sites ($mol.kg^{-1}$), q_t is the total concentration of the active sites ($mol.kg^{-1}$) and C_{Ni}^* is the concentration of nickel in the adsorbed phase ($mol.kg^{-1}$).

When the impregnation solution contains two different elements (in this case, citric acid and nickel), a competitive adsorption is considered. The following reaction is assumed to take place between citrate (Cit^{3-}) and the active site (*), see Eq. 66.

$$Cit^{3-} + * \overset{k_2}{\rightarrow} Cit * \qquad \textbf{Eq. 66}$$

The reaction rate is then given by the following equation.

$$r_2 = k_2[Cit^{3-}][q_*]$$
$$r_2 = k_2\left[C_{Cit}^p\right][q_t - C_{Cit}^*] \qquad \textbf{Eq. 67}$$

Where r_2 is the reaction kinetic rate ($mol.kg^{-1}.s^{-1}$), k_2 is the reaction kinetic constant ($m^3.mol^{-1}.s^{-1}$), $[Cit^{3-}]$ is the citrate ions concentration ($mol.kg^{-1}$) in the fluid phase, q_* is the concentration of occupied active sites, q_t is the total concentration of active sites ($mol.kg^{-1}$) and C_i^* is the concentration of nickel in the adsorbed phase ($mol.kg^{-1}$). The selectivity of this reaction is then proportional to k_2/k_1.

1.2. Model hypothesis

The hypothesis adopted to solve the model are the following:

- Incompressible, continuous, Newtonian and viscous fluid
- Catalyst with a cylindrical geometry instead of a trilobe shape so as to simply the equations resolution
- Time-dependent capillary flow
- Radial concentration gradients inside the pellet (no axial concentration gradients)
- Fickian diffusion, which means a constant diffusion coefficient
- First order irreversible adsorption
- Only one type of nickel species is considered, namely nickel ions in the form of aqua complex, $[Ni(H_2O)_6]^{2+}$
- Only one type of citrate species is considered, namely citrate ions totally deprotonated, Cit^{3-}
- Adsorption of $[Ni(H_2O)_6]^{2+}$ complexes takes place via two OH surface groups
- Adsorption of Cit^{3-} complexes takes place via one OH surface group

1.3. Material balance

In the context of **dry impregnation**, during the contact time between the solution and the support (corresponding to approximately 30 seconds in the present case), the impregnation solution penetrates the porous support by the action of capillary forces. This stage is called the capillary stage. Simultaneously to this convective flow, diffusion of the solution at the interface and adsorption of the solute by the pore walls should also be taken into consideration. Once the support is removed from the solution, it is considered that the catalyst particle is completed wetted. From this step, which is called the diffusion-adsorption stage, the transport of solute is only done by diffusion (bulk and surface diffusion), while adsorption of the solute occurs simultaneously.

In the case of **diffusional impregnation**, no capillary action takes place, since the support is pre-saturated with water before impregnation. Therefore, transport of the metal ions results only from a diffusion phenomenon (bulk diffusion and surface diffusion). Adsorption occurs simultaneously with solute transport.

In the following paragraphs, the mass balances along the crossed section area of a cylindrical catalyst particle are given.

a. Mass balance for compounds in the fluid phase

$$\varepsilon \cdot \frac{\partial C_i^p}{\partial t} = \frac{D_{eff}}{r} \cdot \frac{\partial}{\partial r}\left(r \cdot \frac{\partial C_i^p}{\partial r}\right) + \frac{\varepsilon}{r} \cdot \frac{\partial}{\partial r}\left(r \cdot \bar{v} \cdot C_i^p\right) + \sum_j \mu_{ij} \cdot r_{ki} \cdot \rho_s \qquad \textbf{Eq. 68}$$

Where,

$\varepsilon \cdot \frac{\partial C_i^p}{\partial t}$ corresponds to the accumulation term, in which ε_p is the porosity, C_i^p is the concentration of element i in the fluid phase inside the pore and t is time;

$\frac{D_{eff}}{r} \cdot \frac{\partial}{\partial r}\left(r \cdot \frac{\partial C_i^p}{\partial r}\right)$ corresponds to the diffusive term, in D_{eff} is the effective diffusion coefficient and r is the radius;

$\frac{\varepsilon}{r} \cdot \frac{\partial}{\partial r}\left(r \cdot \bar{v} \cdot C_i^p\right)$ corresponds to the convective flow, in which $\bar{v}$ (penetration rate of the liquid) is obtained through the Washburn model,

$\sum_j \mu_{ij} \cdot r_{ki} \cdot \rho_s$ corresponds to the kinetic term, in which μ_{ij} is the stoichiometric coefficient i for a given element j, r_{ki} is the kinetic rate for reaction i and ρ_s is the catalyst solid density.

b. **Mass balance for compounds in the adsorbed phase**

In this material balance, the effective diffusion coefficient is replace by the surface diffusion coefficient (D_s).

$$\frac{\partial C_i^*}{\partial t} = \frac{D_s}{r} \cdot \frac{\partial}{\partial r}\left(r \cdot \frac{\partial C_i^*}{\partial r}\right) + \sum_j \mu_{ij} \cdot r_{kin} \cdot \rho_s \qquad \textbf{Eq. 69}$$

Where, C_i^* is the concentration of element i in the adsorbed phase.

To sum up, in the case of dry impregnation three material balances are needed: the global material balance to take into account the capillary action (shown by Eq. 61), the one concerning the transport of compounds in the fluid phase (represented by Eq. 68) and the one concerning the transport of compounds on the solid surface (see Eq. 69). In the case of diffusional impregnation, no capillary action takes place and therefore the material balances concern Eq. 68, in which the term of capillarity is neglected and Eq. 69. The variables of the model are then C_i^p (r,t) and C_i^* (r,t).

1.4. Initial and boundary conditions

To solve the material balances in Eq. 61, Eq. 68 and Eq. 69 , the following initial conditions are considered:

$$t = 0: \begin{cases} z = 0 \\ C_i^* = 0 \\ C_i^p = 0 \end{cases} \forall\, r$$

With the following boundary conditions as follows:

$$\left.\frac{\partial C_i^p}{\partial r}\right|_{r=0} = 0, \forall\, t$$

$$\left.\frac{\partial C_i^s}{\partial r}\right|_{r=0} = 0, \forall\, t$$

$$Capillary\ stage: \left. C_i^p \right|_{r=R} = C_i^b, \forall\, t$$

$$Diffusion\ stage: \left. C_i^p \right|_{r>R} = 0, \forall t$$

Where, C_i^b is the concentration of element i the impregnation solution.

2. Model implementation and validation based on MRI experiments

Material balances have been solved using an iso-concentration discretization model. An iso-concentration is a group of cells from the grid, having the same concentration and comprised in the catalyst physical boundaries. Simulations have been made over impregnation time in order to simulate the MRI experiments. The time of each simulation corresponds to time at which MRI image is acquired.

2.1. Model parameters

The support used is a γ-alumina support, whose textural properties have been characterized by mercury porosimetry and nitrogen adsorption-desorption methods (see Table 9, page 70 in Chapter II). The tortuosity (τ) value is taken from the literature [190], where the tortuosity of a support with identical characteristics of the one in the present study has been determined by PFG-NMR technique applied to toluene inside the porosity. Yet, this parameter can also be optimized.

The impregnation solution properties in terms of surface tension (γ) and viscosity (μ) are considered similar with those of water, since nickel diluted solutions are used. The water properties are also taken from the literature [191].

The molecular diffusion coefficient of nickel ions (D_{Ni}) is taken from the literature [173]. Concerning surface diffusion coefficient ($D_{Ni^*,s}$), the estimation done in Chapter III (section 2.1.1.1, page 108) based on MRI results is used as an initial approach (value of 10^{-13} m^2/s).

Concerning the kinetic constant (k), no information has been found in the literature. Therefore, this parameter has been optimized to fit with MRI results.

In Chapter III, the density of the adsorption sites, which corresponds to the OH surface groups has been pointed out as a crucial parameter that influences the final metal distribution profile. For the γ-alumina support used, the OH density surface coverage is approximately 11.8 OH/nm^2, according to Digne's model [176]. Yet, MRI results suggest that there is a selective affinity for different OH groups, which means that concentration of OH adsorption sites cannot be estimated accurately from the literature. Hence, this parameter must be estimated in order to fit with MRI results.

Table 15 gathers the initial adopted parameters. Surface diffusion coefficient ($D_{Ni^*,s}$), kinetic constant rate (k_1) and the total concentration of adsorption sites (q_t) are then estimated.

Table 15 – Model parameters

Parameter	Value
d (m)	0.0012
L (m)	0.0045
D_{pore} (m)	9.4×10^{-9}
ε	0.65
ρ_s (kg/m^3)	2580
γ	72×10^{-2} [191]
μ	1×10^{-3} [191]
θ	1.05 [191]
D_{Ni} (m^2/s)	10^{-10} [173]
D_{H2O} (m^2/s)	10^{-9} [170]
$D_{Ni^{*},s}$ (m^2/s)	10^{-13} **(can be optimized)**
τ	1.7 [190] **(can be optimized)**
k_i (m^3/(kg.s)	**To estimate**
μ_{Ni}	1
μ_{OH}	2
q_t (mol/kg)	**To estimate**

2.2. Parameter estimation

The MRI experimental results give qualitative information concerning the distribution profiles of each compound present in the impregnation solution. Therefore, the parameter estimation is based on the comparison between the trends of the ions distribution profiles evolution observed in MRI images and the ones obtained through the impregnation model.

Moreover, in Table 15, the kinetic reaction constant is defined as a parameter to estimate. Indeed, it has been shown that it takes less than 5 seconds for the water flow reaches the center of the pellet during the capillary stage. Therefore, the fact that Ni ions are not transported together with this capillary flow can be explained by a fast and almost instantaneous adsorption reaction. For this reason, a value of 1 m^3/(kg.s) is assumed.

The parameter estimation has been done as follows:

a. The case of dry impregnation of γ-Al_2O_3 with 0.05M [Ni^{2+}] solution (corresponding to 0.09 Ni atoms/nm^2 in the final catalyst) is used to find the optimal value of the surface diffusion coefficient ($D_{Ni^*,s}$).

Simulations have first been made using the parameters in Table 15 and modifying both the kinetic constant and concentration of adsorption sites (OH groups). Figure 128 shows that considering a surface diffusion coefficient of 10^{-13} m^2/s, an egg-shell distribution of nickel ions is obtained after 17h, which is in good agreement with the MRI experiments.

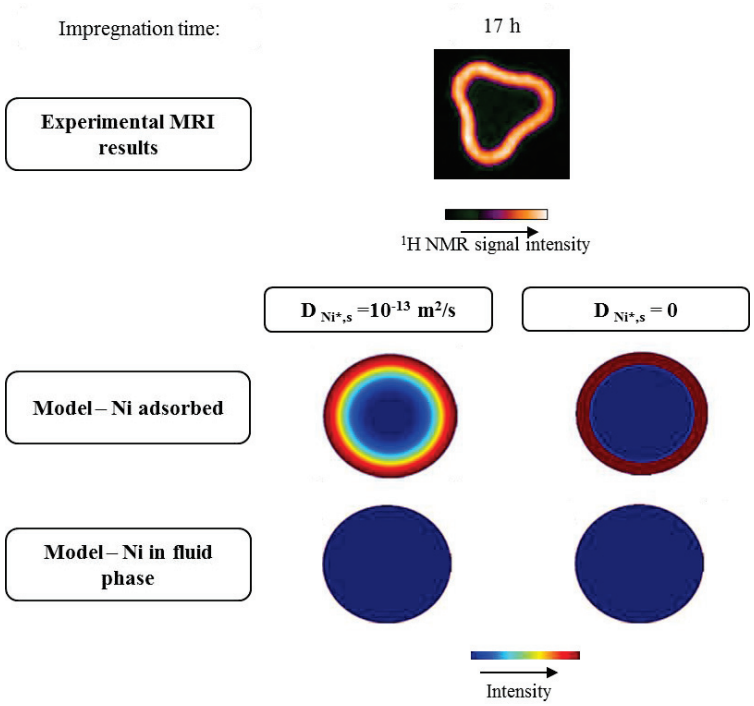

Figure 128 – Simulation of dry impregnation (case of 0.05M [Ni^{2+}]/γ-Al_2O_3), k=1 $m^3/(kg.s)$, q_t=0.21 mol/kg and modifying $D_{Ni^*,s}=10^{-13}$ m^2/s and $D_{Ni^*,s}=0$

b. The case of dry impregnation of γ-Al_2O_3 with 0.1M [Ni^{2+}] solution (corresponding to 0.19 Ni atoms/nm^2 in the final catalyst) at the equilibrium state is used to find the optimal value of the total concentration of the adsorption sites (q_t).

First, the same parameters used in the last case have been tested using a 0.1M [Ni^{2+}] solution. Yet, Figure 129 shows that considering a concentration of adsorption sites of 0.21 mol/kg (corresponding to a surface density of 0.48 OH groups/nm^2), an egg-shell distribution of nickel ions is obtained. Thus, to fit with MRI experimental results, an optimal value of 0.16 mol/kg (corresponding to a surface density 0.36 OH groups/nm^2) has been found. These simulations show that the concentration of adsorption sites is as a key parameter that influences the competition between diffusion and adsorption.

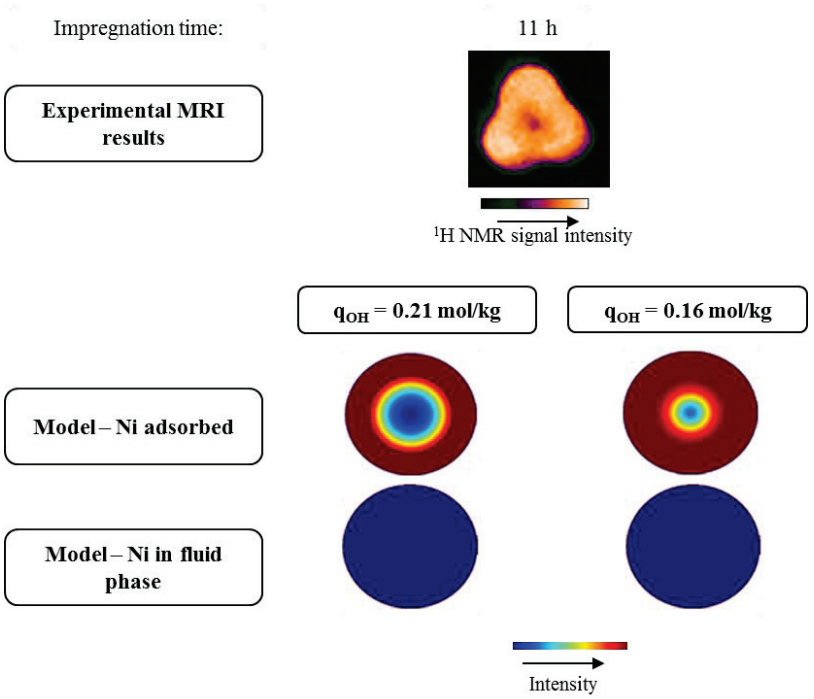

Figure 129 - Simulation of dry impregnation (case of 0.1M $[Ni^{2+}]/\gamma\text{-}Al_2O_3$), k=1 $m^3/(kg.s)$, $D_{Ni^*,s}=10^{-13}$ m^2/s and modifying q_t=0.21 mol/kg and 0.16 mol/kg

Additionally, in the previous figure, one can observe a slight difference in the final nickel adsorbed distribution profile (considering a q_t=0.16 $mol.kg^{-1}$) and the MRI image. Different MRI experiments have been done several times in order to validate the final metal profiles obtained by measuring the average thickness profile. Figure 130 shows that differences between 0.1 mm to 0.2 mm at the equilibrium point are obtained, which remains in agreement with the nickel adsorbed distribution profile obtained through the impregnation model.

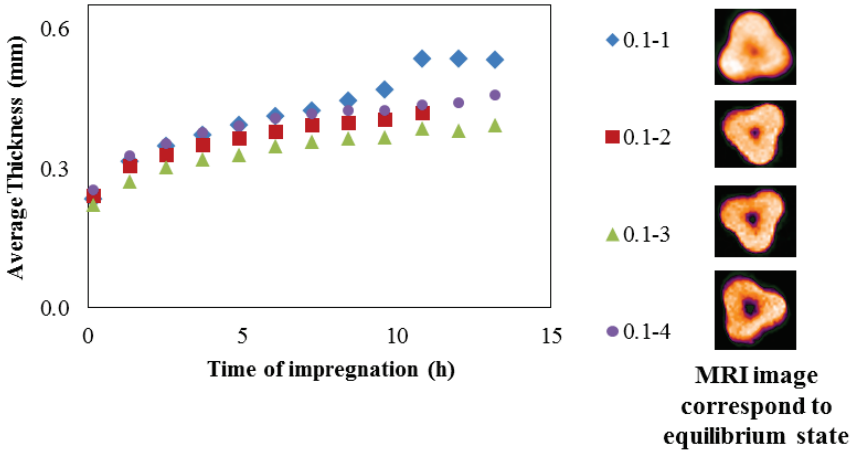

Figure 130 - Repeatability of the MRI experiments concerning dry impregnation of $\gamma\text{-}Al_2O_3$ with 0.1M $[Ni^{2+}]$ solution

These differences in the distribution profiles observed by MRI can be explained as follows:

- Differences in the contact time between support and the impregnation solution during the preparation step, which induces a variation in the nickel concentration introduced.
- Differences in the alumina pellets. For instance, the tortuosity value can even change from one pellet to another.
- Image processing done by Paravision 5.1 software induces modifications of the intensities of the images. Indeed, Paravision 5.1 carries out an individual intensity scaling of each image in a same experiment and between different experiments. Moreover, this software also induces smoothing and artifacts in the observed images.

c. The tortuosity (τ) value has been optimized taking into account one of the intermediate states of dry impregnation with a 0.1M [Ni^{2+}] solution (corresponding to 1.4h after initial impregnation).

In dry impregnation, once the support is withdrawn from the solution, only diffusion contributes to the transport of nickel ions towards the core of the support. This depends on the effective diffusion coefficient and hence, on the tortuosity and porosity of the support. Since the porosity has been determined experimentally, only the tortuosity value has been optimized taking into account the intermediate state of dry impregnation with a 0.1M [Ni^{2+}] solution. Figure 131 shows that the tortuosity value is another key parameter that strongly affects the distribution profile. An optimal value of 2.9 is found, which is in good agreement with the literature [169,190,192].

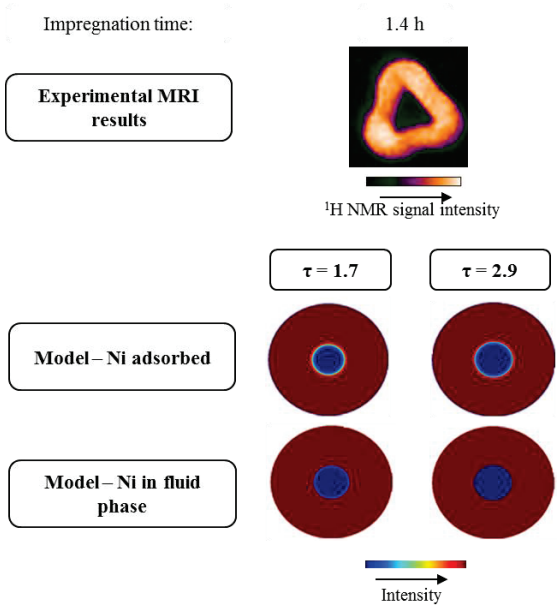

Figure 131 - Simulation of dry impregnation (case of 0.1M [Ni]/γ-Al_2O_3) with $D_{Ni^*,s}=10^{-13}$ m^2/s, k=1 $m^3/(kg.s)$, q_t =0.16 mol/kg and modifying the τ values: 1.7 and 2.9

d. The optimal values found to $D_{Ni^*,s}$, k, q_t and τ have been then verified in the case of dry impregnation with a 0.05M [Ni^{2+}] solution.

Figure 132 shows a good agreement between MRI results and model simulations. Both show an egg-shell distribution of nickel ions in the adsorbed phase and there is no remaining nickel ions in the fluid phase.

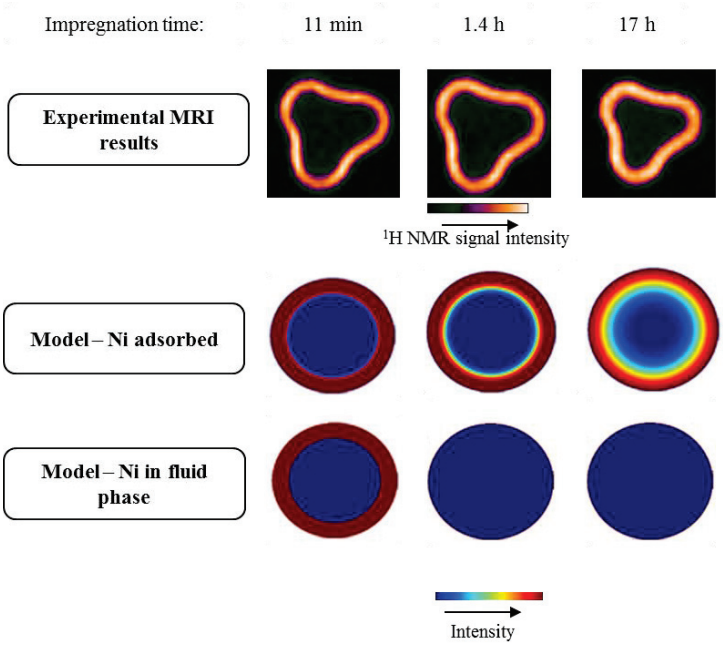

Figure 132 - Simulation of dry impregnation diffusional impregnation (case of 0.05M [Ni]/γ-Al_2O_3) with $D_{Ni^*,s}=10^{-13}$ m^2/s, k=1 $m^3/(kg.s)$, τ=2.9, k=1 $m^3/(kg.s)$, q_t =0.16 mol/kg

To conclude, Table 16 gathers the optimal parameters found to fit with MRI results.

Table 16 – Parameter estimation: optimal values

Parameter	Value
$D_{Ni^*,s}$ (m^2/s)	10^{-13}
τ	2.9
k_i ($m^3/(kg.s)$)	1
q_t (mol/kg)	0.16 (0.36 OH groups/nm^2)

2.3. Validation of the model

The parameters gathered in Table 16 are used to validate the model concerning impregnation of γ-Al_2O_3 with 0.2M [Ni^{2+}] either in dry or diffusional impregnation. For the last case, no capillary action occurs as already discussed. The results are shown in Figure 133 and Figure 134.

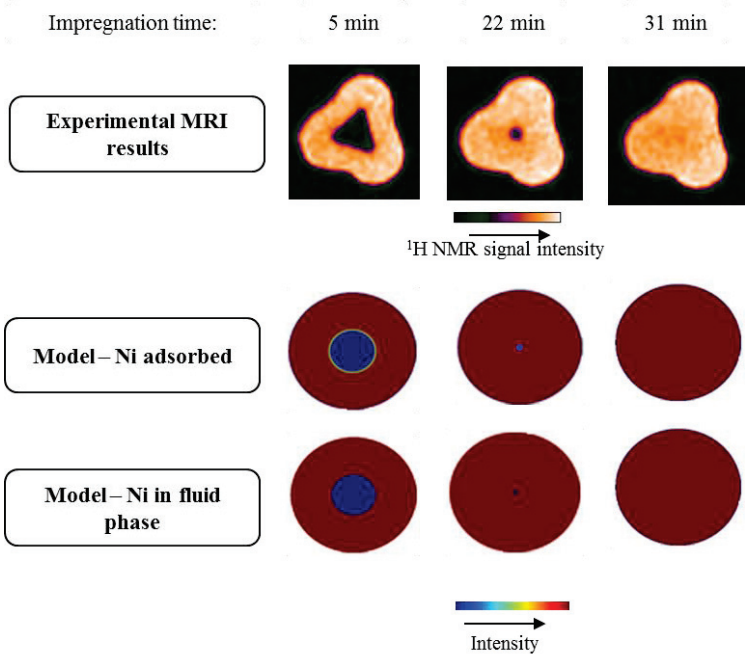

Figure 133 – Model validation: dry impregnation 0.2M [Ni]/γ-Al_2O_3

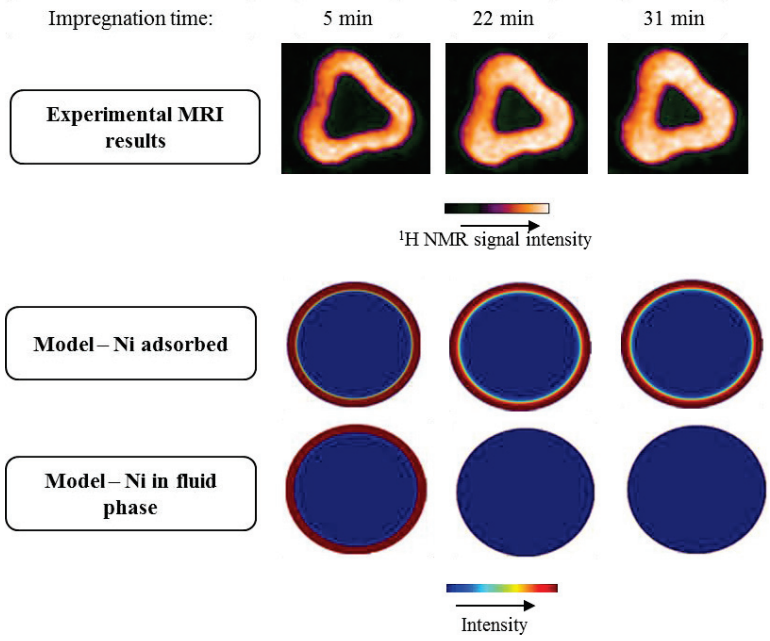

Figure 134 - Model validation: diffusional impregnation 0.2M [Ni^{2+}]/γ-Al_2O_3

The evolution of nickel distribution profile shows the same trend both in the MRI experimental results and in the results of the simulations, which proves the validity of the hypothesis made to solve the model and the optimal parameters found to fit with MRI results.

3. Example of modeling the impregnation of Ni/γ-Al_2O_3 catalyst in the presence of citric acid

In Chapter III, the impact of citric acid on the impregnation of nickel based catalysts has been studied. According to MRI results obtained, for acidic impregnation solutions (pH lower than 2.4), egg-shell distributions of citrate are obtained, while Ni ions are either in an egg-yolk or in egg-white distribution. To evidence the physicochemical phenomena that occur when impregnation step is carried out in the presence of citrate, the impregnation model developed in this chapter is applied. Several hypothesis have been considered:

- Citric acid is totally deprotonated inside the porosity of the support, i.e., in the form of $C_6H_5O_7^{3-}$ (also denoted as Cit^{3-}).
- Competitive adsorption mechanism takes place between $[Ni(H_2O)_6]^{2+}$ and Cit^{3-}: adsorption of nickel ions and citrate occur in the same OH surface sites according to Eq. 64 and Eq. 66, respectively. The adsorption reaction of nickel ions is characterized by a kinetic constant k_1 and the adsorption reaction of citrate ions is characterized by a kinetic constant k_2.

As an example, the case of dry impregnation of γ-Al_2O_3 with a 0.05M [Ni] solution having a CA:Ni molar ratio of 1.2 is considered. The comparison between the experimental MRI results and simulations is shown in Figure 135. Parameters gathered in Table 16 have been applied. Moreover, it is considered that the transport of citrate ions is done not only by diffusion in the fluid phase, but also by surface diffusion in the adsorbed phase. The estimated surface diffusion coefficient of citrate ions in the adsorbed phase is 10^{-13} m^2/s. Additionally, it is considered that the adsorption reaction between citrate and OH surface sites is faster than the reaction between nickel ions and the same OH sites. Therefore, an optimal value of $k_2 = 1.5k_1$ has been estimated.

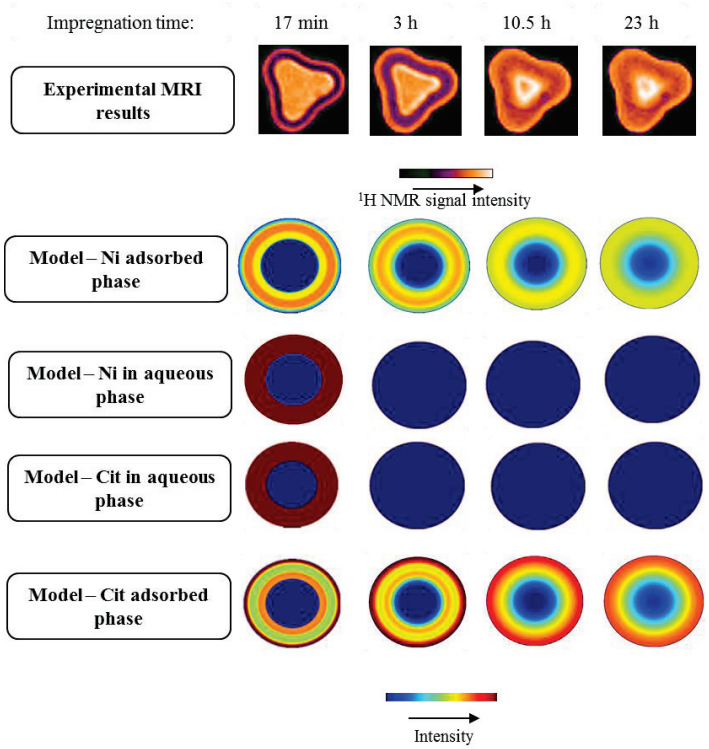

Figure 135 - 0.05M [Ni^{2+}] with CA:Ni=1.2 (molar)/γ-Al_2O_3 : model simulations with parameters of Table 16

Concerning the profile of citrate in the adsorbed phase (see Figure 135), one can observe a higher intensity near the edges, which corresponds to a higher concentration of the organic additive. The opposite behaviour is observed concerning the distribution profile of nickel ions in adsorbed phase. These observations are in good agreement with MRI results. Moreover, as time elapses, no significant differences are observed in the distribution profiles, which fits with MRI images.

To help in this analysis, Figure 136 shows the concentration of either nickel or citrate ions in the adsorbed phase as a function of the position in the pellet at the equilibrium state (23h after impregnation). One can conclude that almost no nickel and citrate are present in the core of the pellet, which is in good agreement with the hypothesis made in the interpretation of MRI images. Moreover, near the edges, concentration in citrate is higher than the concentration of nickel ions.

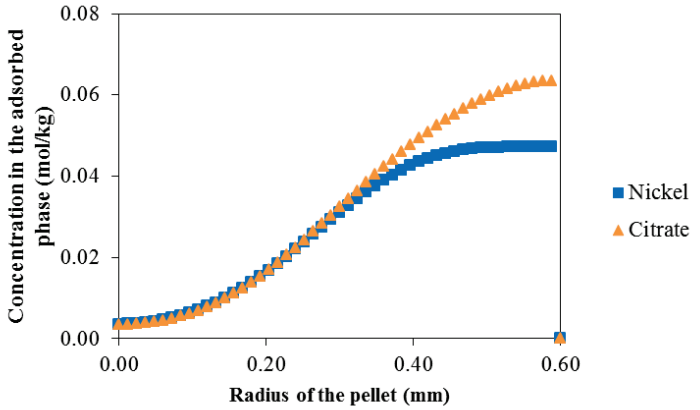

Figure 136 – Impregnation model results concerning concentration of nickel and citrate ions in the adsorbed phase as a function of position in catalyst pellet (0.05M [Ni] with CA:Ni=1.2 (molar)/γ-Al_2O_3, after 23h of impregnation)

4. Conclusion

In the beginning of this study, it has been considered that dry impregnation of Ni/γ-Al_2O_3 catalysts is a result of different phenomena: capillarity, diffusion in the fluid phase, surface diffusion and adsorption.

This impregnation model proves that capillarity is an instantaneous phenomenon. After 5 seconds of contact time between the support and the impregnation solution, water is already present in the entire porosity. Therefore, impregnation is governed through a competition between diffusion and adsorption.

Diffusion depends on the effective diffusion coefficient (D_e), which depends on the tortuosity and the porosity, while adsorption reaction depends on the kinetic constant and the density of adsorption sites (in this case, OH groups). Among these parameters, only the porosity of support has been determined experimentally. Therefore, only the remaining three parameters have been optimized in order to obtain the nickel distribution profiles comparable with the MRI experiments.

An irreversible adsorption with a fast kinetics has been deduced from the dry impregnation capillary stage. The limiting step of impregnation is then diffusion phenomenon. Moreover, the model shows that surface diffusion takes place and the estimated surface diffusion coefficient is 10^{-13} m^2/s. Concerning the concentration of adsorption sites (OH groups), a value of 0.16 $mol.kg^{-1}$ has been obtained, which corresponds to a surface density of 0.36 OH groups/nm^2. This value is very low comparing to the surface OH coverage of γ-alumina known in the literature (11.8 OH/nm^2 at 573K [176]). The small OH density found indicates that not all the OH groups contribute to the hydrolytic adsorption reaction. This observation proves that there is a selective affinity of nickel ions for the γ-alumina OH sites depending on their nucleophilic character, which has already been suggested in Chapter III. Among the literature, several works have already reported on the different nature of surface OH groups of alumina [20,22,176,193]. The tortuosity value strongly influences the transport rate of the advancing front of nickel ions. An optimal value of 2.9 has been estimated, which remains in good agreement with the literature [169,190,192].

When impregnation of nickel based catalysts is carried out in the presence of citrate, a competitive adsorption mechanism between the organic additive and metal ion is highlighted. A preferential adsorption of citrate is indicated according to impregnation model, which is in good agreement with the interpretations made in Chapter III.

Additionally, the model simulations concerning diffusional impregnation proves that the transport rate of metal ions is indeed slower than in the case of dry impregnation, due to the absence of the capillary stage.

To conclude, this mathematical model is an explanatory model, which enables to describe the impregnation step either in dry or diffusional conditions. It can be applied to other type of monometallic catalysts in the presence of additives. Therefore, it can be used as a very useful tool to improve the preparation of catalysts.

Conclusions and Perspectives

In this thesis, the phenomena involved in the preparation of molybdenum (Mo) based catalysts promoted either by nickel (Ni) or cobalt (Co) and supported on alumina (Al_2O_3) have been studied. In order to improve the catalytic performance, it is of crucial importance to understand the phenomena that take place during the impregnation step that are responsible for the genesis of the active phase. Therefore, the aim of this thesis is to identify and describe (in a qualitative and quantitative levels) the interactions inside complex systems during impregnation and to point out the relevant descriptors that influence this step.

Numerous studies have described the different phenomena involved in the impregnation of Mo based catalysts, such as capillarity, diffusion and surface interaction (hydrolytic adsorption, electrostatic interaction and dissolution of alumina). An overview of the state of art concerning the comprehension of impregnation process of HDT catalysts led to the choice of the MRI technique as the most suitable one to study this preparation step. Additionally, Raman Imaging can give access to the chemical nature of molybdenum species with a spatial dimension on the bisected pellet. Nevertheless, this literature review also revealed that MRI studies concern the impregnation step of only monometallic catalysts. A detailed search of the relevant literature showed that none work has been yet performed to study in a non-invasive way the competitive adsorption of several precursors during the impregnation step. More precisely, none study has been carried out to monitor *in-situ* the impregnation step of a traditional HDT catalyst composed of molybdenum and cobalt, in the presence of phosphorus.

First of all, the MRI technique has been adapted and optimized to characterize the impregnation step of monometallic solutions composed either by nickel or cobalt in the presence or not of citric acid. An innovative MRI approach has been implemented to monitor the impregnation step with two or more components solution. An improvement of spatial resolution to 39 μm×39 μm has been achieved. This MRI approach has been validated through a comparison between intensity profiles of MRI images and the EPMA concentration profiles, which enables to obtain a direct correlation between ^1H MRI intensity and concentration of the metal ion within the pellet. Finally, the application of Raman Imaging provides complementary information on the nature and distribution of species inside the catalyst pellet with a spatial resolution of 16.2 μm × 16.2 μm.

Second, the MRI-Raman Imaging characterization methodology has been applied to study the phenomena that take place during the impregnation of a simple solution and the impact of the solution properties (metal ion concentration, pH and viscosity) on this preparation step.

According to this study, the impregnation step of γ-alumina with a nickel solution is governed by capillarity, diffusion and surface interaction. The capillary action is almost an instantaneous process. A competition between diffusion of Ni in the fluid phase and a covalent adsorption at the surface is indicated. A selective affinity with respect to different surface OH groups depending on their

nucleophilic character is also highlighted. The same conclusions can be drawn for the impregnation of cobalt based catalysts.

In the presence of citrate, a faster transport of nickel ions towards the core of the support is observed, for very acidic impregnation solutions (pH lower than 2.4) and regardless the CA:Ni ratio in solution. A competitive adsorption mechanism between citrate and nickel ions is highlighted. A higher affinity between citrate and alumina is indicated rather than a complexation of citrate to nickel ions. Therefore, egg-white or egg-yolk nickel profiles are obtained, while citrate remains near the edges of the support. For higher solution pH, complexation of citrate to nickel ions is favoured, which results in an increase of the interactions between the negatively charged nickel-citrate complex and the protonated support surface. Therefore, egg-shell profiles of nickel-citrate complex are obtained. Thus, by choosing the appropriate CA:Ni ratio and solution pH, is possible to control the desired metal distribution profile.

The same characterization methodology MRI-Raman Imaging has been extended to a more complex case, i.e., a traditional HDT catalyst. Impregnation step of a HDT catalyst with a complex aqueous solution composed simultaneously of molybdenum, cobalt and phosphorus has been for the first time monitored *in-situ* using MRI.

The impact of phosphorus and the nature of the metal promotor (either nickel or cobalt) have been evaluated. For a molybdenum based catalyst, impregnation is governed by a competition between diffusion and an interaction with the OH surface groups of γ-alumina. In the presence of phosphorus, interaction between molybdenum and γ-alumina is limited, since a preferential adsorption to phopshorus is observed. Moreover, less Mo species in covalent interaction with the support are observed. This phenomenon results in an increase in the transport rate of molybdenum complexes. When phosphorus is added to a molybdenum based catalysts promoted by cobalt, a favoured adsorption of phosphorus in relation to Mo or Co ions is clearly observed. A similar behaviour is observed when nickel is used as metal promotor. As a result, impregnation of a Co(Ni)MoP catalysts results in an egg-yolk profiles of Mo, an egg-yolk or egg-white profile of Co (Ni) and an egg-shell profile of P.

When the impregnation of a CoMoP/γ-Al_2O_3 is carried out on the presence of citrate, the effect of the organic additive strongly depends on CA:Mo ratio used in impregnation solution. Mo ions are in an egg-shell distribution either or not in interaction with P, depending on CA:Mo ratio. Co ions can be in the form of aqua complexes in an egg-yolk distribution or in the form of $H_2PMo_{11}CoO_{41}^{5-}$ HPA, depending once again the CA:Mo ratio. This last observation can indeed improve the proximity between Mo and Co ions and therefore the promotor effect of Co.

Finally, an explanatory mathematical model is proposed to describe the impregnation step of monometallic solutions. This model describes the evolution of metal distribution over impregnation

time by taking into account capillarity, diffusion and adsorption phenomena. Furthermore, this model is sensitive to the presence of an additive (by adding a competitive adsorption mechanism) and to the impregnation method (either dry or diffusional impregnation). By optimizing only two parameters (tortuosity and density of adsorption sites) is possible to describe the metal distribution profiles observed in MRI experiments, which evidences the robustness of the model. Among these parameters, the support density in OH surface groups is the parameter that mostly impacts the final metal distribution profile, since it governs the competition between adsorption and diffusion.

The methodology developed in this thesis demonstrates the application of the MRI-Raman Imaging to characterize the impregnation step of a supported catalyst. This work shows the high potential of Magnetic Resonance Imaging as a new tool to monitor *in-situ* the impregnation step of multimetallic catalysts such as hydrotreatment catalysts, which is sensitive towards the presence of an additive (in this case phosphorus and citric acid). MRI not only gives information about spatial distribution of all metal precursors and additives inside the catalyst support, but also suggests different interactions between each precursor and the support. Moreover, the application of Raman Imaging allows one to obtain information about metal speciation and the location of different species with a spatial dimension on the bisected pellet. Additionally, the mathematical model of impregnation step can be extended to similar catalysts.

Further studies using MRI technique can be envisaged. For instance, this technique can be used to study the impregnation step using other metals, such as Pd or Pt. Moreover, it might be advantageous to extend the MRI to other nuclei, in particular to ^{31}P in order to obtain a more precise quantification of the phosphate species. Besides, Chemical Shift Imaging can be used in the case of species whose configuration changes according to the pH, which makes possible a local pH measurement. This technique has been tested in the current thesis, yet the spatial resolution achieved was not enough. Hence, it may be necessary to use innovative imaging tools at the magic angle to improve the signal resolution. Finally, measurement of diffusion coefficients can also be done through MRI, which can provide an evaluation of the local tortuosity. Such information can be very useful in mathematical models to describe impregnation step.

References

[1] H. Topsøe, B. S. Clausen. F. E. Massoth, Hydrotreating Catalysis Science and Technology, Springer, Berlin, 1996.

[2] International Energy Agency, World Energy Outlook 2014, http://www.opec.org/opec_web/en/publications/340.htm, accessed 14 May 2017.

[3] J. Moreau, Rationalisation de l'étape d'imprégnation de catalyseurs à base d'hétéropolyanions de molybdène supportés sur alumine, Université Claude Bernard, Lyon, 2012.

[4] J.A. Bergwerff, T. Visser, Leliveld, Bob R. G., B.D. Rossenaar, K. P. de Jong, B.M. Weckhuysen, Envisaging the physicochemical processes during the preparation of supported catalysts: Raman microscopy on the impregnation of Mo onto Al_2O_3 extrudates, Journal of the American Chemical Society 126 (2004) 14548–14556.

[5] A.A. Lysova, I.V. Koptyug, R.Z. Sagdeev, V.N. Parmon, J.A. Bergwerff, B.M. Weckhuysen, Noninvasive in situ visualization of supported catalyst preparations using multinuclear magnetic resonance imaging, J. Am. Chem. Soc. 127 (2005) 11916–11917.

[6] J.A. Bergwerff, A.A. Lysova, L. Espinosa Alonso, I.V. Koptyug, B.M. Weckhuysen, Probing the transport of paramagnetic complexes inside catalyst bodies in a quantitative manner by magnetic resonance imaging, Angewandte Chemie (International ed. in English) 46 (2007) 7224–7227.

[7] J.A. Bergwerff, A.A. Lysova, L. Espinosa-Alonso, I.V. Koptyug, B.M. Weckhuysen, Monitoring transport phenomena of paramagnetic metal-ion complexes inside catalyst bodies with magnetic resonance imaging, Chemistry A European Journal 14 (2008) 2363–2374.

[8] A.A. Lysova, J.A. Bergwerff, L. Espinosa-Alonso, B.M. Weckhuysen, I.V. Koptyug, Magnetic resonance imaging as an emerging tool for studying the preparation of supported catalysts, Applied Catalysis A: General 374 (2010) 126–136.

[9] E. Marceau, X. Carrier, M. Che, O. Clause, C. Marcilly, Handbook of Heterogeneous Catalysis, 2nd ed., Wiley-VCH, Weinheim, Germany, 2008.

[10] A. Lekhal, B.J. Glasser, J.G. Khinast, Impact of drying on the catalyst profile in supported impregnation catalysts, Chemical Engineering Science 56 (2001) 4473–4487.

[11] H. Jens, Industrial Catalysis: A Practical Approach, 2nd ed., Wiley-VCH, Weinheim, Germany, 2006.

[12] H. Toulhoat, P.Raybaud, Catalysis by transition metal sulphides, Paris, Editions Technip, 2013.

[13] M. Digne, K. Marchand, P. Bourges, Monitoring Hydrotreating Catalysts Synthesis and Deactivation using Raman Spectrometry, Oil & Gas Science and Technology - Rev. IFP 62 (2007) 91–99.

[14] E. Marceau, X. Carrier, M. Che, Synthesis of Solid Catalysts, Wiley-VCH, Weinheim, 2009.

[15] K. Bourikas, C. Kordulis, A. Lycourghiotis, The Role of the Liquid-Solid Interface in the Preparation of Supported Catalysts, Catalysis Reviews 48 (2006) 363–444.

[16]G. Ert, H. Knozinger, J. Weitkamp, Preparation of Solid Catalysts, Wiley-VCH, Weinheim, Germany, 1999.

[17]K. Bourikas, C. Kordulis, J. Vakros, A. Lycourghiotis, Adsorption of cobalt species on the interface, which is developed between aqueous solution and metal oxides used for the preparation of supported catalysts: a critical review, Advances in colloid and interface science 110 (2004) 97–120.

[18]J. F. Le Page, J. Cosyns. P. Courty, Catalyse de Contact: Conception, préparation et mise en oeuvre des catalyseurs industriels, Ed. Technip, Paris, 1978.

[19]S.G. Ferraz, Zotin, Fatima M. Zanon, Araujo, Lucia R. Raddi, J.L. Zotin, Influence of support acidity of NiMoS catalysts in the activity for hydrogenation and hydrocracking of tetralin, Applied Catalysis A: General 384 (2010) 51–57.

[20]H. Knözinger, P. Ratnasamy, Catalytic Aluminas: Surface Models and Characterization of Surface Sites, Catalysis Reviews 17 (1978) 31–70.

[21]G. Busca, V. Lorenzelli, G. Ramis, R.J. Willeyi, Surface Sites on Spinel-Type and Corundum-Type Metal Oxide Powders, Langmuir (1993) 1492–1499.

[22]M. Digne, P. Sautet, P. Raybaud, P. Euzen, H. Toulhoat, Use of DFT to achieve a rational understanding of acid-basic properties of γ-alumina surfaces, Journal of Catalysis 226 (2004) 54–68.

[23]M. Digne, Des hydroxydes d'aluminium aux propriétés chimiques de l'alumine γ en catalyse: une étude théorique *ab initio*, Ecole Normale Supérieure de Lyon, 2003.

[24]S.K. Maity, J. Ancheyta, L. Soberanis, F. Alonso, Catalysts for hydroprocessing of Maya heavy crude, Applied Catalysis A: General 253 (2003) 125–134.

[25]A. Morales, de Agudelo, M. M. Ramírez, F. Hernández, Adsorption mechanism of phosphorus on alumina, Applied Catalysis 41 (1988) 261–271.

[26]A. Morales, de Agudelo, M. M. Ramírez, Promoter role of octahedral Co (and Ni) in modified Co(Ni)Mo-Al2O3 catalysts for hydrodesulfurization reactions, Applied Catalysis 23 (1986) 23–34.

[27]S. Bouwens, J. Vissers, de Beer, V. H. J, R. Prins, Phosphorus poisoning of molybdenum sulfide hydrodesulfurization catalysts supported on carbon and alumina, Journal of Catalysis 112 (1988) 401–410.

[28]J.A. Bergwerff, Leon G. A. van de Water, Tom Visser, Peter de Peinder, Bob R. G. Leliveld, K. P. de Jong, Bert M. Weckhuysen, Spatially resolved Raman and UV-visible-NIR spectroscopy on the preparation of supported catalyst bodies: controlling the formation of $H_2PMo_{11}CoO_{40}^{5-}$ inside Al_2O_3 pellets during impregnation during impregnation, Chemistry A European Journal 11 (2005) 4591–4601.

[29]H. Kraus, R. Prins, Composition of Impregnation Solutions and Wet Impregnated Mo–P/γ-Al_2O_3 Catalysts as Investigated by ^{31}P and ^{95}Mo NMR, Journal of Catalysis 164 (1996) 251–259.

[30]H. Kraus, The Effect of Phosphorus on Oxidic NiMo(CoMo)/γ-Al_2O_3 Catalysts: A Solid State NMR Investigation, Journal of Catalysis 170 (1997) 20–28.

[31]W. Cheng, NMR study of the adsorption of phosphomolybdates on alumina, Journal of Catalysis 109 (1988) 163–169.

[32]A.M. Maitra, N.W. Cant, D.L. Trimm, Novel hydrotreating catalysts prepared from heteropolyanion complexes impregnated on alumina, Applied Catalysis 48 (1989) 187–197.

[33]C.I. Cabello, I.L. Botto, H.J. Thomas, Anderson type heteropolyoxomolybdates in catalysis $(NH_4)_3[CoMo_6O_{24}H_6]\cdot 7H_2O/\gamma\text{-}Al_2O_3$ as alternative of Co-Mo/γ-Al_2O_3 hydrotreating catalysts, Applied Catalysis A: General 197 (2000) 79–86.

[34]C.I. Cabello, M. Muñoz, E. Payen, H.J. Thomas, Influence of cobalt content on the hydrotreatment catalytic activity of $CoMo_6/\gamma\text{-}Al_2O_3$ heteropolyoxomolybdate-based catalyst, Catalysis Letters 92 (2004) 69–73.

[35]C. Martin, C. Lamonier, M. Fournier, O. Mentré, V. Harlé, D. Guillaume, E. Payen, Preparation and characterization of 6-molybdocobaltate and 6-molybdoaluminate cobalt salts. Evidence of a new heteropolymolybdate structure, Inorganic chemistry 43 (2004) 4636–4644.

[36]J. Mazurelle, C. Lamonier, C. Lancelot, E. Payen, C. Pichon, D. Guillaume, Use of the cobalt salt of the heteropolyanion $[Co_2Mo_{10}O_{38}H_4]^{6-}$ for the preparation of CoMo HDS catalysts supported on Al_2O_3, TiO_2 and ZrO_2, Catalysis Today 130 (2008) 41–49.

[37]J. F. Keggin, Structure and Formula of 12-Phosphotungstic Acid, Proc. Roy. Soc. A 144 (1934) 75–100.

[38]J.S. Anderson, Constitution of the Poly-acids, Nature 140 (1937) 850.

[39]A. Griboval, P. Blanchard, E. Payen, M. Fournier, J.L. Dubois, Alumina supported HDS catalysts prepared by impregnation with new heteropolycompounds. Comparison with catalysts prepared by conventional Co–Mo–P coimpregnation, Catalysis Today 45 (1998) 277–283.

[40]G.A. Tsigdinos, Heteropoly compounds of molybdenum and tungsten, in: G.A. Tsigdinos (Ed.), Aspects of molybdenum and related chemistry, Springer, Berlin, 1978, pp. 1–64.

[41]D. Guillaume, E. Payen, C. Lamonier, K. Marchand, US 2008/0020926 A1.

[42]P. Nikulshin, A. Mozhaev, C. Lancelot, P. Blanchard, E. Payen, C. Lamonier, Hydroprocessing catalysts based on transition metal sulfides prepared from Anderson and dimeric Co2Mo10-heteropolyanions. A review, Comptes Rendus Chimie 19 (2016) 1276–1285.

[43]R. Strandberg, Multicomponent Polyanions. IV. The Molecular and Crystal Structure of $Na_6Mo_5P_2O_{23}(H_2O)_{13}$, a Compound Containing Sodium-coordinated Pentamolybdodiphosphate Anions, Acta Chemical Scandinavica 27 (1973) 1004–1008.

[44]B. Dawson, The structure of the 9(18)-heteropoly anion in potassium 9(18)-tungstophosphate, $K_6(P_2W_{18}O_{62}).14H_2O$, Acta Crystallographica 6 (1953) 113–126.

[45]X. Carrier, J. F. Lambert, M. Che, Ligand-Promoted Alumina Dissolution in the Preparation of $MoO_X/\gamma\text{-}Al_2O_3$ Catalysts - Evidence for the Formation and Deposition of an Anderson-type Alumino Heteropolymolybdate, J. Am. Chem. Soc. 119 (1997) 10137–10146.

[46]A. J. van Vandillen, R. Terorde, D. J. Lensveld, J. W. Geus, K. P. de Jong, Synthesis of supported catalysts by impregnation and drying using aqueous chelated metal complexes, Journal of Catalysis 216 (2003) 257–264.

[47]M. Tsuyoshi, I. Yuichiro, I. Akira, EP 0 638 361 B1, 1994.

[48]Takao, S. et al., EP 0 601 722 B1, 1998.

[49]B. Fremon, A. Chaumonnot, K. Marchand, E. Payen, A new approach of hydrotreating catalysts preparation by support functionalization, in: Scientific Bases for the Preparation of Heterogeneous Catalysts, Elsevier, 2006, pp. 291–298.

[50]C. Radlowski, US2009/0298677 A1, 2009.

[51]Gabrielov, A. G., US2010/0236988 A1, 2010.

[52]T. Shimizu, K. Hiroshima, T. Honma, T. Mochizuki, M. Yamada, Highly active hydrotreatment catalysts prepared with chelating agents, Catalysis Today 45 (1998) 271–276.

[53]Y. Ohta, T. Shimizu, T. Honma, M. Yamada, Effect of chelating agents on HDS and aromatic hydrogenation over CoMo-and NiW/Al2O3, Studies in Surface Science and Catalysis 127 (1999).

[54]K. Hiroshima, T. Mochizuki, T. Honma, T. Shimizu, M. Yamada, High HDS activity of modified by some chelates and their surface fine structures, Applied Surface Science 121-122 (1997) 433–436.

[55]Y. Yoshimura, N. Matsubayashi, T. Sato, H. Shimada, A. Nishijima, Molybdate catalysts prepared by a novel impregnation method, Applied Catalysis A: General 79 (1991) 145–159.

[56]Y. Yoshimura, T. Sato, H. Shimada, N. Matsubayashi, M. Imamura, A. Nishijima, M. Higo, S. Yoshitomi, Preparation of nickel-tungstate catalysts by a novel impregnation method, Catalysis Today 29 (1996) 221–228.

[57]J. Bergwerff, M. Jansen, B. Leliveld, T. Visser, K. P. de Jong, B. M. Weckhuysen, Influence of the preparation method on the hydrotreating activity of MoS_2/Al_2O_3 extrudates: A Raman microspectroscopy study on the genesis of the active phase, Journal of Catalysis 243 (2006) 292–302.

[58]Jacob Arie Bergwerff, Spatially Resolved Spectroscopy on the Preparation of $CoMo/Al_2O_3$ Hydrodesulphurization Catalysts, University Utrecht, 2007.

[59]N. Rinaldi, Usman, K. Al-Dalama, T. Kubota, Y. Okamoto, Preparation of $Co–Mo/B_2O_3/Al_2O_3$ catalysts for hydrodesulfurization: Effect of citric acid addition, Applied Catalysis A: General 360 (2009) 130–136.

[60]O.V. Klimov, A.V. Pashigreva, M.A. Fedotov, D.I. Kochubey, Y.A. Chesalov, G.A. Bukhtiyarova, A.S. Noskov, Co–Mo catalysts for ultra-deep HDS of diesel fuels prepared via synthesis of bimetallic surface compounds, Journal of Molecular Catalysis A: Chemical 322 (2010) 80–89.

[61]Hai liang Yin, Tong na Zhou, Yong ming Liu, Chen guang Liu, Study on the structure of active phase in NiMoP impregnation solution using Laser Raman spectroscopy II. Effect of organic additives, Journal of Fuel Chemistry and Technology 39 (2011) 109–114.

[62]Daniele Nicosia, Roel Prins, The effect of glycol on phosphate-doped $CoMo/Al_2O_3$ hydrotreating catalysts, Journal of Catalysis 229 (2005) 424–438.

[63]Daniele Nicosia, Roel Prins, The effect of phosphate and glycol on the sulfidation mechanism of CoMo/Al_2O_3 hydrotreating catalysts: an in situ QEXAFS study, Journal of Catalysis 231 (2005) 259–268.

[64]L. Saravanan, S. Subramanian, Surface chemical studies on the competitive adsorption of poly(ethylene glycol) and ammonium poly(methacrylate) onto alumina, Journal of colloid and interface science 284 (2005) 363–377.

[65]M. Sun, D. Nicosia, R. Prins, The effects of fluorine, phosphate and chelating agents on hydrotreating catalysts and catalysis, Catalysis Today 86 (2003) 173–189.

[66]V. Costa, K. Marchand, M. Digne, C. Geantet, New insights into the role of glycol-based additives in the improvement of hydrotreatment catalyst performances, Catalysis Today 130 (2008) 69–74.

[67]R.I. Bickley, H. Edwards, R. Gustar, S.J. Rose, A vibrational spectroscopic study of nickel(II) citrate $Ni_3(C_6H_5O_7)_2$ and its aqueous solutions, Journal of Molecular Structure 246 (1991) 217–228.

[68]J.A. Bergwerff, L. van de Water, A.A. Lysova, I.V. Koptyug, T. Visser, K.P. de Jong, B.M. Weckhuysen, Monitoring the preparation of (Co)Mo/Al_2O_3 extrudates using spatially resolved spectroscopic techniques, Scientific Bases for the Preparation of Heterogeneous Catalysts 162 (2006) 175–186.

[69]E.N. Baker, H.M. Baker, B.F. Anderson, R.D. Reeves, Chelation of nickel(II) by citrate. The crystal structure of a nickel–citrate complex, $K_2[Ni(C_6H_5O_7)(H_2O)_2]_2 \cdot 4H_2O$, Inorganica Chimica Acta 78 (1983) 281–285.

[70]T.E. Klimova, D. Valencia, J.A. Mendoza-Nieto, P. Hernández-Hipólito, Behavior of NiMo/SBA-15 catalysts prepared with citric acid in simultaneous hydrodesulfurization of dibenzothiophene and 4,6-dimethyldibenzothiophene, Journal of Catalysis 304 (2013) 29–46.

[71]F. Bentaleb, M. Che, A.-C. Dubreuil, C. Thomazeau, E. Marceau, Influence of organic additives on the properties of impregnation solutions and on nickel oxide particle size for Ni/Al_2O_3 catalysts, Catalysis Today 235 (2014) 250–255.

[72]L. Kaufman (Ed.), Calculation of Pourbaix Diagrams for C22 in various well water chemistries, Las Vegas, NV, 2002.

[73]L.O. Ohman, Equilibrium and Structural Studies of Silicon(IV) and Aluminum(III) in Aqueous Solution, Inorg. Chem. 28 (1989) 3629–3632.

[74]Romaric Massard, Etude des effets de contraintes sur catalyseurs bimétalliques PdNi supportés, Université Claude Bernard, Lyon, 2006.

[75]Charles F. Baes, Robert E. Mesmer, The Hydrolysis of Cations, Krieger Publishing Company, Malabar, Florida, 1986.

[76]A. V. Nelmark, L. I. Kheifez, and V. B. Fenelonov, Theory of Preparation of Supported Catalysts, Ind. Eng. Chem. Prod. Res. Dev. 20 (1981) 439–450.

[77]S. Chevalier, Introduction à la capillarité, 2014, http://www.chevalierstephane.fr/downloads/dynamique_impregnation.pdf, accessed 15 March 2017.

[78]Jean-François Daïan, Equilibre et Transferts en Milieux Poreux, Université Joseph Fourier, 2013.

[79]A.V. Neimark, L.I. Kheifets, V.B. Fenelonov, Theory of preparation of supported catalysts, Ind. Eng. Chem. Prod. Res. Dev. 20 (1981) 439–450.

[80]Dr. Mick D. Mantle, Diffusion and Effective Diffusivity in Porous Media, 2010.

[81]M. N. de Pinho, D. M. Prazeres, Fundamentos de Transferência de Massa, IST Press, Lisbon, 2008.

[82]M. Ruthven Douglas, Principles of adsorption and adsorpton processes, J. Wiley & Sons, New York, 1984.

[83]R. Krishna, A unified approach to the modelling of intraparticle diffusion in adsorption processes, Gas Separation & Purification 7 (1993) 91–104.

[84]M. Ruthven Douglas, Principles of adsorption and adsorption processes, J. Wiley and Sons, New York, 1984.

[85]K. Miyabe, Surface diffusion in reversed-phase liquid chromatography using silica gel stationary phases of different C_1 and C_{18} ligand densities, Journal of chromatography. A 1167 (2007) 161–170.

[86]D. Weber, A.J. Sederman, M.D. Mantle, J. Mitchell, L.F. Gladden, Surface diffusion in porous catalysts, Physical chemistry chemical physics 12 (2010) 2619–2624.

[87]J.L. Figueiredo, F. Ramôa Ribeiro, Catálise Heterogénea, 2nd ed., Fundação Caloust Gulbenkian, Lisbon, 2007.

[88]A. Lekhal, B.J. Glasser, J.G. Khinast, Influence of pH and ionic strength on the metal profile of impregnation catalysts, Chemical Engineering Science 59 (2004) 1063–1077.

[89]Dr. Juan Carlos Moreno, Thermodynamics-Interaction Studies-Solids, Liquids and Gases: Comparison of the Thermodynamic Parameters Estimation for the Adsorption Process of the Metals from Liquid Phase on Activated Carbons, InTech, 2011.

[90]S. Verdier, Chimie des ions métalliques en solution aqueuse: Ni(II), Ag(I), Sn(I1) et Sn(1V): Rapport Interne, Institut Français du Pétrole.

[91]S. Brunauer, L.S. Deming, Deming, W. Edwards, E. Teller, On a Theory of the van der Waals Adsorption of Gases, J. Am. Chem. Soc. 62 (1940) 1723–1732.

[92]K. S. W. Sing et al., Reporting physisorption data for gas/solid systems with special reference to the determination of surface area and porosity, Pure & Appl. Chem. 57 (1985) 603–619.

[93]Irving Langmuir, The adsorption of gases on plane surfaces of glass, mica and platinum, J. Am. Chem. Soc. 40 (1918) 1361–1403.

[94]P. H. Tewari, A. B. Campbell, Woon Lee, Adsorption of Co^{2+} by Oxides from Aqueous Solution, Canadian Journal of Chemistry 50 (1972) 1642–1648.

[95]P.H. Tewari, W. Lee, Adsorption of Co(II) at the oxide-water interface, Journal of colloid and interface science 52 (1975) 77–88.

[96]C. J. Chisholm-Brause, P. A. O'Day, G. E. Brown Jr, G. A. Parks, Evidence for multinuclear metal-ion complexes at solid-water interfaces from X-ray absorption spectroscopy, Nature 348 (1990) 528–531.

[97]J. L. Paulhiac, O. Clause, Surface coprecipitation of cobalt(II), nickel(II), or zinc(II) with aluminum(III) ions during impregnation of γ-alumina at neutral pH, J. Am. Chem. Soc. 115 (1993) 11602–11603.

[98]L. Vordonis, N. Spanos, P.G. Koutsoukos, A. Lycourghiotis, Mechanism of Adsorption of Co^{2+} and Ni^{2+} Ions on the " Pure and Fluorinated y-Alumina / Electrolyte Solution " Interface, Langmuir 8 (1992) 1736–1743.

[99]N. Spanos, A. Lycourghiotis, Mechanism of deposition of Co^{2+} and Ni^{2+} ions on the interface between pure and F^- - doped γ-alumina and the impregnating solution, Journal of the Chemical Society, Faraday Transactions 89 (1993) 4101.

[100] J. Vakros, C. Kordulis, A. Lycourghiotis, Cobalt Oxide Supported γ-Alumina Catalyst with Very High Active Surface Area Prepared by Equilibrium Deposition Filtration, Langmuir 18 (2002) 417–422.

[101] T. Hiemstra, W. H. Van Riemsdijk, Surface Structural Ion Adsorption Modeling of Competitive Binding of Oxyanions by Metal (Hydr)oxides, Journal of colloid and interface science 210 (1999) 182–193.

[102] H. Tamura, N. Katayama, R. Furuichi, The Co^{2+} Adsorption Properties of Al_2O_3, Fe_2O_3, Fe_3O_4, TiO_2, and MnO_2 Evaluated by Modeling with the Frumkin Isotherm, Journal of colloid and interface science 195 (1997).

[103] J. Vakros, K. Bourikas, S. Perlepes, C. Kordulis, A. Lycourghiotis, Adsorption of cobalt ions on the "electrolytic solution/γ-alumina" interface studied by diffuse reflectance spectroscopy (DRS), Langmuir 20 (2004) 10542–10550.

[104] J. A. R van Veen, P. A. J. M. Hendriks, R. R. Andréa, E. J. G. M. Romers, Chemistry of Phosphomolybdate Adsorption on Alumina Surfaces. 1. The Molybdate/Alumina System, J. Phys. Chem. (1990) 5275–5282.

[105] N. Spanos, A. Lycourghiotis, Molybdenum-oxo Species Deposited on Alumina by Adsorption - III. Advances in the Mechanism of Mo(VI) Deposition, Journal of Catalysis 147 (1994) 57–71.

[106] J. Vakros, K. Bourikas, C. Kordulis, A. Lycourghiotis, Influence of the Impregnation pH on the Surface Characteristics and the Catalytic Activity of the Mo /γ-Al_2O_3 and CoMo /γ-Al_2O_3 Hydrodesulfurization Catalysts Prepared by Equilibrium Deposition Filtration (EDF), Journal of Physical Chemistry B (2003) 1804–1813.

[107] D. S. Kim, K. Segawa, T. Soeya, I. E. Wachsb, Surface Structures of Supported Molybdenum Oxide Catalysts under Ambient Conditions, Journal of Catalysis 136 (1992) 539–553.

[108] J. Moreau, O. Delpoux, E. Devers, M. Digne, S. Loridant, Impregnation of decamolybdocobaltate heteropolyanions over γ-alumina: detailed description of the physico-chemical phenomena, Langmuir the ACS journal of surfaces and colloids 29 (2013) 207–215.

[109] J. P. Brunelle, Preparation of catalysts by metallic complex adsorption on mineral oxides, Pure & Appl. Chem. 50 (1978) 1211–1229.

[110] Paola D'Angelo, Vincenzo Barone, Giovanni Chillemi, Nico Sanna, Wolfram Meyer-Klaucke, Nicolae Viorel Pavel, Hydrogen and Higher Shell Contributions in Zn^{2+} Ni^{2+} and Co^{2+} Aqueous Solutions: An X-ray Absorption Fine Structure and Molecular Dynamics Study, J. Am. Chem. Soc. 124 (2002) 1958–1967.

[111] T. Hiemstra, W.H. van Riemsdijk, A Surface Structural Approach to Ion Adsorption: The Charge Distribution (CD) Model, Journal of colloid and interface science 179 (1996) 488–508.

[112] G.D. Panagiotou, T. Petsi, K. Bourikas, C.S. Garoufalis, A. Tsevis, N. Spanos, C. Kordulis, A. Lycourghiotis, Mapping the surface (hydr)oxo-groups of titanium oxide and its interface with an aqueous solution: the state of the art and a new approach, Advances in colloid and interface science 142 (2008) 20–42.

[113] X. Carrier, J.-B. d'Espinose de la Caillerie, J.-F. Lambert, M. Che, The Support as a Chemical Reagent in the Preparation of WO_x /γ-Al_2O_3 Catalysts: Formation and Deposition of Aluminotungstic Heteropolyanions, J. Am. Chem. Soc. 121 (1999) 3377–3381.

[114] R. C. Vincent, R. P. Merrill, Concentration profiles in impregnation of porous catalysts, Journal of Catalysis 35 (1974) 206–217.

[115] S.-Y. Lee, R. Aris, The Distribution of Active ingredients in Supported Catalysts Prepared by Impregnation, Catalysis Reviews 27 (1985) 207–340.

[116] M. Komiyama, R. P. Merrill, H. F. Harnserger, Concentration profiles in impregnation of porous catalysts: nickel on alumina, Journal of Catalysis 63 (1980) 35–52.

[117] S. S. Kulkarni, G. R. Mauze, J. A. Schwarz, Concentration profiles and the design of metal-supported catalysts, Journal of Catalysis 69 (1981).

[118] R. Zhang, J.A. Schwarz, Design of inhomogeneous metal distributions within catalyst particles, Applied Catalysis A: General 91 (1992) 57–65.

[119] E. Assaf, L. Jesus, J. Assaf, The active phase distribution in Ni/Al_2O_3 catalysts and mathematical modeling of the impregnation process, Chemical Engineering Journal 94 (2003) 93–98.

[120] M. Morbidelli, A. Servida, A. Varma, Optimal catalyst activity profiles in pellets. 1. The case of negligible external mass transfer resistance, Ind. Eng. Chem. Fund. 21 (1982) 278–284.

[121] O. A. Sceiza, A. A. Castro, D. R. Ardiles, J. M. Parera, Modeling of the impregnation step to prepare supported Pt/Al_2O_3 catalysts, Ind. Eng. Chem. Fundam. 25 (1986) 84–88.

[122] P. Papageorgiou, D. M. Price, A. Gravriilidis, A. Varma, Preparation of Pt/γ-Al_2O_3 Pellets with Internal Step-Distribution of Catalyst: Experiments and Theory, Journal of Catalysis 158 (1996) 439–451.

[123] P. T. Callaghan, Principles of Nuclear Magnetic Resonance Microscopy, 1991.

[124] A.A. Lysova, I.V. Koptyug, Magnetic resonance imaging methods for in situ studies in heterogeneous catalysis, Chemical Society reviews 39 (2010) 4585–4601.

[125] I.V. Koptyug, Magnetic resonance imaging methods in heterogeneous catalysis, Spectrosc. Prop. Inorg. Organomet. Compd 45 (2014) 1–42.

[126] L. Espinosa-Alonso, A.A. Lysova, P. de Peinder, K. P. de Jong, I.V. Koptyug, B.M. Weckhuysen, Magnetic resonance imaging studies on catalyst impregnation processes: discriminating metal ion complexes within millimeter-sized γ-Al_2O_3 catalyst bodies, J. Am. Chem. Soc. 131 (2009) 6525–6534.

[127] Pages Thierry, Application de la chimie colloidal en phase aqueuse a la preparation des catalyseurs metalliques supportees: controle de la taille et de l'agregation des particules, Université de Paris 06, France.

[128] A. Nowacka, J. Moughames, Z. Adem, A.-A. Quoineaud, M. Rolland, F. Guenneau, A. Gédéon, In situ magnetic resonance imaging study of the impregnation of γ-alumina pellets, Applied Catalysis A: General 503 (2015) 111–116.

[129] I.V. Koptyug, MRI of mass transport in porous media: drying and sorption processes, Progress in Nuclear Magnetic Resonance Spectroscopy 65 (2012) 1–65.

[130] V. Costa, K. Marchand, M. Digne, C. Geantet, Compréhension du role des additifs du type glycol sur l'amélioration des performances des catalyseurs d'hydrotraitement, IFP Energies Nouvelles, 2011.

[131] M. A. Vuurman, D. J. Stufkens, O. Goutam, I. E. Wachsb, Combined Raman and IR study of MO_x-V_2O_5/Al_2O_3 (MO_x, = MoO_3, WO_3, NiO,CoO) catalysts under dehydrated conditions, J. Chem. Faraday Trans. 92 (1996) 3259–3265.

[132] H. Knozinger, G. Mestl, Laser Raman spectroscopy – a powerful tool for in situ studies of catalytic materials, Topics in Catalysis 8 (1999) 45–55.

[133] L. Wang, On the genesis of molybdena-alumina catalyst, Journal of Catalysis 66 (1980) 251–255.

[134] I. L. Botto, A. C. Garcia, H. J. Thomas, Spectroscopical approach to some heteropolymolybdates with the Anderson structure, J. Phys. Chem. Solids 53 (1992) 1075–1080.

[135] E.K. Gibson, M.W. Zandbergen, S.D.M. Jacques, C. Biao, R.J. Cernik, M.G. O'Brien, M. Di Michiel, B.M. Weckhuysen, A.M. Beale, Noninvasive Spatiotemporal Profiling of the Processes of Impregnation and Drying within Mo/Al_2O_3Catalyst Bodies by a Combination of X-ray Absorption Tomography and Diagonal Offset Raman Spectroscopy, American Chemical Society 3 (2013) 339–347.

[136] van de Water, Leon G A, J.A. Bergwerff, T.A. Nijhuis, de Jong, Krijn P, B.M. Weckhuysen, UV-Vis microspectroscopy: probing the initial stages of supported metal oxide catalyst preparation, J. Am. Chem. Soc. 127 (2005) 5024–5025.

[137] J. Lynch, Physico-Chemical Analysis of Industrial Catalysts - A Pratical Guide to Characterization, Editions Technip, Paris, 2003.

[138] F. Anabitarte, A. Cobo, J.M. Lopez-Higuera, Laser-Induced Breakdown Spectroscopy: Fundamentals, Applications, and Challenges, ISRN Spectroscopy 2012 (2012) 1–12.

[139] V. Piñon, M.P. Mateo, G. Nicolas, Laser-Induced Breakdown Spectroscopy for Chemical Mapping of Materials, Applied Spectroscopy Reviews 48 (2013) 357–383.

[140] F. Trichard, L. Sorbier, S. Moncayo, Y. Blouët, C.-P. Lienemann, V. Motto-Ros, Quantitative elemental imaging of heterogeneous catalysts using laser-induced breakdown spectroscopy, Spectrochimica Acta Part B: Atomic Spectroscopy 133 (2017) 45–51.

[141] Rama Jayasundar, Laurance D. Hallt, Norman M. Bleehen, Comparison of pH measurements made using 31P NMR and a fibreoptic pH meter, NMR in Biomedicine 5 (1992) 360–363.

[142] D. Canet, J. C. Boubel, E. C. Soulas, La RMN: Concepts, méthodes et applications, 2nd ed., Dunod, Paris, 2002.

[143] L. Brateman, Chemical shift imaging: a review, American Journal of Roentgenology 146 (1986).

[144] J.A. Bergwerff, L. van de Water, T. Visser, P. Peinder, B. Leliveld, K.P. de Jong, B.M. Weckhuysen, Spatially resolved Raman and UV-visible-NIR spectroscopy on the preparation of supported catalyst bodies: controlling the formation of $H_2PMo_{11}CoO_{40}^{5-}$ inside Al_2O_3 pellets during impregnation, Chemistry (Weinheim an der Bergstrasse, Germany) 11 (2005) 4591–4601.

[145] M. A. Elbagermi, A. I. Alajtal, H. G. M. Edwards, G. H. Azimi, K. D. Verma, I. J. Scowen, Journal of Applied Chemical Science International (2015) 1–11.

[146] A. G. Webb, Introduction to Biomedical Imaging, Wiley-IEEE Press, Urbana, 2003.

[147] B. Kastler, D. Vetter, Z. Patay, P. Germain, Comprendre l'IRM Manuel d'auto apprentissage, 6th ed., Masson, 2006.

[148] IMAIOS SAS, L'IRM pas à pas : cours interactif sur l'imagerie par résonance magnétique, https://www.imaios.com/fr/e-Cours/e-MRI, accessed 30 January 2015.

[149] J. Hennig, A. Nauerth, H. Friedburg, RARE Imaging: A Fast Imaging Method for Clinical MR, Magn. Reson. Med 3 (1986).

[150] H. Y. Carr and E. M. Purcell, Effects of Diffusion on Free Precession in Nuclear Magnetic Resonance Experiments, Physical Review 94 (1954).

[151] S. Meiboom, D. Gill, Modified Spin-Echo Method for Measuring Nuclear Relaxation Times, Rev. Sci. Instrum. 29 (1958) 688.

[152] S. Subramanian, N. Devasahayam, R. Murugesan, K. Yamada, J. Cook, A. Taube, J.B. Mitchell, Lohman, Joost A B, M.C. Krishna, Single-point (constant-time) imaging in radiofrequency Fourier transform electron paramagnetic resonance, Magnetic resonance in medicine 48 (2002) 370–379.

[153] S. Gravina, D.G. Cory, Sensitivity and Resolution of Constant-Time Imaging, Journal of Magnetic Resonance, Series B 104 (1994) 53–61.

[154] J. Niemantsverdriet, Spectroscopy in Catalysis, Third ed., Wiley-VCH, 2007.

[155] Bennet et al., US8179526 B2.

[156] P. Thévenaz, T. Blu, M. Unser, Interpolation revisited, IEE Transactions on Medical Imaging 19 (2000) 739–758.

[157] M. Moreaud, F. Cokelaer, Flowing Bilateral Filter: Definition and Implementations, Image Anal Stereol 34 (2015) 101–110.

[158] N. Otsu, A Threshold Selection Method from Gray-Level Histograms, IEE Transactions on Systems, Man, and Cybernetics SMC-9 (1979) 62–66.

[159] L. Sorbier, A.-S. Gay, A. Fecant, M. Moreaud, N. Brodusch, Measurement of palladium crust thickness on catalysts by optical microscopy and image analysis, Microscopy and microanalysis the official journal of Microscopy Society of America, Microbeam Analysis Society, Microscopical Society of Canada 19 (2013) 293–299.

[160] V. Gex, Suivi in situ de la genèse des matériaux par relaxométrie RMN application aux catalyseurs, Université Paris VI Pierre et Marie Curie, 2012.

[161] K. J. Packer, Nuclear spin relaxation studies of molecules adsorbed on surfaces, Progress in Nuclear Magnetic Resonance Spectroscopy 3 (1967) 87–128.

[162] D. Geschke, H. Pfeifer, H. Winkler, Proton relaxation in liquids sorbed on alumina, Journal of colloid and interface science 26 (1968) 287–290.

[163] R. Mackay, J. Zhang, Q. Wu, Y. Li, NMR investigation of concentrated alumina and silica slurries, Colloids and Surfaces A: Physicochemical and Engineering Aspects 250 (2004) 343–348.

[164] J. R. Zimmerman, B. G. Holmes, J. A. Lasater, A study of adsorbed water on silica gel by Nuclear Resonance techniques, Magnolia Petroleum Company, Field Research Laboratory (1956).

[165] J. R. Zimmerman, J. A. Lasater, Nuclear Magnetic Resonance Relaxation Studies of Adsorbed Water on Silica Gel, Magnolia Petroleum Company, Field Research Laboratory (1958).

[166] C. P. Constantin et al., Improved Contrast Agents for Magnetic Nuclear Resonance Medical Imaging, Journal of Advanced Research in Physics 2 (2011).

[167] T. Parella (2010).

[168] M.D. Mantle, D.I. Enache, E. Nowicka, S.P. Davies, J.K. Edwards, C. D'Agostino, D.P. Mascarenhas, L. Durham, M. Sankar, D.W. Knight, L.F. Gladden, S.H. Taylor, G.J. Hutchings, Pulsed-Field Gradient NMR Spectroscopic Studies of Alcohols in Supported Gold Catalysts †, J. Phys. Chem. C 115 (2011) 1073–1079.

[169] C. D'Agostino, J. Mitchell, L.F. Gladden, M.D. Mantle, Hydrogen Bonding Network Disruption in Mesoporous Catalyst Supports Probed by PFG-NMR Diffusometry and NMR Relaxometry, J. Phys. Chem. C 116 (2012) 8975–8982.

[170] C. D'Agostino, L.F. Gladden, M.D. Mantle, A.P. Abbott, E.I. Ahmed, A.Y.M. Al-Murshedi, R.C. Harris, Molecular and ionic diffusion in aqueous - deep eutectic solvent mixtures: probing inter-molecular interactions using PFG NMR, Physical chemistry chemical physics PCCP 17 (2015) 15297–15304.

[171] E.M. Forman, M.A. Trujillo, K.J. Ziegler, S.A. Bradley, H. Wang, S. Prabhakar, S. Vasenkov, Self-diffusion of heptane inside aggregates of porous alumina particles by pulsed field gradient NMR, Microporous and Mesoporous Materials 229 (2016) 117–123.

[172] J. Crank, The Mathematics of Diffusion, 2nd ed., Oxford University Press, 1975.

[173] J. Buffle, Z. Zhang, K. Startchev, Metal Flux and Dynamic Speciation at (Bio)interfaces. Part I: Critical Evaluation and Compilation of Physicochemical Parameters for Complexes with Simple Ligands and Fulvic/Humic Substances, Environ. Sci. Technol. 41 (2007) 7609–7620.

[174] F. Négrier, E. Marceau, M. Che, J.-M. Giraudon, L. Gengembre, A. Löfberg, A systematic study of the interactions between chemical partners (metal, ligands, counterions, and support) involved in the design of Al_2O_3-supported nickel catalysts from diamine-Ni(II) chelates, Journal of Physical Chemistry B 109 (2005) 2836–2845.

[175] M. Komiyama, R. P. Merrill, H. F. Harnserger, Concentration profiles impregnation of porous catalysts: nickel on alumina, Journal of Catalysis 63 (1980) 35–52.

[176] M. Digne, P. Sautet, P. Raybaud, P. Euzen, H. Toulhoat, Hydroxyl Groups on γ-Alumina Surfaces: A DFT Study, Journal of Catalysis 211 (2002) 1–5.

[177] M. Benkhaled, S. Morin, C. Pichon, C. Thomazeau, C. Verdon, D. Uzio, Synthesis of highly dispersed palladium alumina supported particles: Influence of the particle surface density on physico-chemical properties, Applied Catalysis A: General 312 (2006) 1–11.

[178] T. Hiemstra, W. H. Van Riemsdijk, G. H. Bolt, Multsite proton adsorption modeling at the solid/solution interface of (hydr)oxides: a new approach, Journal of colloid and interface science 133 (1989) 91–104.

[179] Multisite proton adsorption modeling at the solid/solution interface of (hydr)oxides: a new approach, Journal of colloid and interface science 133 (1989) 105–117.

[180] C. Contescu, J. Jagiello, J.A. Schwarz, Heterogeneity of proton binding sites at the oxide/solution interface, Langmuir 9 (1993) 1754–1765.

[181] C. Contescu, J. Hu, J. A. Schwarz, 1-pK Multisites description of charge development at the aqueous alumina interface, Journal of the Chemical Society, Faraday Transactions 89 (1993) 4091–4099.

[182] O.Y. Zelenin, Interaction of the Ni^{2+} ion with citric acid in an aqueous solution, Russ J Coord Chem 33 (2007) 346–350.

[183] L. L. Bihan, P. Blanchard, M. Fournier, J. Grimblot, E. Payen, Raman spectroscopic evidence for the existence of 6-molybdoaluminate entities on an Mo/Al_2O_3 oxidic precursor, Journal of the Chemical Society, Faraday Transactions 94 (1998) 937–940.

[184] H. Jeziorowski, H. Knozinger, Raman and Ultraviolet spectroscopic characterization of molybdena on alumina catalysts, The Journal of Physical Chemistry 83 (1979) 1166–1173.

[185] T. Hiemstra, J. C. M. de Wit, W. H. Van Riemsdijk, Multisite proton adsorption modeling at the solid/solution interface of (hydr)oxides: a new approach, Journal of colloid and interface science 133 (1989) 105–117.

[186] J. Moreau, O. Delpoux, K. Marchand, M. Digne, S. Loridant, Rationalization of the aqueous impregnation of molybdenum heteropolyanions on γ-alumina support, in: Scientific Bases for the Preparation of Heterogeneous Catalysts - Proceedings of the 10th International Symposium, Louvain-la-Neuve, Belgium, July 11-15, 2010, Elsevier, 2010, pp. 397–400.

[187] J.A. Bergwerff, T. Visser, B.M. Weckhuysen, On the interaction between Co- and Mo-complexes in impregnation solutions used for the preparation of Al_2O_3-supported HDS catalysts: A combined Raman/UV-vis-NIR spectroscopy study, Catalysis Today 130 (2008) 117–125.

[188] N. Midoux, Mécanique et Rhéologie des fluides en génie chimique, Technique et Documentation - Lavoisier, 1985.

[189] E.W. Washburn, The Dynamics of Capillary Flow, Physical Review 17 (1921) 273–283.

[190] F. Gaulier, Etude de la diffusion des charges lourdes en conditions reelles dans les catalyseurs d'hydrotraitement., Université Claude Bernard Lyon I, Lyon, France, 2016.

[191] P.-G.d. Gennes, F. Brochard-Wyart, Gouttes, bulles, perles et ondes, Nouv. éd. avec CD-Rom. ed., Échelles, Belin, Paris, DL 2005.

[192] S. Kolitcheff, E. Jolimaitre, A. Hugon, J. Verstraete, P.-L. Carrette, M. Tayakout-Fayolle, Tortuosity of mesoporous alumina catalyst supports: Influence of the pore network organization, Microporous and Mesoporous Materials 248 (2017) 91–98.

[193] M. Digne, Use of DFT to achieve a rational understanding of acid-basic properties of γ-alumina surfaces, Journal of Catalysis 226 (2004) 54–68.

[194] J. R. Welty, C. E. Wicks, R. E. Wilson, G. L. Rorrer, Fundamentals of Momentum, Heat and Mass Transfer, 5th ed., John Wiley & Sons, Inc., 2007.

Annexes

Annex A: Measurement of average thickness of nickel based catalysts

The results concerning the evolution of the average thickness as a function of time are gathered in Figure A. 1, for solution concentrations lower than 0.1M [Ni^{2+}] and Figure A. 2, for solution concentrations higher than 0.1M [Ni^{2+}].

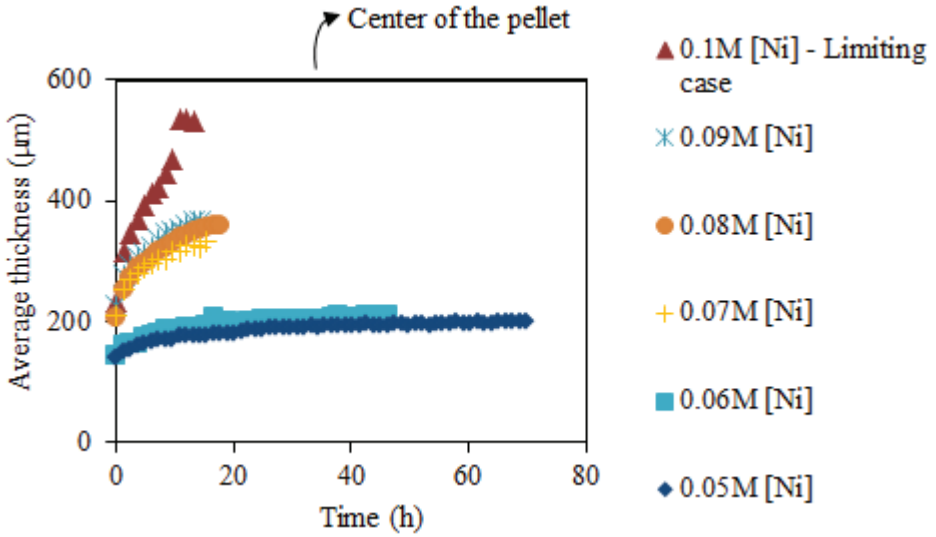

Figure A. 1 - Measurement of the average thickness of nickel ions as a function of time by Indigo© for [Ni^{2+}] concentrations ≤ 0.1M in impregnation solution.

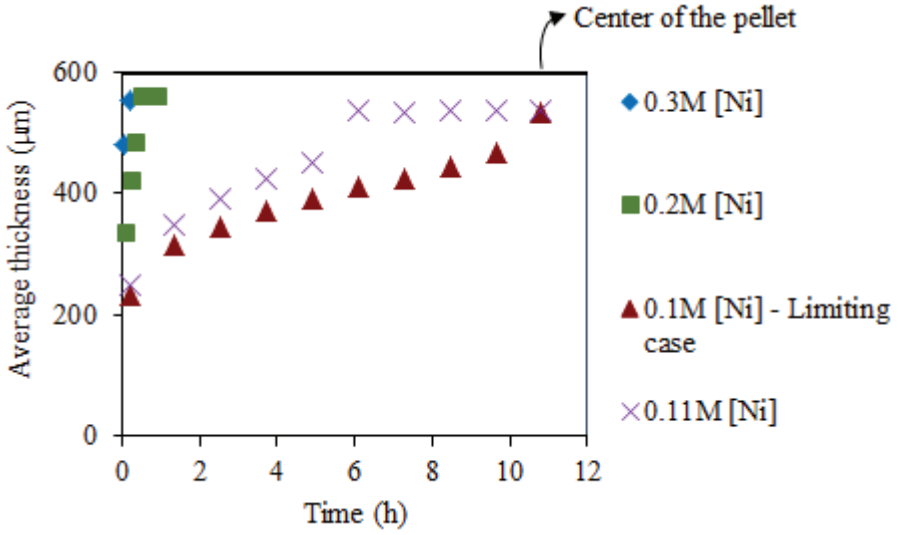

Figure A. 2 - Measurement of the average thickness of nickel ions as a function of time by Indigo© for [Ni^{2+}] concentrations ≥ 0.1M in impregnation solution (For the highest concentration tested, there are not many experimental points, since right at the first measurement the pellet had already an almost homogenous profile.)

Annex B: Characterization of γ-alumina support by Raman spectroscopy

Raman spectroscopy has been performed in γ-alumina. Results are gathered in Figure B. 1. Raman band at 980 cm^{-1} is attributed to the presence of sulfates, which come from support preparation.

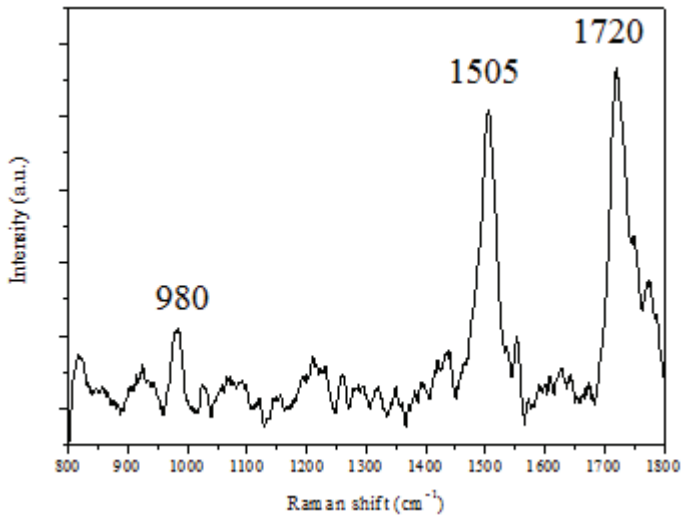

Figure B. 1 - Raman spectra recorded at different positions within a γ-alumina pellet

Annex C: Capillary suction model

Upon dry impregnation, replacement of fluid inside the pore space (called capillary) by impregnation solution takes place through the action of capillary forces. Figure C. 1 shows a schematic picture of a cylindrical pore with radius R_{pore} in contact with the impregnation solution.

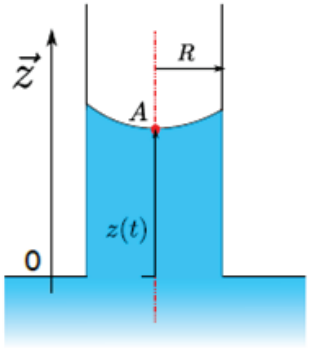

Figure C. 1 - Capillary in contact with wetting fluid

The evolution of the distance travelled by the liquid into the pore (z) as a function of time (t) depends on three different forces:

- Capillary force, $\vec{F}_{capillary}$,
- Friction force , $\vec{F}_{friction}$,
- Gravity force, $\vec{P}$, which is negligible compared to the first ones [188].

To obtain z(t), Washburn model is widely used in the literature as already mentioned in Chapter I, section 2.3, page 45. The following paragraphs explain how to obtain z(t) based on Washburn model.

The linear momentum balance with respect to a control volume is given by the following equation [194]:

$$\begin{aligned}(Sum\ of\ forces\ acting\ on\ control\ volume) \\ = (Rate\ of\ momentum\ out\ of\ control\ volume) \\ - (Rate\ of\ momentum\ into\ control\ volume) \\ + (Rate\ of accumulation\ of\ momentum\ within\ control\ volume)\end{aligned} \qquad \textbf{Eq. C. 1}$$

Recalling the conservation of linear moment and Newton's second law, Eq. C. 1 results in:

$$\sum \vec{F} = \frac{d(m.\vec{v})}{dt} \quad \textbf{Eq. C. 2}$$

Where,

$\Sigma\vec{F}$ is the sum of forces acting on control volume,

m corresponds to mass,

$\vec{v}$ corresponds to velocity

t stands for time.

The evolution of the solution front is a result of capillary and friction forces Eq. C. 2 can be written as:

$$\frac{d(m.\vec{v})}{dt} = \vec{F}_{capillary} + \vec{F}_{friction} \quad \textbf{Eq. C. 3}$$

Capillary force applied in the cross section (S) of the cylindrical pore is based on Young-Laplace equation ($\Delta P_{Laplace}$) and is defined in Eq. C. 4.

$$F_{capillary} = \Delta P_{Laplace} \cdot S = \frac{2 \cdot \gamma \cdot cos\theta}{R_{pore}} \cdot \pi \cdot R_{pore}^2 \quad \textbf{Eq. C. 4}$$

$$F_{capillary} = 2 \cdot \pi \cdot R_{pore} \cdot \gamma \cdot cos\theta \quad \textbf{Eq. C. 5}$$

Where,

R_{pore} stands for the pore radius,

γ is the interfacial tension,

θ is the wetting angle of the wetting fluid on the surface of the capillary.

To define the **friction force**, a linear momentum balance within the control volume schematized in Figure C. 2, which represents the section of a cylindrical tube of radius R and length L is required. The following assumptions are adopted [188]:

- Incompressible, continuous, Newtonian and viscous fluid flowing at steady state within a cylindrical tube
- Fully developed fluid, which means that velocity profile does not change along the flow direction (in this case, z)

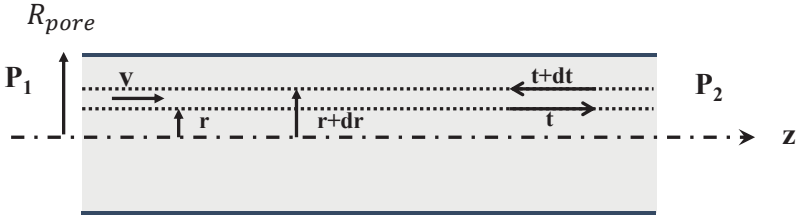

Figure C. 2 - Control volume for a flow within a cylindrical tube of radius R [188]

The momentum balance equation is based on Eq. C. 1. Since the velocity profile does not change along z direction, the resulting force acting on the system is zero. This resulting force is composed of:

- Viscous friction forces (related with shear stress tensor τ), due to radial motion of momentum at a molecular scale
- Pressure forces (P) exerted at the extremities
- Gravity force, which is negligible compared to the first ones [188]

Additionally, the accumulation term is also zero.

Therefore, the linear momentum balance with respect to the control volume schematized in Figure C. 2 is given in Eq. C. 6.

$$(P_1 - P_2) \cdot 2 \cdot \pi \cdot r \cdot dr + 2 \cdot \pi \cdot r \cdot z \cdot \tau - 2 \cdot \pi \cdot (r + dr) \cdot z \cdot (\tau + d\tau) = 0 \qquad \textbf{Eq. C. 6}$$

With,

$$\tau + d\tau = \tau + \frac{d\tau}{dr} dr \qquad \textbf{Eq. C. 7}$$

Rearranging Eq. C. 6 the following relation (Eq. C. 8) is obtained, where $\Delta P_{friction} = P_1 - P_2$:

$$d(r \cdot \tau) = \frac{\Delta P_{friction} \cdot r \cdot dr}{L} \qquad \textbf{Eq. C. 8}$$

Whether,

$$\tau = \frac{\Delta P_{friction} \cdot r}{2L} + \frac{Cte}{r} \qquad \textbf{Eq. C. 9}$$

The first boundary condition is given by:

$$r = 0 : \tau \neq \infty$$

Thus, shear stress is defined in the following equation.

$$\tau = \frac{\Delta P_{friction} \cdot r}{2L} \qquad \textbf{Eq. C. 10}$$

This relation is valid for all viscous fluids in laminar flow in a cylindrical tube. As one of the hypothesis stated is that the fluid is a Newtonian one, the shear stress is given by:

$$\tau = -\mu \cdot \frac{dv}{dr} \qquad \textbf{Eq. C. 11}$$

Where,

μ is the shear viscosity of the fluid

dv/dr is the velocity gradient that corresponds to the deformation rate of a fluid element.

Combining Eq. C. 10 and Eq. C. 11 and integrating between radius, r and pore radius, R_{pore}:

$$\int_{v_r}^{v_{wall}} dv = \int_{r}^{R_{pore}} -\frac{\Delta P_{friction} \cdot r \cdot dr}{2 \cdot \mu \cdot z} \qquad \textbf{Eq. C. 12}$$

To solve integral given by Eq. C. 12, a second boundary condition is necessary.

$$r = R_{pore} : v = 0$$

Therefore, Eq. C. 12 gives:

$$v(r) = \frac{\Delta P_{friction}}{4 \cdot \mu \cdot z} \cdot \left(r^2 - R_{pore}^2\right) \qquad \textbf{Eq. C. 13}$$

The average velocity is given by:

$$\bar{v} = \frac{\int_0^{2\pi} \int_0^R v\,(r).rdrd\theta}{\pi R^2} \qquad \textbf{Eq. C. 14}$$

Hence, the average velocity results in Eq. C. 14, which corresponds to Hagen-Poiseuille equation that relates the average flow velocity with the pressure drop due to friction.

$$\bar{v} = \frac{\Delta P_{friction} \cdot R_{pore}^2}{8 \cdot \mu \cdot z} \qquad \textbf{Eq. C. 15}$$

Finally, friction force ($F_{friction}$) applied in the cross section (S) of the cylindrical pore is defined in Eq. C. 16:

$$F_{friction} = \Delta P_{friction} \cdot S \Leftrightarrow$$
$$F_{friction} = 8 \cdot \pi \cdot \mu \cdot z.\bar{v} \qquad \textbf{Eq. C. 16}$$

The friction force is more important as velocity increases. It is also proportional to the length z of the tube. Eq. C. 17 is then used to calculate the capillary impregnation dynamics, in which $\bar{v}$ represents the penetration rate, which is given by the following equation:

$$\bar{v} = \frac{dz}{dt} \qquad \textbf{Eq. C. 17}$$

Washburn model [189] is used to calculate the penetration rate. This model is valid for low Reynolds number ($Re < 1$) and viscous fluid. It is also assumed that the flow of the impregnation solution in the pore is characterized by Poiseuille steady stated. Therefore, the small inertia effects are neglected. According to Washburn model, becomes:

$$\frac{d(m.\vec{v})}{dt} = \vec{F}_{capillary} + \vec{F}_{friction} = 0 \qquad \textbf{Eq. C. 18}$$

Combining Eq. C. 5, Eq. C. 16 and Eq. C. 18, one obtains:

$$2 \cdot \pi \cdot R_{pore} \cdot \gamma \cdot cos\theta - 8 \cdot \pi \cdot \mu \cdot z.\bar{v} = 0 \qquad \textbf{Eq. C. 19}$$

Combining Eq. C. 17 and Eq. C. 19, it results:

$$\frac{dz^2}{dt} = \frac{R_{pore} \cdot \gamma \cdot cos\theta}{2 \cdot \mu} \qquad \textbf{Eq. C. 20}$$

Assuming that $z(0) = 0$, the **distance z that the impregnation solution travels into the pore** is given by:

$$z = \sqrt{\frac{R_{pore} \cdot \gamma \cdot cos\theta}{2 \cdot \mu} \cdot t} \qquad \textbf{Eq. C. 21}$$

Scientific Production

- **Publication**

L. Catita, A.-A. Quoineaud, D. Espinat, C.Pichon, O. Delpoux, Application of Magnetic Resonance Imaging and Raman Imaging to study the impact of phosphorus in impregnation of hydrotreatment catalysts, Applied Catalysis A:General 547 (2017), 164-175, doi: https://doi.org/10.1016/j.apcata.2017.08.039

- **Conference proceedings**

L. Catita, A.-A. Quoineaud, M. Moreaud, D. Espinat, C.Pichon, O. Delpoux, Impact of citric acid in impregnation of CoMoP/γ-Al_2O_3 catalysts: a MRI-Raman Imaging approach, Topics in Catalysis, in preparation for submission on October 2017

- **Oral communications in international congresses**

L. Catita, A.-A. Quoineaud, O. Delpoux, C.Pichon, Contribution of NMR and Raman imaging to study the impact of citric acid in the impregnation of hydrotreatment catalysts, 13th European Congress on Catalysis , Florence, Italy, 2017

L. Catita, A.-A. Quoineaud, O. Delpoux, C.Pichon, Contribution of NMR and Raman imaging to monitor the impregnation step of hydrotreatment catalysts, 25th North American Catalysis Society Meeting, Denver, USA, 2017

L. Catita, A. Nowacka, F. Guenneau, A. Nossov, O. Delpoux, A.-A. Quoineaud, A. Gédéon, Operando monitoring of Ni and Co ions impregnation inside catalyst pellets by Magnetic Resonance Imaging, 24th North American Catalysis Society Meeting, Pittsburgh, USA, 2015

- **Poster communications in international congresses**

L. Catita, A.-A. Quoineaud, O. Delpoux, A. Gédéon, C.Pichon, Contribution of NMR Imaging to monitor impregnation step of HDT catalysts, 7th International Symposium on Molecular Aspects of Catalysis by Sulfides, Doorn, The Netherlands, 2015

- **Others**

L. Catita, A.-A. Quoineaud, O. Delpoux, A. Gédéon, C.Pichon, Contribution of NMR and Raman imaging for the modelisation and rationalization of impregnation process of metallic salt in porous media, Journée de l'Ecole Doctorale de Chimie de Lyon (2016), Villeurbanne, France